OPTIMAL PANEL ZONE PARTICIPATION IN STEEL MOMENT FRAMES

A Dissertation

by

THANH TAT NGO

Submitted to the Office of Graduate and Professional Studies of
Texas A&M University
in partial fulfillment of the requirements for the degree of

DOCTOR OF PHILOSOPHY

Chair of Committee,	Gary T. Fry
Committee Members,	Harry L. Jones
	Stefan Hurlebaus
	Anastasia Muliana
Head of Department,	Robin Autenrieth

May 2014

Major Subject: Civil Engineering

ABSTRACT

This work investigates the role of panel zones in the seismic response of buildings using steel moment frames. To address this debated matter requires well-developed finite element models that can accurately simulate the behavior of frame systems under a variety of ground motions. A procedure to form an optimally designed frame subassemblage is proposed to maximize its inelastic deformation energy capacity. The proposed procedure is then applied to an available steel moment frame for evaluating its overall seismic performance.

A new frame finite element is developed to have a feature that is not present in available structural analysis softwares. The feature is to capture the local buckling of thin-wall structural members by using line elements. The performance of the developed theory for the new element is verified with a highly refined finite element model using shell elements. A robust analytical solution is also developed for simulating the behavior of beam-to-column connections in steel lateral force-resisting frames. The results obtained from the developed theory for the connections remarkably match available experimental results.

This study proposed a procedure to maximize the inelastic deformation energy of steel moment frame subassemblages. It was found that the high ratio of the column strength to the panel zone strength has considerably positive effects on maximizing the inelastic deformation capacity. The proposed procedure can be applied to a whole frame system to increase the overall seismic performance of that frame. As a result, the safety or reliability of a steel moment frame under earthquakes can be improved while maintaining the fabrication of the structure at an effective cost.

To the memory of my grandfather, Phạm Đắc Lực

To my mother, Phạm Quốc Sử, and my father, Ngô Đăng Lầu

ACKNOWLEDGEMENTS

I wish to thank my PhD committee chair, Dr. Gary T. Fry, for his patience, support, and guidance. I would like to thank my committee members, Dr. Harry Jones, Dr. Stefan Hurlebaus, and Dr. Anastasia Muliana for their help and advice. Their guidance enabled me to explore interesting knowledge horizons. My sincere thanks are to Dr. Krista Stacey, Dr. Robert Webb, Dr. Bowen Loftin, and Dr. Larry Johnson for their critical support and advice to help me overcome difficult times during my study. I thank Ms. Amy White for her help with editorial review of my dissertation. I also thank Prof. Laurence Oeth and Dr. Cassandra Oeth for their friendship and valuable advice. I must acknowledge different kinds of support from other professors, colleagues, and friends over several past years.

I am grateful to Dr. Nguyễn Cao Dương at Vietnam Institute for Building Science and Technology and Dr. Chris Letchford at Rensselaer Polytechnic Institute for their constant encouragement and valuable advice. Lastly, I am always grateful to my family for their endless love and unconditional support. They give me strength to overcome challenges in life.

TABLE OF CONTENTS

Page

Page

LIST OF FIGURES

Page

Page

Page

LIST OF TABLES

Page

CHAPTER I

INTRODUCTION AND LITERATURE REVIEW

This work addresses the role of panel zones in the seismic performance of steel moment frames. It contributes to resolving the long-standing debate over how panel zones should be designed. This study proposes an innovative approach for designing safer and more cost effective steel buildings.

I.1. Panel zone role

Steel moment frames have been constructed in a large number of buildings since the 1960s. Moment frames are defined as frames with restrained connections between columns and beams for the frames to resist lateral loads (FEMA 2004). Buildings designed with this structural system have no height limitation as specified in (ASCE 2005). Until the 1994 earthquake in Northridge, CA, the moment frame system was strongly believed to be capable of withstanding large inelastic deformation without significant degradation in strength or the development of instability. Fractures in the beam-to-column welded connections were discovered after the Northridge event, as well as the 1995 earthquake in Kobe, Japan (FEMA 2000a; Kunnath and Malley 2002). Extensive studies have been performed following the two disasters. However, one remaining issue is the role of panel zones at the beam-to-column connections.

The panel zone (PZ) is the web area of the beam-to-column connection bordered by the column flanges and the extension of beam flanges (AISC 2010c). Significant shear forces develop in the PZ of a moment frame under lateral loads. Weak PZs can exhibit a large cyclic inelastic deformation capacity (Krawinkler et al. 1971), providing the frame with a great source of energy dissipation during seismic events. The deformation of the PZ can significantly contribute to the overall dynamic be-

havior of the frame and the story drift (Hsiao et al. 2008; Kim and Engelhardt 2002; Krawinkler 1978).

Beam-to-column connections with relatively weak PZs were encouraged in design practice from 1985 to 1994 (FEMA 2000b). The purpose of weak PZs was to provide the building with significant ductility. The intent was to make structural systems capable of withstanding large inelastic deformations without suffering significant strength degradation or instability development that could result in a collapse. Following the 1994 Northridge earthquake, premature brittle fractures of beam-to-column connections were found in a number of steel moment frames (SMF). Report FEMA 350 (FEMA 2000a) reported that the damaged buildings had a number of stories ranging from 1 to 26. At the time of the earthquake, the age range spanned from newly built structures to 30 year-old buildings.

The buildings damaged during the Northridge earthquake met the basic intent of the building codes by limiting structural damage without a collapse. However, premature brittle fractures of the frame connections were not anticipated or desired. The connection damage caused considerable economic losses associated with damage investigation and repair. Signs of structural damage such as permanent drifts and damage to architectural elements were not overt, making post-earthquake evaluations difficult. Repairing the damaged connection is more costly than earthquake damage detection, and with such high repair costs, it may be more practical to demolish the building than to repair the frame connections.

There is a consensus in the engineering and science communities that the columns and beams built prior to 1994 are weakened at the frame connection. In addition, the joint penetration welds between the beam flanges and column flanges often introduce significant discontinuities and slag inclusions at the weld root. Cracks can therefore initiate from these stress raisers if large inelastic shear distortion is demanded.

However, there is some debate among researchers regarding the design of PZs for moment frames. For example, a balanced design was advised in Report FEMA 355D to obtain the best performance for the structures (FEMA 2000b). The balanced design allows shear yielding of the PZ and flexural yielding of the beam to occur at nearly the same load. Nonetheless, Ricles et al. (2002) performed a number of experiments on welded unreinforced beam-to-column moment connections and advised the use of strong PZs to enhance connection performance. Lee et al. (2005) found in many previous studies that weak or under-designed PZs also performed satisfactorily. For instance, test specimens with considerably weak PZs still exhibited excellent performance in Jones et al. (2002). Essentially all yielding occurred in the PZs of those specimens, resulting in large story drifts without strength degradation.

Figure I.1 illustrates two limiting cases: a) plastic hinges in the beams, and b) plastic hinges in the column panel zones. In the former case, the energy is dissipated largely through the inelastic deformation of the designed plastic hinges in the beams. In the latter case, the energy dissipation comes from the inelastic shear deformation of PZs.

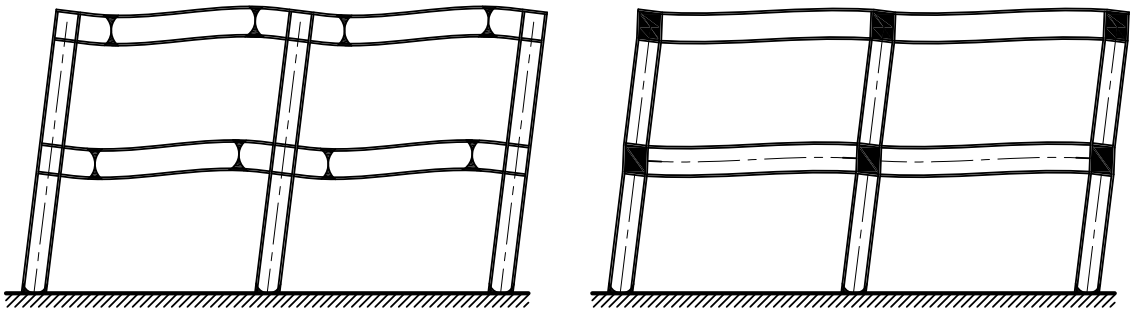

a) Plastic hinges in beams b) Platic hinges in panel zones

Figure I.1: Formation of plastic hinges in SMFs.

Recent US building codes tend to increase the strength of PZs in the frames de-

spite the effectiveness of weak PZs in many studies (AISC 2010c; Lee et al. 2005). As a result, column sizes need to increase, or doubler plates need to be welded to the column flanges, increasing construction cost, sometimes substantially, and reducing the energy dissipation capacity of the frames. Kim and Engelhardt (2002) found that doubler plates were not fully effective in contributing to PZ strength and stiffness. Hajjar et al. (2003) pointed out a tendency toward a more conservative design and detailing of steel moment-resisting connections in the wake of the 1994 Northridge earthquake. Doubler plates were often specified when they were found to be unnecessary or if the plates were thicker than required. In addition, the reinforcement with doubler plates may actually be detrimental to the connection since it results in more complicated stress and strain fields in the connection and introduces potential flaws during fabrication. A detailed study on how much strength the PZ requires is needed.

I.2. Panel zone models for frame simulation

Analytical models that can accurately describe the PZ behavior under loading are critical in evaluating PZ effects on the performance of a structural system. Several analytical PZ models have been developed in order to account for the PZ participation in the overall seismic performance of SMF buildings. These models produce agreeable results in the elastic range of the PZ response. However, significant discrepancies are found in the inelastic range. The PZ model proposed by Krawinkler et al. (1971) is found to be among the earliest models. The researchers performed a number of experiments and analyses. They proposed a mathematical model relating the PZ shear force to the PZ shear deformation. Nonlinear rotational springs are created based on this relationship to represent PZs in structural models.

Kim and Engelhardt (2002) pointed out that the models developed by Krawinkler and other researchers were based on specimens with relatively thin column flanges. They therefore developed a different PZ model for monotonic and cyclic loading. The cyclic model is based on the bounding surface theory and the rules of bound movement. The bounding surface always encloses the yield surface in the stress space for the material under cyclic loading (Dafalias and Popov 1975, 1976). The rules of bound movement describe the movement of stress bounds in the cyclic stress-strain curve (Cofie and Krawinkler 1985). Jin (2002) also reviewed available PZ models and proposed an updated model based on Krawinkler's model and the bounding surface theory. Jin calibrated parameters in Krawinkler's model to previous experimental results that include small to large size PZs.

I.3. Seismic performance of SMFs

It is often of interest to investigate the effect of PZs on the overall seismic performance of SMFs. A multi-story frame can have different PZs due to the change of beam and column sizes from one story to another. Every PZ in a moment-frame building, not just a single PZ, plays a role in the seismic behavior of the frame. The distribution of mass and stiffness throughout the frame and the loading conditions, i.e. gravity loads, and the characteristics of ground motions simultaneously dictate the seismic behavior of the frame. Additionally, beams can significantly yield well before some instability sets into the PZ region. Deterioration can act much faster in beams than in the beam-to-column connection (Krishnan and Muto 2011).

A limited number of studies on the seismic response of PZs in SMF buildings are found in the literature. A noticeable study is performed by Jin and El-Tawil (2005). They assessed the role of PZs in steel moment-frame buildings. A large number of dynamic analyses were implemented to investigate the seismic behavior of 4-, 8-, and

6-story moment steel frames, which were designed based on FEMA-350. The PZ participation in the behavior of the three frames was considerably low, suggesting the need for further studies.

Hsiao et al. (2008) analyzed multistory moment steel frames with welded flange plate connections by comparing the story drift between the structural models with and without a PZ model. They suggested the use of correction factors to obtain the story drift from the model without using a PZ model (line-element model). The frame connections in their study were designed in accordance with FEMA-350 (FEMA 2000a); however, the allowable level of PZ participation in the structures is not conclusive.

I.4. Objectives and scope

This research is aimed at determining an optimal participation of PZs in the inelastic deformation of SMFs. Such optimal participation is obtained by maximizing the energy dissipation capacity of SMFs. Constraints for this optimization problem are developed based on the seismic provision for special moment frames specified in ANSI/AISC 341-10 (AISC 2010b). According to this provision, SMF columns shall remain elastic at least until the fully yielded and strain-hardened SMF beams. Thus, the yielding of the beams needs to be designed proportionally to that of their corresponding PZs.

Conventionally, nonlinear finite element (FE) analyses of steel frame systems do not account for local buckling of beams and columns. Local buckling effects can be included in the analyses that use shell elements (Kim and Kang 2004; Wang 2011). However, using shell elements is not a practical solution. This solution needs a myriad of shell elements, leading to difficulties in modeling of structural systems and increased computational cost in analyses. A viable solution is to use line elements

in frame analyses. The nonlinear inelastic behavior of a line element is commonly simulated by using a fiberized section. This fiberized element is yet to be able to account for local buckling of beams and columns (Cordova et al. 2004; Nakata et al. 2012).

To achieve the research goal, research activities comprise

1. Developing a line element that can account for local buckling of beams and columns,
2. Developing an economic connection model for the analysis of SMF connections,
3. Implementing new line elements and a connection model in a commonly used FE framework,
4. Applying the developed connection model and line element to experimental studies,
5. Proposing a methodology to optimize the PZ participation in the behavior of beam-to-column connections of SMFs under lateral loading effects,
6. Building FE models for different SMF systems using suites of ground motions to perform nonlinear time history analyses, and
7. Evaluating the overall seismic performance of SMFs with optimal participation of PZs.

The next section presents a methodology to develop a line element that accounts for local buckling effects.

CHAPTER II

FORCE-BASED ELEMENTS WITH LOCAL BUCKLING CONSIDERATION

Recent studies have highlighted advantages in formulating the finite element model of frame systems based on the force-based approach. In this approach, beam and column elements or frame elements are developed based on force interpolation functions. Using force interpolation functions always ensures exact equilibrium conditions, reducing the error related to discretizing frame systems. Meanwhile, it is often impossible to find exact displacement interpolation functions, in the more traditional displacement-based approach (De Souza 2000; Spacone 1994). Thus, the force-based element approach is used with the consideration of local buckling of beams and columns.

Local buckling of SMF beams and columns is treated by applying an effective width concept to a nonlinear finite element method. The plates of beams and columns can continue carrying loads even after buckling (Subramanian 2011). This post-buckling capacity is determined by using the effective width concept (von Karman et al. 1932; Yu and LaBoube 2010). Based on this concept, the width of the element flanges under compression is reduced to an effective width due to buckling. The computation for this element is implemented using the C++ programming language (Soulie 2007) and is coded following the pattern as in Scott et al. (2008). It is incorporated into the finite element framework of OpenSees (McKenna et al. 2000).

II.1. Transformation of nodal displacements and forces

In the Cartesian coordinate system formed by three unit vectors $\mathbf{i}_1$, $\mathbf{i}_2$, and $\mathbf{i}_3$, the components of any vector $\mathbf{v}$ is

$$\mathbf{v}_i = \mathbf{v} \bullet \mathbf{i}_i \tag{II.1}$$

Another Cartesian coordinate system described by vectors $\mathbf{i}'_1$, $\mathbf{i}'_2$, and $\mathbf{i}'_3$ can be related to the former system as

$$\begin{Bmatrix} \mathbf{i}'_1 \\ \mathbf{i}'_2 \\ \mathbf{i}'_3 \end{Bmatrix} = \underbrace{\begin{bmatrix} c_{11} & c_{12} & c_{13} \\ c_{21} & c_{22} & c_{23} \\ c_{31} & c_{32} & c_{33} \end{bmatrix}}_{\mathbf{c}} \begin{Bmatrix} \mathbf{i}_1 \\ \mathbf{i}_2 \\ \mathbf{i}_3 \end{Bmatrix} \tag{II.2}$$

where $c_{ij} = \cos(\mathbf{i}'_i, \mathbf{i}_j)$. It is noted that by derivation based on the preservation of a vector length in the transformation, the transpose and the inverse of $\mathbf{c}$ are equal (Collins 2004; Lai et al. 2010). Now the components of $\mathbf{v}$ in the latter coordinate system can be derived as

$$v'_i = c_{ij} v_j \tag{II.3}$$

Figure II.1 shows a 2-D frame element with the nodal displacements, $\mathbf{U}^g$, and nodal forces, $\mathbf{F}^g$, in the global coordinate system $(\mathbf{i}_1, \mathbf{i}_2, \mathbf{i}_3)$ and in its local coordinate system $(\mathbf{i}'_1, \mathbf{i}'_2, \mathbf{i}'_3)$. The displacements and forces are respectively expressed as

$$\mathbf{U}^g = \begin{bmatrix} U_1^g & U_2^g & U_3^g & U_4^g & U_5^g & U_6^g \end{bmatrix}^T \tag{II.4}$$

$$\mathbf{F}^g = \begin{bmatrix} F_1^g & F_2^g & F_3^g & F_4^g & F_5^g & F_6^g \end{bmatrix}^T \tag{II.5}$$

Figure II.2 shows the element with the nodal displacement components, $\mathbf{U}^l$, and

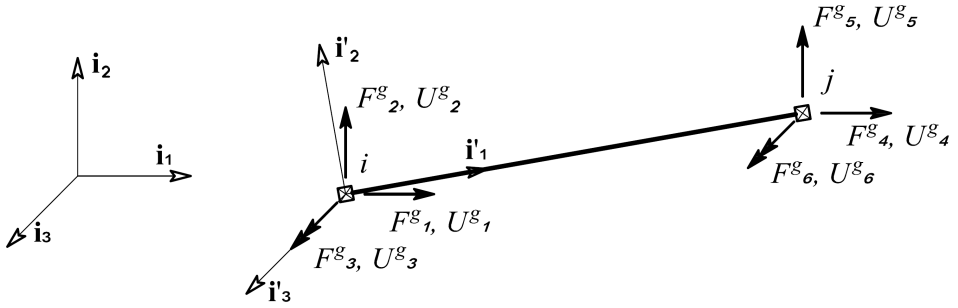

Figure II.1: 2D frame elements with global nodal displacements and forces.

nodal force components, $\mathbf{F}^l$, in the local coordinate system. Using the result obtained as in (II.3) gives

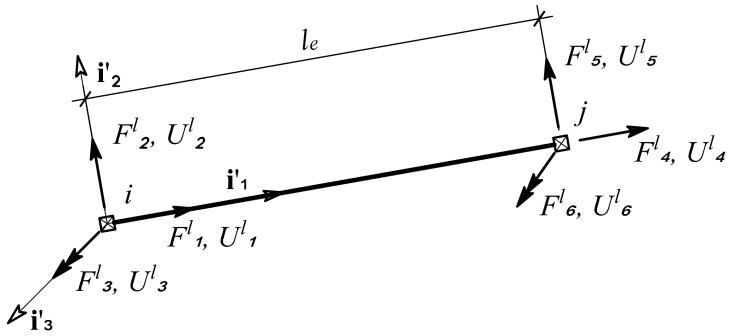

Figure II.2: 2D frame elements with local nodal displacements and forces.

$$\mathbf{U}^l = \begin{Bmatrix} U_1^l \\ U_2^l \\ U_3^l \\ U_4^l \\ U_5^l \\ U_6^l \end{Bmatrix} = \underbrace{\begin{bmatrix} c_{11} & c_{12} & 0 & 0 & 0 & 0 \\ c_{21} & c_{22} & 0 & 0 & 0 & 0 \\ 0 & 0 & 1 & 0 & 0 & 0 \\ 0 & 0 & 0 & c_{11} & c_{12} & 0 \\ 0 & 0 & 0 & c_{21} & c_{22} & 0 \\ 0 & 0 & 0 & 0 & 0 & 1 \end{bmatrix}}_{\mathbf{C}^{gl}} \begin{Bmatrix} U_1^g \\ U_2^g \\ U_3^g \\ U_4^g \\ U_5^g \\ U_6^g \end{Bmatrix} = \mathbf{C}^{gl} \times \mathbf{U}^g \qquad \text{(II.6)}$$

and

$$\mathbf{U}^g = \left(\mathbf{C}^{gl}\right)^{-1} \mathbf{U}^l \qquad \text{or} \qquad \mathbf{U}^g = \left(\mathbf{C}^{gl}\right)^{T} \mathbf{U}^l \tag{II.7}$$

where $C_{ij}^{gl} = \cos(U_i^l, U_j^g)$. Similarly, the local nodal forces and the global nodal forces are related by

$$\mathbf{F}^l = \begin{bmatrix} F_1^l & F_2^l & F_3^l & F_4^l & F_5^l & F_6^l \end{bmatrix}^T = \mathbf{C}^{gl} \times \mathbf{F}^g \tag{II.8}$$

$$\text{or} \qquad \mathbf{F}^g = \left(\mathbf{C}^{gl}\right)^{T} \mathbf{F}^l \tag{II.9}$$

II.2. Compatibility conditions

In the Euler-Bernoulli beam theory, the longitudinal strain in a beam can be determined from the longitudinal strain at the beam reference axis, $\varepsilon_r(x)$, and the curvature of this axis, $\kappa_z(x)$ (Carol and Murcia 1989; Kassimali 2005). The reference axis (axis x) usually originates from joint i and points to joint j of an element, see Figures II.2 and II.3. These two quantities are formulated respectively as

$$\varepsilon_r\left(x\right) = \frac{\mathrm{d}u_x}{\mathrm{d}x} \tag{II.10}$$

$$\kappa_z(x) \simeq \frac{\mathrm{d}^2 u_y}{\mathrm{d}x^2} = \frac{\mathrm{d}\theta_z}{\mathrm{d}x} \tag{II.11}$$

where u_x and u_y are the longitudinal displacement and the transverse displacement at the reference axis. The rotation of a cross section at x is determined as

$$\theta_z\left(x\right) = \frac{\mathrm{d}u_y}{\mathrm{d}x} \tag{II.12}$$

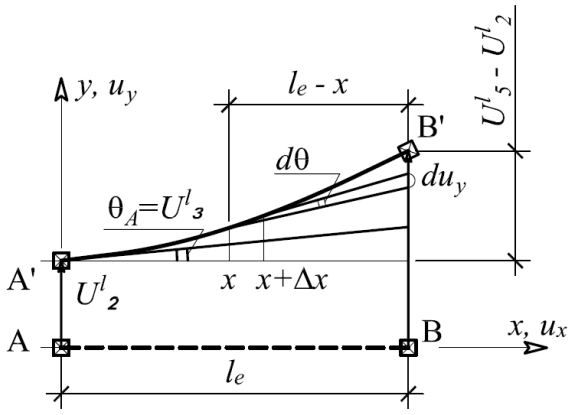

Figure II.3: Analytical geometry of deflected beams.

Integrating (II.10) and (II.11) gives

$$U_4^l - U_1^l = \int_0^{l_e} \varepsilon_r \mathrm{d}x \tag{II.13}$$

$$U_6^l - U_3^l = \int_0^{l_e} \kappa_z \mathrm{d}x \tag{II.14}$$

where l_e = length of the beam element.

Figure II.3 shows the analytical geometry of a deflected beam. Based on the assumption of small deformations, the following relationship is obtained:

$$U_5^l - U_2^l - U_3^l l_e = \int_{\theta_A}^{\theta_B} (l_e - x)\, \mathrm{d}\theta = \int_0^{l_e} (l_e - x)\, \kappa_z \mathrm{d}x \Leftrightarrow \tag{II.15}$$

$$\frac{U_5^l - U_2^l}{l_e} - U_3^l = \int_0^{l_e} \kappa_z \left(1 - \frac{x}{l_e}\right) \mathrm{d}x \tag{II.16}$$

Combining (II.14) and (II.15) gives

$$U_6^l - \frac{U_5^l - U_2^l}{l_e} = \int_0^{l_e} \frac{x}{l_e} \kappa_z \mathrm{d}x \tag{II.17}$$

If displacement vector **U** is defined as

$$\begin{Bmatrix} U_1 \\ U_2 \\ U_3 \end{Bmatrix} = \begin{Bmatrix} U_4^l - U_1^l \\ \dfrac{U_5^l - U_2^l}{l_e} - U_3^l \\ U_6^l - \dfrac{U_5^l - U_2^l}{l_e} \end{Bmatrix} \tag{II.18}$$

vector **U** is the non-rigid-body displacement vector of the beam element (Neuenhofer and F.C. 1997). Component U_1 is the non-rigid-body axial displacement of the element. Components U_2 and U_3 are non-rigid-body rotations at the two element end nodes as shown in Figure II.4.

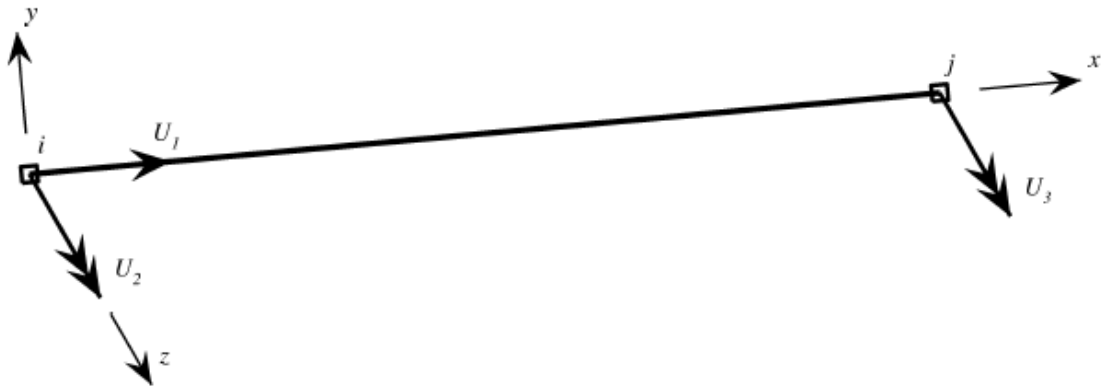

Figure II.4: 2D frame elements with nodal displacements in the non-rigid-body mode.

The matrix that transforms the local nodal displacements to the non-rigid-body

displacement can be formulated as follows:

$$\mathbf{U} = \begin{Bmatrix} U_1 \\ U_2 \\ U_3 \end{Bmatrix} = \underbrace{\begin{bmatrix} -1 & 0 & 0 & 1 & 0 & 0 \\ 0 & -\dfrac{1}{l_e} & -1 & 0 & \dfrac{1}{l_e} & 0 \\ 0 & \dfrac{1}{l_e} & 0 & 0 & -\dfrac{1}{l_e} & 1 \end{bmatrix}}_{\mathbf{C}^{lUn}} \begin{Bmatrix} U_1^l \\ U_2^l \\ U_3^l \\ U_4^l \\ U_5^l \\ U_6^l \end{Bmatrix} \qquad \text{or} \qquad \text{(II.19)}$$

$$\mathbf{U} = \mathbf{C}^{lUn} \times \mathbf{U}^l = \mathbf{C}^{lUn} \times \mathbf{C}^{gl} \times \mathbf{U}^g \qquad \text{(II.20)}$$

Vector $\mathbf{U}$ can now determined as

$$\mathbf{U} = \begin{Bmatrix} U_1 \\ U_2 \\ U_3 \end{Bmatrix} = \int_0^{l_e} \underbrace{\begin{bmatrix} 1 & 0 \\ 0 & 1 - \dfrac{x}{l_e} \\ 0 & \dfrac{x}{l_e} \end{bmatrix}}_{\mathbf{b}^T(x)} \underbrace{\begin{Bmatrix} \varepsilon_r \\ \kappa_z \end{Bmatrix}}_{\boldsymbol{\varepsilon}(x)} \mathrm{d}x \Leftrightarrow \qquad \text{(II.21)}$$

$$\mathbf{U} = \int_0^{l_e} \mathbf{b}^T(x)\, \boldsymbol{\varepsilon}(x)\, \mathrm{d}x \qquad \text{(II.22)}$$

For numerical integration in the domain of $\{-1 \leq \xi \leq 1\}$, it is noted that

$$\frac{x}{l_e} = \frac{\xi + 1}{2} \qquad \text{and} \qquad \mathrm{d}x = \frac{l_e}{2}\mathrm{d}\xi \qquad \text{(II.23)}$$

Using Gauss-Lobatto integration scheme (Burgoyne and Crisfield 2005; Eslahchi et al.

2005), $\mathbf{U}$ can be evaluated as

$$\mathbf{U} = \int_{-1}^{1} \mathbf{b}^T \left(\frac{\xi + 1}{2} l_e \right) \boldsymbol{\varepsilon} \left(\frac{\xi + 1}{2} l_e \right) \frac{l_e}{2} \mathrm{d}\xi \tag{II.24}$$

$$\mathbf{U} = \frac{l_e}{2} \sum_{i=1}^{n} \mathbf{b}^T \left(\frac{\xi_i + 1}{2} l_e \right) \boldsymbol{\varepsilon} \left(\frac{\xi_i + 1}{2} l_e \right) w_i \tag{II.25}$$

where ξ_i = Gauss-Lobatto points or coordinates; w_i = integration weights.

II.3. Equilibrium conditions

Figure II.5 shows the nodal responses of a frame element with and without rigid-body modes. Based on the equilibrium conditions for the element, the relationship between the non-rigid-body nodal forces and the local nodal forces can be formulated as (Carol and Murcia 1989)

$$\mathbf{F}^l = \begin{Bmatrix} F_1^l \\ F_2^l \\ F_3^l \\ F_4^l \\ F_5^l \\ F_6^l \end{Bmatrix} = \underbrace{\begin{bmatrix} -1 & 0 & 0 \\ 0 & -\frac{1}{l_e} & \frac{1}{l_e} \\ 0 & -1 & 0 \\ 1 & 0 & 0 \\ 0 & \frac{1}{l_e} & -\frac{1}{l_e} \\ 0 & 0 & 1 \end{bmatrix}}_{\mathbf{C}^{nFl}} \underbrace{\begin{Bmatrix} F_1 \\ F_2 \\ F_3 \end{Bmatrix}}_{\mathbf{F}} = \mathbf{C}^{nFl} \times \mathbf{F} \tag{II.26}$$

where $\mathbf{C}^{nFl}$ is the transformational matrix to transform from the local nodal forces to the non-rigid forces. The non-rigid-body nodal force vector can also be extracted

from the local nodal forces using

$$\mathbf{F} = \underbrace{\begin{bmatrix} -1 & 0 & 0 & 0 & 0 & 0 \\ 0 & 0 & -1 & 0 & 0 & 0 \\ 0 & 0 & 0 & 0 & 0 & 1 \end{bmatrix}}_{\mathbf{C}^{lFn}} \times \mathbf{F}^l = \mathbf{C}^{lFn} \times \mathbf{F}^l \tag{II.27}$$

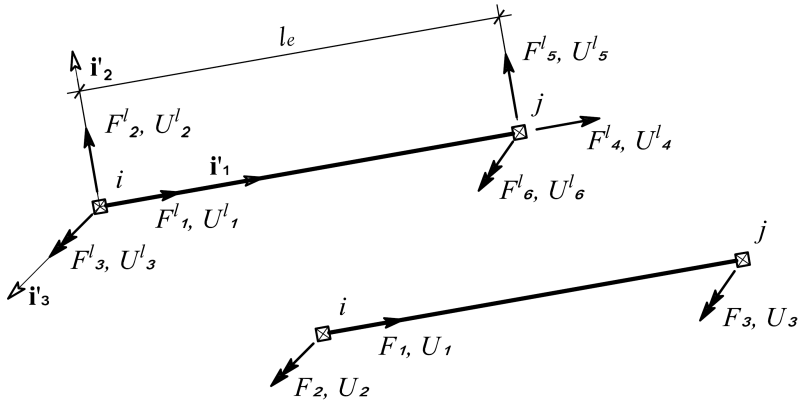

Figure II.5: Nodal responses with and without rigid-body modes.

Section forces include the axial force, $f_1(x)$, moment, $f_2(x)$, and the shear force. The shear force is dependent on the moment and can be derived as $-\mathrm{d}f_2/\mathrm{d}x$. The independent section forces can be visualized by the axial force and moment diagrams and are formulated as

$$\mathbf{f}(x) = \begin{Bmatrix} f_1(x) \\ f_2(x) \end{Bmatrix} = \underbrace{\begin{bmatrix} 1 & 0 & 0 \\ 0 & 1-\xi & \xi \end{bmatrix}}_{\mathbf{b}(x)} \underbrace{\begin{Bmatrix} F_1 \\ F_2 \\ F_3 \end{Bmatrix}}_{\mathbf{F}}, \qquad \xi = \frac{x}{l_e} \tag{II.28}$$

$$\text{or} \qquad \mathbf{f}(x) = \mathbf{b}(x) \times \mathbf{F} \tag{II.29}$$

It is noted that although the matrix of force interpolation functions, $\mathbf{b}(x)$, is used, the formulation is not approximate but exact in determining the section forces, $\mathbf{f}(x)$, in terms of generalized nodal forces, $\mathbf{F}$.

II.4. Effective width

The effective width, b_e, of a plate under compression can be determined as a function of compressive strain as (Wang et al. 1975)

$$\frac{b_e}{b_0} = \sqrt{\frac{\varepsilon_{cr}}{\varepsilon_{\max}}}\left(1 - \xi_b\sqrt{\frac{\varepsilon_{cr}}{\varepsilon_{\max}}}\right) \tag{II.30}$$

where b_0 = initial width of the plate; $\varepsilon_{\max}$ = maximum edge strain; ε_{cr} = critical buckling strain; ξ_b = modification factor. The critical buckling strain is a function of the slenderness, material properties, and boundary conditions of the plate:

$$\varepsilon_{cr} = \frac{k\pi^2}{12\left(1-\nu^2\right)\left(\frac{b_0}{t}\right)^2} \tag{II.31}$$

where k = boundary condition and aspect ratio coefficient; ν = Poisson's ratio; t = plate thickness.

The change of the effective width with respect to the compressive strain is determined by the following differentiation($\varepsilon_{\max} \equiv \varepsilon$):

$$\frac{\mathrm{d}b_e}{\mathrm{d}\varepsilon} = b_0\xi_b\frac{\varepsilon_{cr}}{\varepsilon^2} - \frac{b_0}{2}\sqrt{\frac{\varepsilon_{cr}}{\varepsilon^3}} \tag{II.32}$$

II.5. Section stiffness matrix

The section stiffness matrix is the differentiation of the section force vector with respect to the section deformation vector. It can hence be formulated as

(Carol and Murcia 1989)

$$\mathbf{k}_s(x) = \frac{\mathrm{d}\mathbf{f}(x)}{\mathrm{d}\boldsymbol{\varepsilon}(x)} = \begin{bmatrix} \dfrac{\partial f_1}{\partial \varepsilon_r} & \dfrac{\partial f_1}{\partial \kappa_z} \\ \dfrac{\partial f_2}{\partial \varepsilon_r} & \dfrac{\partial f_2}{\partial \kappa_z} \end{bmatrix} \equiv \begin{bmatrix} \dfrac{\partial N_x}{\partial \varepsilon_r} & \dfrac{\partial N_x}{\partial \kappa_z} \\ \dfrac{\partial M_z}{\partial \varepsilon_r} & \dfrac{\partial M_z}{\partial \kappa_z} \end{bmatrix} \tag{II.33}$$

Vector $\mathbf{f}$ on an element cross section is obtained by integrating the normal stress over the entire cross-section area, A, as

$$N_x = \int_A \sigma(x, y)\, \mathrm{d}A \tag{II.34}$$

$$M_z = -\int_A y\sigma(x, y)\, \mathrm{d}A \tag{II.35}$$

where A varies with x and is a function of the effective width, b_e, which is in turn dependent on the strain state in the cross section at x:

$$A \equiv A(x) = A\left[b_e\left[\varepsilon_{\max}(x)\right]\right] \tag{II.36}$$

Figure II.6 shows an increment of a beam element under deformation. As shown, the strain at any layer can be determined as the following:

$$\frac{\varepsilon' \Delta x}{y} = \frac{\Delta x}{\rho} \Leftrightarrow \frac{\varepsilon'}{y} = \kappa_z \Rightarrow \tag{II.37}$$

$$\varepsilon(x, y) = \varepsilon_r(x) - y\kappa_z(x) \tag{II.38}$$

The differentiation of the section forces with respect to each section deformation

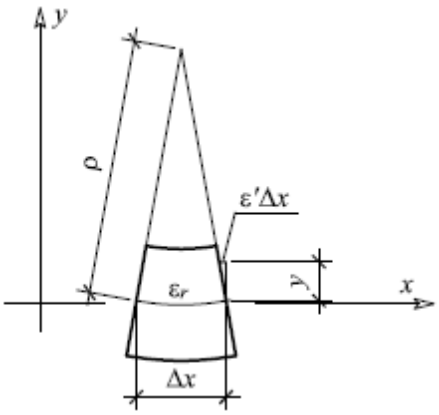

Figure II.6: Deformation of an element increment.

component can be implemented as

$$\frac{\partial N_x}{\partial \varepsilon_r} = \int\limits_A \frac{\partial \sigma(x,y)}{\partial \varepsilon_r} \mathrm{d}A + \int\limits_A \sigma(x,y) \frac{\partial}{\partial \varepsilon_r} \mathrm{d}A \tag{II.39}$$

For a wide-flange(W) shape under in-plane deformation, by dropping local coordinates x and y,

$$\frac{\partial N_x}{\partial \varepsilon_r} = \int\limits_A \frac{\partial \sigma}{\partial \varepsilon_r} \mathrm{d}A + \int\limits_{t_{fx}} \sigma \frac{\partial}{\partial \varepsilon_r} (b_{bx} \mathrm{d}y) + \int\limits_{d_{wx}} \sigma \frac{\partial}{\partial \varepsilon_r} (t_{wx} \mathrm{d}y) + \int\limits_{t_{fx}} \sigma \frac{\partial}{\partial \varepsilon_r} (b_{tx} \mathrm{d}y) \tag{II.40}$$

where t_{fx} = effective flange thickness; b_{tx} , b_{bx} = effective flange widths; $d_{wx} = d_x - 2t_{fx}$ = clear width of the web; d_x = section depth; t_{wx} = web thickness. Since $\partial\varepsilon/\partial\varepsilon_r = 1$, this equation is equivalent to

$$\frac{\partial N_x}{\partial \varepsilon} = \int\limits_A \frac{\partial \sigma}{\partial \varepsilon} \mathrm{d}A + \int\limits_{t_{fx}} \sigma \frac{\partial b_{bx}}{\partial \varepsilon} \mathrm{d}y + \int\limits_{d_{wx}} \sigma \frac{\partial t_{wx}}{\partial \varepsilon} \mathrm{d}y + \int\limits_{t_{fx}} \sigma \frac{\partial b_{tx}}{\partial \varepsilon} \mathrm{d}y \tag{II.41}$$

$$t_{wx} d_{wx} = b_{wx} t_w \Rightarrow \frac{\mathrm{d}t_{wx}}{\mathrm{d}\varepsilon} = \frac{t_w}{d_{wx}} \frac{\mathrm{d}b_{wx}}{\mathrm{d}\varepsilon} \tag{II.42}$$

where t_w = original web thickness; b_{wx} = effective width of the web.

Similar derivation results in

$$\frac{\partial N_x}{\partial \kappa_z} = \int\limits_A \frac{\partial \sigma\left(x,y\right)}{\partial \kappa_z} \mathrm{d}A + \int\limits_A \sigma(x,y) \frac{\partial}{\partial \kappa_z} \mathrm{d}A \Leftrightarrow \tag{II.43}$$

$$\frac{\partial N_x}{\partial \kappa_z} = \int\limits_A \frac{\partial \sigma}{\partial \kappa_z} \mathrm{d}A - \int\limits_A y\sigma \frac{\partial}{\partial \varepsilon} \mathrm{d}A \Leftrightarrow \tag{II.44}$$

$$\frac{\partial N_x}{\partial \kappa_z} = -\int\limits_A yE_t\left(x,y\right) \mathrm{d}A - \int\limits_{t_{fx}} y\sigma \frac{\partial b_{bx}}{\partial \varepsilon} \mathrm{d}y - \int\limits_{d_{wx}} y\sigma \frac{\partial t_{wx}}{\partial \varepsilon} \mathrm{d}y - \int\limits_{t_{fx}} y\sigma \frac{\partial b_{tx}}{\partial \varepsilon} \mathrm{d}y \tag{II.45}$$

$$\frac{\partial M_z}{\partial \varepsilon_r} = \frac{\partial N_x}{\partial \kappa_z} \tag{II.46}$$

$$\frac{\partial M_z}{\partial \kappa_z} = -\int\limits_A y \frac{\partial \sigma\left(x,y\right)}{\partial \kappa_z} \mathrm{d}A - \int\limits_A y\sigma(x,y) \frac{\partial}{\partial \kappa_z} \mathrm{d}A \tag{II.47}$$

$$\frac{\partial M_z}{\partial \kappa_z} = \int\limits_A y^2 E_t\left(x,y\right) \mathrm{d}A + \int\limits_{t_{fx}} y^2\sigma \frac{\partial b_{bx}}{\partial \varepsilon} \mathrm{d}y + \int\limits_{d_{wx}} y^2\sigma \frac{\partial t_{wx}}{\partial \varepsilon} \mathrm{d}y + \int\limits_{t_{fx}} y^2\sigma \frac{\partial b_{tx}}{\partial \varepsilon} \mathrm{d}y \tag{II.48}$$

II.6. Element flexibility and stiffness matrices

The element flexibility matrix, $\mathbf{f}_e$, is derived by differentiating the nodal displacement vector, $\mathbf{U}$, with respect to the nodal force vector, $\mathbf{F}$:

$$\mathbf{f}_e = \frac{\mathrm{d}\mathbf{U}}{\mathrm{d}\mathbf{F}} \tag{II.49}$$

Applying the compatibility condition for $\mathbf{U}$ as in (II.22), $\mathbf{f}_e$ becomes

$$\mathbf{f}_e = \frac{\mathrm{d}}{\mathrm{d}\mathbf{F}} \left[\int_0^{l_e} \mathbf{b}^T(x)\, \boldsymbol{\varepsilon}(x)\, \mathrm{d}x \right] = \int_0^{l_e} \mathbf{b}^T(x)\, \frac{\mathrm{d}\boldsymbol{\varepsilon}(x)}{\mathrm{d}\mathbf{F}} \mathrm{d}x \tag{II.50}$$

Referring to (II.33) leads to

$$\frac{\mathrm{d}\boldsymbol{\varepsilon}(x)}{\mathrm{d}\mathbf{F}} = \frac{\mathbf{k}_s^{-1}(x)\, \mathrm{d}\mathbf{f}(x)}{\mathrm{d}\mathbf{F}} = \frac{\mathbf{k}_s^{-1}(x) \mathrm{d}\left[\mathbf{b}(x)\mathbf{F}\right]}{\mathrm{d}\mathbf{F}} = \mathbf{k}_s^{-1}(x)\mathbf{b}(x) \tag{II.51}$$

Thus, the element flexibility matrix is determined by

$$\mathbf{f}_e = \int_0^{l_e} \mathbf{b}^T(x)\mathbf{k}_s^{-1}(x)\mathbf{b}(x)\mathrm{d}x \tag{II.52}$$

Similarly to the numerical evaluation of the displacement vector, $\mathbf{U}$, as in (II.25), $\mathbf{f}_e$ can be evaluated by

$$\mathbf{f}_e = \frac{l_e}{2} \sum_{i=1}^{n} \mathbf{b}^T\left(\frac{\xi_i + 1}{2} l_e\right) \mathbf{k}_s^{-1} \left(\frac{\xi_i + 1}{2} l_e\right) \mathbf{b}\left(\frac{\xi_i + 1}{2} l_e\right) w_i \tag{II.53}$$

The stiffness of a finite element in the global coordinate system is needed in forming the stiffness matrix of a structural system and analyzing the system in nonlinear finite element frameworks. The element stiffness in the global coordinate system can be derived as follows:

$$\mathbf{K}_e = \frac{\mathrm{d}\mathbf{F}^g}{\mathrm{d}\mathbf{U}^g} = \underbrace{\frac{\mathrm{d}\mathbf{F}^g}{\mathrm{d}\mathbf{F}^l}}_{\mathbf{J}^{Fgl}} \underbrace{\frac{\mathrm{d}\mathbf{F}^l}{\mathrm{d}\mathbf{F}}}_{\mathbf{J}^{Fl}} \frac{\mathrm{d}\mathbf{F}}{\mathrm{d}\mathbf{U}} \underbrace{\frac{\mathrm{d}\mathbf{U}}{\mathrm{d}\mathbf{U}^l}}_{\mathbf{J}^{Ul}} \underbrace{\frac{\mathrm{d}\mathbf{U}^l}{\mathrm{d}\mathbf{U}^g}}_{\mathbf{J}^{Ulg}} \tag{II.54}$$

where

$$J_{ij}^{Fgl} = \frac{\partial F_i^g}{\partial F_j^l} = C_{ji}^{gl}, \qquad F_i^g = C_{ji}^{gl} F_j^l \tag{II.55}$$

$$J_{ij}^{Fl} = \frac{\partial F_i^l}{\partial F_j} = C_{ij}^{nFl}, \qquad F_i^l = C_{ij}^{nFl} F_j \tag{II.56}$$

$$J_{ij}^{Ul} = \frac{\partial U_i}{\partial U_j^l} = C_{ij}^{lUn}, \qquad U_i = C_{ij}^{lUn} U_j^l \tag{II.57}$$

$$J_{ij}^{Ulg} = \frac{\partial U_i^l}{\partial U_j^g} = C_{ij}^{gl}, \qquad U_i^l = C_{ij}^{gl} U_j^g \tag{II.58}$$

Or equivalently, the element global stiffness matrix can be written as

$$\mathbf{K}_e = \mathbf{J}^F \frac{\mathrm{d}\mathbf{F}}{\mathrm{d}\mathbf{U}} \mathbf{J}^U = \mathbf{J}^F \mathbf{f}_e^{-1} \mathbf{J}^U \tag{II.59}$$

where

$$J_{ij}^F = J_{ik}^{Fgl} J_{kj}^{Fl} = C_{ki}^{gl} C_{kj}^{nFl} \tag{II.60}$$

$$J_{ij}^U = J_{ik}^{Ul} J_{kj}^{Ulg} = C_{ik}^{lUn} C_{kj}^{gl} \tag{II.61}$$

II.7. Solution algorithm

Figure II.7 presents an algorithm to solve for the nonlinear relationship between the nodal force vector, $\mathbf{F}$, and the nodal displacement vector, $\mathbf{U}$, by minimizing the residual nodal displacements, $\boldsymbol{\delta}_{\mathbf{U}}$. In this algorithm, the solving process at both the section level and element level is implemented simultaneously, avoiding local iterations (Spacone et al. 1996).

As shown in Figure II.7, the nodal force vector at step $i+1$, $\mathbf{F}^{(i+1)}$, is to be determined from a given vector of incremental displacements, $\Delta\mathbf{U}^{(i)}$, and from the element state at the previously solved step (step i). The solution to be found needs to be on the dashed curve, i.e. $\mathbf{F}^{(i+1)} = f(\mathbf{U}^{(i+1)})$, where $\mathbf{U}^{(i+1)} = \mathbf{U}^{(i)} + \Delta\mathbf{U}^{(i)}$. The element state refers to information about the following quantities: the displace-

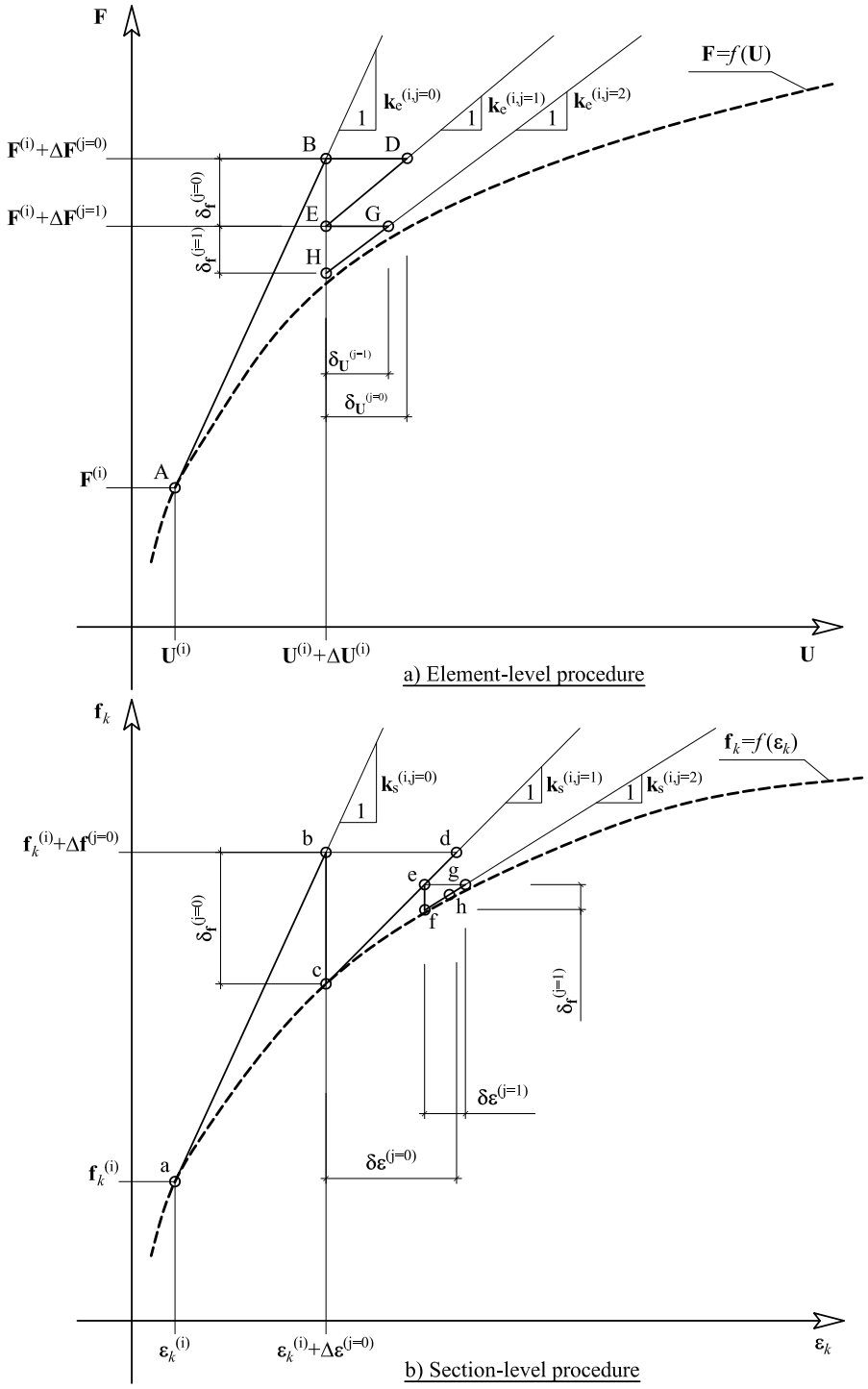

Figure II.7: Solution algorithm for force-based finite elements.

ment vector, $\mathbf{U}$, the force vector, $\mathbf{F}$, the element tangent stiffness matrix, $\mathbf{k}_e^{(i,j=0)}$, section deformation vectors, $\boldsymbol{\varepsilon}_k^{(i)}$, section force vectors, $\mathbf{f}_k^{(i)}$, and section stiffness matrices, $\mathbf{k}_s^{(i,j=0)}$. The strains, stresses, and material tangent moduli are also known at integration points in the element.

A new element state is obtained by iteratively evaluating the following sequence of equations:

1. Nodal force increments (to get point B)

$$\Delta\mathbf{F}^{(i,j=0)} = \mathbf{k}_e^{(i,j=0)}\Delta\mathbf{U}^{(i)} = \left[\mathbf{f}_e^{(i)}\right]^{-1}\Delta\mathbf{U}^{(i)}$$

2. Section force increments (to get point b)

$$\Delta\mathbf{f}^{(i,j)} = \mathbf{b}(x)\Delta\mathbf{F}^{(i,j)}$$

3. Section deformation increments

$$\Delta\boldsymbol{\varepsilon}^{(i,j)}(x) = \mathbf{f}_s^{(i)}(x)\Delta\mathbf{f}^{(i,j)}$$

4. Strain state

$$\boldsymbol{\varepsilon}^{(i+1,j)}(x) = \boldsymbol{\varepsilon}^{(i)}(x) + \Delta\boldsymbol{\varepsilon}^{(i,j)}(x)$$

$$\varepsilon^{(i+1,j)}(x,y) = \varepsilon_r^{(i+1,j)}(x) - y\kappa_z^{(i+1,j)}(x)$$

5. Material tangent moduli, stresses, and section geometry

$$\varepsilon^{(i+1,j)}(x,y) \rightarrow E_t^{(i+1,j)}(x,y), \sigma^{(i+1,j)}(x,y), \text{ and } A^{(i+1,j)}(x)$$

6. New section forces determined from the resulting material state

$$\mathbf{f}^{(i+1,j)}(x) = \Psi\left[\sigma^{(i+1,j)}(x,y), A^{(i+1,j)}(x)\right]$$

7. Section force residuals (to get point c)

$$\boldsymbol{\delta}_{\mathbf{f}}^{(j)}(x) = \mathbf{f}^{(i)}(x) + \Delta\mathbf{f}^{(i,j)}(x) - \mathbf{f}^{(i+1,j)}(x)$$

8. Section deformation residuals (to point d)

$$\boldsymbol{\delta}_{\boldsymbol{\varepsilon}}^{(j)}(x) = \mathbf{f}_s^{(i+1,j)}(x)\boldsymbol{\delta}_{\mathbf{f}}^{(j)}(x)$$

where $\mathbf{f}_s^{(i+1,j)}(x)$ is determined from the resulting material state:

$$\mathbf{f}_s^{(i+1,j)}(x) = \left[\mathbf{k}_s^{(i+1,j)}(x)\right]^{-1} = f\left[E_t^{(i+1,j)}(x,y), A^{(i+1,j)}(x)\right]$$

9. Updated section deformation increments

$$\Delta\boldsymbol{\varepsilon}^{(i,j)}(x) = \Delta\boldsymbol{\varepsilon}^{(i,j)}(x) + \boldsymbol{\delta}_{\boldsymbol{\varepsilon}}^{(j)}(x)$$

10. Calculated element nodal displacement increments (to get point D)

$$\Delta\mathbf{U}^{(i,j)} = \int_0^{l_e} \mathbf{b}^T(x)\Delta\boldsymbol{\varepsilon}^{(i,j)}(x)\mathrm{d}x$$

11. Element nodal displacement residuals (to get point E)

$$\boldsymbol{\delta}_{\mathbf{U}}^{(j)} = \Delta\mathbf{U}(i,j) - \Delta\mathbf{U}^{(i)}$$

if $\boldsymbol{\delta}_{\mathbf{U}}^{(j)} \simeq \mathbf{0}$, the solution is obtained as

$$\mathbf{F}^{(i+1)} = \mathbf{F}^{(i)} + \Delta\mathbf{F}^{(i,j)}$$

else the next following steps are implemented.

12. New element flexibility matrix determined from the resulting material state

$$\mathbf{f}_e^{(i+1,j)} = \int_0^{l_e} \mathbf{b}^T(x)\mathbf{f}_s^{(i+1,j)}(x)\mathbf{b}(x)\mathrm{d}x$$

13. Element nodal force residuals or unbalanced nodal forces

$$\boldsymbol{\delta}_{\mathbf{F}}^{(j)} = \left[\mathbf{f}_e^{(i+1,j)}\right]^{-1}\boldsymbol{\delta}_{\mathbf{U}}^{(j)}$$

14. Adjusted nodal force increments for the next iteration

$$\Delta\mathbf{F}^{(i,j+1)} = \Delta\mathbf{F}^{(i,j)} - \boldsymbol{\delta}_{\mathbf{F}}^{(j)}$$

II.8. Application of elemental loads

The following procedure is developed based on Taucer et al. (1991):

- Determine section force vectors due to all the elemental loads using a simply-supported beam model,
- Determine the (incremental) vectors of corresponding elastic section deformations,
- Determine the vectors of section force residuals and the array of section flexibility matrices,

- Determine the section deformation residuals and the corresponding element stiffness matrix,
- Integrate the section deformation residuals to obtain the nodal displacement residuals,
- Check if convergence occurs when the nodal displacement residuals are approximately zero,
- If convergence has not occurred, determine nodal force residuals and update nodal forces
- Subtract the nodal force residuals from the element section forces
- Subtract the just obtained section deformation residuals from the previous section deformation residuals,
- Update section deformations,
- Determine the section force residuals, the section flexibility matrices, and continue this iteration until nodal displacement residuals to be approximately zero or until the number of iterations is too large.

II.9. Mass matrix

The kinetic energy of a solid body is given as

$$K_V = \frac{1}{2} \int_V \dot{\mathbf{u}}^T \dot{\mathbf{u}} \rho \mathrm{d}V \tag{II.62}$$

where $\mathbf{u}$ = displacement field of the body; ρ = density of the body material; V = volume of the body. In the 2D frame element, the displacement field includes

displacement components u_x and u_y respectively along and across the element: $\mathbf{u} = [u_x, u_y]^T$.

The displacement field is related to the local nodal displacement vector as

$$\mathbf{u} = \mathbf{C}^{ul}\mathbf{U}^l \tag{II.63}$$

or

$$\begin{Bmatrix} u_x \\ u_y \end{Bmatrix} = \begin{bmatrix} S_1 & 0 & 0 & S_2 & 0 & 0 \\ 0 & H_1 & l_e H_2 & 0 & H_3 & l_e H_4 \end{bmatrix} \begin{Bmatrix} U_1^l \\ U_2^l \\ U_3^l \\ U_4^l \\ U_5^l \\ U_6^l \end{Bmatrix} \tag{II.64}$$

where the shape functions, S_1 and S_2 can be derived as

$$S_1 = 1 - \xi, \qquad S_2 = \xi \tag{II.65}$$

The Hermite shape functions (Chandrupatla and Belegundu 2002), H_1, H_2, H_3, and H_4 are of cubic order polynomials and can be formed based on their values and their derivative values as in Table II.1.

Table II.1: Hermite shape function values

Coordinate	H_1	H_1'	H_2	H_2'	H_3	H_3'	H_4	H_4'
$\xi = 0$	1	0	0	1	0	0	0	0
$\xi = 1$	0	0	0	0	1	0	0	1

$$H_1 = 1 - 3\xi^2 + 2\xi^3, \qquad H_2 = \xi - 2\xi^2 + \xi^3$$
$$H_3 = 3\xi^2 - 2\xi^3, \qquad H_4 = -\xi^2 + \xi^3 \tag{II.66}$$

Substituting (II.63) into (II.62), the kinetic energy becomes

$$K_V = \frac{1}{2}\left(\dot{\mathbf{U}}^l\right)^T \left[\int_V \left(\mathbf{C}^{ul}\right)^T \mathbf{C}^{ul} \rho \mathrm{d}V\right] \dot{\mathbf{U}}^l = \frac{1}{2}\left(\dot{\mathbf{U}}^l\right)^T \mathbf{M}_e^l \dot{\mathbf{U}}^l \tag{II.67}$$

where $\mathbf{M}_e^l$ = element mass matrix in the local coordinate system. In the global coordinate system,

$$K_V = \frac{1}{2}\left(\dot{\mathbf{U}}^g\right)^T \left[\left(\mathbf{C}^{gl}\right)^T \int_V \left(\mathbf{C}^{ul}\right)^T \mathbf{C}^{ul} \rho \mathrm{d}V \mathbf{C}^{gl}\right] \dot{\mathbf{U}}^g \tag{II.68}$$

Thus, the global mass matrix is formulated as

$$\mathbf{M}_e^g = \left(\mathbf{C}^{gl}\right)^T \mathbf{M}_e^l \mathbf{C}^{gl} \tag{II.69}$$

The element mass matrix in the local coordinate system can be determined using (II.67) as

$$\mathbf{M}_e^l = \int_{l_e} \left(\mathbf{C}^{ul}\right)^T \mathbf{C}^{ul} \rho A_e \mathrm{d}x \tag{II.70}$$

where A_e = cross-section area of the element. This element mass matrix can be written as

$$\mathbf{M}_e^l = \rho A_e l_e \int_0^1 \left(\mathbf{C}^{ul}\right)^T \mathbf{C}^{ul} \mathrm{d}\xi \Leftrightarrow \tag{II.71}$$

$$\mathbf{M}_e^l = \rho A_e l_e \int_0^1 \begin{bmatrix} S_1^2 & 0 & 0 & S_1S_2 & 0 & 0 \\ & H_1^2 & l_eH_1H_2 & 0 & H_1H_3 & l_eH_1H_4 \\ & & l_e^2H_2^2 & 0 & l_eH_2H_3 & l_e^2H_2H_4 \\ & & & S_2^2 & 0 & 0 \\ & & & & H_3^2 & l_eH_3H_4 \\ sym. & & & & & l_e^2H_4^2 \end{bmatrix} \mathrm{d}\xi \tag{II.72}$$

$$\mathbf{M}_e^l = \rho A_e l_e \begin{bmatrix} \frac{1}{3} & 0 & 0 & \frac{1}{6} & 0 & 0 \\ & \frac{13}{35} & \frac{11}{210}l_e & 0 & \frac{9}{70} & -\frac{13}{420}l_e \\ & & \frac{1}{105}l_e^2 & 0 & \frac{13}{420}l_e & -\frac{1}{140}l_e^2 \\ & & & \frac{1}{3} & 0 & 0 \\ & & & & \frac{13}{35} & -\frac{11}{210}l_e \\ sym. & & & & & \frac{1}{105}l_e^2 \end{bmatrix} \tag{II.73}$$

II.10. Refined finite element analysis comparison

The performance of the line element developed here is investigated using a much more sophisticated finite element model. In this more refined finite element model, components of a wide flange shape are highly meshed using shell elements in Abaqus (DSS 2009). A structural member under a combined axial force and bending moment is selected for analysis. The response of this structure obtained from using the line element developed herein is then compared with that obtained from using the sophisticated, presumably highly accurate, finite element model.

Figure II.8 shows a structural member whose AISC section is W24x62 (AISC 2013). The structure has one fixed end (A) and one roller-supported end (B). A rigid element, connecting B and C, is used to generate a bending moment from the axial force (Fz). The response from the two finite element modeling approaches is

represented by the relationship bewteen axial force Fz and the longitudinal displacement at C, Uz.

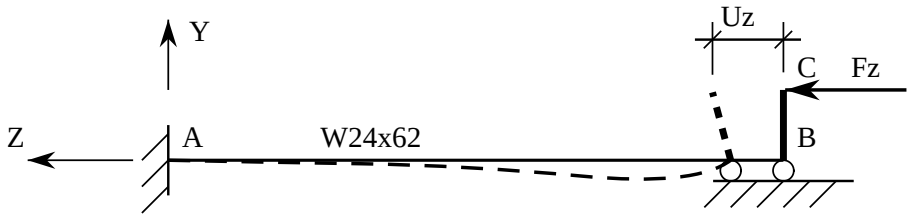

Figure II.8: Element under combined bending and compression.

Figure II.9 shows a finite element model developed in Abaqus. The wide flange section is called from the database of AISC shapes using the Python programming language (Van Rossum and Drake Jr. 2010). Two rigid end plates are used to model the boundary condition of the structure. By this way, the responses obtained from the two modeling approaches can be comparable.

Figure II.10 is the deformation of the structure under the combined actions of loading. The figure also shows the distribution of von Mises stress whose intensity increases from blue to red. As shown in the figure, at the roller end of the structure, the upper flange and part of the web of the shape are under high stress and deformation. The compression effect causes the flange to deform locally and significantly out of its plane.

The responses obtained from the line element developed in this study and from the more sophisticated finite element modeling are compared in Figure II.11. In this case, the structure using the line element developed in this study to account for local buckling effects behaves similarly to the refined finite element model analyzed in Abaqus. The developed element with local buckling causes the strength degradation

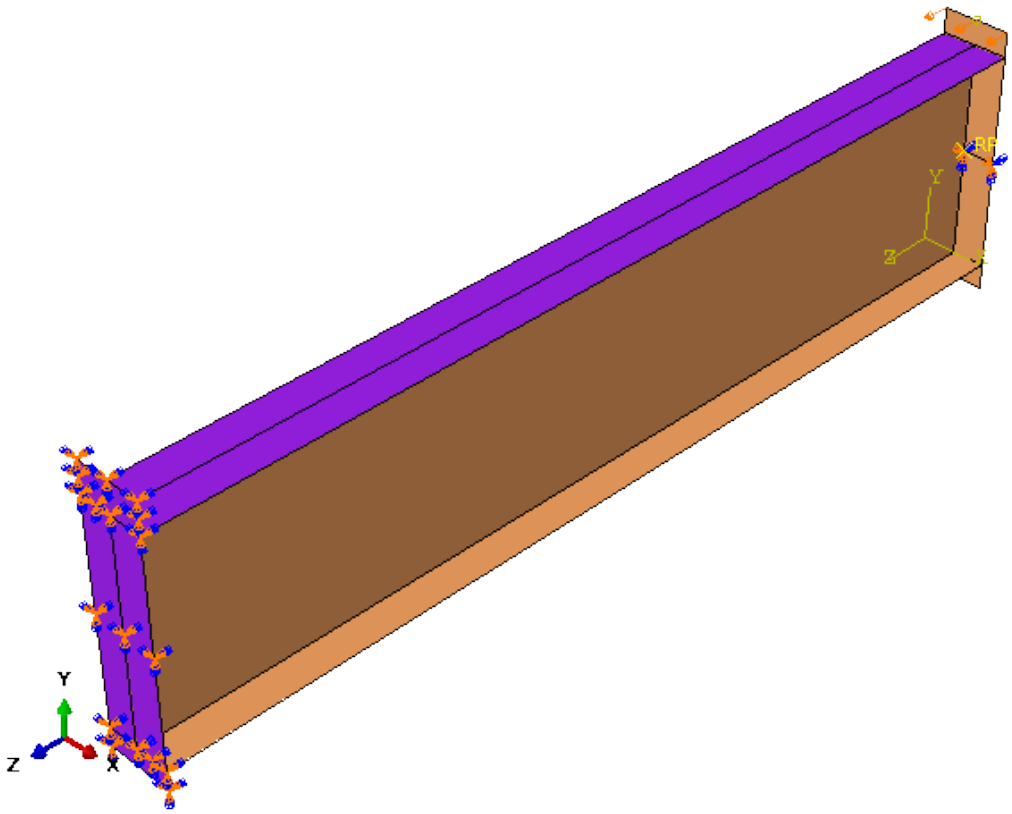

Figure II.9: Refined finite element modeling in ABAQUS.

at the displacement of approximately 1.1 in. Meanwhile, the response of the regular line element without local buckling consideration does not exhibit the degradation feature.

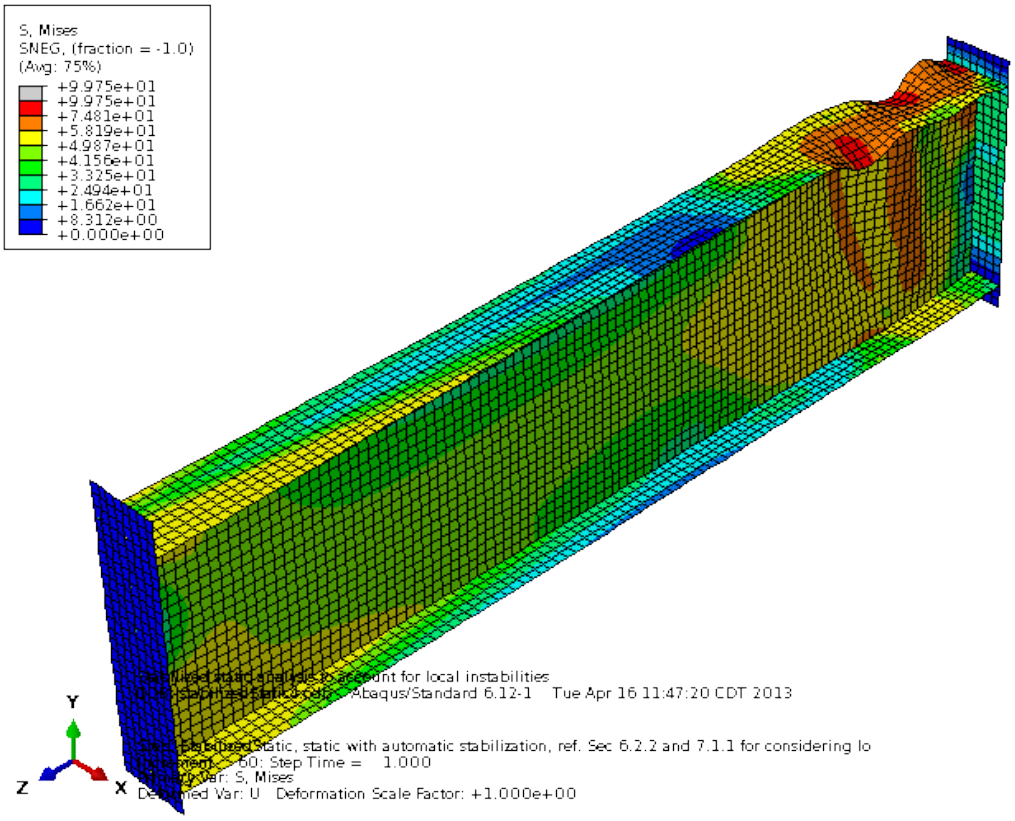

Figure II.10: Behavior of the refined finite element model.

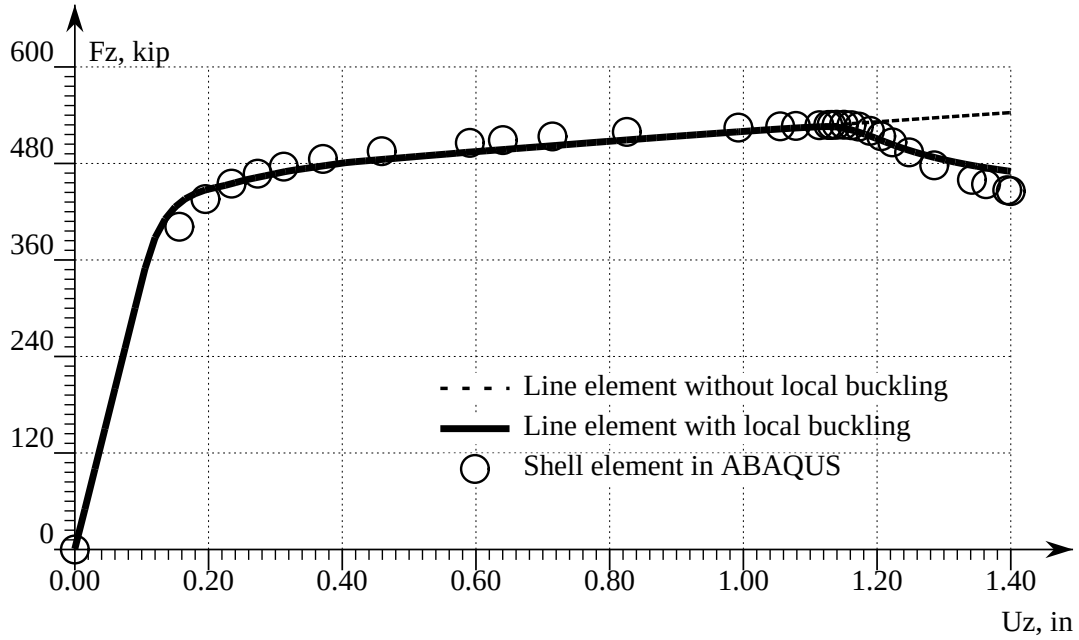

Figure II.11: Response of the developed line FEM and the ABAQUS shell FEM.

CHAPTER III

MODELING OF SMF CONNECTIONS

Each SMF connection is modeled as a system of a spring element and rigid links. The shear resistance of the PZ and the bending resistance of the column flanges are accounted for in the spring element. In this chapter, an innovative approach is presented to develop a computational model for simulating this element.

Using shell elements is not an economic solution for frame analyses. The number of shell elements needed to model a sub-assemblage could be up to about 10,000. The modeling effort and computing time would be enormous if multiple frame stories are analyzed. A viable solution is to use line elements to model the response of beam and columns and spring elements to model the response of the connection. In this approach, the number of elements per sub-assemblage is just a few (see Figure III.1).

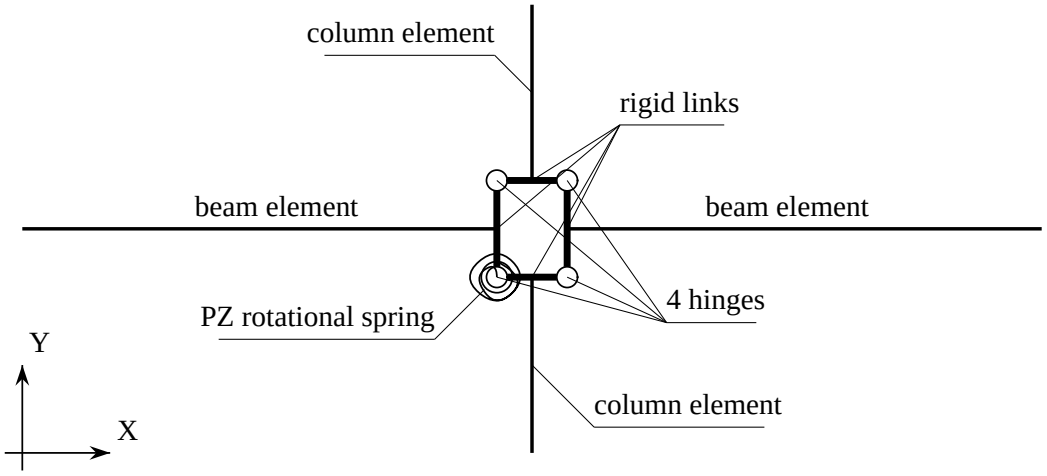

Figure III.1: Nonlinear FE model of a frame subassemblage.

A frame model often comprises main elements, such as beam and column nonlin-

ear elements, PZ spring elements, and rigid elements. Figure III.1 illustrates the FE model for a typical frame subassemblage. PZ elements include four rigid links connected by four hinges and a rotational spring element. The rotational spring is used to simulate the behavior of PZ. For the systems similar to Figure III.1, to include the behavior of panel zone in the PZ spring relies mainly on the shear deformation of the panel zone and the local bending of the column flanges.

Mathematical models developed in this study are based on the principle of energy conservation (Achenbach 1973; Lai et al. 2010). For a mass system, the change rate of the sum of its kinetic energy and the internal energy balances out the change rate of the work done by external forces plus the other energies that enter and leave the system. For the beam-to-column connection, the kinetic energy is considered negligible due to its mass being insignificant to that of the frame system. The energies that enter and leave the connection are assumed to be zero.

III.1. Compatibility conditions

Let the origin of the rectangular Cartesian distance coordinate system, $Oxyz$, be fixed in a PZ plane as shown in Figure III.2. The x–axis points to the longitudinal direction of the girders, the y–axis points in the longitudinal direction of the column. As indicated in the figure, the displacement coordinate system, $Ou_xu_yu_z$, is formed correspondingly to $Oxyz$.

III.1.1. Strains in the PZ

The PZ is considered to be deformed under a plane stress condition. Thus, the strain components of consideration in a PZ include the normal strain, ε_{yy}, and the shear strain, ε_{xy}. Assuming that the strains are uniform in the PZ and using symbol "*"

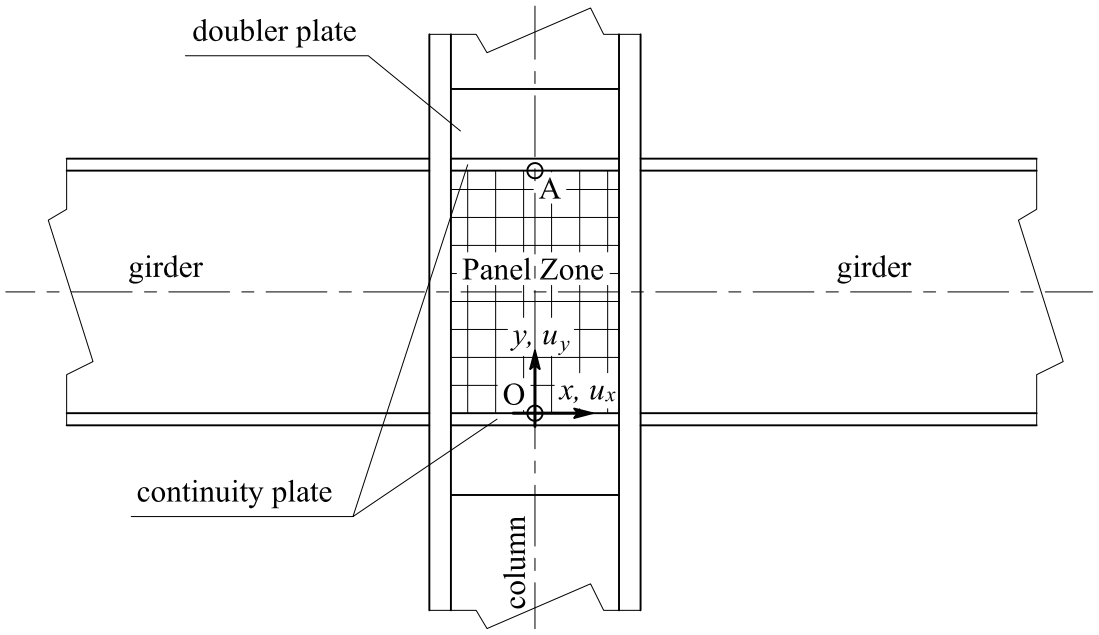

Figure III.2: Illustration of a typical SMF connection.

to distinguish these strains with the other variable strain fields gives

$$\varepsilon^*_{yy} = \frac{u_{yA}}{y_A} \Rightarrow \mathrm{d}\varepsilon^*_{yy} = \frac{1}{y_A}\mathrm{d}u_{yA} \tag{III.1}$$

$$\varepsilon^*_{xy} = -\frac{1}{2}\gamma_{PZ} \Rightarrow \mathrm{d}\varepsilon^*_{xy} = -\frac{1}{2}\mathrm{d}\gamma_{PZ} \tag{III.2}$$

where $u_{yA} = u_y(y_A)$; γ_{PZ} = rotation of a column flange around the z–axis relative to that of the continuity plates.

III.1.2. Strains in the flange

The column flanges experience local bending (Jones 2000; Kim and Engelhardt 2002; Krawinkler 1978) in addition to axial deformation, $\varepsilon_r(y)$, due to the column axial

force. The longitudinal strain in a column flange, $\varepsilon_{yy}(x, y)$, can be determined as

$$\varepsilon_{yy}(x, y) = \varepsilon_r(y) \mp \kappa_z(y)\,(x - x_r) \tag{III.3}$$

$$\text{and} \quad \mathrm{d}\varepsilon_{yy} = \mathrm{d}\varepsilon_r \mp (x - x_r)\,\mathrm{d}\kappa_z \tag{III.4}$$

where $\mp \equiv -$ for the upper parts of the column flange under local bending; $\mp \equiv +$ for the lower parts of the column flange; $\varepsilon_r(y)$ denotes the longitudinal strain at a reference plane; x_r = coordinate of the reference plane that is parallel to the column flange plane; $\kappa_z(y)$ = bending curvature of the column flange.

Based on the Euler–Bernoulli beam theory (Kassimali 2005; Zienkiewicz and Taylor 2005), the relationship between the curvature of the bent column flange and the PZ shear deformation can be determined as

$$\kappa_z = \frac{\gamma_{PZ}}{l_{cf}} \Rightarrow \mathrm{d}\kappa_z = \frac{1}{l_{cf}}\mathrm{d}\gamma_{PZ} \tag{III.5}$$

where l_{cf} is the column flange length under local bending due to the PZ shear deformation.

The longitudinal reference strain can be conveniently determined as

$$\varepsilon_r = \frac{u_{yA}}{y_A} \Rightarrow \mathrm{d}\varepsilon_r = \frac{1}{y_A}\mathrm{d}u_{yA} \tag{III.6}$$

It appears that $\varepsilon_r = \varepsilon^*_{yy}$, and therefore $\mathrm{d}\varepsilon_r = \mathrm{d}\varepsilon^*_{yy}$.

Substituting (III.5) and (III.6) into (III.4) and (III.3) gives

$$\varepsilon_{yy}(x, y) = \frac{u_{yA}}{y_A} \mp \frac{\gamma_{PZ}}{l_{cf}}(x - x_r) \tag{III.7}$$

$$\mathrm{d}\varepsilon_{yy} = \frac{1}{y_A}\mathrm{d}u_{yA} \mp \frac{x - x_r}{l_{cf}}\mathrm{d}\gamma_{PZ} \tag{III.8}$$

III.2. External work on a SMF connection

Figure III.3 shows the deformation of a typical SMF connection and its derived analytical model. A resultant force and a moment can be obtained from the beam and column internal forces. Neglecting the insignificant axial forces in the beams, the external action on the connection can be modeled as consisting of F_{ca} and an equivalent shear force, V_{eq} as showed in the figure.

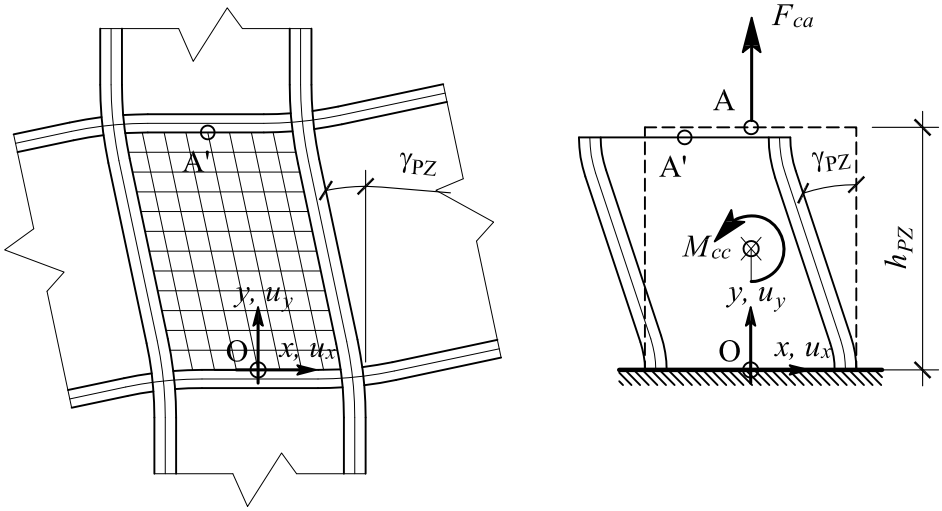

Figure III.3: Deformation of a typical SMF connection and its analytical model.

The external work done on a SMF connection is approximately divided into two parts. The first part is done by the equivalent shear force, V_{eq}, that causes the shear deformation of the PZ, γ_{PZ}. The other part is done by the column axial force, F_{ca}, that causes the axial deformation of the column in the connection. As shown in FEMA (2000a) and Jin and El-Tawil (2005), the external work done by the shear forces can be considered equivalent to the work done by the moment at the center of the panel zone, M_{cc}, that causes the shear deformation. The shear deformation is determined as the rotation of the column flange relative to that of the continuity

plate. Thus, the increment of the external work can be formulated as

$$\mathrm{d}W = M_{cc}\mathrm{d}\gamma_{PZ} + F_{ca}\mathrm{d}u_{yA} \tag{III.9}$$

where $M_{cc} = V_{eq}h_{PZ}$; $h_{PZ} = d_b - t_{bf} - t_{con} \equiv y_A$; d_b = beam section depth; t_{bf} = beam flange thickness; t_{con} = continuity plate thickness; u_{yA} = vertical displacement of point A with reference to the bottom of the PZ (see Figure III.3).

III.3. Internal deformation energy of a SMF connection

It is assumed that the behavior of the connection is not influenced by the temperature. The internal energy is the sum of the strain energy due to the shear deformation of the panel zone and the local bending of the column and beam flanges. Thus, the increment of its internal energy density can be written as

$$\mathrm{d}I_\rho = \sigma_{ij}\mathrm{d}\varepsilon_{ij} \tag{III.10}$$

where σ_{ij} and ε_{ij} are the stress and strain components of the stress and strain tensors, respectively. Indices i and j are integers; each index varies from 1 through 3 to represent the Cartesian coordinates x, y, and z, correspondingly. The total increment of the internal energy of the frame connection due to the panel zone deformation is hence determined as

$$\mathrm{d}I_\sum = \mathrm{d}I_{PZ} + \mathrm{d}I_{CF} \tag{III.11}$$

$$\mathrm{d}I_{PZ} = \int_{V_{PZ}} (\mathrm{d}I_\rho)\,\mathrm{d}V_{PZ} \tag{III.12}$$

$$\mathrm{d}I_{CF} = \int_{V_{CF}} (\mathrm{d}I_\rho)\,\mathrm{d}V_{CF} \tag{III.13}$$

where $\mathrm{d}I_{PZ}$ and $\mathrm{d}I_{CF}$ respectively denote the incremental internal energies in the panel zone and the column flanges, respectively. V_{CF} is the volume of the column flanges under the local bending due to the panel zone deformation. V_{PZ} is the volume of the panel zone under (shear) deformation:

$$V_{PZ} = t_{PZ}\left(d_c - 2t_{cf}\right)h_{PZ} \tag{III.14}$$

where t_{PZ} = panel zone thickness; d_c = column section depth; t_{cf} = column flange thickness; h_{PZ} = clear height of the PZ.

III.3.1. PZ deformation energy increment

It is assumed that the stress field in the PZ is uniformly distributed, and the PZ is under a plane-stress condition. The non-zero stress components of consideration are σ^*_{xy} and σ^*_{yy}. The strain energy in the panel zone can then be derived as

$$\mathrm{d}I_{PZ} = \int_{V_{PZ}} \mathrm{d}V_{PZ}\left(\sigma_{12}\mathrm{d}\varepsilon_{12} + \sigma_{21}\mathrm{d}\varepsilon_{21}\right) + \int_{V_{PZ}} \mathrm{d}V_{PZ}\left(\sigma_{22}\mathrm{d}\varepsilon_{22}\right) \Leftrightarrow \tag{III.15}$$

$$\mathrm{d}I_{PZ} = 2V_{PZ}\sigma_{12}\mathrm{d}\varepsilon_{12} + V_{PZ}\sigma_{22}\mathrm{d}\varepsilon_{22} \Leftrightarrow \tag{III.16}$$

$$\mathrm{d}I_{PZ} = 2V_{PZ}\sigma^*_{xy}\mathrm{d}\varepsilon_{xy} + V_{PZ}\sigma^*_{yy}\mathrm{d}\varepsilon_{yy} \tag{III.17}$$

Applying the compatibility conditions for the strains in the PZ leads to

$$\mathrm{d}I_{PZ} = -V_{PZ}\sigma^*_{xy}\mathrm{d}\gamma_{PZ} + \frac{V_{PZ}\sigma^*_{yy}}{y_A}\mathrm{d}u_{yA} \tag{III.18}$$

III.3.2. Column flange deformation energy increment

To determine the strain energy due to the local bending of the column flanges, each column flange is assumed to be bent uniformly across the flange width, i.e. normal stress and strain are constant across the width. All the associated column flanges undergo similar deformations. The formulation is therefore formulated as

$$\mathrm{d}I_{CF} = n_{cf} \int_{l_c} \int_{t_{cf}} \sigma_{yy} \mathrm{d}\varepsilon_{yy} w_c \mathrm{d}x\mathrm{d}y = n_{cf} w_c \int_{l_c} \int_{x_b}^{x_t} \sigma_{yy}\, \mathrm{d}\varepsilon_{yy} \mathrm{d}x\mathrm{d}y \tag{III.19}$$

where $n_{cf} = 2$, number of column flanges under the local bending; l_c = column flange length, $l_c = y_A = h_{PZ}$; w_c = column flange width; y = local coordinate along the column height. The local coordinate, x, is perpendicular to the column flange; x_b and x_t are the coordinates of the surfaces of the considered flange.

Using the compatibility condition for the strain in the column flange leads to

$$\begin{aligned} \mathrm{d}I_{CF} =& n_{cf} w_c \int_{0}^{l_{cf}} \int_{x_b}^{x_t} \sigma_{yy}\, \mathrm{d}\varepsilon_{yy} \mathrm{d}x\mathrm{d}y + n_{cf} w_c \int_{l_{cf}}^{l_c - l_{cf}} \int_{x_b}^{x_t} \sigma_{yy}\, \mathrm{d}\varepsilon_{yy} \mathrm{d}x\mathrm{d}y + \\ &+ n_{cf} w_c \int_{l_c - l_{cf}}^{l_c} \int_{x_b}^{x_t} \sigma_{yy}\, \mathrm{d}\varepsilon_{yy} \mathrm{d}x\mathrm{d}y \end{aligned} \tag{III.20}$$

$$\begin{aligned} \mathrm{d}I_{CF} =& n_{cf} w_c \int_{0}^{l_{cf}} \int_{x_b}^{x_t} \sigma_{yy} \left(\frac{1}{y_A} \mathrm{d}u_{yA} + \frac{x - x_r}{l_{cf}} \mathrm{d}\gamma_{PZ} \right) \mathrm{d}x\mathrm{d}y + \\ &+ n_{cf} w_c \int_{l_{cf}}^{l_c - l_{cf}} \int_{x_b}^{x_t} \sigma_{yy} \frac{1}{y_A} \mathrm{d}u_{yA} \mathrm{d}x\mathrm{d}y + \\ &+ n_{cf} w_c \int_{l_c - l_{cf}}^{l_c} \int_{x_b}^{x_t} \sigma_{yy} \left(\frac{1}{y_A} \mathrm{d}u_{yA} - \frac{x - x_r}{l_{cf}} \mathrm{d}\gamma_{PZ} \right) \mathrm{d}x\mathrm{d}y \Leftrightarrow \end{aligned} \tag{III.21}$$

$$\mathrm{d}I_{CF} = \frac{n_{cf}w_c}{y_A}\int_0^{l_c}\int_{x_b}^{x_t}\sigma_{yy}\mathrm{d}x\mathrm{d}y\mathrm{d}u_{yA} + \frac{n_{cf}w_c}{l_{cf}}\int_0^{l_{cf}}\int_{x_b}^{x_t}(x-x_r)\sigma_{yy}\mathrm{d}\gamma\mathrm{d}x\mathrm{d}y + \\ - \frac{n_{cf}w_c}{l_{cf}}\int_{l_c-l_{cf}}^{l_c}\int_{x_b}^{x_t}(x-x_r)\sigma_{yy}\mathrm{d}\gamma\mathrm{d}x\mathrm{d}y \tag{III.22}$$

III.3.3. Total internal energy

Substituting (III.18) and (III.22) into (III.11) leads to the following total deformation energy increment:

$$\mathrm{d}I_{\sum} = -V_{PZ}\sigma^*_{xy}\mathrm{d}\gamma_{PZ} + \frac{V_{PZ}\sigma^*_{yy}}{y_A}\mathrm{d}u_{yA} + \frac{n_{cf}w_c}{y_A}\int_0^{l_c}\int_{x_b}^{x_t}\sigma_{yy}\mathrm{d}x\mathrm{d}y\mathrm{d}u_{yA} + \\ + \frac{n_{cf}w_c}{l_{cf}}\left[\int_0^{l_{cf}}\int_{x_b}^{x_t}(x-x_r)\sigma_{yy}\mathrm{d}x\mathrm{d}y - \int_{l_c-l_{cf}}^{l_c}\int_{x_b}^{x_t}(x-x_r)\sigma_{yy}\mathrm{d}x\mathrm{d}y\right]\mathrm{d}\gamma_{PZ} \tag{III.23}$$

$$\mathrm{d}I_{\sum} = \left(\frac{V_{PZ}\sigma^*_{yy}}{y_A} + \frac{n_{cf}w_c}{y_A}\int_0^{l_c}\int_{x_b}^{x_t}\sigma_{yy}\mathrm{d}x\mathrm{d}y\right)\mathrm{d}u_{yA} - V_{PZ}\sigma^*_{xy}\mathrm{d}\gamma_{PZ} + \\ \frac{n_{cf}w_c}{l_{cf}}\left[\int_0^{l_{cf}}\int_{x_b}^{x_t}(x-x_r)\,\sigma_{yy}\mathrm{d}x\mathrm{d}y - \int_{l_c-l_{cf}}^{l_c}\int_{x_b}^{x_t}(x-x_r)\,\sigma_{yy}\mathrm{d}x\mathrm{d}y\right]\mathrm{d}\gamma_{PZ} \tag{III.24}$$

III.4. Equilibrium conditions

Regarding the principle of energy conservation gives

$$\mathrm{d}W = \mathrm{d}I_{\sum} \tag{III.25}$$

Using the results obtained for the external work increment and the total internal energy increment leads to

$$M_{cc}\mathrm{d}\gamma_{PZ} + F_{ca}\mathrm{d}u_{yA} = \left(\frac{V_{PZ}\sigma^*_{yy}}{y_A} + \frac{n_{cf}w_c}{y_A}\int_0^{l_c}\int_{x_b}^{x_t}\sigma_{yy}\mathrm{d}x\mathrm{d}y\right)\mathrm{d}u_{yA} - V_{PZ}\sigma^*_{xy}\mathrm{d}\gamma_{PZ} + \\ + \frac{n_{cf}w_c}{l_{cf}}\left[\int_0^{l_{cf}}\int_{x_b}^{x_t}(x-x_r)\,\sigma_{yy}\mathrm{d}x\mathrm{d}y - \int_{l_c-l_{cf}}^{l_c}\int_{x_b}^{x_t}(x-x_r)\,\sigma_{yy}\mathrm{d}x\mathrm{d}y\right]\mathrm{d}\gamma_{PZ} \tag{III.26}$$

Equation (III.26) should hold true for any small increment of γ_{PZ} and u_{yA}. Therefore, the following equilibrium conditions are determined:

$$M_{cc} = -V_{PZ}\sigma^*_{xy} + \frac{n_{cf}w_c}{l_{cf}}\left[\int_0^{l_{cf}}\int_{x_b}^{x_t}(x-x_r)\sigma_{yy}\mathrm{d}x\mathrm{d}y - \int_{l_c-l_{cf}}^{l_c}\int_{x_b}^{x_t}(x-x_r)\sigma_{yy}\mathrm{d}x\mathrm{d}y\right] \tag{III.27}$$

$$F_{ca} = \frac{V_{PZ}\sigma^*_{yy}}{y_A} + \frac{n_{cf}w_c}{y_A}\int_0^{l_c}\int_{x_b}^{x_t}\sigma_{yy}\mathrm{d}x\mathrm{d}y \Leftrightarrow \tag{III.28}$$

$$F_{ca} = \frac{V_{PZ}\sigma^*_{yy}}{y_A} + \frac{n_{cf}w_c}{y_A}\left(\int_0^{l_{cf}}\int_{x_b}^{x_t}\sigma_{yy}\mathrm{d}x\mathrm{d}y + \int_{l_{cf}}^{l_c-l_{cf}}\int_{x_b}^{x_t}\sigma_{yy}\mathrm{d}x\mathrm{d}y + \int_{l_c-l_{cf}}^{l_c}\int_{x_b}^{x_t}\sigma_{yy}\mathrm{d}x\mathrm{d}y\right) \tag{III.29}$$

Now the locally bent column flange can be divided into n_{cl} small layers in the direction of the flange thickness. The axial force, F_{ca}, and the equivalent moment, M_{cc}, can be determined as

$$F_{ca} = \frac{V_{PZ}}{y_A}\sigma^*_{yy} + \frac{n_{cf}w_c(l_c-2l_{cf})t_{cf}}{y_A}\sigma^m_{yy} + \frac{n_{cf}w_c l_{cf}\delta_x}{y_A}\sum_{i=1}^{n_{cl}}\left(\sigma^{bi}_{yy} + \sigma^{ti}_{yy}\right) \tag{III.30}$$

$$M_{cc} = -V_{PZ}\sigma^*_{xy} + n_{cf}w_c\delta_x\sum_{i=1}^{n_{cl}}\left(\sigma^{bi}_{yy} - \sigma^{ti}_{yy}\right)(x_i - x_r) \tag{III.31}$$

where x_i = local coordinate of layer i; δ_x = thickness of each of the layers; σ_{yy}^m = longitudinal stress in the flange length $l_{cf} \leq y \leq l_c - l_{cf}$; σ_{yy}^{bi} and σ_{yy}^{ti} are respectively the stress in layer i in the flange length $0 \leq y \leq l_{cf}$ and that in the flange length $l_c - l_{cf} \leq y \leq l_c$. It is noted that σ_{yy}^{bi} and σ_{yy}^{ti} are assumed to distribute in each layer uniformly.

III.5. Comparison between connection models and experiments

Krawinkler et al. (1971) performed a detailed experimental study for steel moment frame subassemblages. Two types of subassemblages of a 20-story 4-bay office building were investigated. One subassemblage taken from the 5th floor and the other from the 17th floor provide a good range of behavior of connections in tall building moment frames.

Table III.1 presents two test specimens selected from their work. The table includes geometry information about each connection specimen and compressive axial forces. In the table, w_b indicates the beam flange width; σ_{wy} and E_s respectively denote the yield strength and the strain hardening modulus of the column web.

Table III.1: Information about test specimens

Specimen	t_{PZ}	d_c	d_b	t_{cf}	t_{bf}	w_c	w_b	σ_{wy}	E_s	F_{ca}, kip
1	0.254	8.03	10.04	0.395	0.271	5.79	4.04	41.0	660	85.0
2	0.627	9.09	13.72	0.908	0.327	8.16	5.04	47.0	800	338.0
Notes: dimension unit = in; unit of σ_{wy} and E_s = ksi.										

Figure III.4 shows stress-strain curves obtained from tension tests for the column web of the two connection specimens (Krawinkler 1978). The yield strength of Specimen 2 is higher than that of Specimen 1; however, the yield plateau is much shorter in Specimen 2 than Specimen 1. These stress-strain relationships including

the strain-hardening branch are critical for accurate estimates of the response of the frame connection.

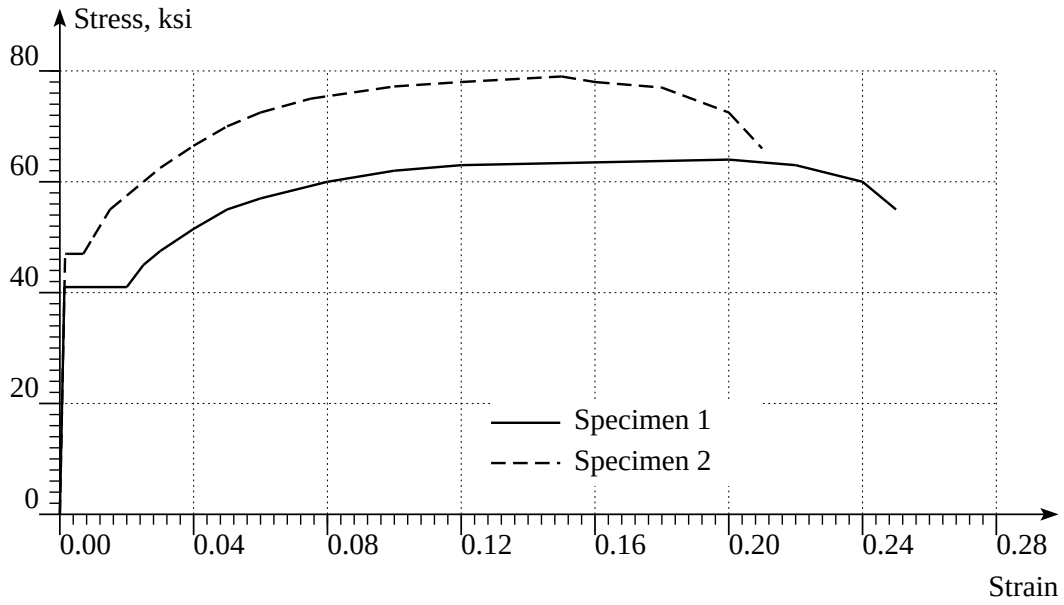

Figure III.4: Strain-stress curve for the column webs.

Figure III.5 shows the test results of the two connection specimens. The two curves are determined based on the information given in Krawinkler (1978). The figure shows two apparently distinct responses for the two types of subassemblages. The two test specimens have a significant difference in the yield strength, elastic stiffness, and inelastic tangent.

Two different available mathematical models are selected for comparison with the mathematical model developed in this study. The first model developed by Krawinkler (1978) is simple and is used in current building standards (AISC 2010c; FEMA 2000a). The second model developed by Kim and Engelhardt (2002) is in a complex form and requires additional computational steps and coefficients. Results obtained by using these three models are plotted with the test results for comparison

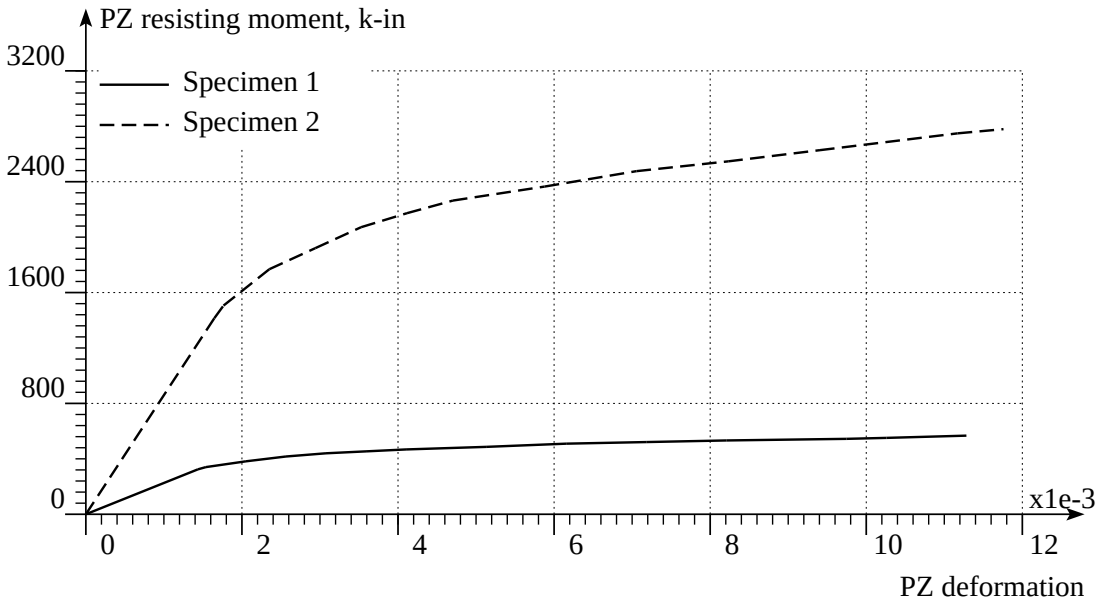

Figure III.5: Behavior of the test specimens from experiments.

as shown in Figures III.6 and III.7. It is noted that in the model developed by Kim and Engelhardt (2002), the ratio of the average shear deformation to the initial yield shear deformation is chosen as $C_y = 0.9$ within the range suggested by the authors.

The mathematical model developed in this study is applied to the computation as follows. The strains in the panel zone and column flanges are determined as a function the panel zone shear deformation. The stress components developed in the connection is then tracked by using those two stress-strain relationships. The panel zone resisting moment can hence be determined by using Equations (III.30) and (III.31).

In the application of the developed PZ model, the following parameters were found to provide a rational fit between the developed model and the experiments.

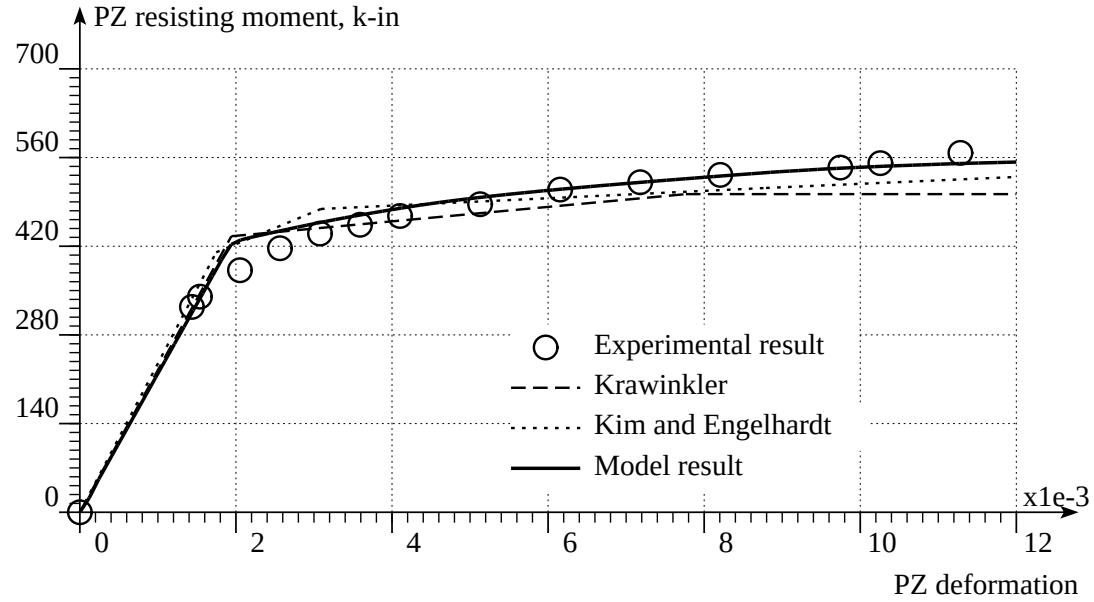

Figure III.6: Comparison of the developed model and the test result for Specimen 1.

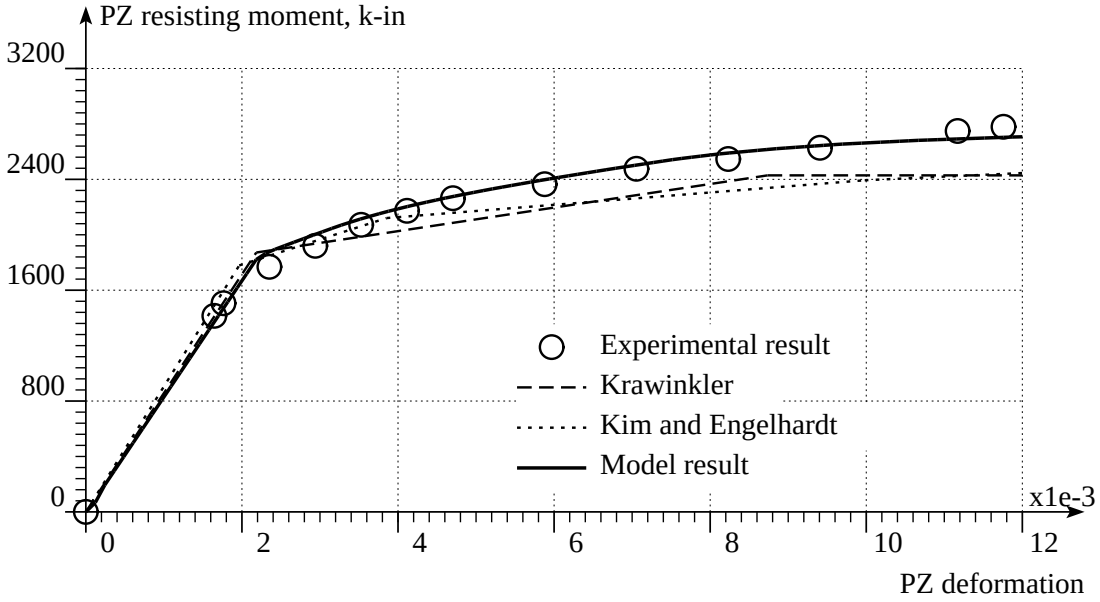

Figure III.7: Comparison of the developed model and the test result for Specimen 2.

The length of the column flange under local bending is determined by

$$l_{cf} = t_{cf} + 0.25 l_c \tag{III.32}$$

Considering the column flange in the positive direction of the x-axis (refer Figure III.3), the location of the reference plane is determined as

$$x_r = \left(0.467 \frac{t_{cf}}{t_{PZ}} - 0.277\right)(d_c - t_{cf}) \tag{III.33}$$

Figure III.6 shows that the model proposed by Kim and Engelhardt (2002) has a more conservative estimate of the response of the connection after it yields. The other two models have similar estimates except that Krawinkler suggested the connection strength would practically not increase after the PZ deformation exceeded four times the yield deformations. These two models also present a reasonable fit with the test results.

For Specimen 2, Figure III.7 also shows that all three models exhibit good behavior in estimating the response of the frame connection up until right after its yielding. The models developed by Krawinkler (1978) and Kim and Engelhardt (2002) underestimate the response of the connection after the yielding. The model developed in this study successfully estimates the connection response both in the elastic and inelastic ranges.

CHAPTER IV
EXPERIMENTAL STUDY

The frame element with local buckling consideration and the beam-to-column connection model developed in the last chapters are used for experimental studies in this chapter. Several full-scale specimens were fabricated and tested at the University of Minnesota's Multi-Axial Subassemblage Testing (MAST) System(NEES 2013). This chapter describes the test specimens, presents the development of finite element models for simulating the specimen response, and compares these experimental and analytical results.

IV.1. Experimental setup

Figure IV.1 presents a typical experimental setup for beam-to-column subassemblages. The two half beams are supported by two ancillary actuators. Each actuator acts as a rigid link and is free to rotate around its ends. The horizontal distance between the two ancillary actuators is 14 feet 10 and 3/16 inches (L=14'-10 3/16"). The column is hinge-connected to the stiff floor. The column length is 13 feet and 7.25 inches. The load is transferred to this beam-to-column subassemblage through the rigid cross-head on the top of the column. The loading protocol complies with the seismic provision for cyclic tests of beam-to-column connections specified in ANSI/AISC 341-10 (AISC 2010b).

Table IV.1 lists seven test specimens to be investigated in this study. The table presents the doubler plate thickness and wide-flange shape sections for the column and beam. It is noted that for specimens 3, 5, and 6, two doubler plates are welded to two sides of the column web.

Figures IV.2 and IV.3 are photographs of Specimen 1 prior to testing and at

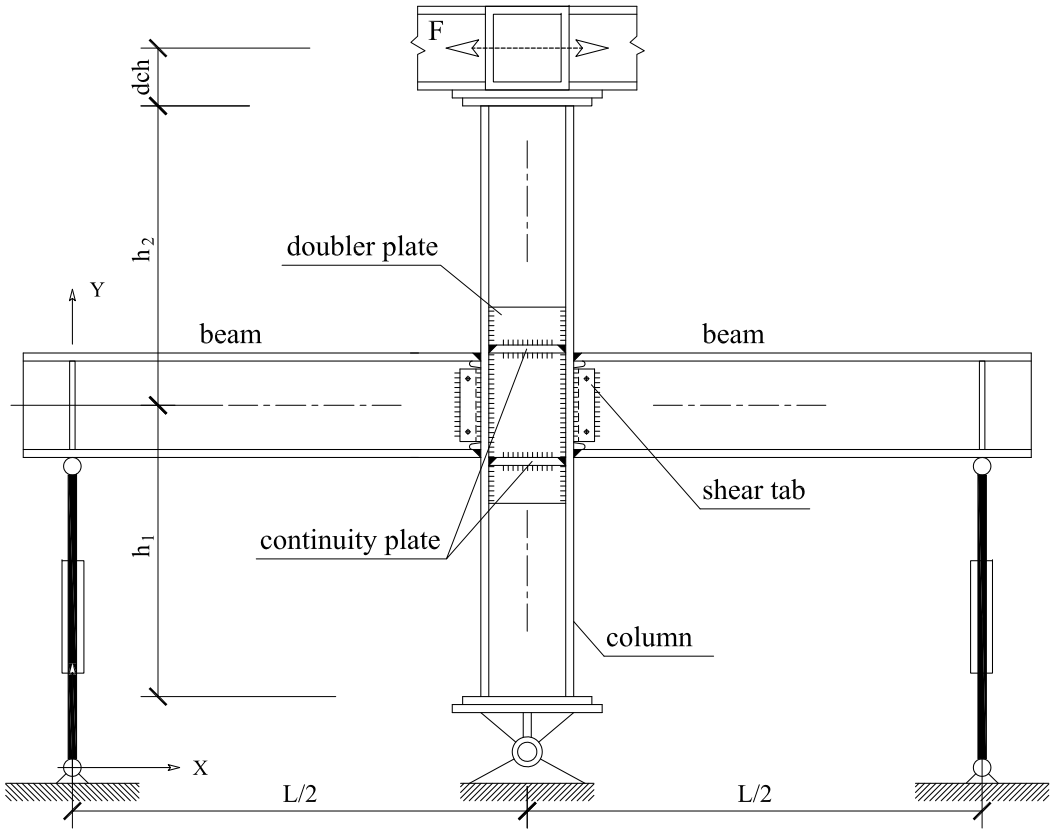

Figure IV.1: Typical experimental setup.

failure, respectively. The latter figure shows that the panel zone is under significant shear deformation and the beam top flange is under local buckling. The crack starts from this flange and progresses to the beam web.

IV.2. Finite element model

Figure IV.4 shows a typical nonlinear finite model for the subassemblage specimens. The numbers contained in the circles represents some nodes of the models. Straight thin lines denote beam or column elements. Thick lines are rigid elements. Dashed thick lines represent translational constraints (in both the horizontal and vertical

Table IV.1: List of test specimens

Specimen	Doubler plate thickness, in	Column section	Beam section
1	0.0	W33x263	W30x108
2	0.5	W33x263	W30x108
3	2*0.5	W33x263	W30x108
4	0.0	W14x398	W36x150
5	2*0.5	W14x398	W36x150
6	2*(9/8)	W14x398	W36x150
7	5/8	W12x106	W24x55

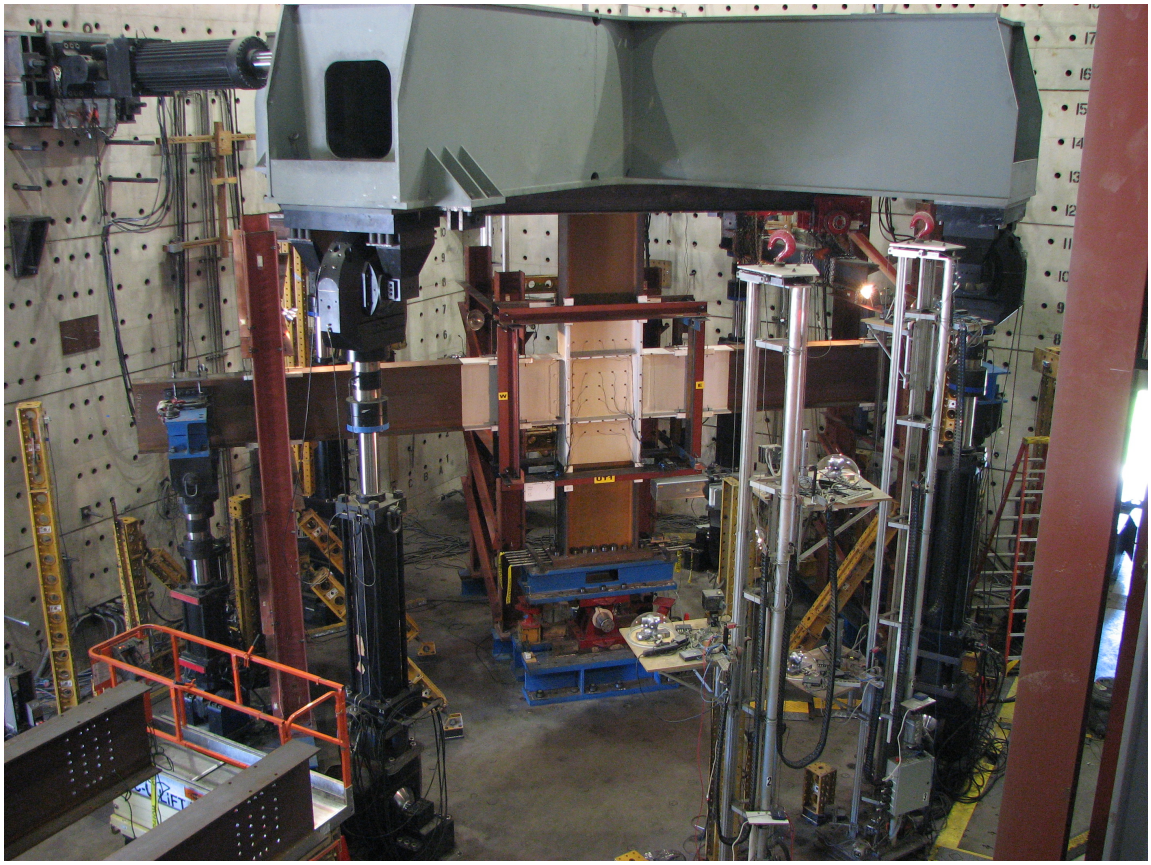

Figure IV.2: Specimen 1 prior to testing.

directions). External force as indicated as F in the figure is exerted on the system at Node 22.

Figure IV.3: Specimen 1 at failure.

Beam and column elements are connected to the rigid elements of the panel zone. All the beams and columns of the structural system are modeled using nonlinear finite elements with local buckling consideration. Sections of beams and columns are discretized into fibers as shown in the figure (Sections A-A and B-B). Panel zone elements include four rigid links connected by four hinges and a rotational spring element. This developed nonlinear spring element simulates the moment-shear deformation response of the panel zone.

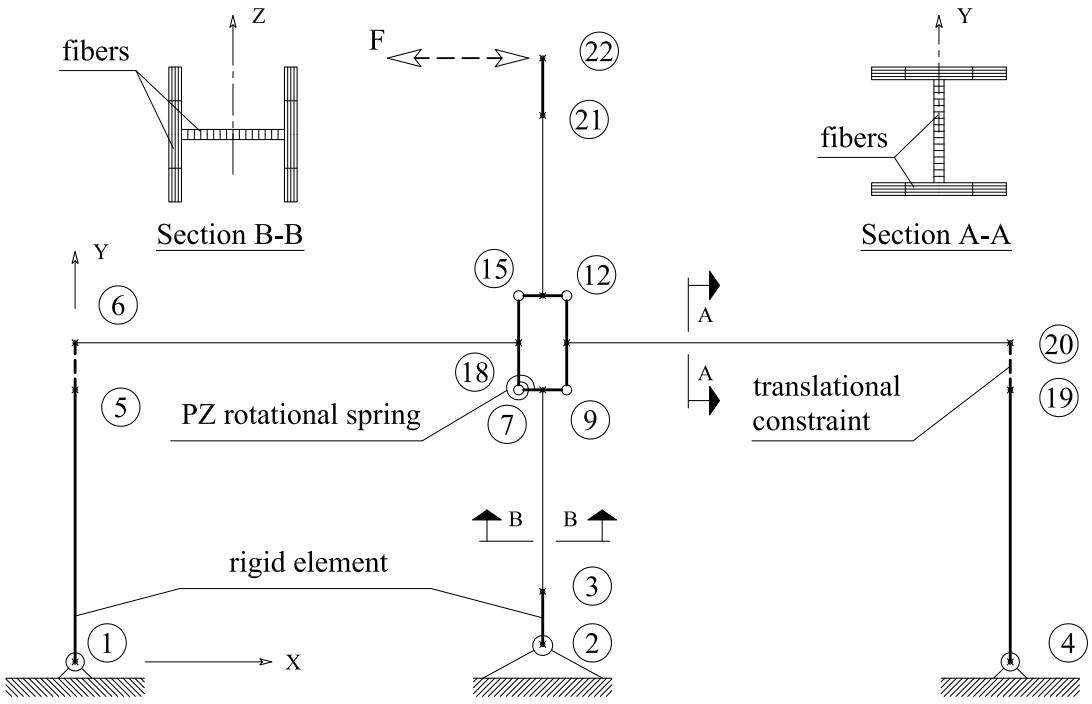

Figure IV.4: Typical nonlinear finite element model for test specimens.

IV.3. Results

Figures IV.5 to IV.11 show a comparison between the experimental results and simulation results in terms of the cyclic response of the seven test specimens. The response is represented by the relationship between the upper column shear or lateral force at the column tip and the drift ratio of the column.

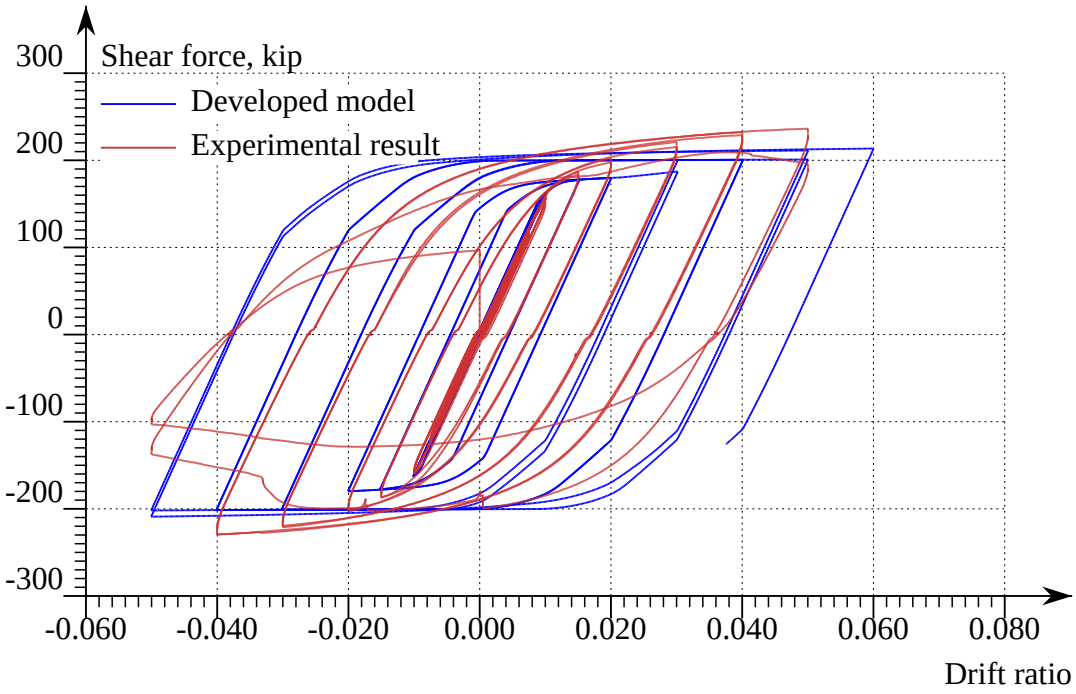

Figure IV.5: Cyclic response of Specimen 1.

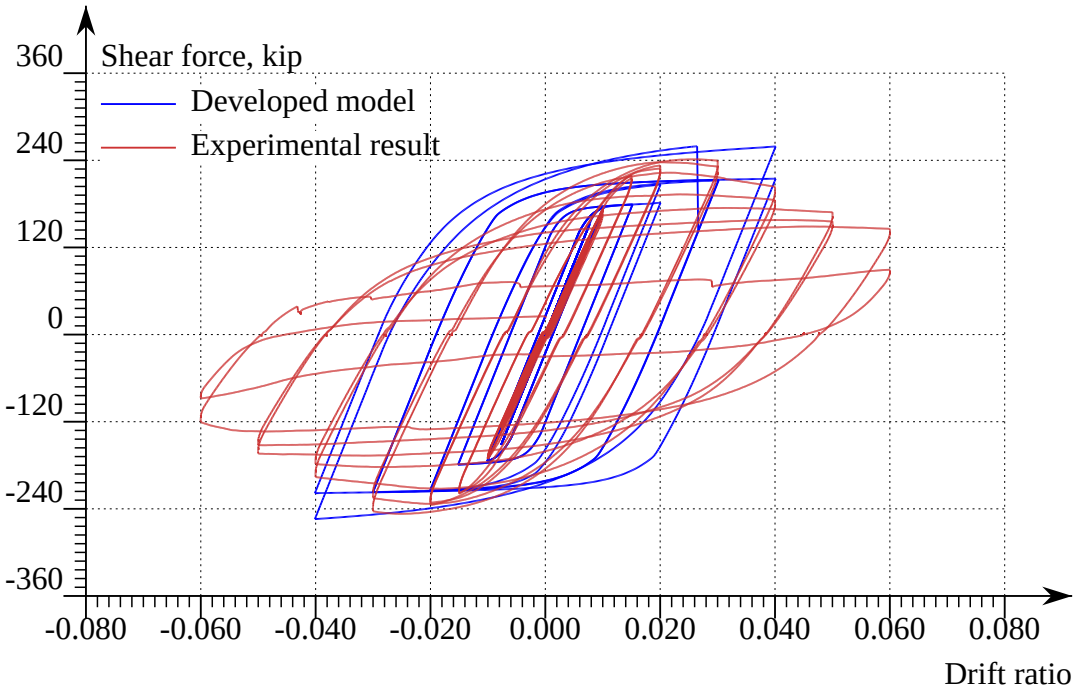

Figure IV.6: Cyclic response of Specimen 2.

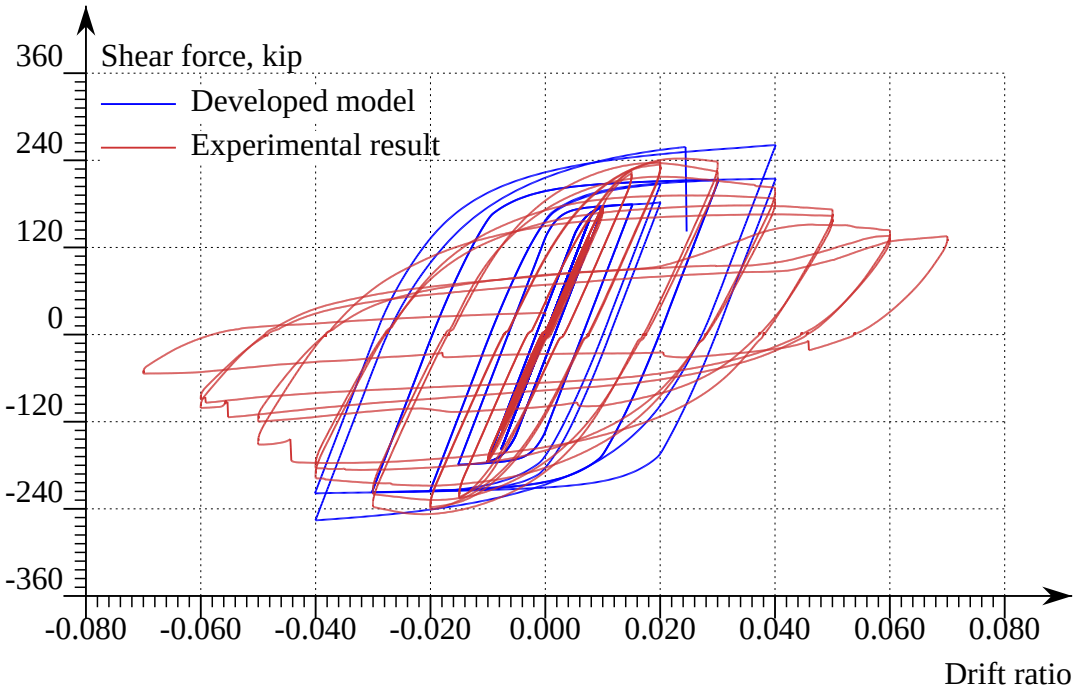

Figure IV.7: Cyclic response of Specimen 3.

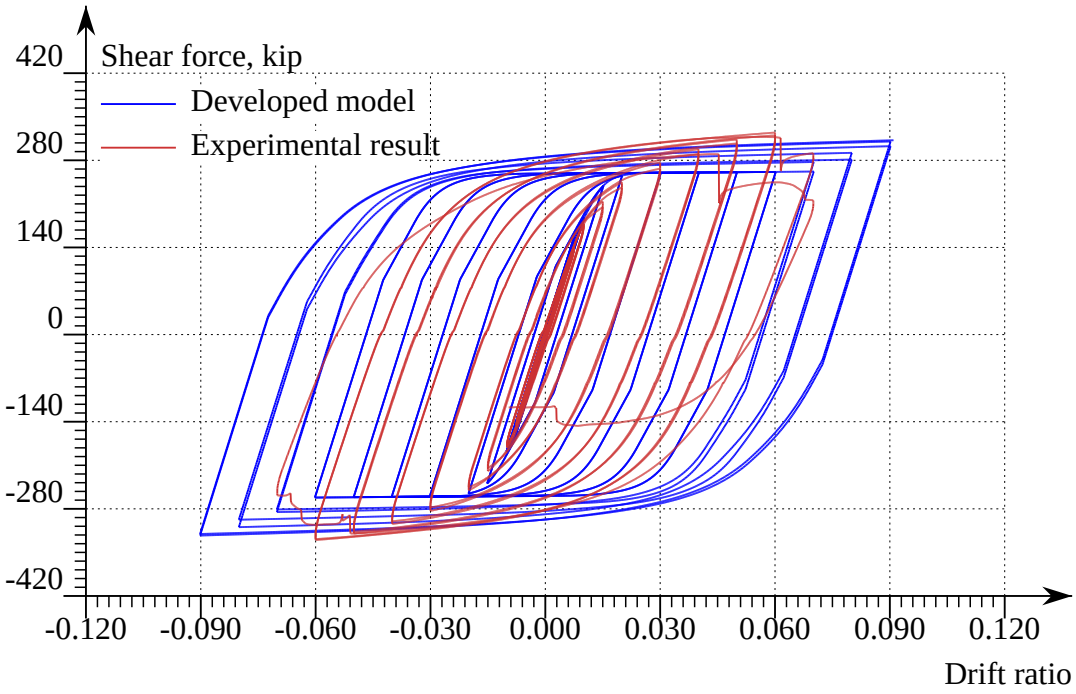

Figure IV.8: Cyclic response of Specimen 4.

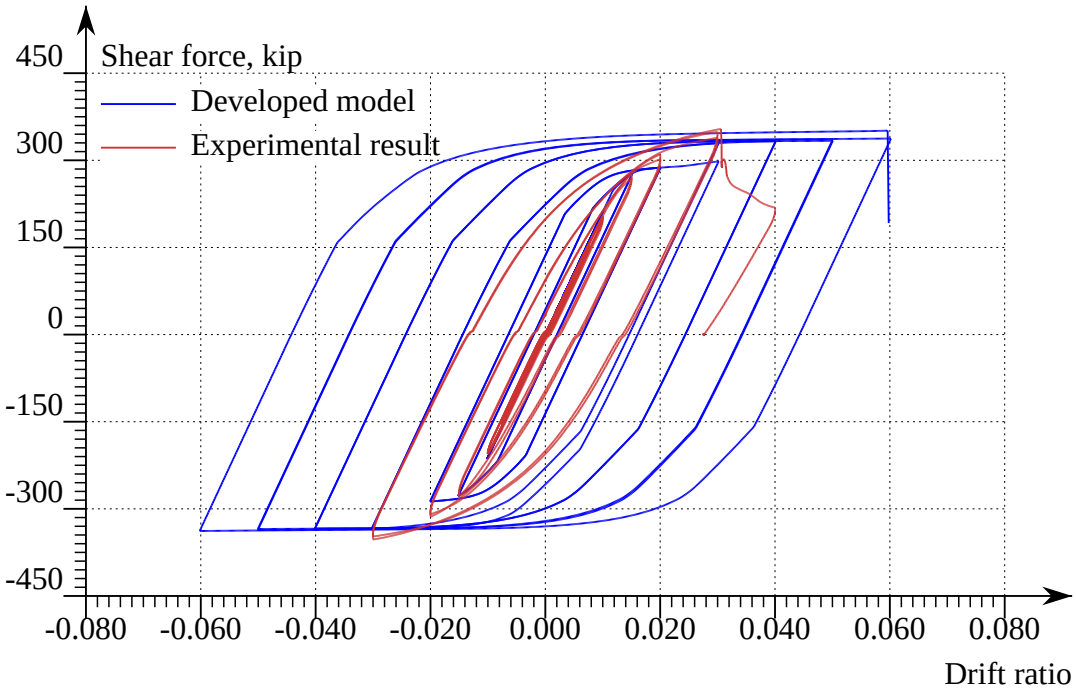

Figure IV.9: Cyclic response of Specimen 5.

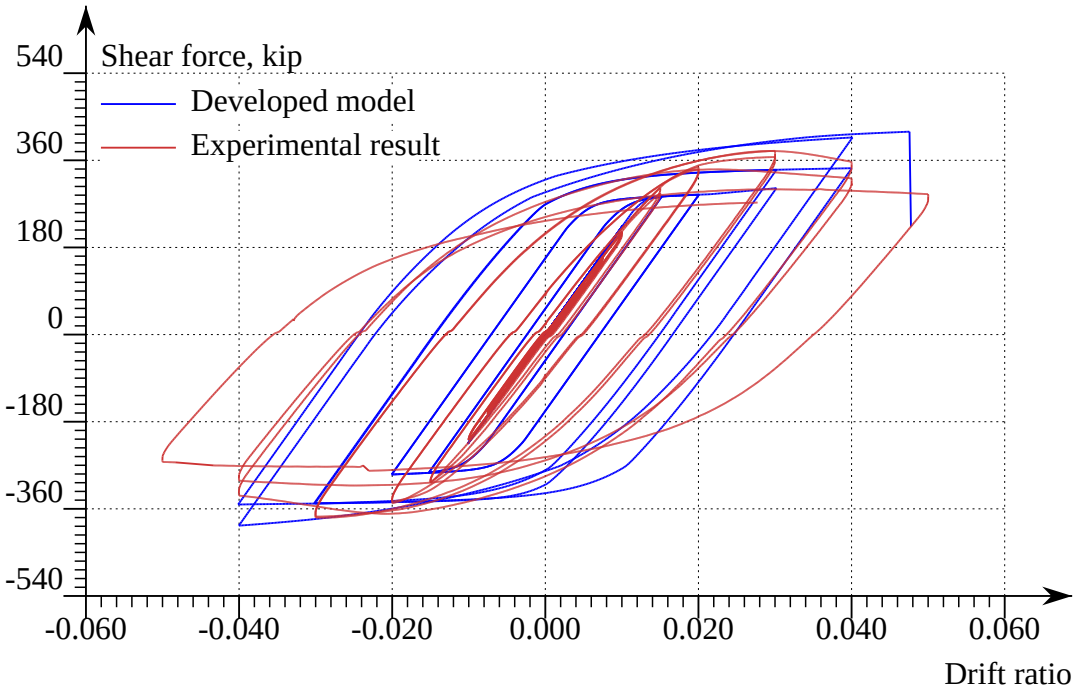

Figure IV.10: Cyclic response of Specimen 6.

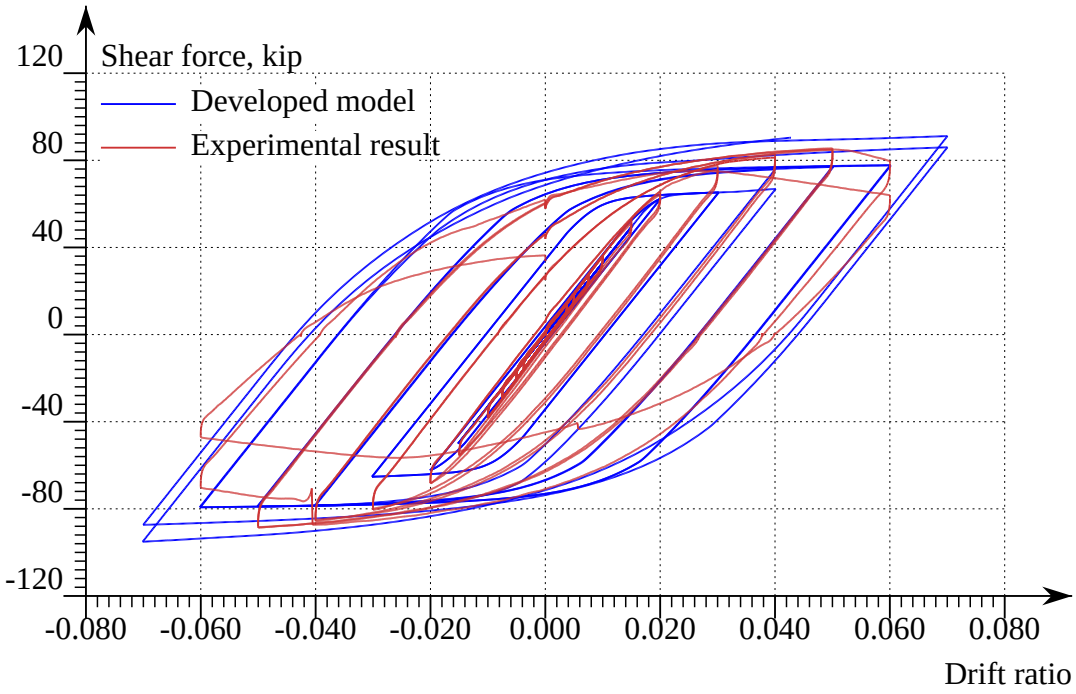

Figure IV.11: Cyclic response of Specimen 7.

CHAPTER V

OPTIMIZATION OF PANEL ZONE PARTICIPATION

This chapter introduces a methodology to optimize the panel zone (PZ) participation in the behavior of steel moment frames (SMFs) under lateral loading effects. In practice, as an approximation, a SMF can be separated at its inflection locations into beam-to-column subassemblages. The optimal PZ participation is defined so that the subassemblage exhibits the most inelastic deformation energy given an ultimate drift angle. Two yielding ratios are selected as decision variables for evaluating the PZ participation: (1) the ratio of the strength at the girder yielding to that at the PZ yielding, and (2) the ratio of the strength at the column yielding to that at the PZ yielding. In addition, the design of SMF subassemblages is constrained by the seismic provision for special moment frames specified in ANSI/AISC 341-10 (AISC 2010b).

V.1. Subassemblage finite element model

Figure V.1 shows the modeling of a typical SMF subassemblage. The model boundary condition approximately simulates the subassemblage constrained in the entire SMF system under lateral loading effects. The two outmost rigid links are used to ensure the same vertical displacement for both the beam ends while not preventing their displacements. The plastic hinges in the beams are located where the beam section is smallest and the bending moment is largest. As shown in the figure, H and P respectively denote the lateral and vertical forces.

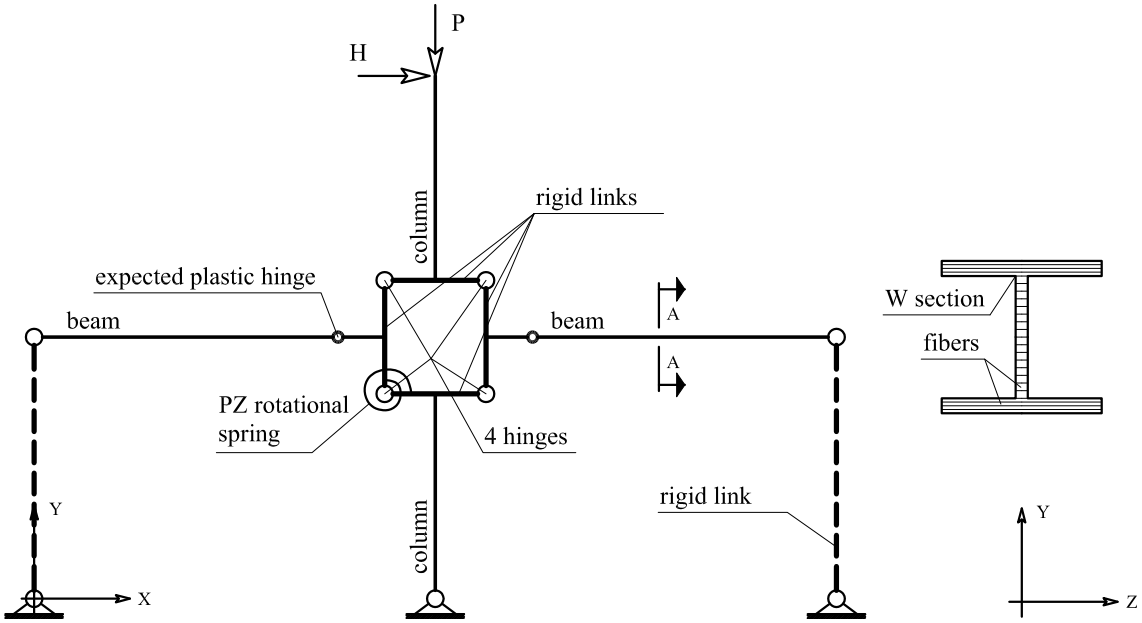

Figure V.1: Typical SMF subassemblage model.

V.2. Characterized response of subassemblages

Figure V.2 characterizes the monotonic response of a SMF subassemblage based upon the seismic provision for special moment frames. Under an increasing lateral force, denoted as H in Figure V.1, the subassemblage deformation increases, resulting increased column drift and shear. When H reaches the ultimate strength of the subassemblage, V_u, the structural system exhibits unstable deformation. The story or column drift ratio is the relative lateral displacements of the lowermost and uppermost column ends, as in Figure V.1, divided by their distance.

The subassemblage experiences different yielding stages as shown in Figure V.2. The PZ is designed to yield first; the shear yielding of PZs is more stable than the yielding of beams (Krishnan and Muto 2011). Thus, the subassemblage yields first at point P_y when the PZ initially yields. As the PZ yielding progresses, the beams yield. The yielding of both beams occurs approximately at point P_2. One column

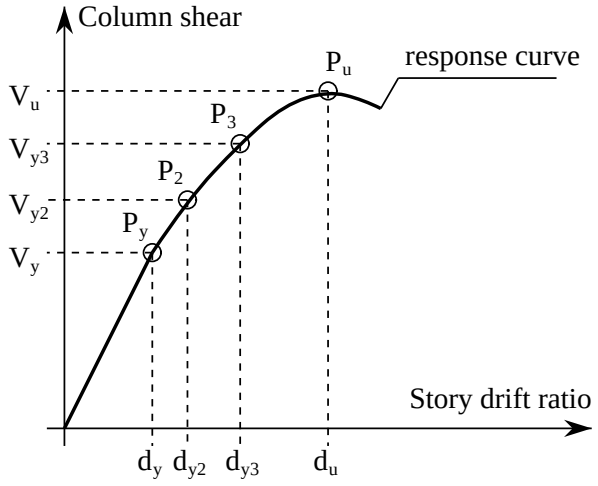

Figure V.2: Characterized monotonic response of typical SMF subassemblages.

yields at point P_3, only after the fully yielded and strain-hardened beams, as complied with ANSI/AISC 341-10. The subassemblage strength can continue to develop until point P_u as the yielding of the column progresses. The structural system continues deforming drastically if the lateral force does not decrease in magnitude.

V.3. Objective function

The remaining question is the optimal participation of the PZ in the behavior of a subassemblage. In other words, where is the best location on the monotonic response curve (Figure V.2) for the structural members to begin to yield? The best location is herein defined as where the inelastic deformation energy is maximized. The yield locations are described by a beam yield ratio, denoted r_{yb}, and a column yield ratio, r_{yc}:

$$r_{yb} = \frac{V_{y2}}{V_y}, \qquad r_{yc} = \frac{V_{y3}}{V_y} \tag{V.1}$$

where V_y = first yield strength of the subassemblage; V_{y2} = strength of the subassemblage when one of the beams begins yielding; and V_{y3} = strength of the subassemblage

when one of the columns begins yielding. As shown on Figure V.2, the corresponding story drift ratios are d_y, d_{y2}, and d_{y3}, respectively.

Figure V.3 shows a characterized cyclic response of a typical subassemblage model. The area inside a hysteretic loop represents the inelastic deformation energy of the model in that loading cycle. The energy dissipation capacity to be optimized is the area of the hysteretic loop that corresponds to the ultimate drift angle. Test results have shown that ultimate failure typically occurs due to low cycle fatigue fracture at drift angles of 5% to 7% AISC (2010a). FEMA 350 recommends qualifying drift angles for special steel moment frame systems. The strength degradation qualifying drift angle is 4 %, and the ultimate qualifying drift angle is 6% (AISC 2010b; FEMA 2000a). Thus, the energy dissipation capacity is determined at the drift angle of 6%.

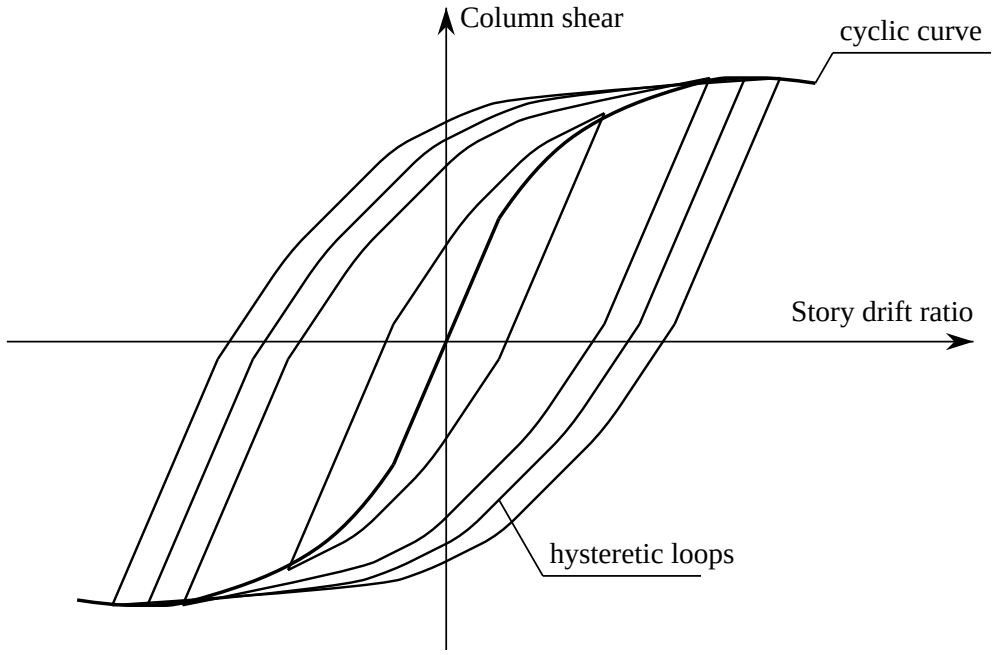

Figure V.3: Characterized cyclic response of SMF subassemblages

The energy dissipation capacity is denoted as E_d. In order to determine E_d, a nonlinear finite element model is developed for the subassemblage. The loading protocol complies with the seismic provision for cyclic tests of beam-to-column connections specified in ANSI/AISC 341-10 (AISC 2010b). Thus, the objective function for the optimal participation of PZs is formulated as

$$E_d = f\left(r_{yb}, r_{yc}\right) \tag{V.2}$$

where $f(\cdot)$ is limited by the optimization constraints.

V.4. Optimization constraints

The objective function as presented in (V.2) is constrained by the following conditions:

- The strong-column weak-beam philosophy is applied such that columns yield after the PZ yielding and the fully yielded beams,
- The lateral elastic stiffness is relatively the same for all subassemblages to minimize the redistribution of internal forces due to the change of designed structural members.
- The PZ thickness shall meet the required minimal values to minimize the shear buckling of the PZ during its inelastic deformation (AISC 2010b):

$$t_{PZ\min} = \frac{d_b - 2t_{fb} + d_c - 2t_{fc}}{90} \tag{V.3}$$

V.5. Lateral elastic stiffness of a subassemblage

The lateral stiffness of a subassemblage reflects the relationship between the story drift ratio and the lateral force acting on the subassemblage. Figure V.4 shows an analytical model for SMF subassemblages. The stiffness of a subassemblage is mainly contributed by the flexural or bending stiffness of the girders and columns and by the shear stiffness of the PZ.

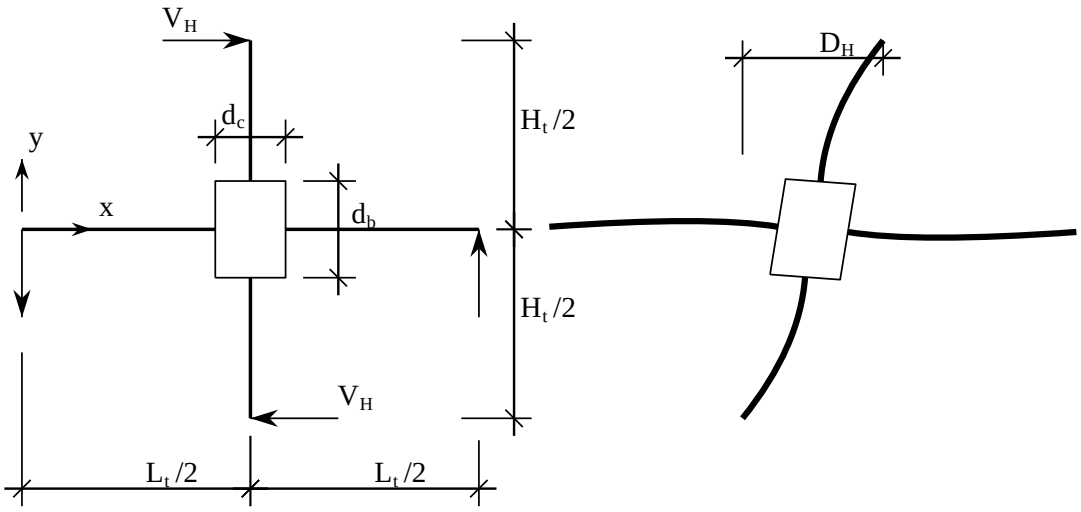

Figure V.4: Analytical model for SMF subassemblage.

By applying compatibility and equilibrium conditions to the structural model and balancing the external work with the internal elastic deformation energy, the lateral stiffness of a subassemblage can approximately be derived as presented in the following procedure.

The external work done by the lateral force, V_H, on the subassemblage is determined by

$$W_e = \frac{1}{2} V_H D_H \tag{V.4}$$

The internal elastic deformation energy in the two girders is determined as

$$I_g = 2\int_{V_b} \frac{1}{2}\sigma_{ij}\varepsilon_{ij}\mathrm{d}V \Leftrightarrow \tag{V.5}$$

where V_g = volume of the girder; σ_{ij} and ε_{ij} respectively denote stress and strain components in the girder. The flexural energy can therefore be derived as

$$I_g = \int_0^{l_b}\int_{A_b} \frac{\sigma_x^2}{E_s}\mathrm{d}A\mathrm{d}x \Leftrightarrow \tag{V.6}$$

$$I_g = \int_0^{l_b} \frac{M_z^2}{I_{zg}E_s}\mathrm{d}x \tag{V.7}$$

where $l_b = 0.5(L_t - d_c)$ = length of the girder; A_b = cross-section area of the girder; E_s = material elastic modulus; σ_x = girder longitudinal stress; M_z = bending moment along the girder; I_{zg} = moment inertia around the strong axis of the girder cross section that is perpendicular to the plane of the subassemblage.

By equilibrium conditions, the bending moment in the girder is determined as

$$M_z = R_b x = \frac{V_H H_t}{L_t}x \tag{V.8}$$

where R_b = reaction or shear force at the girder ends. If I_{zg} is assumed constant along the girder, the deformation energy becomes

$$I_g = \frac{1}{24 I_{zg}E_s}\frac{H_t^2}{L_t^2}V_H^2\left(L_t - d_c\right)^3 \tag{V.9}$$

Similarly, the internal flexural energy in the two columns can be derived and

determined by

$$I_c = \frac{1}{24 I_{zc} E_s} V_H^2 \left(H_t - d_b\right)^3 \tag{V.10}$$

The internal energy in the PZ due to shear deformation can approximately be determined as

$$I_{PZ} = \int\limits_{V_{PZ}} \frac{1}{2} \left(\sigma_{12}\varepsilon_{12} + \sigma_{21}\varepsilon_{21}\right) \mathrm{d}V \Leftrightarrow \tag{V.11}$$

$$I_{PZ} = V_{PZ} \tau_{yx}^2 \frac{1}{2G_s} \Leftrightarrow \tag{V.12}$$

$$I_{PZ} = \frac{d_b}{2 t_{PZ} d_c G_s} V_H^2 \tag{V.13}$$

where V_{PZ} = PZ volume; $\tau_{yx} \equiv \sigma_{21}$ = shear stress in the PZ; G_s = shear modulus of the PZ material; t_{PZ} = PZ thickness; d_c = column section depth; d_b = girder section depth.

Balancing the sum of the above internal energy with the external work gives

$$W_e = I_g + I_c + I_{PZ} \Leftrightarrow \tag{V.14}$$

$$\frac{D_H}{V_H} = \frac{H_t^2 (L_t - d_c)^3}{12 L_t^2 I_{zg} E_s} + \frac{\left(H_t - d_b\right)^3}{12 I_{zc} E_s} + \frac{d_b}{t_{PZ} d_c G_s} \tag{V.15}$$

where the right side is the lateral flexibility of the subassemblage. The lateral elastic stiffness of the subassemblage can now be obtained by inversion as

$$K_{sub} = \frac{V_H}{D_H} \tag{V.16}$$

V.6. Yield strengths

To determine the shear demand on the panel zone, the resultant bending moment from all the girders at the centerline of the column is approximated by the action of a force couple each which acts at the level of the mid plane of the girder flanges (FEMA 2000a; Jin and El-Tawil 2005). By equilibrium conditions, the magnitude of each force of the couple can therefore be determined as

$$V_b = \frac{H_t}{d_b - t_{fb}} V_H \tag{V.17}$$

where t_{fb} = girder flange thickness. The shear demand on the panel zone is now equal to

$$V_{PZ} = V_b - V_H = \frac{H_t - d_b + t_{fb}}{d_b - t_{fb}} V_H \tag{V.18}$$

The yielding of the panel zone starts when the demand shear force in the panel zone reaches

$$V_{PZ} = \tau_y t_{PZ} d_c \tag{V.19}$$

where τ_y = yield shear strength of the PZ material. Based on von Mises yield criterion (De Souza Neto et al. 2008; Jain 1989), τ_y can be derived and determined by

$$\tau_y = \sqrt{\frac{f_y^2 - \sigma_{11}^2}{3}} \tag{V.20}$$

where f_y = yield strength of the PZ material; $\sigma_{11} = P/A_c$ accounts for the effect of the column axial force (P); A_c = column cross-section area. Combining Equations (V.18) and (V.19) gives the lateral force that causes the panel zone to begin yielding as

$$V_H \equiv V_{HPZ}^y = \frac{d_b - t_{fb}}{H_t - d_b + t_{fb}} \tau_y t_{PZ} d_c \tag{V.21}$$

The expected plastic hinge in the girders (see Figure V.1) begins to yield when the lateral force reaches the magnitude that satisfies

$$\frac{M_{zy}}{I_{zp}}\frac{d_b}{2} = f_y \tag{V.22}$$

where I_{zp} = moment inertia of the plastic hinge. The bending moment that causes the start of the yielding of the expected plastic hinge can approximately be determined as

$$M_{zy} = \frac{H_t}{L_t}V_H\left(\frac{L_t - d_c}{2} - l_p\right) \tag{V.23}$$

where l_p is the closest distance from the column flange to the center of the plastic hinge. The lateral force that causes the yielding of the girders to begin can therefore be determined by

$$\frac{H_t}{L_t}V_H\left(\frac{L_t - d_c}{2} - l_p\right) = f_y S_{zp} \tag{V.24}$$

or equivalently,

$$V_H \equiv V_{HP}^y = \frac{2L_t}{H_t(L_t - d_c - 2l_p)}f_y S_{zp} \tag{V.25}$$

where S_{zp} = elastic section modulus around the strong axis of the cross section at the center of the plastic hinge.

Similarly, the start of the column yielding can be determined as the lateral force reaches the magnitude such that

$$V_H\frac{H_t - d_b}{2I_{zc}}\frac{d_c}{2} + \sigma_{11} = f_y \tag{V.26}$$

or equivalently,

$$V_H \equiv V_{HC}^y = \frac{4I_{zc}(f_y - \sigma_{11})}{d_c(H_t - d_b)} \tag{V.27}$$

V.7. Optimization procedure

1. Obtain a full list of AISC wide-flange(W) sections,

2. Search for W shapes that have approximately the same cross-section area and plastic section modulus as the designed column,

3. Search for W shapes that have approximately the same plastic section modulus as the designed girders. The clear span-to-depth ratio is at least 7.

4. Determine the panel zone thickness, t_{PZ}, by imposing the minimal required thickness as given in Equation (V.3) and by the lateral elastic stiffness of the designed subassemblage as determined by Equations (V.15) and (V.16),

5. Create RBS sections that conforms with AISC 358 (AISC 2010a) . The cut radius of RBS is determined by

$$r_{RBS} = \frac{4c^2 + b^2}{8c} \tag{V.28}$$

where a = shortest distance from the column flange to the start of an RBS cut; b = cut length; c = cut depth. These dimensions satisfy the following requirements:

$$0.5b_{bf} \leq a \leq 0.75b_{bf} \tag{V.29}$$

$$0.65d_b \leq b \leq 0.85d_b \tag{V.30}$$

$$0.1b_{bf} \leq c \leq 0.25b_{bf} \tag{V.31}$$

6. Apply the yielding order constraint to obtain a population of subassemblages with information about structural member sections and panel zone thickness,

7. Perform structural analysis to determine the response of the obtained subassemblages under cyclic loading,

8. Determine the energy dissipation capacity for each subassemblage system and select the system with the most dissipation capacity as the one with an optimal design.

V.8. Computation

A subassemblage is extracted from one of the SAC model buildings (FEMA 2000c). It is a 3-story office building located in Los Angeles whose design conforms with FEMA 267 (FEMA 1995). The story height is 13 ft, the span length of its moment frame is 30 ft. Wide flange shapes W30x116 and W14x311 are used for the girders and columns of the moment frames. In addition, 0.75-in-thick cover plates are welded to both the bottom and top flanges of girder ends. The width of the top cover plates reduces gradually over the distance of l_p, from the column flange surface to the expected plastic hinge location.

The theoretical lateral stiffness of the subassemblage is determined by using Equations (V.15) and (V.16) and is $K_{sub} = 176.8$ kip/in.

The lateral forces that cause the panel zone, the girders, and the columns to begin to yield are determined from using Equations (V.21), (V.25), and (V.27). The forces are respectively $F^y_{HPZ} = 175.9$ kip, $F^y_{HG} = 268.0$ kip, and $F^y_{HC} = 437.5$ kip. It is noted that the column axial force is determined based on ASCE Standard ASCE/SEI 7-10, Minimum Design Loads for Buildings and Other Structures (ASCE 2010) and FEMA P695, Quantification of Building Seismic Performance Factors (FEMA 2009).

Using Equation (V.1) to determine the yield ratio gives $r_y = 0.34$.

Table V.1 presents a list of subassemblages obtained by using the optimization procedure presented in the last section. The table includes both the systems designed with cover end plates and the systems with reduced beam sections (RBS). The length and depth of RBS cuts, $b_{RBS} = 0$ and $c_{RBS} = 0$, indicate the systems with cover plates. Finite element analyses are implemented to investigate the behavior of these structural systems.

Table V.1: Population of subassemblages to be analyzed

System	Column	Girder	t_{PZ}, in	l_p, in	b_{RBS}, in	c_{RBS}, in	r_{yb}	r_{yc}
1	W14X311	W30X108	1.71	18.00	0.00	0.00	1.15	2.10
2	W12X336	W27X129	1.86	18.00	0.00	0.00	1.39	2.06
3	W12X336	W27X129	1.86	16.60	20.70	1.00	1.15	2.06
4	W12X336	W27X129	1.86	16.60	20.70	1.15	1.11	2.06
5	W12X336	W27X129	1.86	16.60	20.70	1.30	1.08	2.06
6	W12X336	W27X129	1.86	16.60	20.70	1.45	1.05	2.06
7	W12X336	W27X129	1.86	16.60	20.70	1.60	1.01	2.06
8	W14X311	W27X129	2.51	18.00	0.00	0.00	1.01	1.57
9	W14X311	W30X116	1.41	18.00	0.00	0.00	1.52	2.54
10	W14X311	W30X116	1.41	17.81	22.50	1.05	1.28	2.54
11	W14X311	W30X116	1.41	17.81	22.50	1.21	1.25	2.54
12	W14X311	W30X116	1.41	17.81	22.50	1.37	1.21	2.54
13	W14X311	W30X116	1.41	17.81	22.50	1.52	1.18	2.54
14	W14X311	W30X116	1.41	17.81	22.50	1.68	1.14	2.54
15	W14X311	W30X116	1.41	17.81	22.50	1.84	1.11	2.54
16	W14X311	W30X116	1.41	17.81	22.50	2.00	1.07	2.54
17	W14X311	W30X116	1.41	17.81	22.50	2.15	1.03	2.54
18	W14X311	W30X124	1.78	18.00	0.00	0.00	1.30	2.00
19	W14X311	W30X124	1.78	17.89	22.65	1.05	1.09	2.00
20	W14X311	W30X124	1.78	17.89	22.65	1.21	1.06	2.00
21	W14X311	W30X124	1.78	17.89	22.65	1.37	1.03	2.00
22	W14X311	W30X124	1.78	17.89	22.65	1.52	1.00	2.00

Figure V.5 shows a nonlinear finite element model that is developed for analyzing the population of structural systems in Table V.1. A lateral force acting at the

column top increases in amplitude until the system fails. It is noted that the finite element program is coded such that a structural system fails if the strain in any part of that system exceeds the ultimate strain limit.

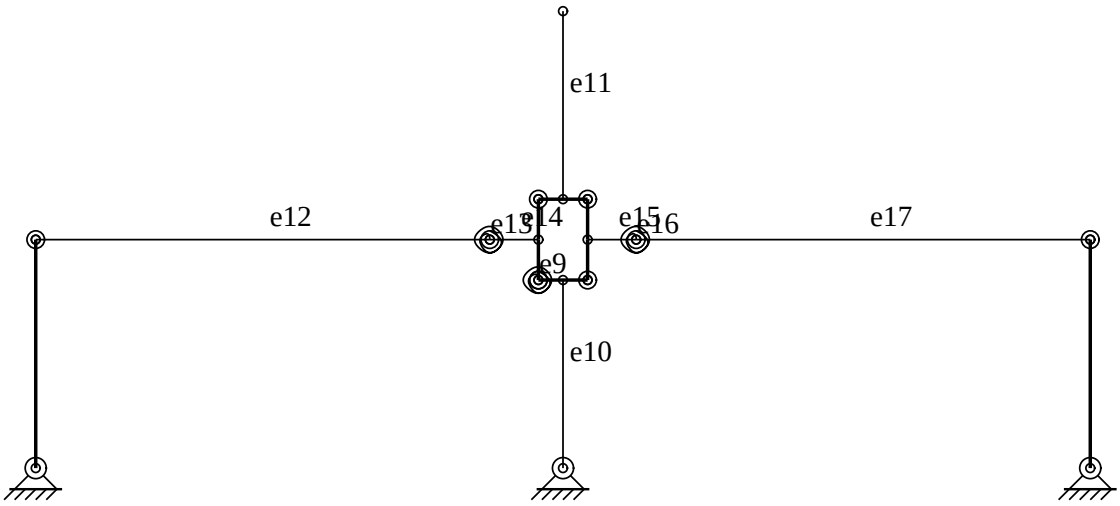

Figure V.5: Location of elements on the nonlinear finite element model.

The loading applied to each system in Table V.1 follows the loading sequence for beam-to-column connections given in AISC 341 (AISC 2010b). The cyclic response of those structural systems is presented in Figure V.6. The magnitude of the lateral force, H, at the top of the column normalized by the yield strength of the designed system is plotted versus the drift ratio between the bottom and top ends of the column.

A finite element analysis coded such that it is aborted if the strain in any structural element exceeds the material ultimate strain, and the systems is declared failure. For the panel zone under both shear and axial stress effects, it fails when the distortion energy exceeds its maximal distortion energy. As plotted in Figure V.6, some systems fail before the target drift ratio of 6% is reached. The analysis result shows that the strain in Element 12 of System 1 exceeds its material ultimate strain.

Systems 8, 18, 19, 20, 21, and 22 correspondingly fail at Elements 10, 17, 14, 10, 13, and 13.

In Table V.2, $\bar{E}_d$ denotes the energy dissipation capacity normalized by the energy dissipation capacity of System 19, which has the smallest energy dissipation among all the investigated systems. System 2 has the highest energy dissipation capacity that is approximately 24 times the capacity of System 19. Apparently selecting appropriate sections for structural members can significantly increase the energy dissipation capacity of a steel moment system. Insufficient column yield ratios could have detrimental effects on the behavior of structural systems.

Table V.2: Energy Dissipation Capacity of Subassemblages

System	Column	Girder	r_{yb}	r_{yc}	Failed Element	$\bar{E}_d$
1	W14X311	W30X108	1.15	2.10	12	12.9
2	W12X336	W27X129	1.39	2.06	-	24.6
3	W12X336	W27X129	1.15	2.06	-	24.0
4	W12X336	W27X129	1.11	2.06	-	24.0
5	W12X336	W27X129	1.08	2.06	-	24.0
6	W12X336	W27X129	1.05	2.06	-	24.0
7	W12X336	W27X129	1.01	2.06	-	24.0
8	W14X311	W27X129	1.01	1.57	10	6.4
9	W14X311	W30X116	1.52	2.54	-	23.1
10	W14X311	W30X116	1.28	2.54	-	22.7
11	W14X311	W30X116	1.25	2.54	-	22.6
12	W14X311	W30X116	1.21	2.54	-	22.6
13	W14X311	W30X116	1.18	2.54	-	22.6
14	W14X311	W30X116	1.14	2.54	-	22.6
15	W14X311	W30X116	1.11	2.54	-	22.6
16	W14X311	W30X116	1.07	2.54	-	22.5
17	W14X311	W30X116	1.03	2.54	-	22.5
18	W14X311	W30X124	1.30	2.00	17	5.6
19	W14X311	W30X124	1.09	2.00	14	1.0
20	W14X311	W30X124	1.06	2.00	10	4.6
21	W14X311	W30X124	1.03	2.00	13	4.8
22	W14X311	W30X124	1.00	2.00	13	4.9

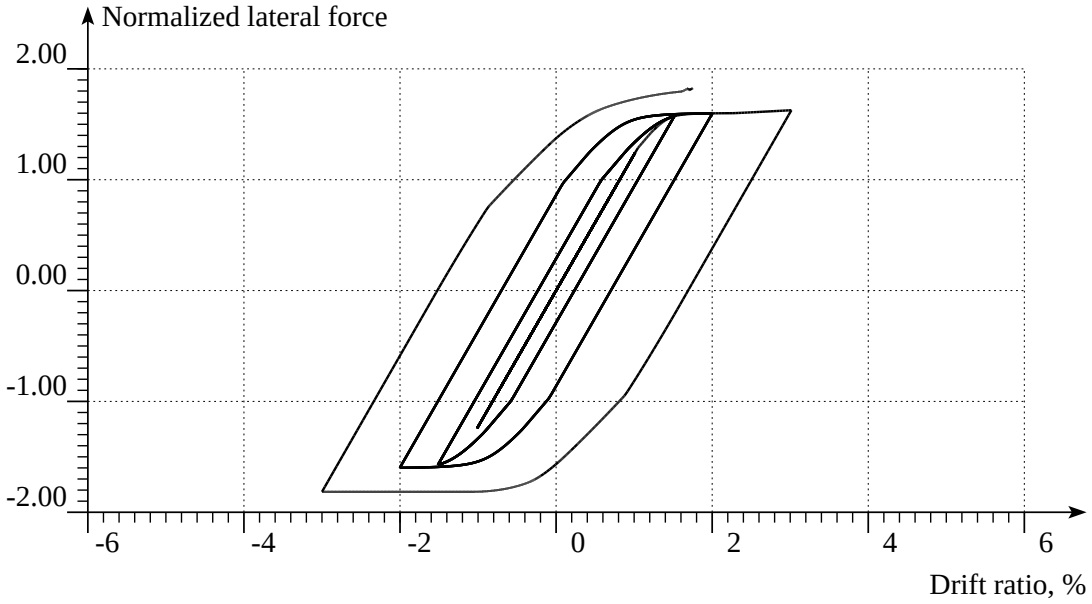

System 1

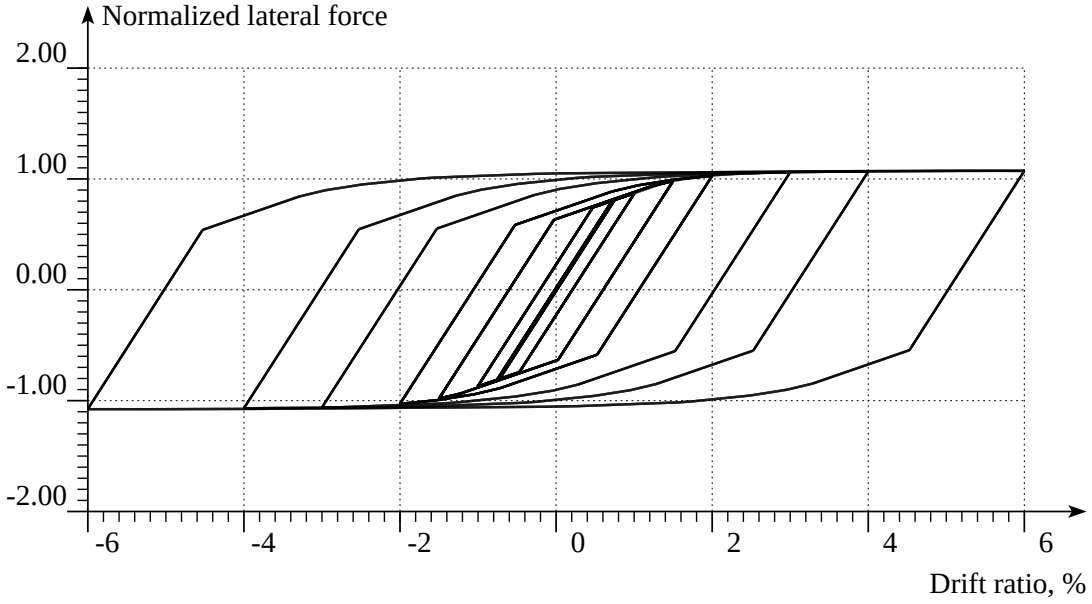

System 2

Figure V.6: Response of subassemblage systems under lateral loading.

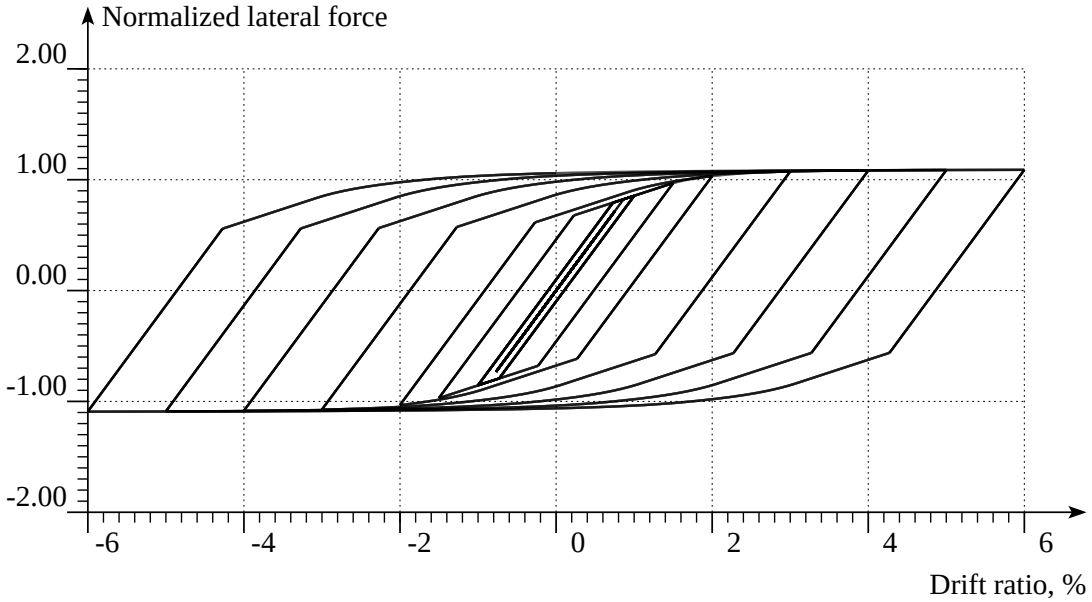

System 3

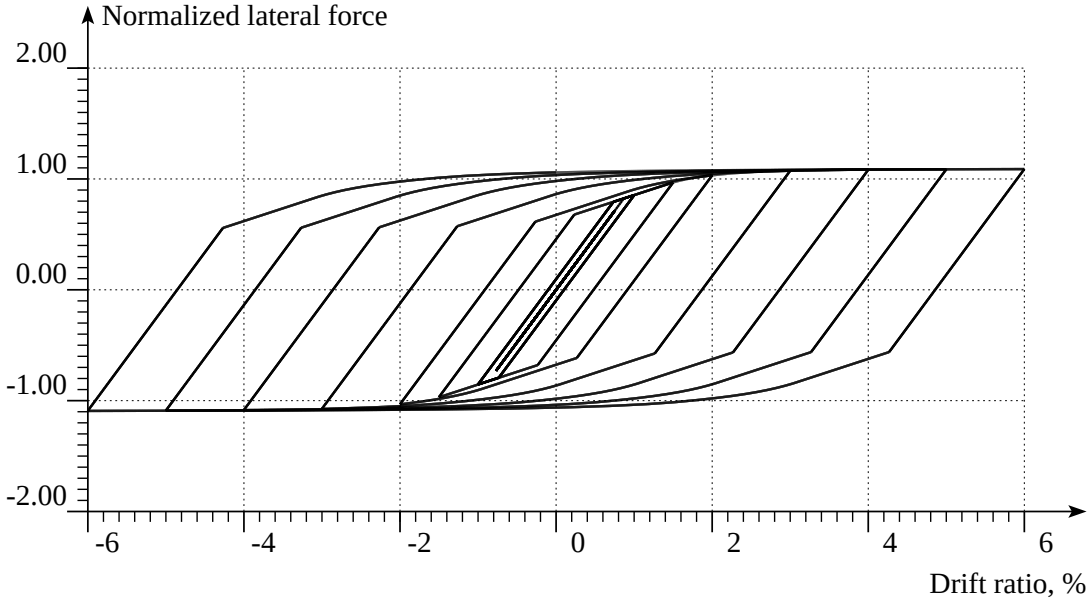

System 4

Figure V.6: Continued.

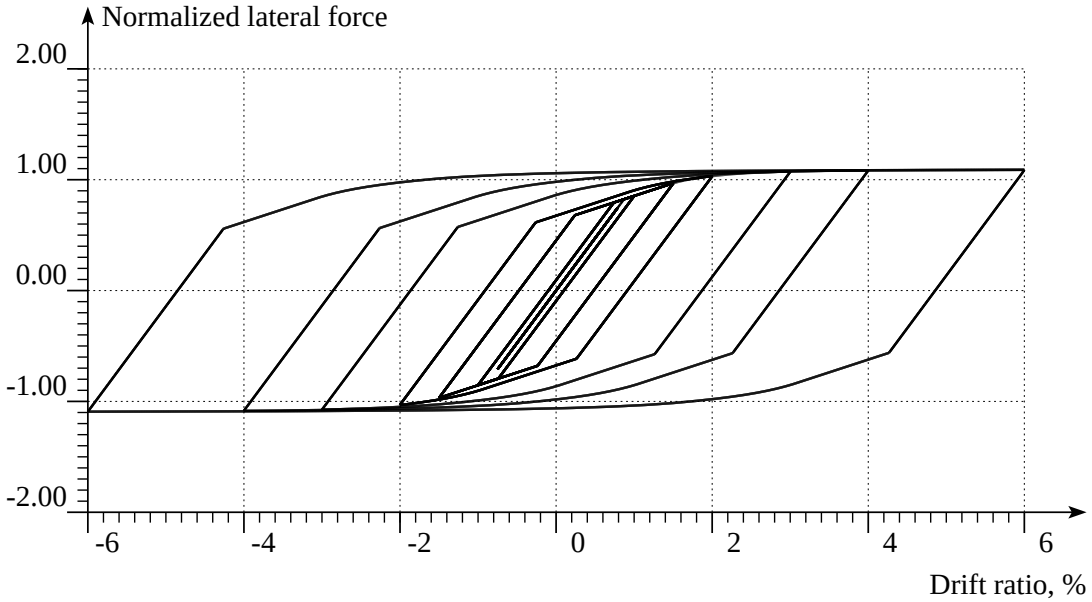

System 5

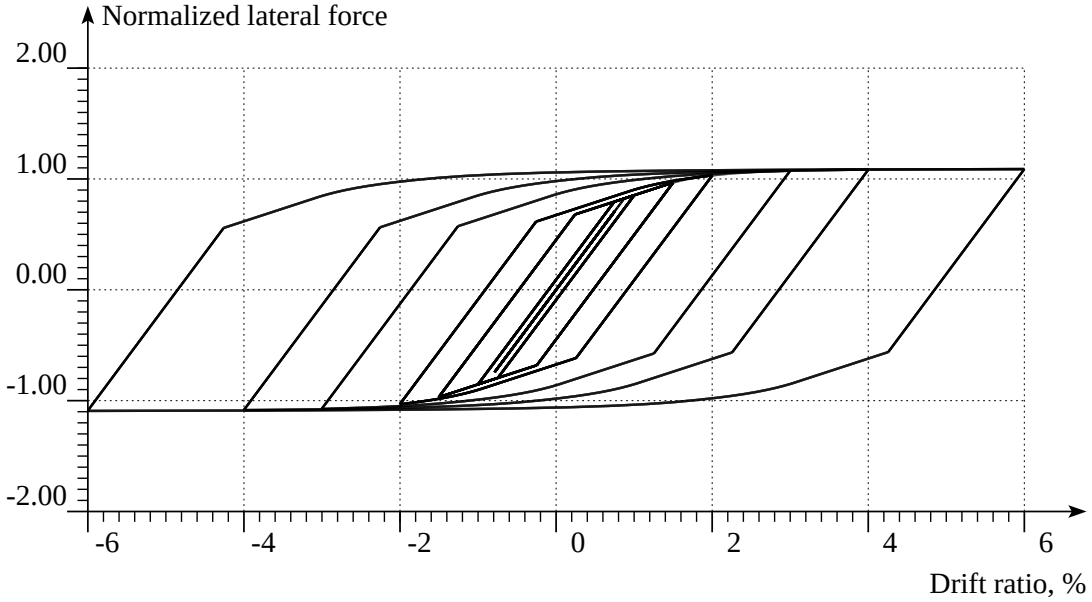

System 6

Figure V.6: Continued.

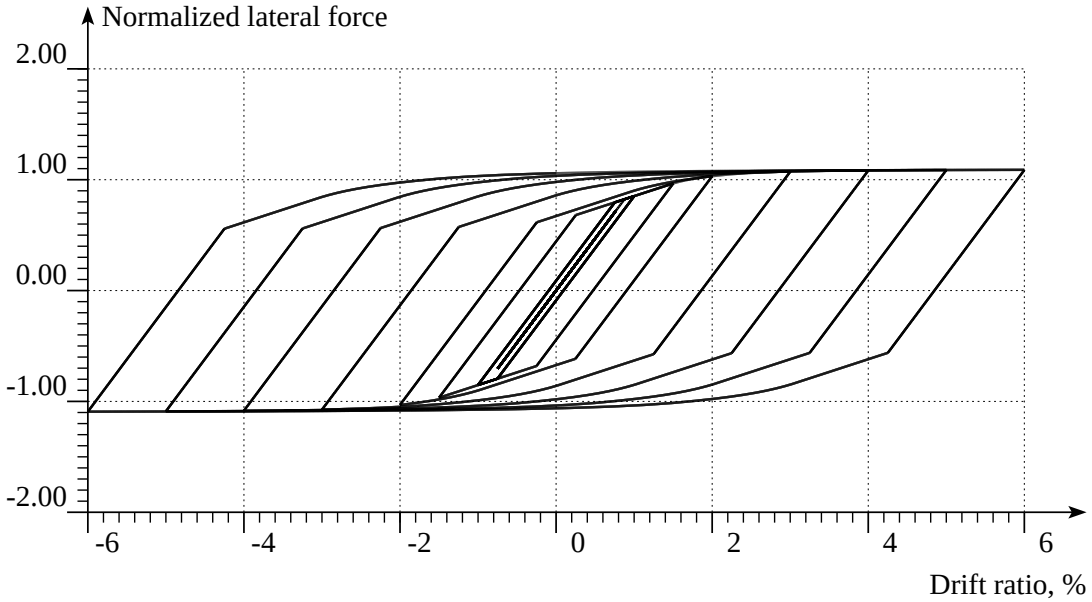

System 7

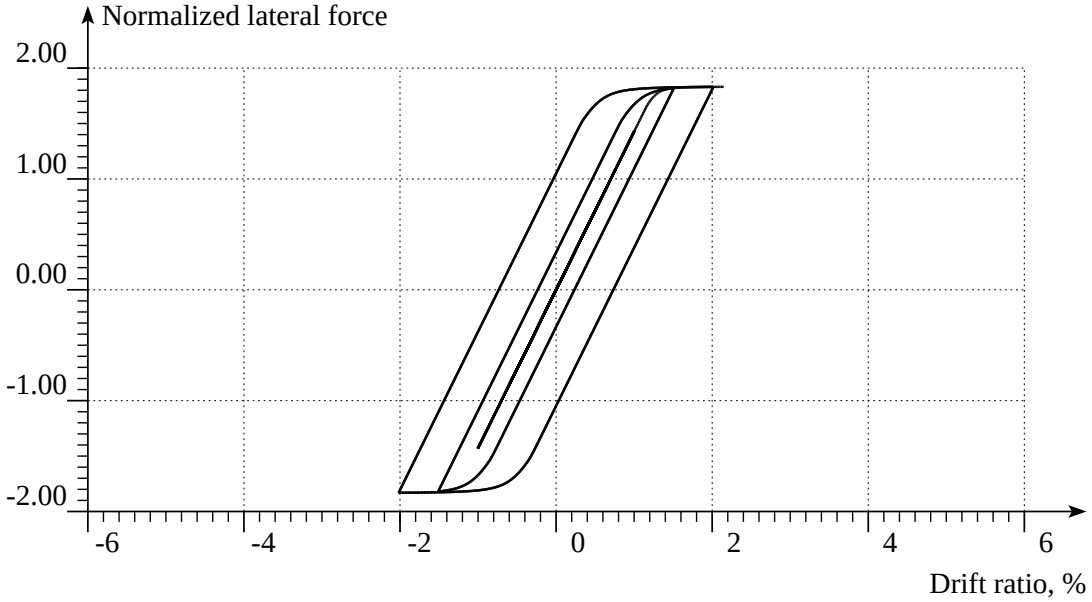

System 8

Figure V.6: Continued.

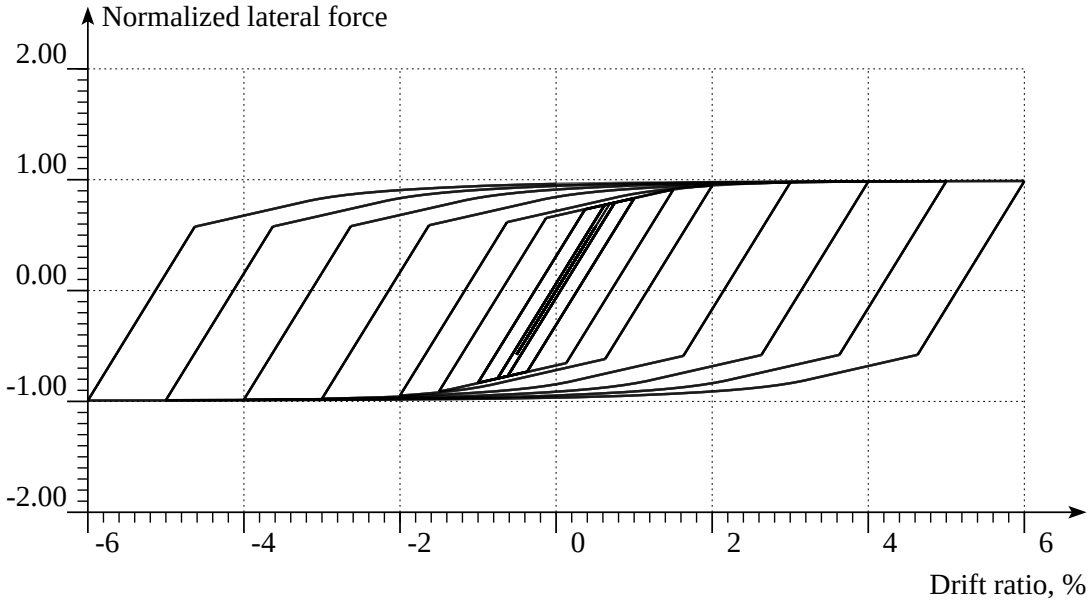

System 9

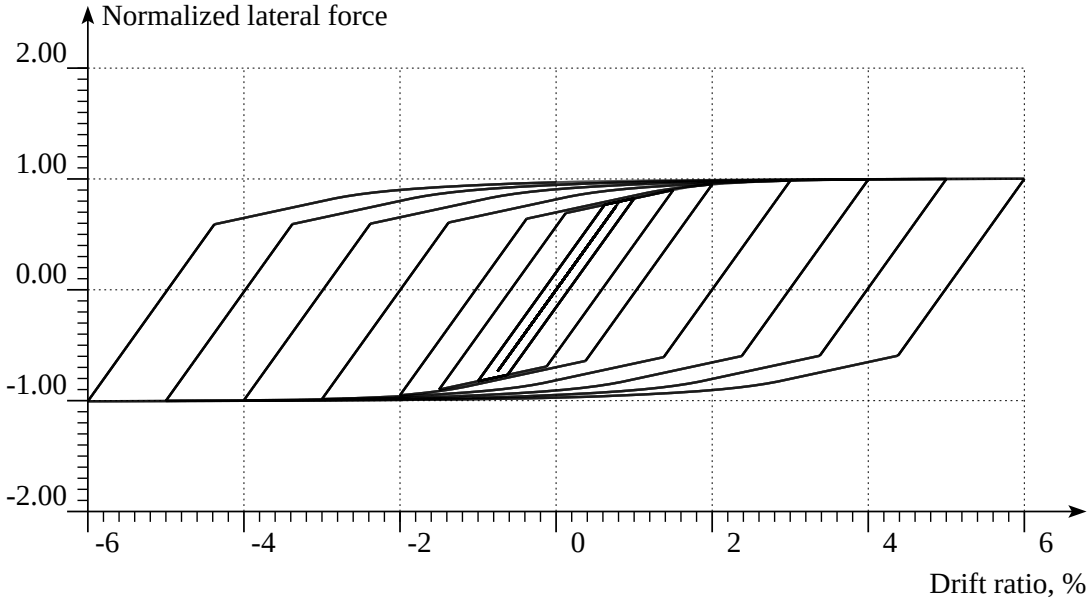

System 10

Figure V.6: Continued.

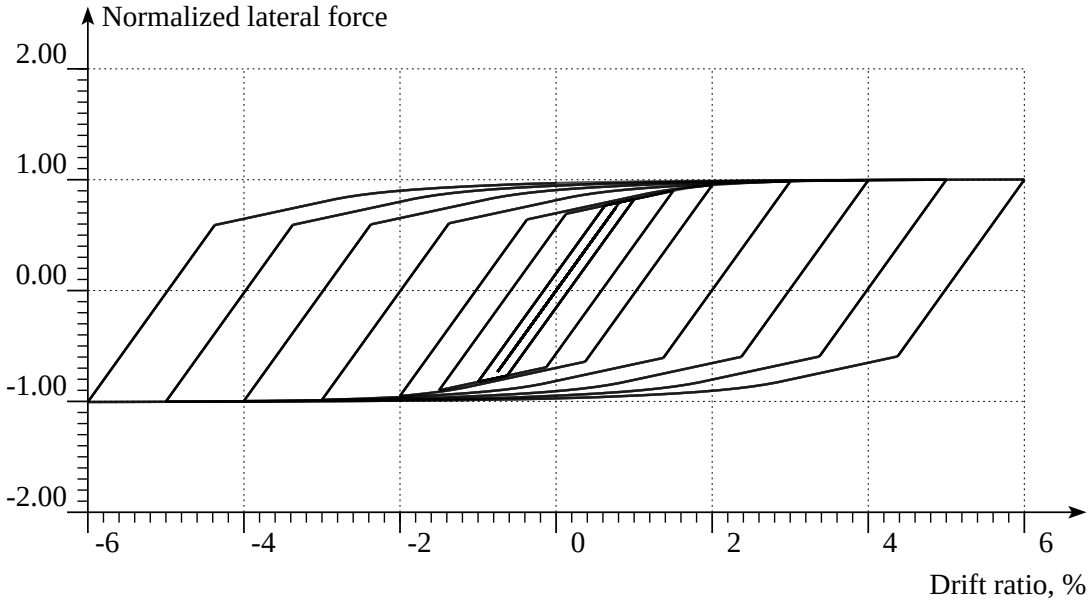

System 11

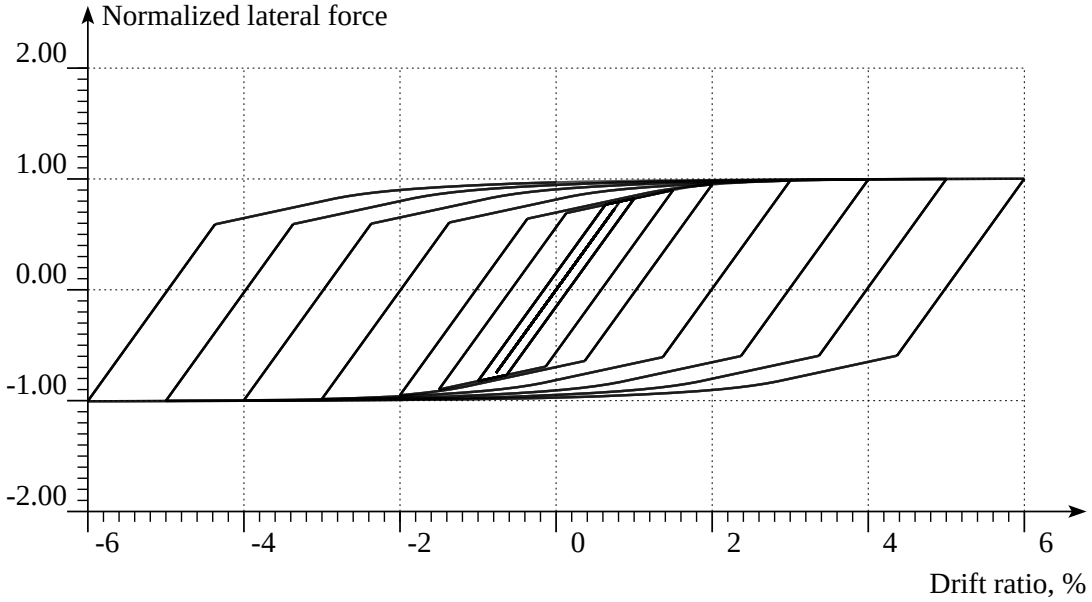

System 12

Figure V.6: Continued.

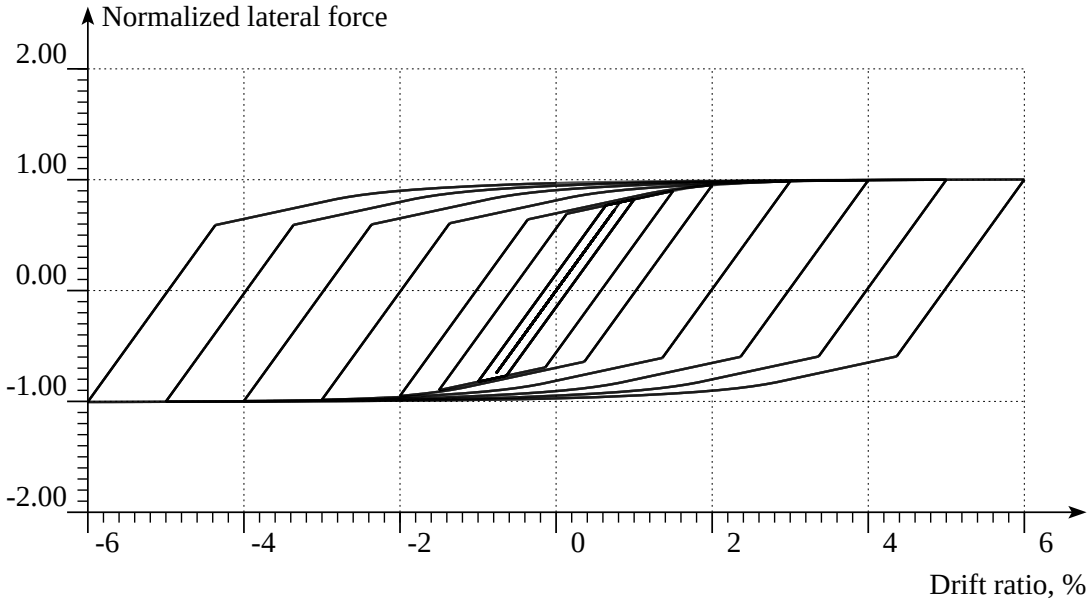

System 13

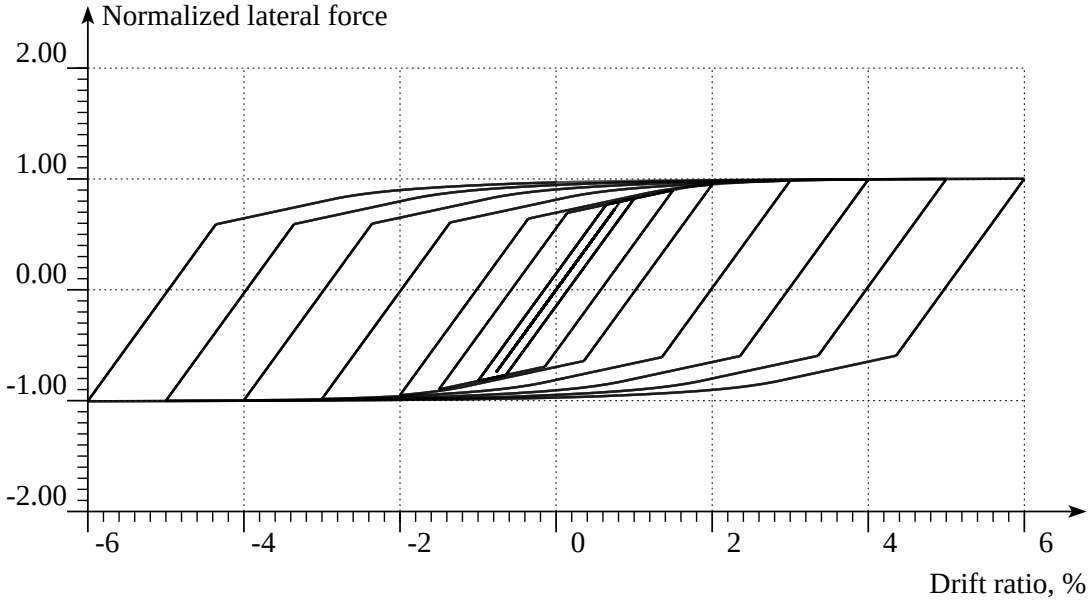

System 14

Figure V.6: Continued.

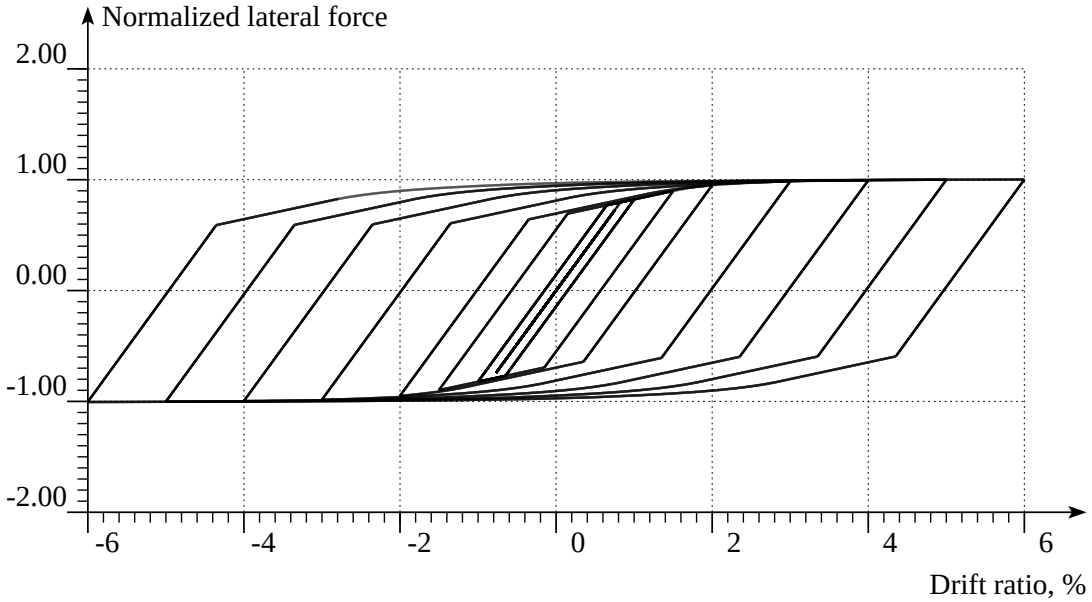

System 15

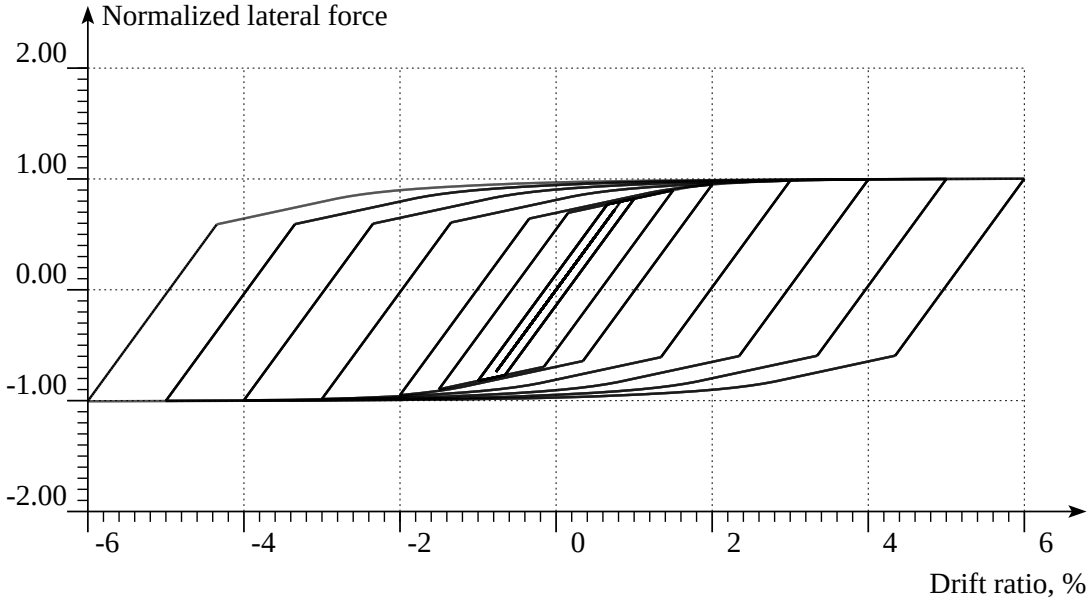

System 16

Figure V.6: Continued.

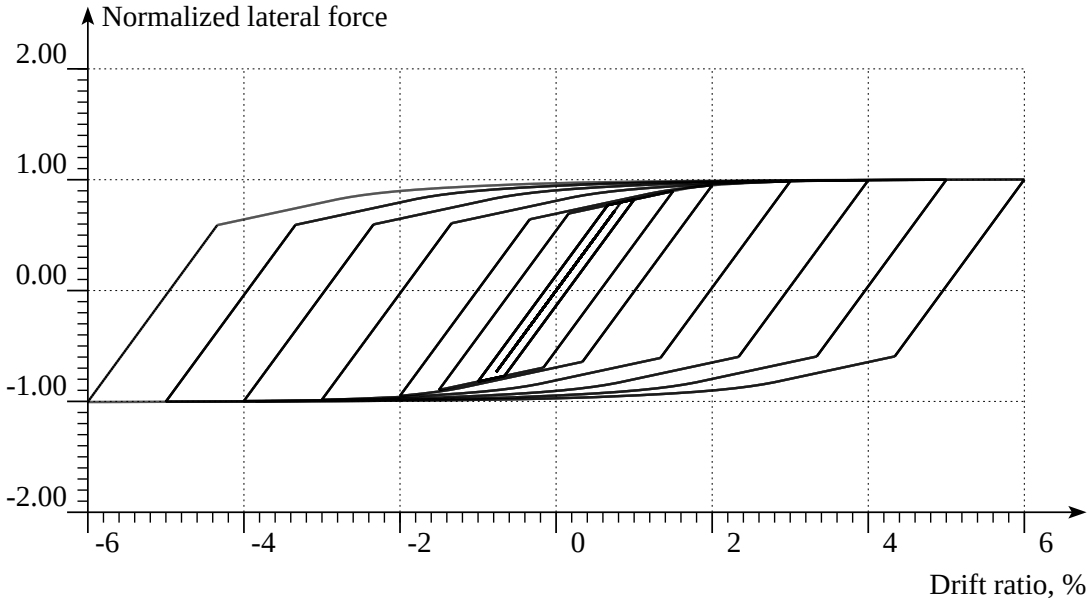

System 17

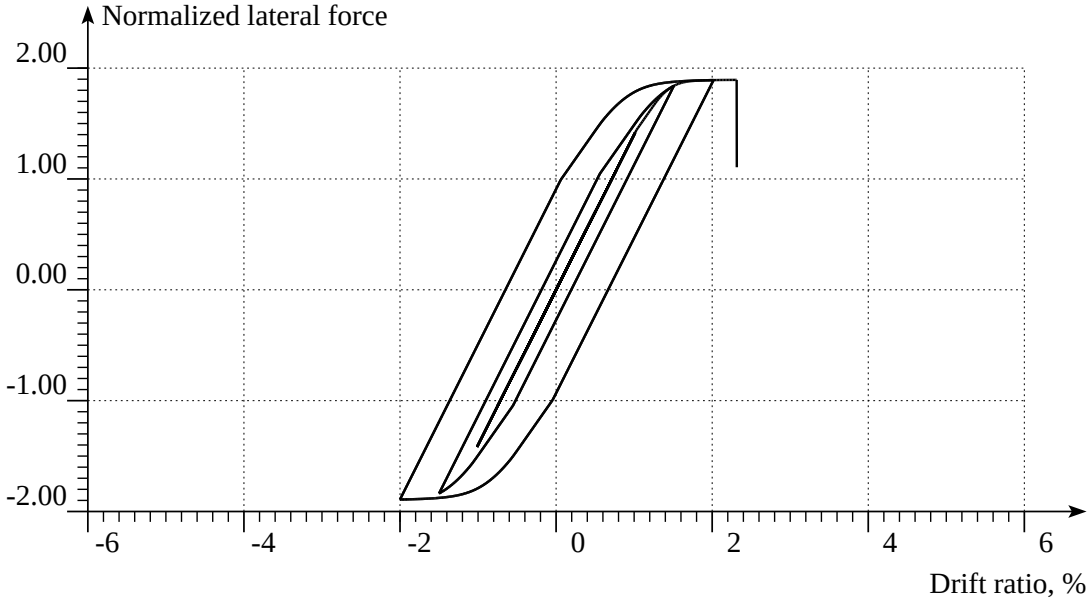

System 18

Figure V.6: Continued.

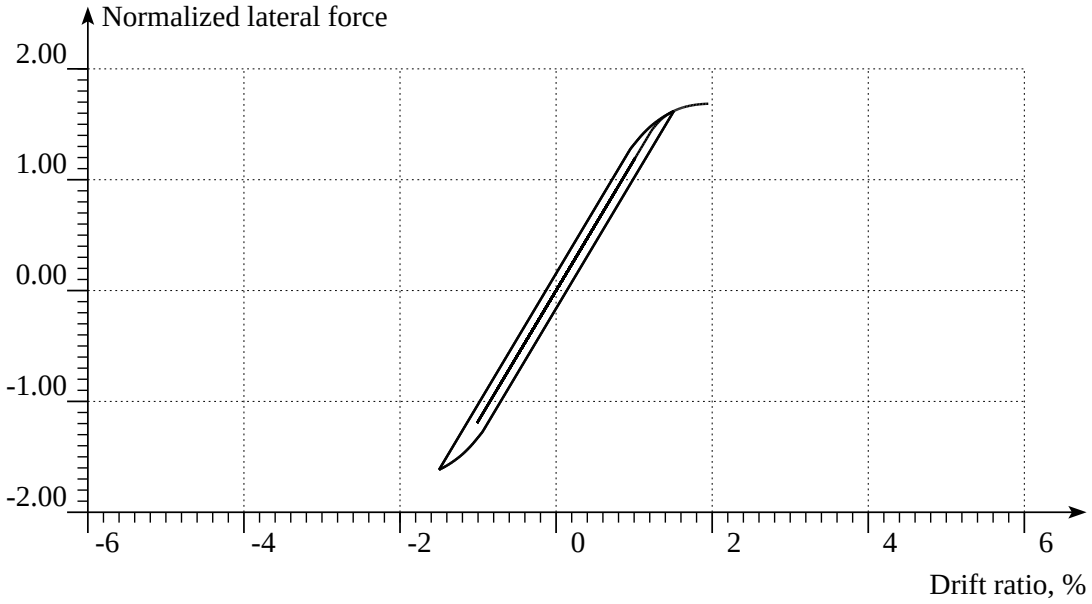

System 19

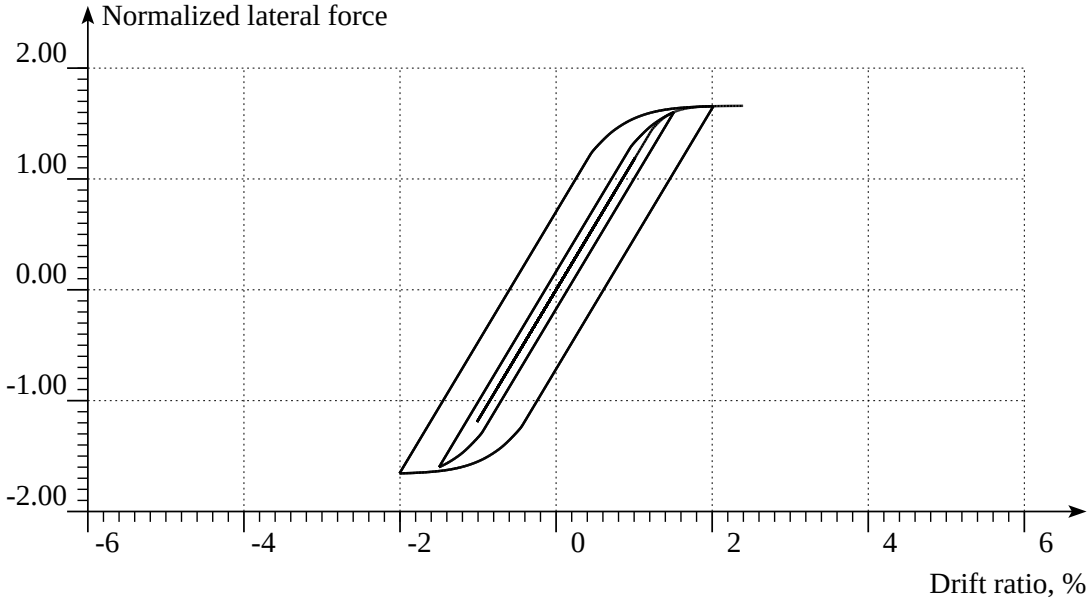

System 20

Figure V.6: Continued.

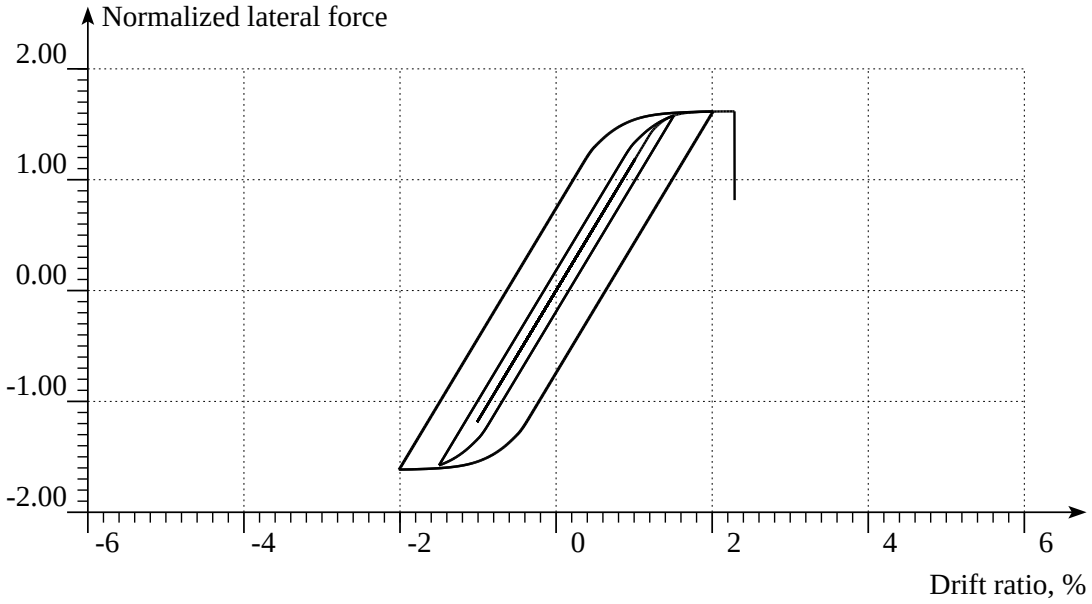

System 21

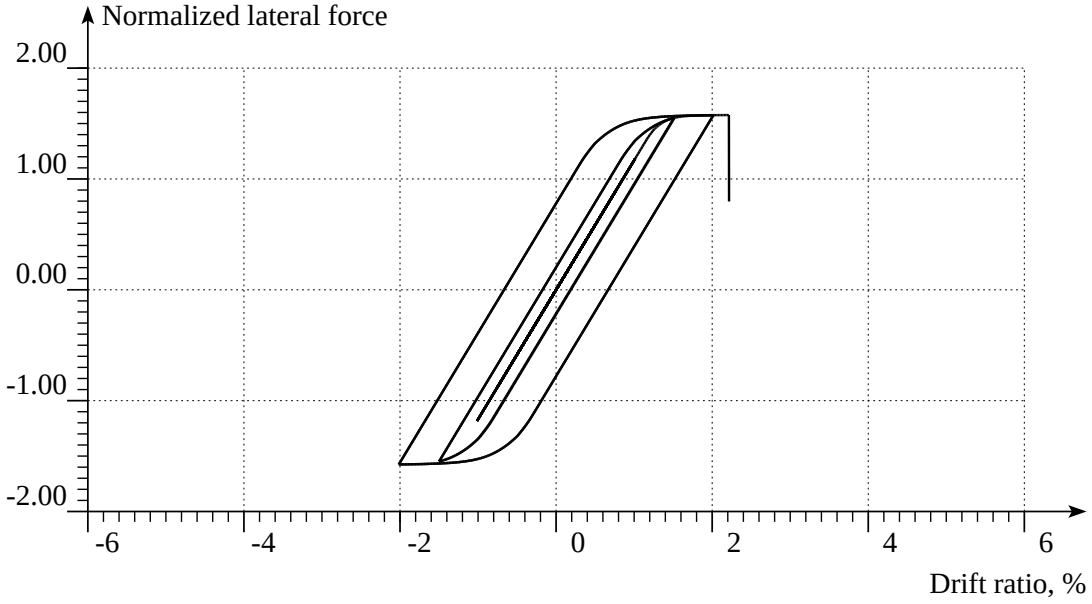

System 22

Figure V.6: Continued.

The energy dissipation capacity of a system is determined by numerically integrating the area of the outermost loop of the cyclic response. Figure V.7 plots the energy dissipation capacity versus the girder and column yield ratios. The area of the circles represent the dissipation capacity of one system relatively to that of the other systems. The black-filled circles denote the systems with cover plate design that includes Systems 1, 2, 8, 9, and 18, the others circles are for the systems with the RBS design.

Figure V.7 shows that high column yield ratios, greater than 2.0 especially for the systems using RBSs, consistently exhibit high energy dissipation capacities. Remarkably, the girder yield ratio does not clearly have an effect on the inelastic deformation energy. These results imply the benefit of high ratios of the column flange thickness to the column web thickness. In other words, weaker panel zones provide SMF systems with more inelastic deformation energy.

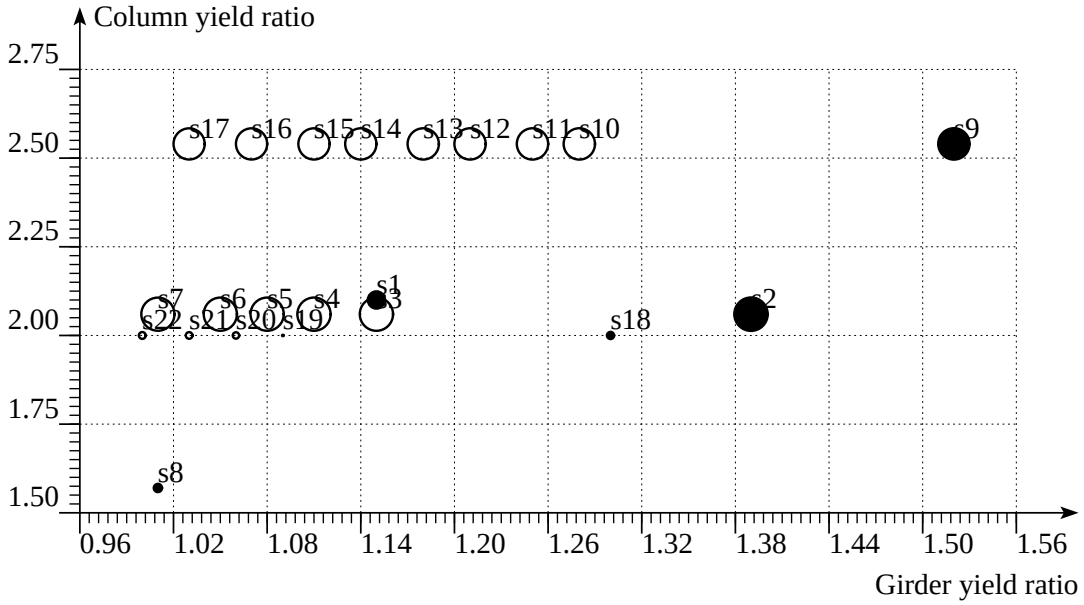

Figure V.7: Energy dissipation capacity of SMF subassemblages.

CHAPTER VI

EVALUATION OF THE SEISMIC PERFORMANCE OF SMFs

This chapter investigates the effects of panel zone (PZ) strength on the overall seismic performance of steel moment frames (SMFs). The seismic performance is represented by the collapse margin ratio. The safety of a structural system under seismic effects is proportional to this collapse margin ratio.

The effect of PZ strength on the seismic performance of SMFs is evaluated based on a benchmark steel building. The methodology for optimizing the PZ participation developed in Chapter V is used to obtain a new SMF. The seismic performance of this optimized frame is then assessed in comparison with the performance of the benchmark frame. This assessment also includes developing a nonlinear finite element model and performing nonlinear static and dynamic analyses for the frames. The finite element model uses the line element developed in Chapter II and the SMF connection model developed in Chapter III. The nonlinear analyses involves determination of gravity loads and ground motion records as guided in FEMA P695, *Quantification of Building Seismic Performance Factors* (FEMA 2009).

VI.1. Collapse margin ratio

The collapse margin ratio, *CMR*, is determined by

$$CMR = \frac{\hat{S}_{CT}}{S_{MT}} \tag{VI.1}$$

where $\hat{S}_{CT}$ represents the median 5%-damped spectral acceleration of the collapse level ground motions (GMs), which is determined from nonlinear dynamic or time history analyses of a frame system, at the fundamental period, T, of that frame.

Meanwhile, S_{MT} is the 5%-damped spectral acceleration of the Maximum Considered Earthquake (MCE) ground motions, which is defined in Section 11.4 of ASCE 7, at the fundamental period.

Figure VI.1 illustrates *CMR* in relation with seismic response spectra. A pushover curve is obtained from nonlinear static analysis in terms of the base shear and the roof lateral displacement. As shown in the figure, the base shear has been normalized by the effective seismic mass. The associated effective seismic weight includes the total dead load and other live loads as specified in Section 12.7.2 of ASCE 7 (ASCE 2010). $S_{\max}$ corresponds to the maximal strength of a fully yielded frame, and the seismic response coefficient, C_s, is the design base shear, V, normalized by the effective seismic weight. R is the response modification coefficient, $R = V_E/V$, where V_E represents the base shear force level that would be developed in the structural system, if the system remained linearly elastic when subjected to a design earthquake. It is noted that the factor of 1.5 used for determining the roof lateral displacement associated with the design bases shear accounts for the fact that the effects of the design earthquake ground motions are two-thirds of the corresponding MCE ground motions.

VI.2. Benchmark building moment frame

A benchmark building is considered for evaluating the effect of panel zone strength on the global seismic performance of steel moment frames. The benchmark building or SAC model building is a 9-story office building situated on stiff soil, which is Site Class D in ASCE 7 (FEMA 2000c). The building was designed in accordance with the local code requirements fo the City of Los Angeles. The design conforms to the provisions of FEMA 267 (post-Northridge design philosophy) (FEMA 1995). The lateral force-resisting system includes steel moment frames in which cover end plates

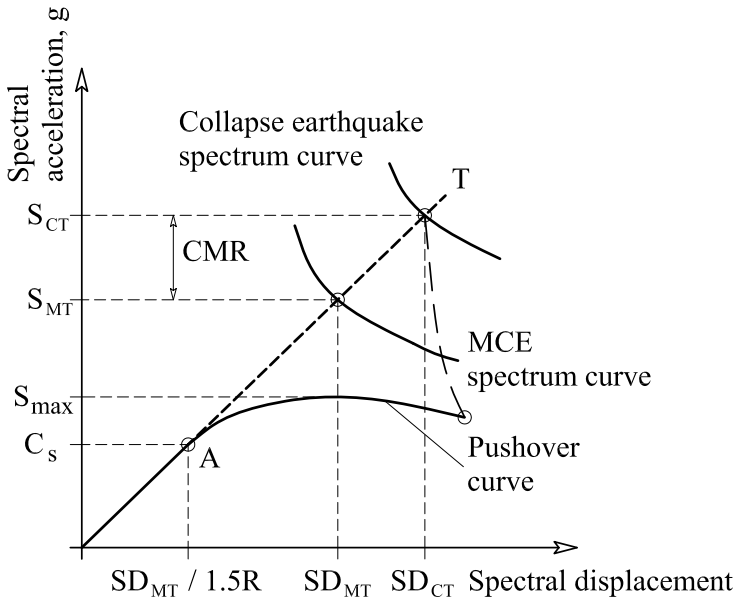

Figure VI.1: Illustration of the collapse margin ratio.

are welded to the beam flanges next to the beam-to-column connection. The cover plates were used to create an expected plastic hinge in the beam but away from the column.

Figure VI.2 shows the typical plan and the elevation of one moment frame of the 9-story benchmark building. On the plan, the moment frames denoted as bold lines are located at the perimeter of the building. All the columns in the frames bend about the strong axis of their cross section. The girder in one exterior bay of each moment frame has one moment-resisting connection with the interior column and one hinge connection to the corner column. This hinge connection helps avoid bi-axial bending in the corner column. The shaded area on the plan denotes the area of the penthouse on the roof floor. Each of the five bays in each direction is 30 ft wide.

The moment frames have a similar design. The frames have total 10 stories including one basement story. The story height is typically 13 ft, except for the first

story height of 18 ft and the basement story height of 12 ft. One north-south (NS) frame is hence considered for analyses and defined as a benchmark frame.

The wide-flange sections for the columns and girders of the considered moment frame is organized in Table VI.1. 0.5-in-thick doubler plates are used for the interior columns of Floors 7 and 9. Cover plates are 18 in long and are welded to the top and bottom of the girder flanges. The bottom cover plate (CP) is rectangular. The top cover plate uniformly tapers from the column flange face to an end with a width of 3 in.

Table VI.1: Structural member sections used for the benchmark frame

Floor	Exterior column	Interior column	Girder	Bottom CP	Top CP
1	W14X370	W14X500	W36X150	14"x0.750"	10"x1.000"
2	W14X370	W14X500	W36X150	14"x0.750"	10"x1.000"
3	W14X370	W14X455	W36X150	14"x0.750"	10"x1.000"
4	W14X370	W14X455	W33X141	13"x0.750"	9"x1.000"
5	W14X283	W14X370	W33X141	13"x0.750"	9"x1.000"
6	W14X283	W14X370	W33X141	13"x0.750"	9"x1.000"
7	W14X257	W14X283	W33X130	13"x0.750"	9"x1.000"
8	W14X257	W14X283	W27X102	12"x0.625"	9"x0.750"
9	W14X233	W14X257	W27X94	11"x0.625"	8"x0.750"
Roof	W14X233	W14X257	W24X62	9"x0.500"	5"x0.750"

VI.3. Optimally designed moment frame

The interior subassemblages of the benchmark frame are considered for optimal analysis. The computational procedure presented in the last chapter is used to determine subassemblage candidates. Results obtained from the optimal analysis are summarized in Table VI.2. For Floors 4 and 8, no candidates are found in the AISC shape database to be better than the existing subassemblages. Therefore, the design for those floors remains the same as the design of the benchmark frame. Other informa-

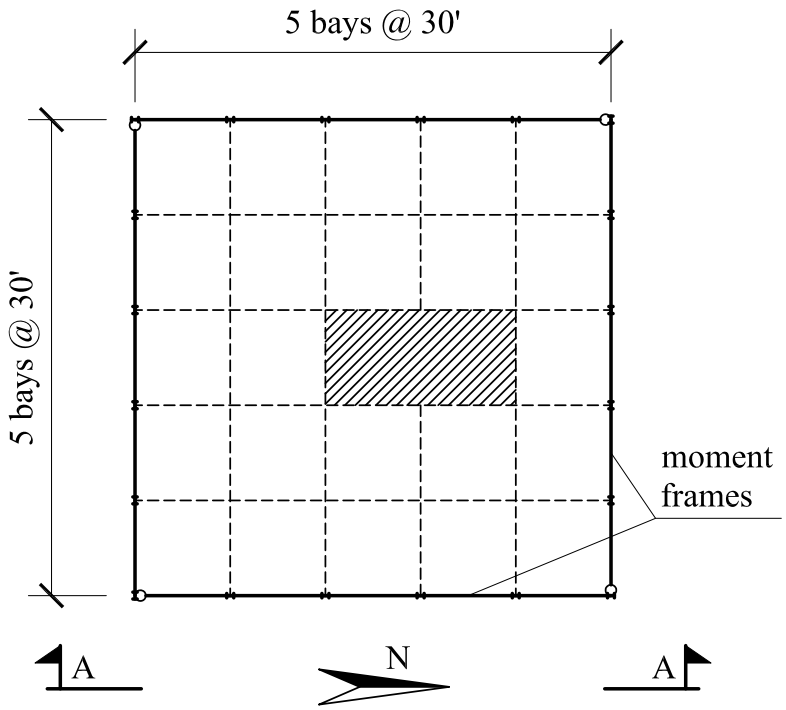

(a) Plan view

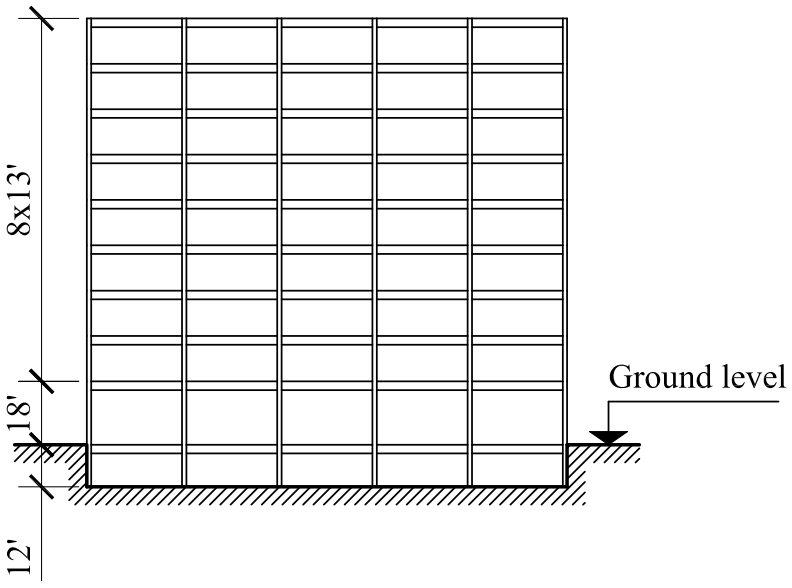

(b) Elevation view (A-A)

Figure VI.2: Typical plan and moment frame elevation of the benchmark building.

tion about the newly determined frame is also the same as the benchmark frame.

Table VI.2: Optimal design of girders and interior columns

Floor	Column	Girder	l_p, in	b_{RBS}, in	c_{RBS}, in
2	W14x500	W33x169	19.86	25.35	1.15
3	W14x455	W30x173	20.77	22.80	1.50
4	W14x455	W33x141	18.00	0.00	0.00
5	W14x370	W33x141	19.67	24.97	1.15
6	W14x370	W33x141	19.67	24.97	1.15
7	W14x283	W30x148	18.07	23.02	1.05
8	W14x283	W27x102	18.00	0.00	0.00
9	W14x257	W27x102	16.41	20.33	1.00

VI.4. Finite element models

Finite models for the benchmark and optimally designed frames are developed for analyses using OpenSees, which stands for the Open System for Earthquake Engineering Simulation. OpenSees was created by PEER (OpenSees 2006) and is a software framework for developing structural models and simulating their seismic response. The framework allows nonlinear static and dynamic analyses of structural systems to be implemented as required. It has been widely used in research and practice.

Analysis of a structural system in the software framework follows complex steps. Scripts are to be written in Tcl programming language (Tcl 2012) in order to build a finite element model for the structural system. Users can write Tcl scripts and use available built-in materials, elements, and algorithms to perform their simulation (Mazzoni et al. 2007). Unavailable models such as the SMF connection and force-based element models developed in this study are coded in programming language C++ (Soulie 2007). The program must then interface with OpenSees source code and

is compiled before the structure can be built and analyzed. The material properties used herein is of Steel A992 (Royster 2007). The material model developed for analysis uses the bounding surface theory (Cofie and Krawinkler 1985).

Figure VI.3 shows a finite element model for the benchmark frame. All the columns are pin-connected to the foundation. The first floor is restrained from lateral displacement by the basement wall. Each of the beam-to-column moment-resisting connections is simulated by rigid links, four hinges, and one rotational spring. This spring represents the response of the connection whose mathematical model was developed in a previous chapter. The columns and girders of the moment frame are simulated by line elements that were developed in a previous chapter for local buckling consideration. The left exterior girders are hinged to the exterior column which is a lateral force-resisting member of the perpendicular moment frame. The P-delta system is denoted by dashed bold lines. It is included and is formed by additional column elements connected at hinges and rigidly linked to the frame at floor levels. The P-delta system is used to capture the P-delta effects of the seismic mass/weight of the building that is not tributary to the moment frame.

Figure VI.4 shows a finite element model built for the optimally designed frame. The model is similar to the model for the benchmark frame except for the following. Cover plates are removed, and RBS elements are introduced at the plastic hinges on Floors 2, 3, 5, 6, 7, and 9. A zero-length finite element is developed to simulate all the RBSs.

Based on the finite element model developed for the benchmark frame, an additional finite element model is also developed without including panel zones and the P-delta system. This model serves to compare the seismic response of the benchmark frame in this study to the corresponding frame investigated by Ohtori et al. (2004). These researchers used a bilinear hysteretic model to simulate columns and beams.

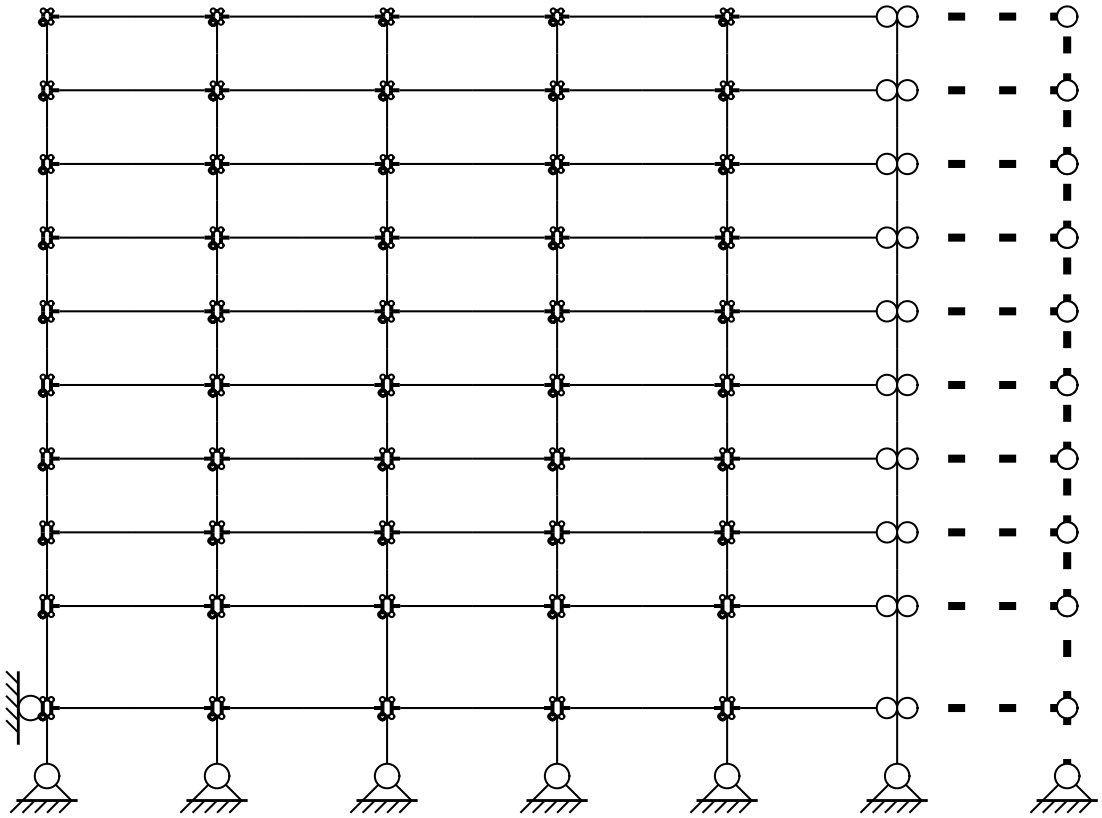

Figure VI.3: Benchmark frame finite element model.

At each floor level, the building mass was distributed uniformly to the beam-to-column joints of their frame.

VI.5. Ground motion records

To determine the collapse level ground motions (GMs) as described in FEMA P695 needs a reasonable set of GMs. A SAC GM suite for Los Angeles is collected to perform time history analyses for the SMFs. These GM records downloaded from PEER (2011). The suite has 10 pairs of horizontal GMs. The exceedance probability of GMs is 2% in 50 years that corresponds to collapse prevention design. A total of

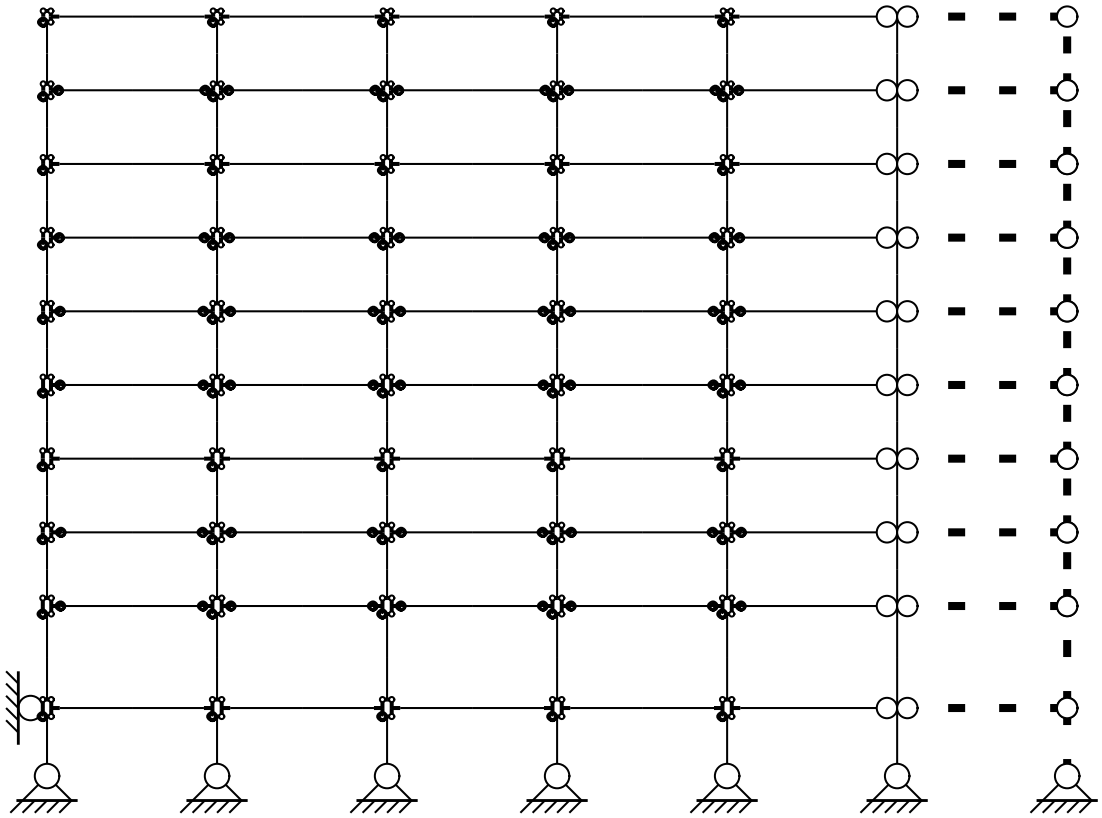

Figure VI.4: Optimally designed frame finite element model.

20 GM records are used for analyses of each of the SMFs. The records are named LA21 to LA40. This 20-record suite provides a sufficient number of GMs to permit statistical assessment of record-to-record variability and collapse margins.

Following FEMA P695, the 20-ground motions are further scaled to provide a more appropriate suite of ground motions for nonlinear dynamic analyses. First, individual records are normalized by their respective peak ground acceleration (PGA). This step helps eliminate unwanted variability between records due to differences in event magnitude, distance to source, source type, and site conditions while the GM overall characteristics are still maintained. Second, the normalized GMs are simul-

taneously scaled to different intensity levels until the median spectral acceleration of the scaled record set matches the spectral acceleration of the MCE GMs at the fundamental period of each frame. This step helps reduce the number of times to scale the ground motion suites to the collapse level, during nonlinear dynamic analyses.

The Maximum Considered Earthquake Spectral Response Acceleration (S_{ma}) is determined in accordance with Chapter 11 of ASCE 7 (ASCE 2010). The site soil measured shear wave velocity is between 600 and 1200 ft/s (FEMA 2000c). In regard to the site classification procedure specified in ASCE 7, the building site is classified as Class D soil for site response analysis of ground motions. The MCE spectral acceleration is determined by

$$S_{ma} = 1.5 S_a \tag{VI.2}$$

$$S_a = \begin{cases} S_{DS}\left(0.4 + 0.6\dfrac{T_1}{T_0}\right) & \text{if } T_1 \le T_0 \\ S_{DS} & \text{if } T_0 \le T_1 \le T_S \\ \dfrac{S_{D1}}{T_1} & \text{if } T_S \le T_1 \le T_L \\ \dfrac{S_{D1} T_L}{T_1^2} & \text{if } T_L \le T_1 \end{cases} \tag{VI.3}$$

where S_a = design spectral response acceleration; T_1 = fundamental or first period of a structure (T_{bn1} or T_{on1}); $T_S = S_{D1}/S_{DS}$; $T_0 = 0.2 T_S$; T_L = mapped long-period transition period; all periods are measured in second (s); according to the seismic design map (ASCE 2010; USGS 2009), T_L can be 8 or 12 s, depending on the exact location of the building. S_{DS} and S_{D1} denote the design spectral response acceleration parameters respectively at short periods and at 1-s period and are determined by

$$S_{DS} = \frac{2}{3} F_a S_S \tag{VI.4}$$

$$S_{D1} = \frac{2}{3} F_v S_1 \tag{VI.5}$$

where S_S and S_1 are mapped MCE spectral response acceleration parameters at the periods of 0.2 and 1.0 s, correspondingly. In regard to the seismic design map for ASCE 7 (USGS 2009), those parameters are taken as $S_S = 2.00g$ and $S_1 = 1.00g$ for the building site. The associated site coefficients are $F_a = 1.0$ and $F_v = 1.5$.

Performing eigenvalue analysis results in vibration periods for the two frame systems. First three vibration periods are recorded for the benchmark frame and optimized frame. The first three periods of the benchmark frame are $T_{bn1} = 2.25$ s, $T_{bn2} = 0.84$ s, and $T_{bn3} = 0.48$ s. Those of the optimized frame are $T_{on1} = 2.40$ s, $T_{on2} = 0.88$ s, and $T_{on3} = 0.50$ s. The periods of the benchmark frame are consistent with the results obtained by (Razavi 2013). It is noted that the periods of the benchmark frame are a bit smaller than those of the optimized frame, implying the former to be stiffer than the latter.

Applying the above computational procedure results in the MCE spectral response accelerations for the benchmark frame and optimized frame, respectively, as $S_{MTb} = 0.667g$ and $S_{MTo} = 0.625g$, where g is the gravity acceleration.

Response spectrum analysis is implemented for individual ground motions in each scaled ground motion suite to determine the median spectral response acceleration of that suite. Spectral response acceleration is determined by applying the average acceleration method to the equation of motion. The average acceleration method was developed by N.M. Newmark (Chopra 2001; Newmark 1959). The inherent damping ratio of 5% is assumed (ASCE 2010; FEMA 2009).

Figure VI.5 plots the acceleration response spectra for the ground motion suite that has been normalized and scaled to match the spectral response acceleration of the benchmark structure at the first natural period. The median response spectral

acceleration for the site is also plotted as a blue thick curve in the figure. This scaled ground motion suite is now defined as the MCE ground motion set.

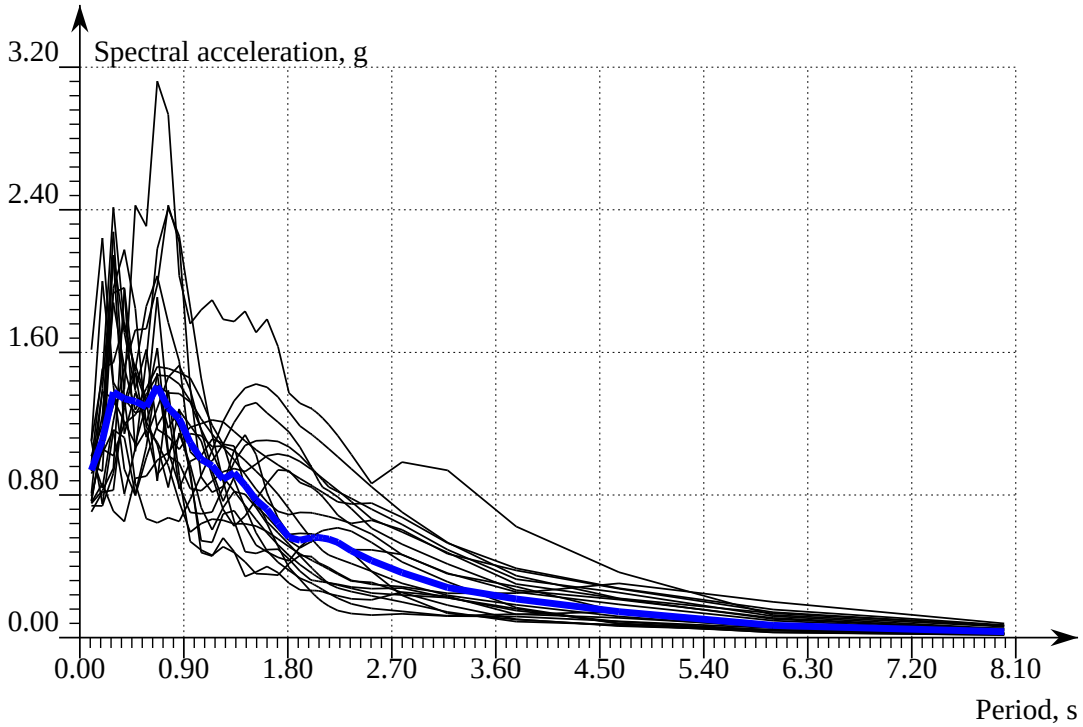

Figure VI.5: MCE 5%–damping spectral acceleration for the benchmark structure.

The acceleration response spectra of the MCE ground motion set for the optimized structure is plotted in Figure VI.6. It is noted that the acceleration spectra of the MCE ground motion set is slightly larger than those for the benchmark structure.

VI.6. Nonlinear time history analyses

The response of the benchmark frame without including panel zone effects and the P-delta system is first compared to the response of the corresponding frame investigated by Ohtori, Christenson, Spencer, and Dyke (Ohtori et al. 2004). A time history

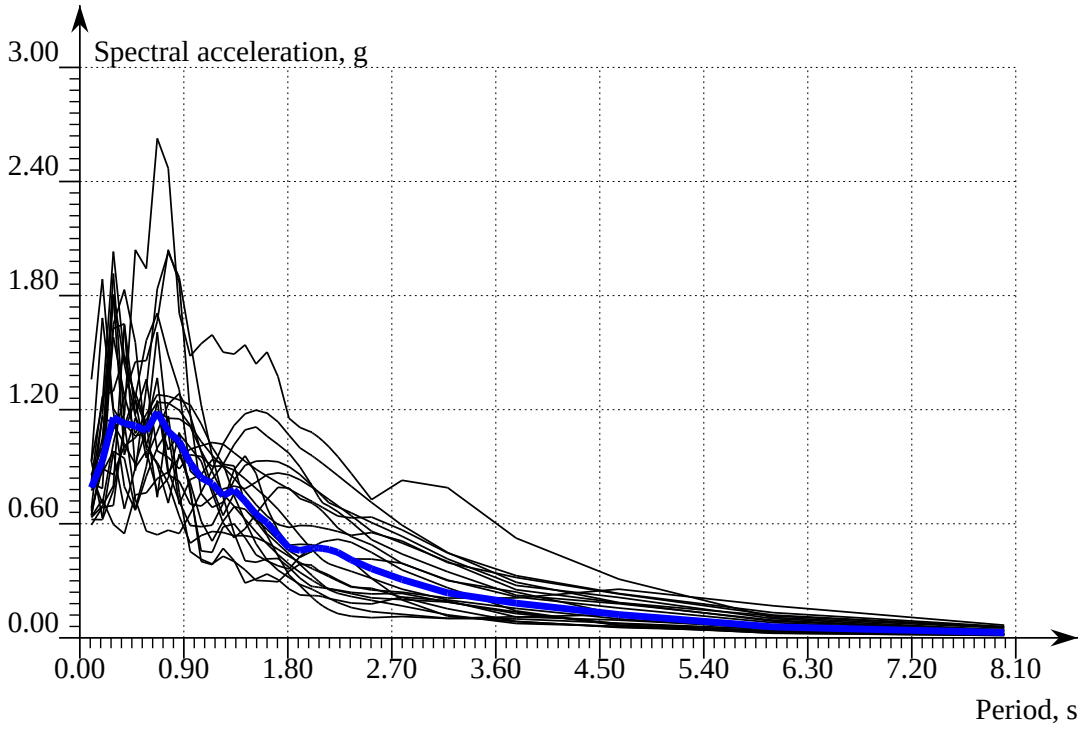

Figure VI.6: MCE 5%–damping spectral acceleration for the optimized structure.

analysis is implemented using the North-South component of its ground acceleration recorded on May 18, 1940, at the Imperial Valley Irrigation District substation in El Centro, California. It is noted that the former benchmark frame was designed using the post-Northridge design philosophy, and the corresponding frame investigated by Ohtori et al. (2004) was designed using the pre-Northridge design philosophy. The first five natural periods of vibration of the two frames are compared in Table VI.3.

Table VI.3: Comparison of the first five natural periods

Frame	T_1, s	T_2, s	T_3, s	T_4, s	T_5, s
Ohtori	2.26	0.85	0.49	0.32	0.23
This study	2.22	0.83	0.48	0.32	0.24

Table VI.4 shows results obtained from time history analyses for the Ohtori frame

and for the benchmark frame in this study. The maximal story drift ratios, $\delta_{\max}$, and the maximal lateral displacements of frame floors, $x_{\max}$, are significantly comparable for three different intensity for scale factors 0.5, 1.0, and 1.5.

Table VI.4: Seismic response comparison

Quantity	Intensity factor = 0.5		Intensity factor = 1.0		Intensity factor = 1.5	
	Ohtori	This study	Ohtori	This study	Ohtori	This study
$\delta_{\max}$, %	0.860	0.670	1.510	1.220	2.130	1.880
$x_{\max}$, m	0.200	0.179	0.385	0.355	0.488	0.413

A great number of nonlinear time history analyses need to be performed in order to assess the median collapse capacity and determine the collapse margin ratio for the benchmark and optimized frames. The median collapse capacity of a frame is defined as the intensity of a GM set whose half of its GMs cause the frame to collapse. Each SMF is subjected to a number of GM suites that are scaled from its MCE ground motion set. Per FEMA P695, these ground motions are systematically scaled to different intensities until half of the set cause a frame to collapse. The collapse level ground motion set is determined by repetitive nonlinear history analyses of each frame.

Collapse of a frame is determined conservatively by the material failure of any part of the structure. The material fails when the strain demand exceeds the material ultimate strain. This failure criterion applies to girders and columns. Evaluating the failure of the panel zone under combined shear and axial forces uses the maximal distortion energy criterion (Hamrock et al. 1999; Keyak and Rossi 2000; Wang and Dixon 1997). Failure is determined when the distortion energy exceeds the distortion energy at ultimate stress. In some cases, the failure of a frame subject to a ground motion excitation is determined when dynamic instability occurs. In this event, the deformation of structural members becomes considerably large

and the strain in some members exceeds the material ultimate strain. Convergent dynamic analysis steps becomes impossible.

In large-displacement cases, it is difficult for analysis steps to converge. Those analysis steps are then divided multiple times into smaller steps, and different solution algorithms are tried on the smaller steps before failed analysis is declared. Newton algorithm is tried first before the modified Newton algorithm (Hauser 2009; Reddy 2004). Next tried algorithms are the line search or Riks (Crisfield 1991; Riks 1984) and Krylov-Newton (Carlson and Miller 1998; Scott and Fenves 2009).

Rayleigh damping is used for the equation of motion of the structural systems (Chopra 2001). The damping matrix is a linear combination of stiffness and mass matrices. The two damping coefficients in the combination are determined from the first and third vibration modes. Newmark's average acceleration method is used to approximate the time derivatives of displacement, i.e. velocity and acceleration (Newmark 1959; Zienkiewicz and Taylor 2005).

The response of the benchmark and optimal frames to their corresponding MCE ground motion set is presented in Appendix VII in terms of story drift histories. Figures A.1 through A.20 show the response of the benchmark frame. Figures A.21 through A.40 are for the optimal frame. The story drift versus time is plotted for Stories 1 through 9 for each ground motion record in the MCE set of each frame. The SAC ground motion set was normalized and scaled as the aforementioned procedure to become two MCE sets for the two frames. The records in each MCE set are now labeled as MCE LA21 through MCE LA40. The figures exhibit unrecoverable deformation of the two frames under most MCE ground motion excitations, implying significant damages in terms of inelastic deformation in the structural systems.

Table VI.5 summarizes the maximal story drift ratio of the benchmark and optimized frames under the effects of their corresponding maximal MCE ground motion

records. For scaled MCE ground motion sets, the response of the two frames is summarized in Tables A.1 through A.8. It is noted that for one scale, MCE LAs has a higher value of the median spectral acceleration for the optimized frame than for the benchmark frame. This increase in seismic demand in terms of spectral acceleration is due to the slight increase in the fundamental period of the optimized frame as shown in Figures VI.5 and VI.6. The table presents the story associated with each maximal story drift ratio together with the indication of whether or not a frame fails. The table shows that analyses fail when the story drift is significantly large.

Table VI.5: Summary of frame maximal story drifts

Record	Benchmark frame			Optimized frame		
	Max drift, %	Story	FAIL/OK	Max drift, %	Story	FAIL/OK
MCE LA21	1.3	1	OK	1.1	5	OK
MCE LA22	1.3	1	OK	1.3	1	OK
MCE LA23	2.4	1	OK	1.9	1	OK
MCE LA24	22.0	1	FAIL	5.8	1	FAIL
MCE LA25	2.0	1	OK	2.3	8	OK
MCE LA26	1.9	4	OK	3.2	7	OK
MCE LA27	2.1	1	OK	2.4	6	OK
MCE LA28	1.4	1	OK	1.7	8	OK
MCE LA29	1.2	1	OK	1.6	8	OK
MCE LA30	1.8	1	OK	2.0	1	OK
MCE LA31	1.1	7	OK	2.0	8	OK
MCE LA32	1.3	7	OK	1.4	7	OK
MCE LA33	5.2	1	FAIL	3.1	4	OK
MCE LA34	2.2	1	OK	3.3	4	FAIL
MCE LA35	6.2	1	FAIL	2.5	1	FAIL
MCE LA36	4.6	1	FAIL	3.3	4	OK
MCE LA37	6.0	1	FAIL	4.0	6	FAIL
MCE LA38	6.8	1	FAIL	1.7	1	FAIL
MCE LA39	2.2	1	OK	2.6	7	OK
MCE LA40	6.2	1	FAIL	3.1	1	FAIL

VI.7. Seismic performance assessment

Nonlinear dynamic analysis results presented in Tables A.1 through A.8 show that following the procedure recommended in FEMA P695 does not necessarily reduce the number of time history analyses. It is difficult, if not impossible, to obtain the collapse ground motion set whose half ground motions cause a structure to fail.

Thus, it is assumed that the distribution of the spectral acceleration capacities is lognormal to determine the median collapse spectral acceleration. Table VI.6 presents spectral acceleration capacities of the benchmark and optimized frames under each earthquake. The spectral acceleration capacity for each earthquake is determined as the minimum spectral acceleration that is obtained from all the scaled ground motions of that earthquake causing a frame to fail. Fitting the spectral acceleration capacities to the lognormal distribution is based on the normal probability paper method (Nowak and Collins 2000). Linear regression analysis is implemented to determine the mean and standard deviation of the probability density function.

Figures VI.7 and VI.8 show collapse fragility curves for the benchmark frame and the optimized frame, respectively. The collapse fragility of a structure is the failure probability (P_f) of that structure given a seismic intensity measure (Ibarra and Krawinkler 2005; Razavi 2013). In this case, the ground motion spectral acceleration (S_a) is the intensity measure. The failure probability is the probability that the spectral acceleration capacity of a frame is less than the spectral acceleration demand.

From the collapse fragility for each frame, the median spectral acceleration of the collapse level ground motion is $\hat{S}_{CTb} = 1.54g$ for the benchmark frame and $\hat{S}_{CTo} = 1.88g$ for the optimized frame. Using Equation VI.1 and the results for the MCE spectral accelerations obtained in Section VI.5., the collapse margin ratios for

Table VI.6: Spectral acceleration capacity

Scaled MCE	Benchmark frame, g	Optimized frame, g
la21	2.04	1.91
la22	1.97	1.69
la23	1.29	1.28
la24	2.63	2.72
la25	1.83	2.91
la26	2.65	2.82
la27	0.90	1.39
la28	1.10	2.41
la29	0.69	0.98
la30	0.71	0.94
la31	2.25	2.23
la32	1.79	4.08
la33	1.38	1.48
la34	1.50	1.46
la35	0.99	1.02
la36	1.19	1.42
la37	1.65	1.62
la38	1.70	1.77
la39	2.14	3.10
la40	1.37	1.58

the former and latter are, respectively,

$$CMR_b = \frac{\hat{S}_{CTb}}{S_{MTb}} = \frac{1.55g}{0.667g} = 2.33$$

$$CMR_o = \frac{\hat{S}_{CTo}}{S_{MTo}} = \frac{1.88g}{0.625g} = 3.01$$

Figure VI.9 shows the seismic fragility curve of the optimal frame in comparison with that of the benchmark frame. Given a ground motion intensity level (S_a), the failure probability (P_f) of the optimal frame is consistently lower than that of the benchmark frame. The optimal frame exhibits a remarkable improvement in seismic performance over the benchmark frame.

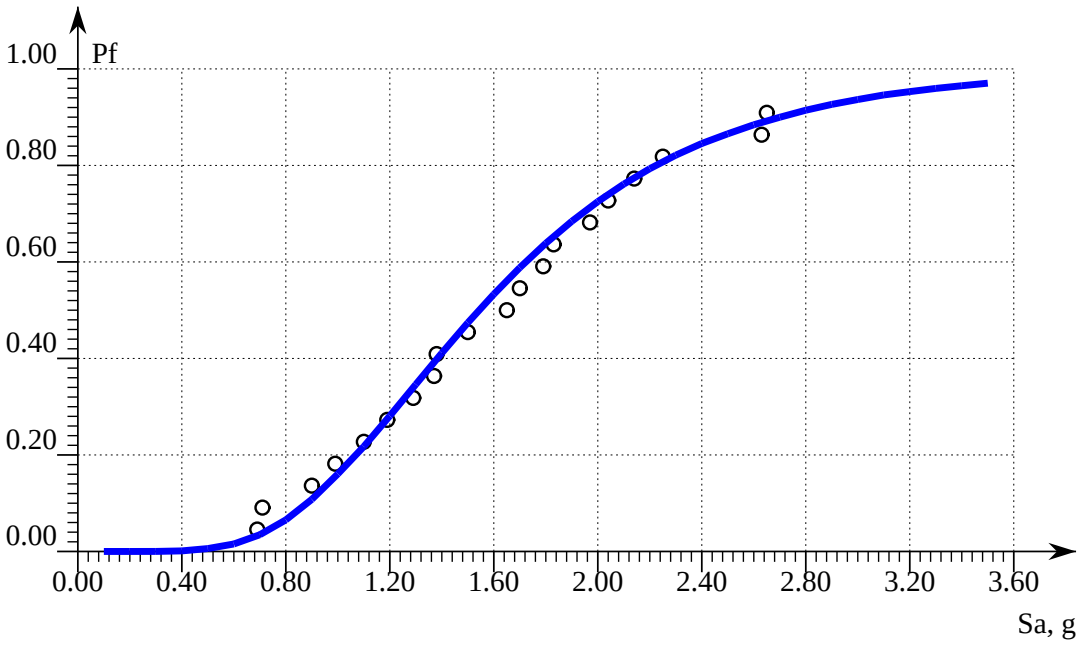

Figure VI.7: Seismic fragility of the benchmark frame.

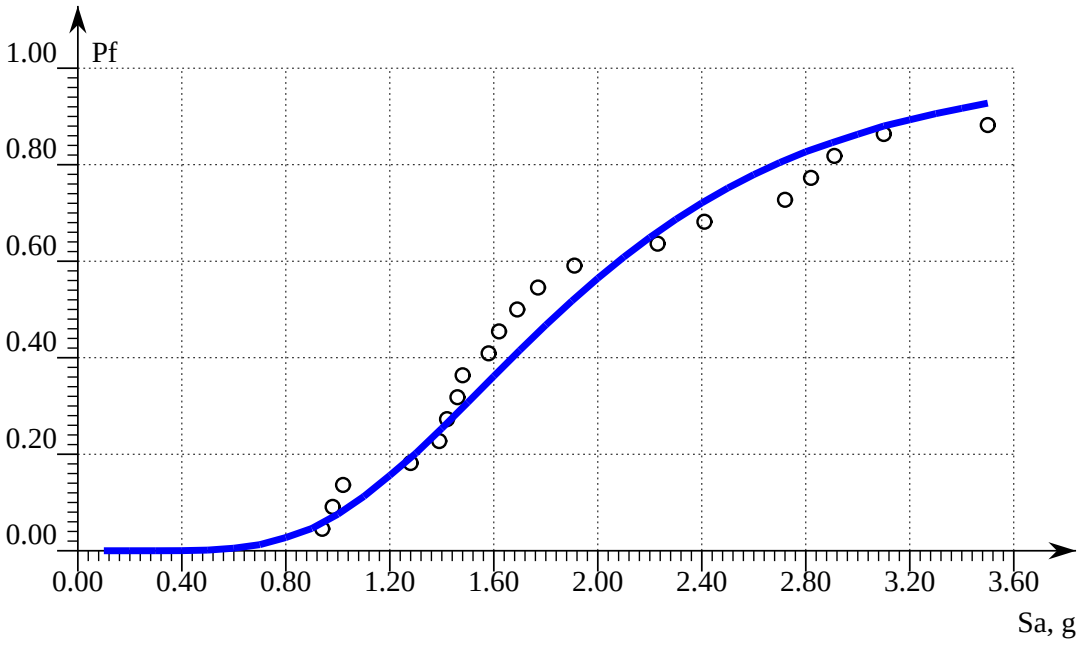

Figure VI.8: Seismic fragility of the optimized frame.

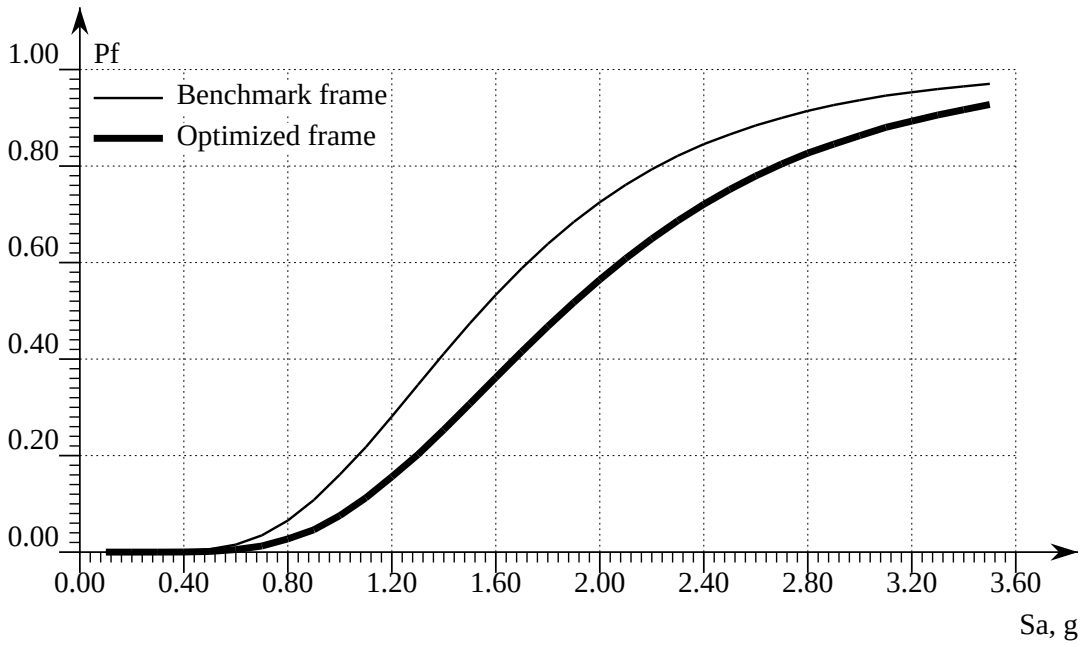

Figure VI.9: Seismic fragility curves of the optimal and benchmark frame.

CHAPTER VII

SUMMARY AND CONCLUSION

This study has introduced a new line finite element that is capable of capturing the local buckling of thin-wall structural members. The element is developed based on a force-based approach, in which the section force vector, consisting of axial force and bending moment, along the element is determined as a function of element nodal forces and interpolation functions. The local buckling of thin-wall structures such as wide-flange beams and columns is accounted for by using an effective width concept to the finite element formulation. Based on this concept, the dimensions of the structural member cross-section reduce with increasing compression. The computation of the line element was coded in C++ language and interacted with the finite element framework of OpenSees (McKenna et al. 2000). The response of the element was verified with a highly refined finite element model developed in Abaqus (DSS 2009). In the refined finite element model, components of a structural member were meshed using shell elements. Analyses of the line element model and the shell element model yield similar results for the structural member.

A new robust analytical solution has also been developed for simulating the behavior of beam-to-column connections in steel lateral force-resisting frames. As in the practice, the connection is modeled using a system of a rotational spring element and rigid links. The shear resistance of the panel zone and the bending resistance of the column flanges are accounted for in the spring element. Not as in previous studies, mathematical models in this work are obtained based on the principle of energy conservation. The work done by external forces on the connection is balanced with the internal deformation energy of the panel zone and column flanges. The mathematical models were verified with experiments on two different connection

specimens. The results obtained from the developed theory can remarkably match the experimental results. Differently from previously developed connection models, the model developed herein can account for axial load effects on the response of the connection under any lateral loading scenarios.

This study proposed a methodology to maximize the inelastic deformation energy of steel moment frame subassemblages. Structural components of a subassemblage include a moment-resisting connections, girders, and columns. The line element and the moment frame connection developed herein are now used to investigate the effect of the strength proportion of the structural components on the energy absorption capacity of the subassemblage. Two yielding ratios are determined as decision variables for evaluating the absorption capacity: (1) the ratio of the strength at the girder yielding to that at the panel zone yielding, and (2) the ratio of the strength at the column yielding to that at the panel zone yielding. Optimizing a subassemblage design is constrained by the strong-column weak-beam philosophy and by the occurrence of first yielding at the panel zone. The panel zone thickness is also constrained by the required minimal values to minimize the shear buckling during inelastic deformation. The lateral elastic stiffness of all subassemblage candidates is kept relatively the same for the optimization. Cyclic analysis was performed for a population of steel moment frame subassemblages, consisting of both girder cover end plate and RBS designs. It was found that the ratio of the column strength to the panel zone strength has considerably positive effects on the behavior of the subassemblages. The subassemblages using RBS design and having that ratio greater than 2.0 consistently exhibit high energy dissipation capacities. The ratio of the girder strength to the panel zone strength does not show a clear effect on the energy dissipation capacity. High ratios of the column flange thickness to the column web thickness are beneficial to increasing the energy dissipation capacity of a subassemblage.

The effect of weak panel zones on the overall seismic performance of steel moment frames has also been investigated in this study. The seismic performance of the benchmark frame and the new or optimized frame was represented by a collapse margin ratio. Complex nonlinear static and dynamic analyses for the two structural systems were implemented upon highly sophisticated nonlinear finite element models. The finite element models used a P-delta system attached to the frames to capture the effects of the weight of the building that is not tributary to the frames. Those finite element models used the line element developed in this study for such structural components as girders, RBS sections, and cover plate sections. The developed mathematical model for the beam-to-column moment-resisting connection was used to simulate the rotational spring at individual connections of the two frames. Gravity loads and combinations were determined based on ASCE 7 (ASCE 2010) and FEMA P695 (FEMA 2009). Two sets of maximum considered earthquake (MCE) ground motions were derived from a set of 10 pairs of SAC ground motions with variety of spectral response shapes. Each MCE set was scaled to different levels of intensity to investigate the failure of the benchmark frame and the optimized frame. It was found that the collapse margin ratio (CMR) determined per FEMA P695 by scaling was difficult. It was also found that the optimization methodology proposed for steel moment frame subassemblages could be applied to a whole frame system to increase the overall seismic performance of that system. The safety or reliability of a steel moment frame under earthquakes can hence be considerably improved while maintaining the fabrication of the structure at an effective cost.

REFERENCES

Achenbach, J. (1973). *Wave Propagation in Elastic Solids*. North-Holland, New York, NY.

AISC (2010a). *Prequalified Connections for Special and Itermediate Steel Moment Frames for Seismic Applications*. Standard ANSI/AISC 358-10. American Institute of Steel Construction, Chicago, IL.

AISC (2010b). *Seismic Provisions for Structural Steel Buildings*. Standard ANSI/AISC 341-10. American Institute of Steel Construction, Chicago, IL.

AISC (2010c). *Specification for Structural Steel Buildings*. Standard ANSI/AISC 360-10. American Institute of Steel Construction, Chicago, IL.

AISC (2013). *Steel Construction Manual Shapes Database*. American Institute of Steel Construction, Chicago, IL. `http://www.aisc.org/content.aspx?id=2868`.

ASCE (2005). *Minimum Design Loads for Buildings and Other Structures*. ASCE Standard ASCE 7-05. American Society of Civil Engineers, Reston, VA.

ASCE (2010). *Minimum Design Loads for Buildings and Other Structures*. ASCE Standard ASCE 7-10. American Society of Civil Engineers, Reston, VA.

Burgoyne, C. and Crisfield, M. (2005). "Numerical integration strategy for plates and shells." *International Journal for Numerical Methods in Engineering*, 29, 105–121.

Carlson, N. and Miller, K. (1998). "Design and application of a gradient-weighted moving finite element code I: in one dimension." *Journal on Scientific Computing*, 19(3), 728–765.

Carol, I. and Murcia, J. (1989). "Nonlinear time-dependent analysis of planar frames using an 'exact' formulation–I. Theory." *Computers & Structures*, 33(1), 79–87.

Chandrupatla, T. and Belegundu, A. (2002). *Introduction to Finite Elements in Engineering*. Prentice-Hall, Upper Saddle River, NJ.

Chopra, A. (2001). *Dynamics of Structures: Theory and Applications to Earthquake Engineering*. Prentice Hall, Upper Saddle River, NJ.

Cofie, N. and Krawinkler, H. (1985). "Uniaxial cyclic stress-strain behavior of structural steel." *Journal of Engineering Mechanics*, 111(9), 1105–1120.

Collins, G. (2004). *The Foundations of Celestial Mechanics*. Pachart Foundation, Tucson, AZ.

Cordova, P., Chen, C., Lai, W., Deierlein, G., and Tsai, K. (2004). "Pseudo-dynamic test of full-scale rcs frame: Part II–analysis and design implications." *Proc. of ASCE-SEI 2004 Structures Congress*, Nashville, TN.

Crisfield, M. (1991). *Nonlinear Finite Element Analysis of Solids and Structures*. John Wiley & Sons, New York, NY.

Dafalias, Y. and Popov, E. (1975). "A model of nonlinearly hardening materials for complex loadings." *Acta Mechanica*, 21(3), 173–192.

Dafalias, Y. and Popov, E. (1976). "Plastic internal variables formalism of cyclic plasticity." *Journal of Applied Mechanics*, 43(4), 645–651.

De Souza, R. (2000). "Force-based finite element for large displacement inelastic analysis of frames." Ph.D. thesis, Department of Civil and Environmental Engineering, University of California, Berkeley, CA.

De Souza Neto, E., Peric, D., and Owen, D. (2008). *Computational Methods for Plasticity: Theory and Applications*. John Wiley & Sons Ltd., West Sussex, UK.

DSS (2009). *Abaqus 6.9 Documentation*. Dassault Systemes Simulia Corporation, Waltham, MA.

Eslahchi, M., Masjed-Jamei, M., and Babolian, E. (2005). "On numerical improvement of Gauss–Lobatto quadrature rules." *Applied Mathematics and Computation*, 164(3), 707–717.

FEMA (1995). "Interim guidelines: Evaluation, repair, modification and design of steel moment frames." *Report No. FEMA-267*, prepared by the SAC Joint Venture, Federal Emergency Management Agency, Washington, DC.

FEMA (2000a). "Recommended seismic design criteria for new steel moment frame buildings." *Report No. FEMA-350*, Federal Emergency Management Agency, Washington, DC.

FEMA (2000b). "State of the art report on connection performance." *Report No. FEMA-355D*, Federal Emergency Management Agency, Washington, DC.

FEMA (2000c). "State of the art report on systems performance of steel moment frames subject to earthquake ground shaking." *Report No. FEMA-355C*, Federal Emergency Management Agency, Washington, DC.

FEMA (2004). "NEHRP recommended provisions and commentary for seismic regulations for new building and other structures." *Report No. FEMA-450*, Federal Emergency Management Agency, Washington, DC.

FEMA (2009). "Quantification of building seismic performance factors." *Report No. FEMA-P695*, Federal Emergency Management Agency, Washington, DC.

Hajjar, J., Dexter, R., Ojard, S., Ye, Y., and Cotton, S. (2003). "Continuity plate detailing for steel moment-resisting connections." *Engineering Journal*, 40(4), 81–97.

Hamrock, B., Schmid, S., Jacobson, B., and Jacobson, B. (1999). *Fundamentals of Machine Elements*. WCB/McGraw-Hill, Columbus, OH.

Hauser, J. (2009). *Numerical Methods for Nonlinear Engineering Models*. Springer Science+Business Media B.V., 3311 GX Dordrecht, Netherlands.

Hsiao, J., Schultz, W., Petersen, T., and Vaicik, S. (2008). "Computation of story drifts considering panel zone deformations for multistory steel moment frames with welded flange plate connections." *The Structural Design of Tall and Special Buildings*, 17(2), 419–443.

Ibarra, L. and Krawinkler, H. (2005). "Global collapse of frame structures under seismic excitations." *Report No. PEER 2005/06*, Pacific Earthquake Engineering Research Center, Department of Civil & Environmental Engineering, Stanford University, Stanford, CA.

Jain, S. (1989). *Introduction to Theories of Plasticity*. Engineering Publications, Blacksburg, VA.

Jin, J. (2002). "Seismic performance of steel RBS moment frame buildings." Ph.D. thesis, Department of Civil and Environmental Engineering, University of Central Florida, Orlando, FL.

Jin, J. and El-Tawil, S. (2005). "Evaluation of fema-350 seismic provisions for steel panel zones." *Journal of Structural Engineering*, 131(2), 250–258.

Jones, S. (2000). "An analysis procedure to facilitate performance-based design of steel moment frame buildings with reduced beam section joints." Ph.D. thesis,

Zachry Department of Civil Engineering,Texas A&M University, College Station, TX.

Jones, S., Fry, G., and Engelhardt, M. (2002). "Experimental evaluation of cyclically loaded reduced beam section moment connections." *Journal of Structural Engineering*, 128(4), 441–451.

Kassimali, A. (2005). *Structural Analysis*. Cengage Learning, Stamford, CT.

Keyak, J. and Rossi, S. (2000). "Prediction of femoral fracture load using finite element models: an examination of stress- and strain-based failure theories." *Journal of Biomechanics*, 33(2), 209–214.

Kim, K. and Engelhardt, M. (2002). "Monotonic and cyclic loading models for panel zones in steel moment frames." *Journal of Constructional Steel Research*, 58, 605–635.

Kim, S. and Kang, K. (2004). "Large-scale testing of 3-D steel frame accounting for local buckling." *International Journal of Solids and Structures*, 41, 5003–5022.

Krawinkler, H. (1978). "Shear in beam-column joints in seismic design of steel frames." *Engineering Journal*, 15(3), 82–91.

Krawinkler, H., Bertero, V., and Popov, E. (1971). "Inelastic behavior of steel beam-column subassemblages." *Report No. EERC 71/07*, Department of Civil and Environmental Engineering, University of California, Berkeley, CA.

Krishnan, S. and Muto, M. (2011). "Mechanism of collapse, sensitivity to ground motion features, and rapid estimation of the response of tall steel moment frame buildings to earthquake excitation." *Report No. EERL 2011-02*, California Institute of Technology, Pasadena, CA.

Kunnath, S. and Malley, J. (2002). "Advances in seismic design and evaluation of steel moment frames: Recent findings from FEMA/SAC Phase II Project." *Journal of Structural Engineering*, 128 (4), 415–419.

Lai, W., Rubin, D., and Krempl, E. (2010). *Introduction to Continuum Mechanics*. Butterworth-Heinemann, Burlington, MA.

Lee, D., Cotton, S., Hajjar, J., Dexter, R., and Ye, Y. (2005). "Cyclic behavior of steel moment-resisting connections reinforced by alternative column stiffener details II. panel zone behavior and doubler plate detailing." *Engineering Journal*, 4th Quarter, 215–238.

Mazzoni, S., McKenna, F., Scott, M., Fenves, G., and et al (2007). *OpenSees Command Language Manual*. Pacific Earthquake Engineering Research Center, University of California, Berkeley, CA.

McKenna, F., Fenves, G. L., and Scott, M. H. (2000). *Open System for Earthquake Engineering Simulation*. Pacific Earthquake Engineering Research Center, University of California, Berkeley, CA. Retrieved Jul 7, 2011. `http://opensees.berkeley.edu`.

Nakata, N., Schafer, B., and Madsen, R. (2012). "Seismic design of multi-story cold-formed steel buildings: the CFS-NEES archetype building." *Proc. of 2012 Structures Congress*, Reston, VA.

NEES (2013). *MAST Laboratory Overview*. George E. Brown, Jr. Network for Earthquake Engineering Simulation, University of Minnesota, Minneapolis, MN. Retrieved Oct 28, 2013. `http://nees.umn.edu/overview.php`.

Neuenhofer, A. and F.C., F. (1997). "Evaluation of nonlinear frame finite element models." *Journal of Structural Engineering*, 123(7), 958–966.

Newmark, N. (1959). "A method of computation for structural dynamics." *Journal of the Engineering Mechanics Division*, 85, 67–94.

Nowak, A. and Collins, K. (2000). *Reliability of Structures.* McGraw-Hill, New York, NY.

Ohtori, Y., Christenson, R., Spencer Jr., B., and Dyke, S. (2004). "Benchmark control problems for seismically excited nonlinear buildings." *Journal of Engineering Mechanics*, 130(4), 366–385.

OpenSees (2006). *Open System for Earthquake Engineering Simulation.* Pacific Earthquake Engineering Research Center, University of California, Berkeley, CA. Retrieved Jul 7, 2011. `http://opensees.berkeley.edu`.

PEER (2011). *Suites of Earthquake Ground Motions for Analysis of Steel Moment Frame Structures.* Pacific Earthquake Engineering Research Center, Richmond, CA. Retrieved Jan 19, 2011. `http://nisee.berkeley.edu/data/strong_motion/sacsteel/`.

Razavi, M. (2013). "On the concept of earthquake resistant hybrid steel frames." Ph.D. thesis, The University of Texas at Arlington, The University of Texas at Arlington.

Reddy, J. (2004). *An Introduction to Nonlinear Finite Element analysis.* Oxford University Press, New York, NY.

Ricles, J., Mao, C., Lu, L., and Fisher, J. (2002). "Inelastic cyclic testing of welded unreinforced moment connections." *Journal of Structural Engineering*, 128(4), 429–440.

Riks, E. (1984). "Some computational aspects of the stability analysis of nonlinear

structures." *Computer Methods in Applied Mechanics and Engineering*, 47(3), 219–259.

Royster, P. (2007). "Localized low cycle fatigue failure of welded steel moment connections." M.S. thesis, North Carolina State University, Raleigh, NC.

Scott, M. and Fenves, G. (2009). "Krylov subspace accelerated Newton algorithm: Application to dynamic progressive collapse simulation of frames." *Journal of Structural Engineering*, 136(5), 473–480.

Scott, M., Fenves, G., McKenna, F., and Filippou, F. (2008). "Software patterns for nonlinear beam-column models." *Journal of Structural Engineering*, 134(4), 562–571.

Soulie, J. (2007). *C++ Language Tutorial*. Retrieved Jul 25, 2012. `http://www.cplusplus.com`.

Spacone, E. (1994). "Flexibility-based finite element models for the nonlinear static and dynamic analysis of concrete frame structures." Ph.D. thesis, Department of Civil and Environmental Engineering, University of California, Berkeley, CA.

Spacone, E., Ciampi, V., and Filippou, F. (1996). "Mixed formulation of nonlinear beam finite element." *Computers & structures*, 58(1), 71–83.

Subramanian, N. (2011). *Steel Structures: Design and Practice*. Oxford University Press, New Delhi, India.

Taucer, F., Spacone, E., and Filippou, F. (1991). "A fiber beam-column element for seismic response analysis of reinforced concrete structures." *Report No. UCB/EERC-91/17*, Earthquake Engineering Research Center, College of Engineering, University of California, Berkeley, CA.

Tcl (2012). *Tcl Developer Xchange*. Retrieved Mar 30, 2012. `http://www.tcl.tk`.

USGS (2009). *Seismic Design Maps for NEHRP Provisions*. U.S. Geological Survey, Retrieved Jul 31, 2013. `http://earthquake.usgs.gov/hazards/designmaps/`.

Van Rossum, G. and Drake Jr., F. (2010). *The Python Language Reference*. Python Software Foundation, Beaverton, OR.

von Karman, T., Sechler, E., and Donnell, L. (1932). "The strength of thin plates in compression." *Transactions ASME*, 54, 53–57.

Wang, L. (2011). "Analysis methods investigation of steel frames accounting for local buckling." *Advanced Materials Research*, 243–249, 1391–1395.

Wang, S. and Dixon, M. (1997). "A new static failure criterion for ductile materials." *The Journal of Strain Analysis for Engineering Design*, 32(5), 345–350.

Wang, S., Errera, S., and Winter, G. (1975). "Behavior of cold-rolled stainless steel members." *Journal of the Structural Division*, 101(11).

Yu, W. and LaBoube, R. (2010). *Cold-Formed Steel Design*. John Wiley & Sons, Hoboken, NJ.

Zienkiewicz, O. and Taylor, R. (2005). *The Finite Element Method for Solid and Structural Mechanics*. Elsevier Butterworth-Heinemann, Oxford, UK.

APPENDIX A

TIME HISTORY ANALYSIS

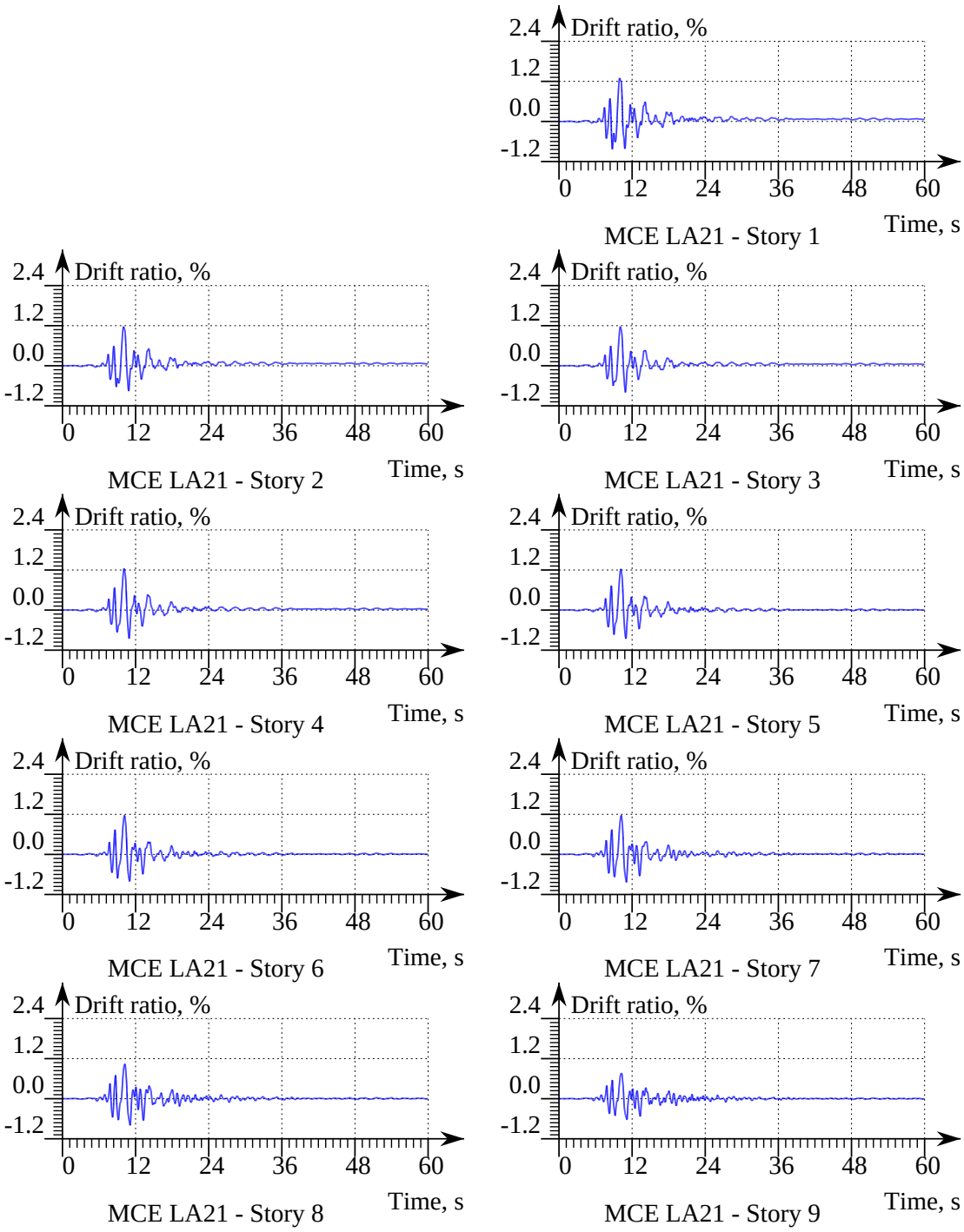

Figure A.1: Story Drift of the Benchmark Frame under MCE LA21.

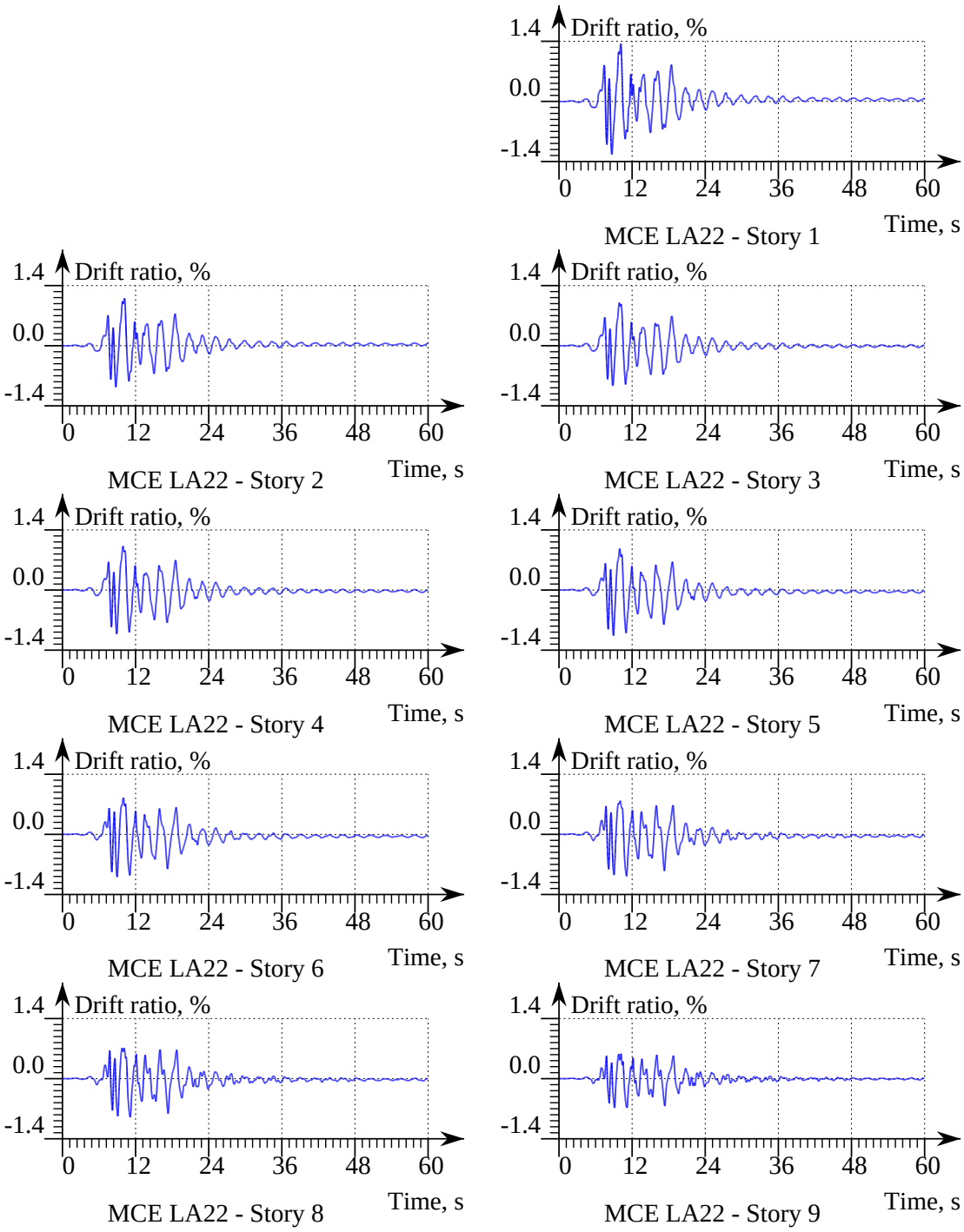

Figure A.2: Story Drift of the Benchmark Frame under MCE LA22.

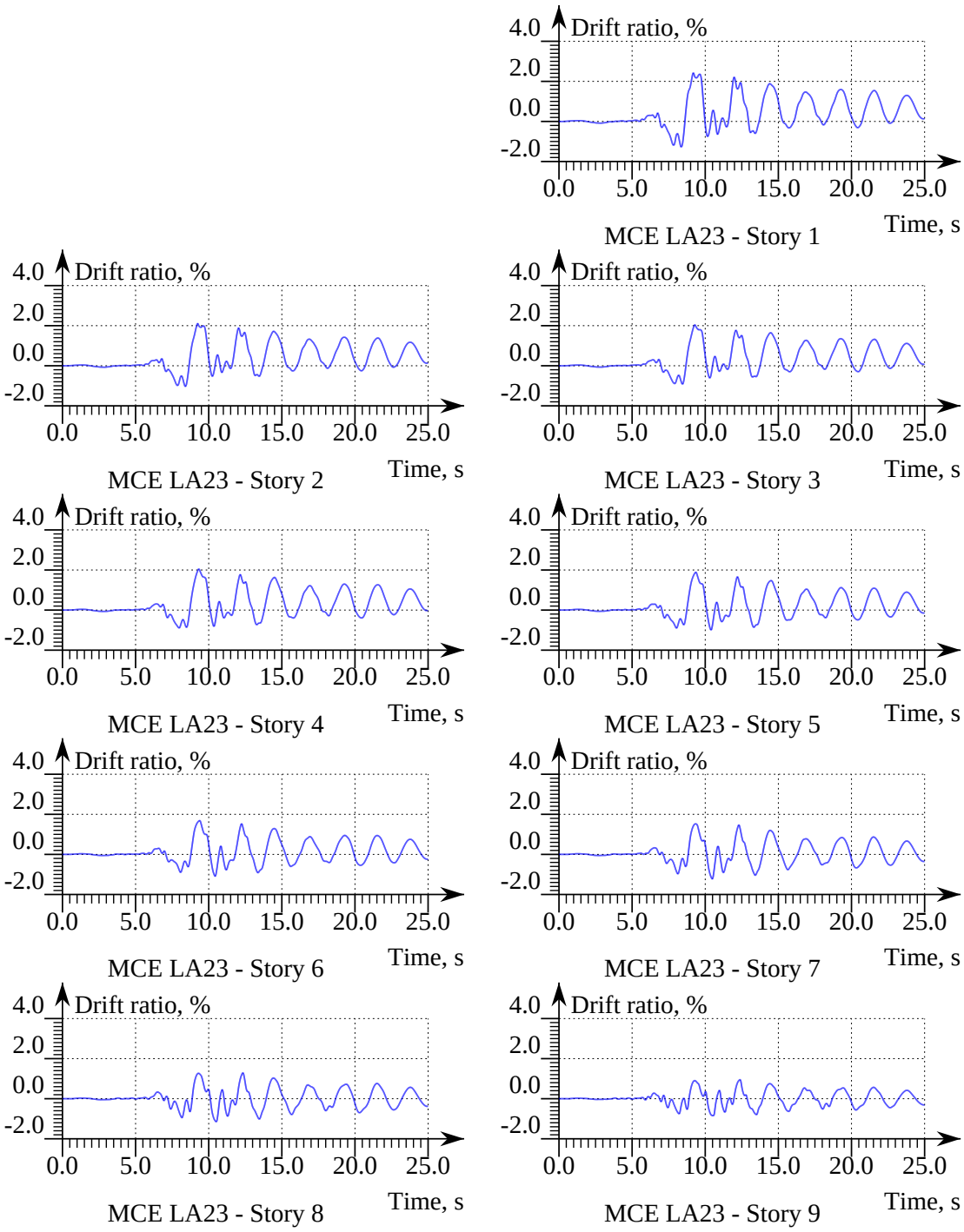

Figure A.3: Story Drift of the Benchmark Frame under MCE LA23.

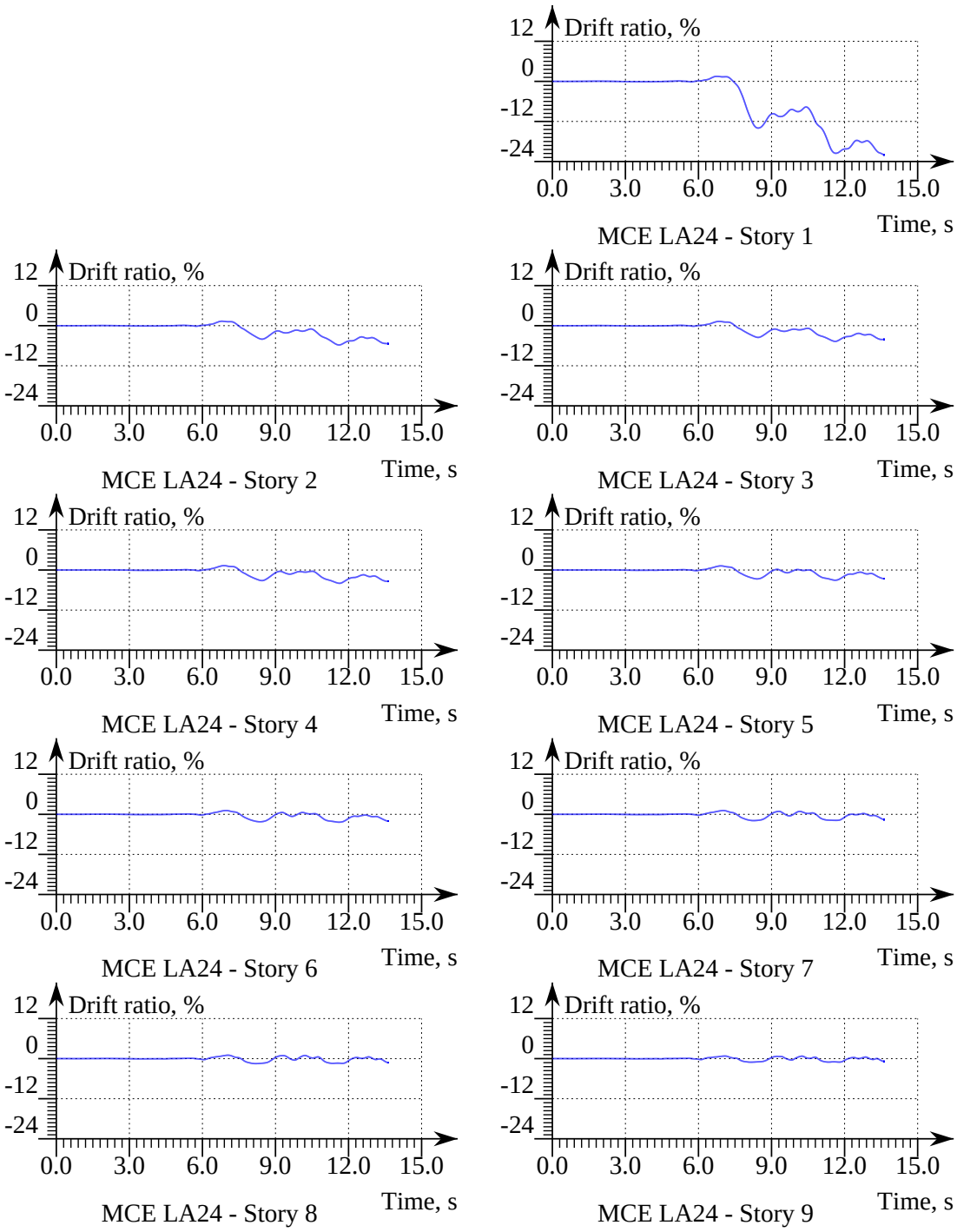

Figure A.4: Story Drift of the Benchmark Frame under MCE LA24.

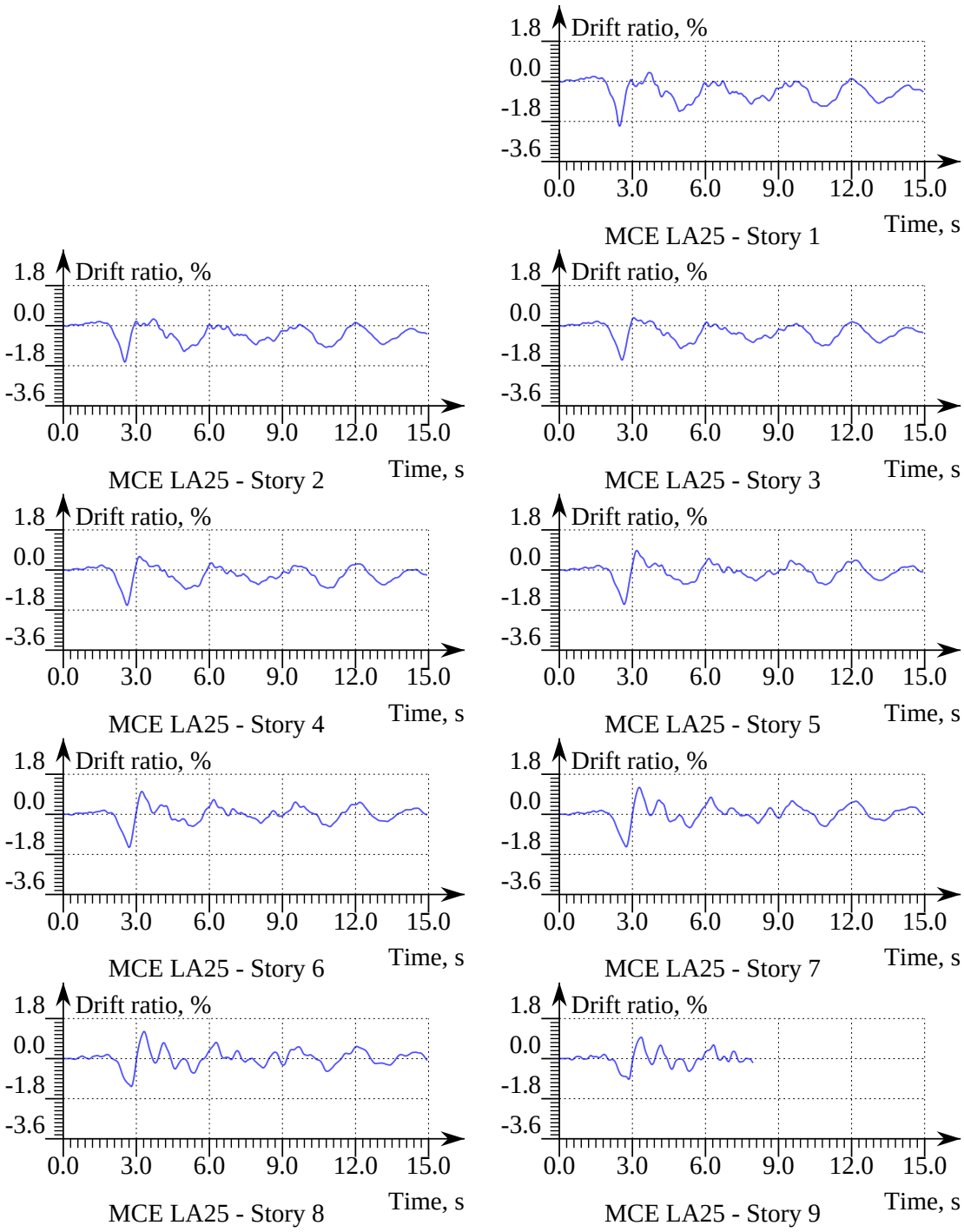

Figure A.5: Story Drift of the Benchmark Frame under MCE LA25.

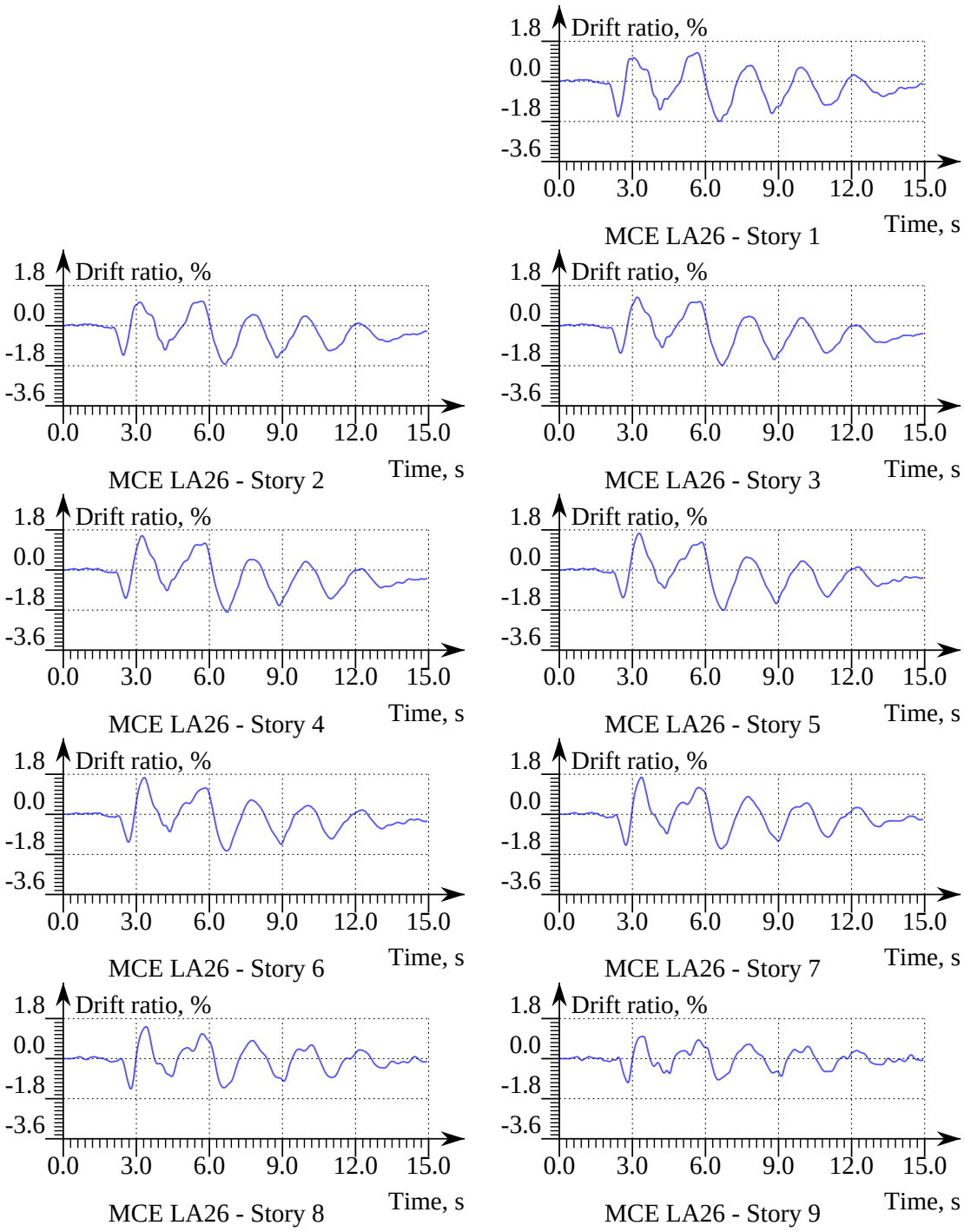

Figure A.6: Story Drift of the Benchmark Frame under MCE LA26.

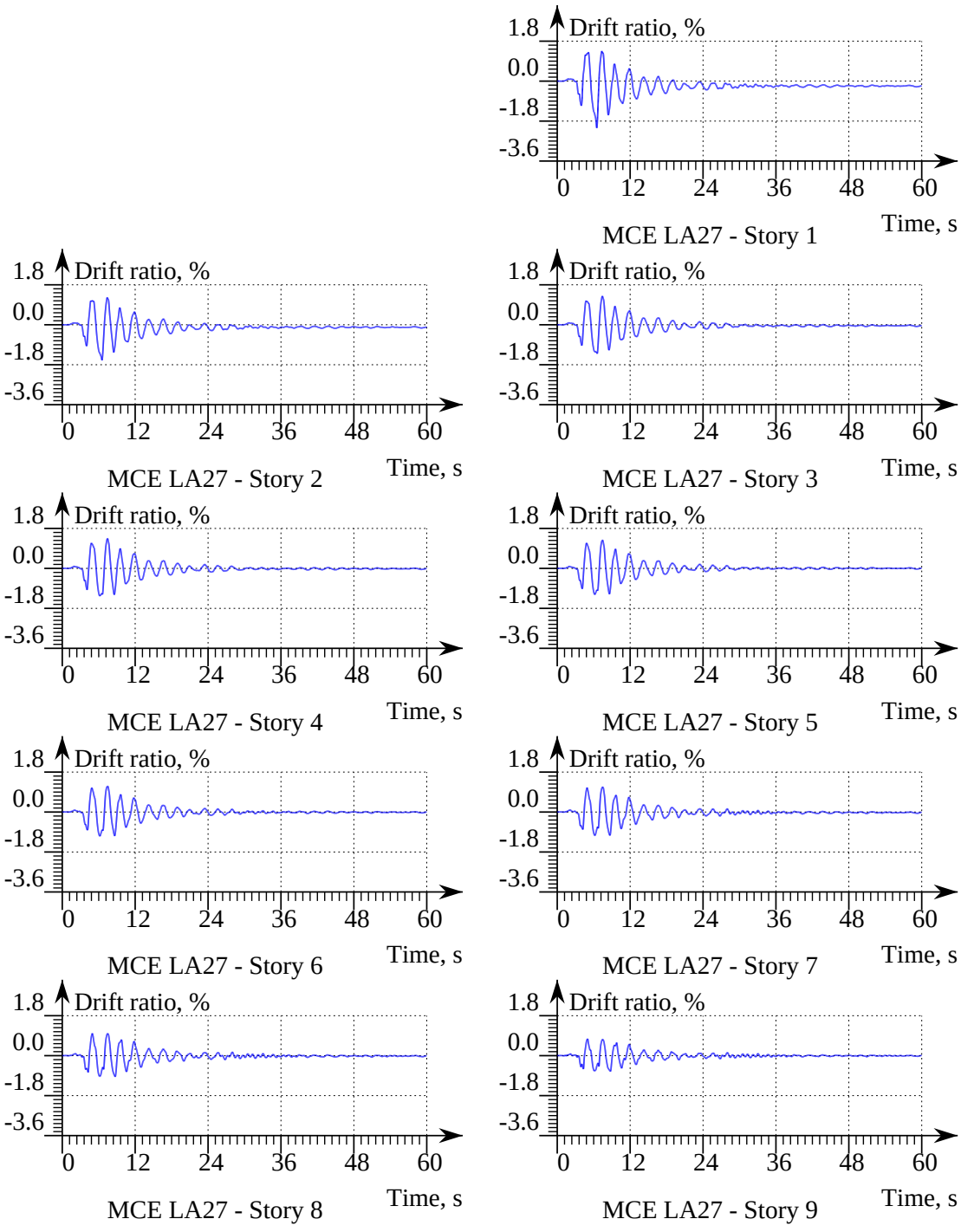

Figure A.7: Story Drift of the Benchmark Frame under MCE LA27.

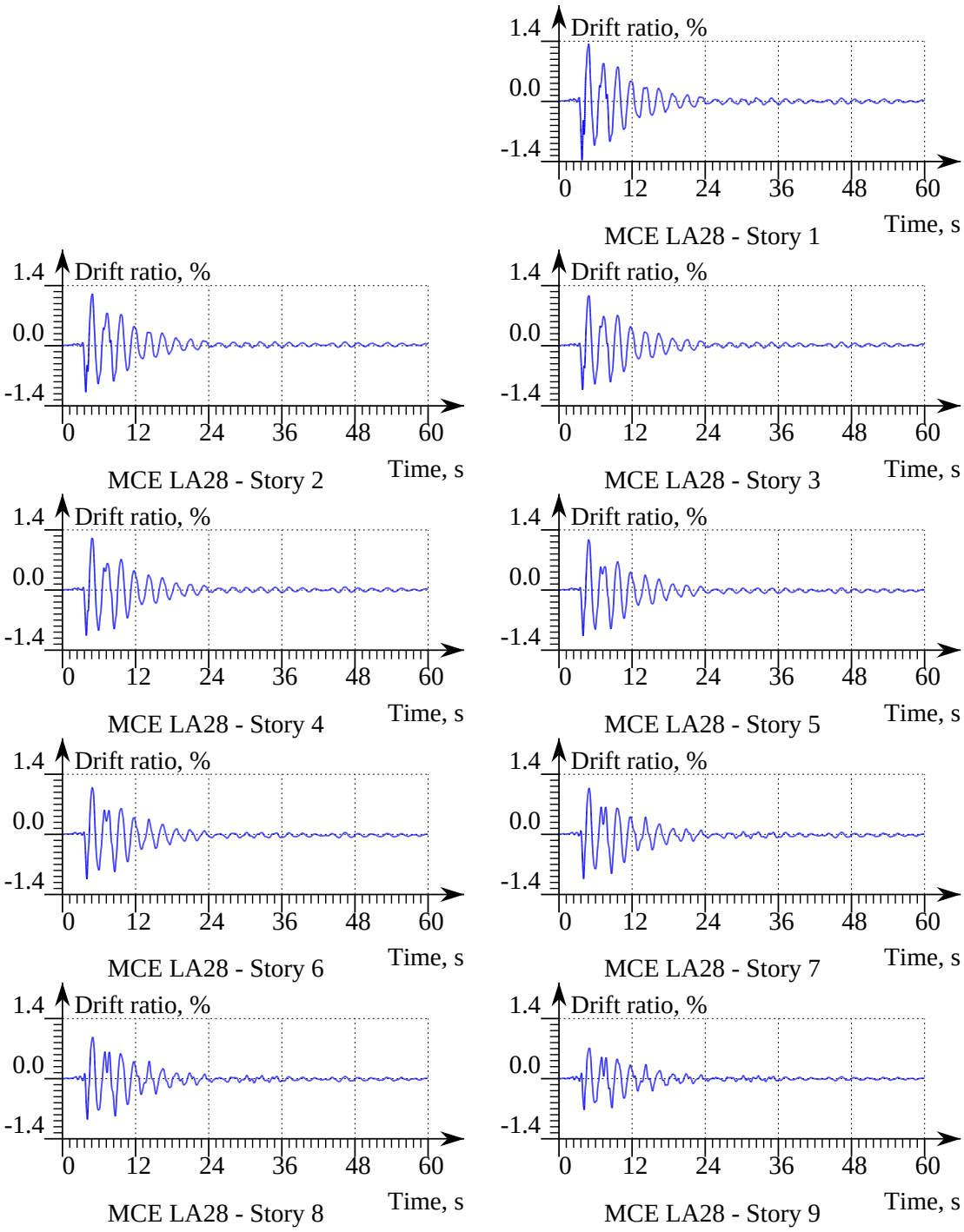

Figure A.8: Story Drift of the Benchmark Frame under MCE LA28.

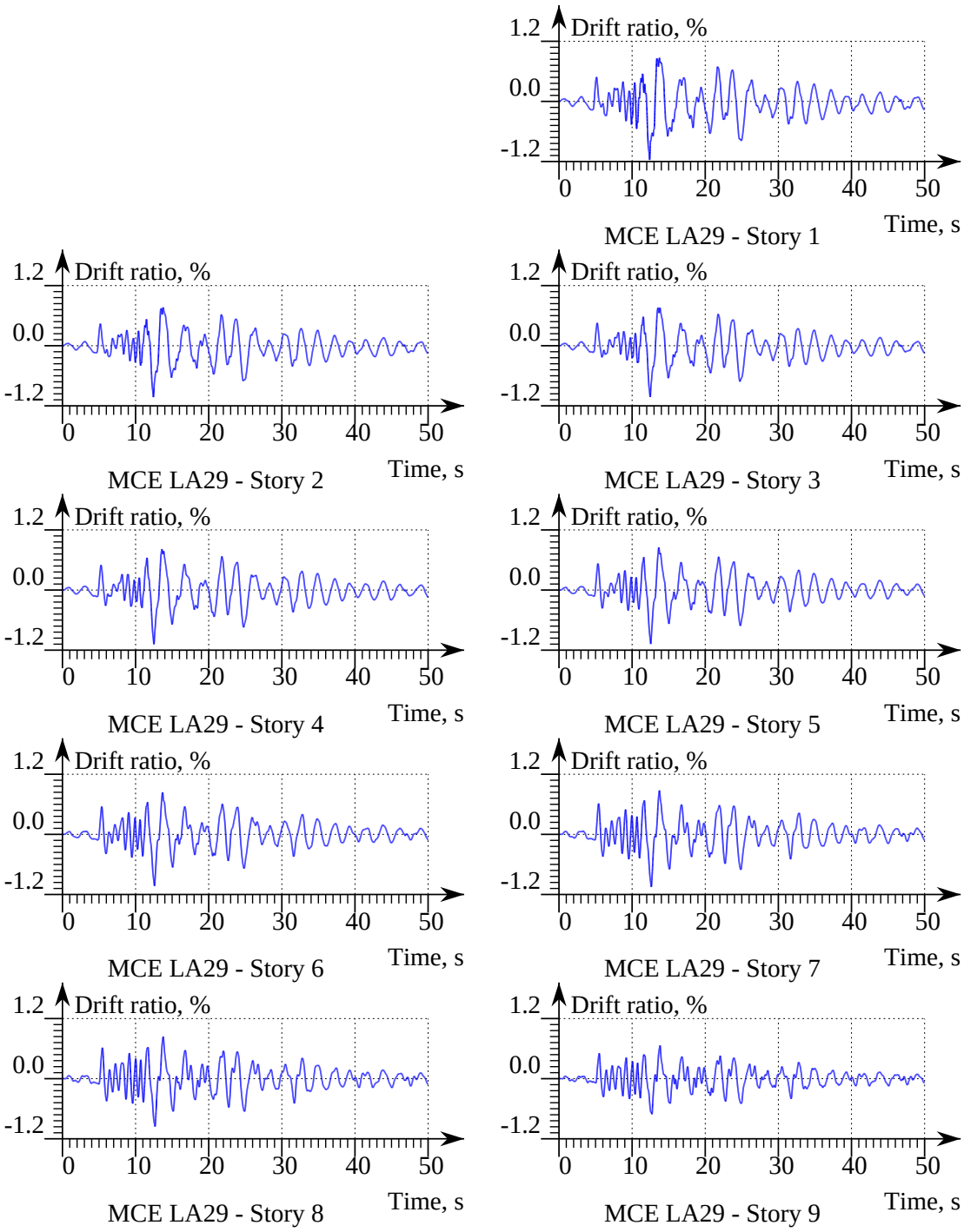

Figure A.9: Story Drift of the Benchmark Frame under MCE LA29.

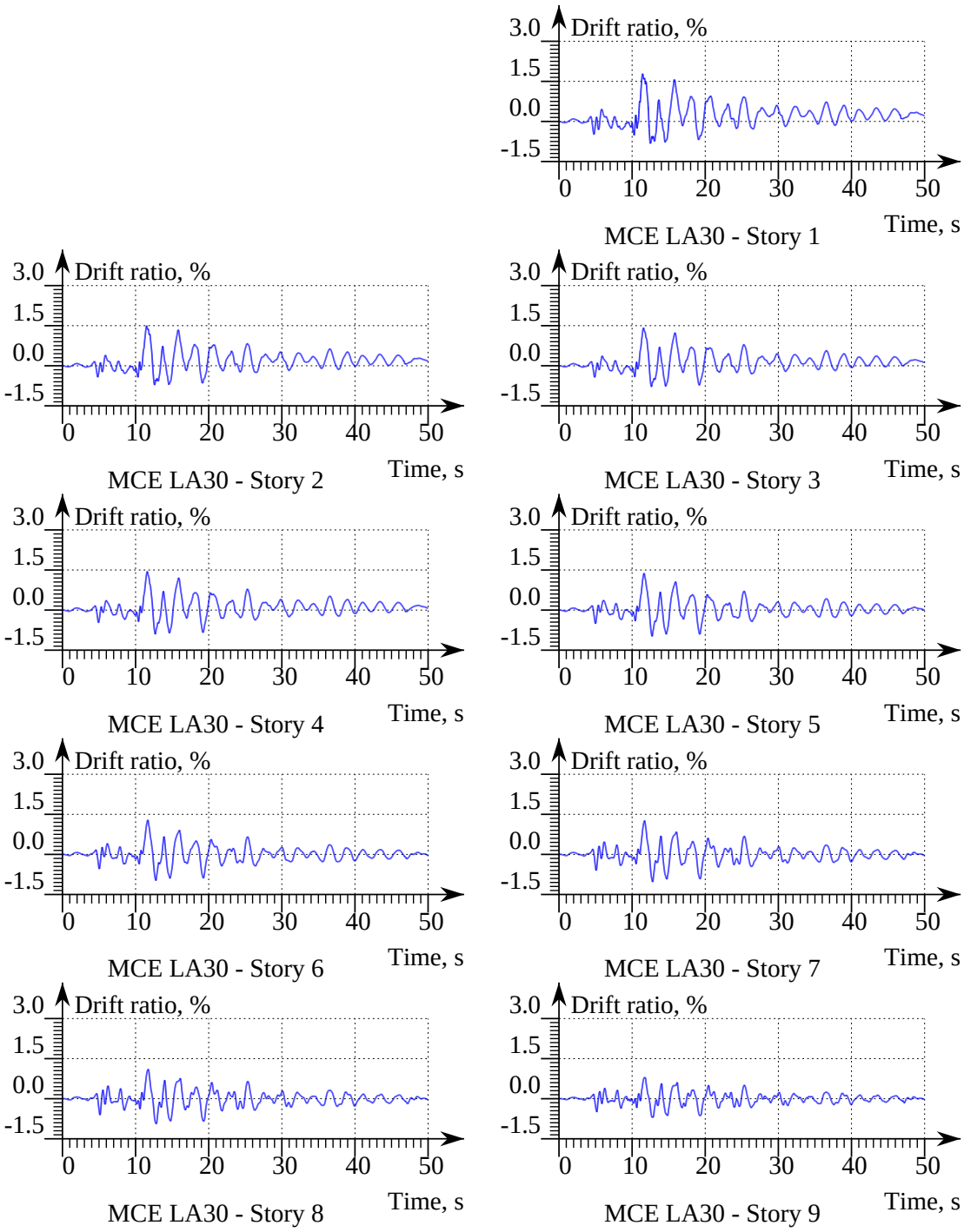

Figure A.10: Story Drift of the Benchmark Frame under MCE LA30.

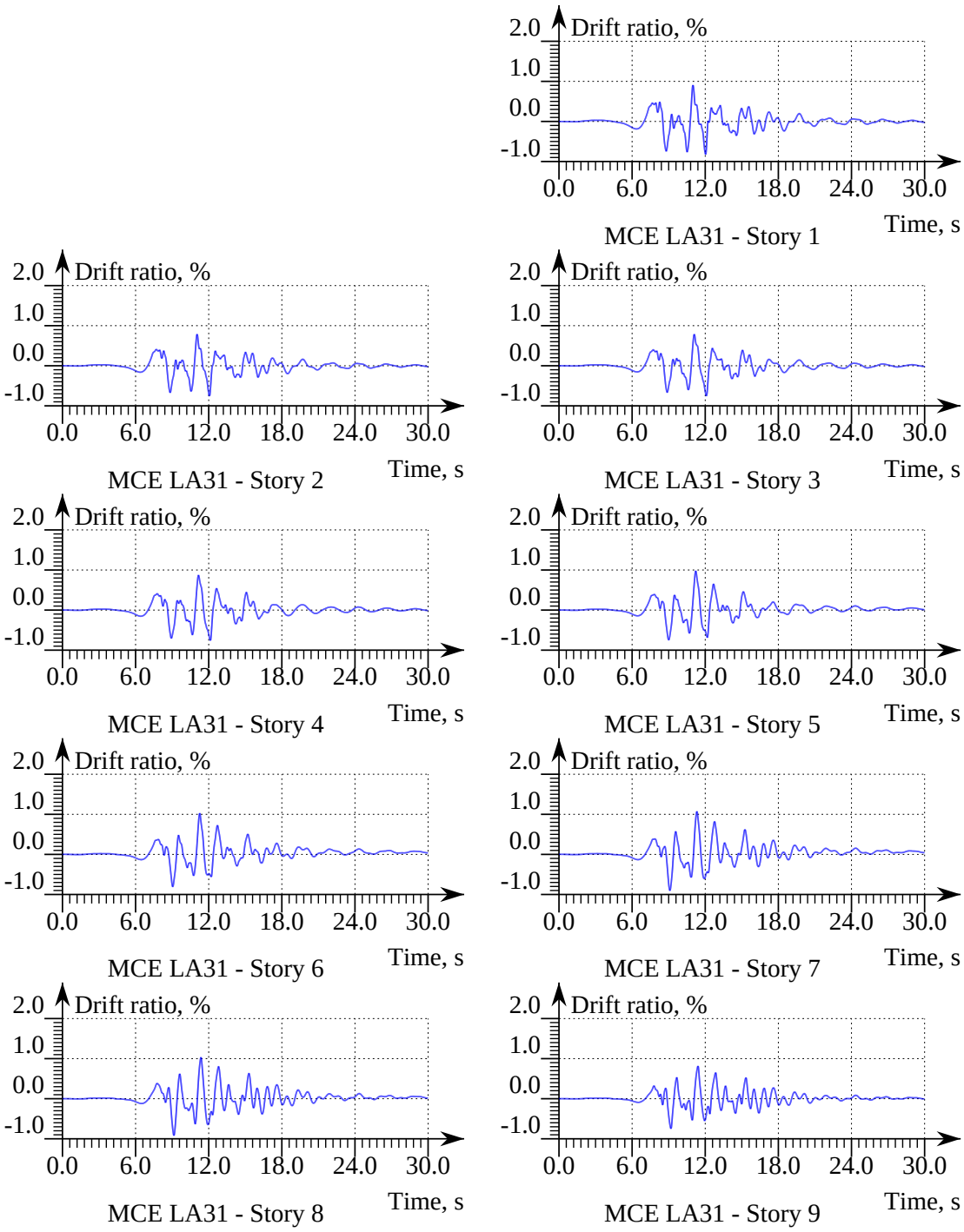

Figure A.11: Story Drift of the Benchmark Frame under MCE LA31.

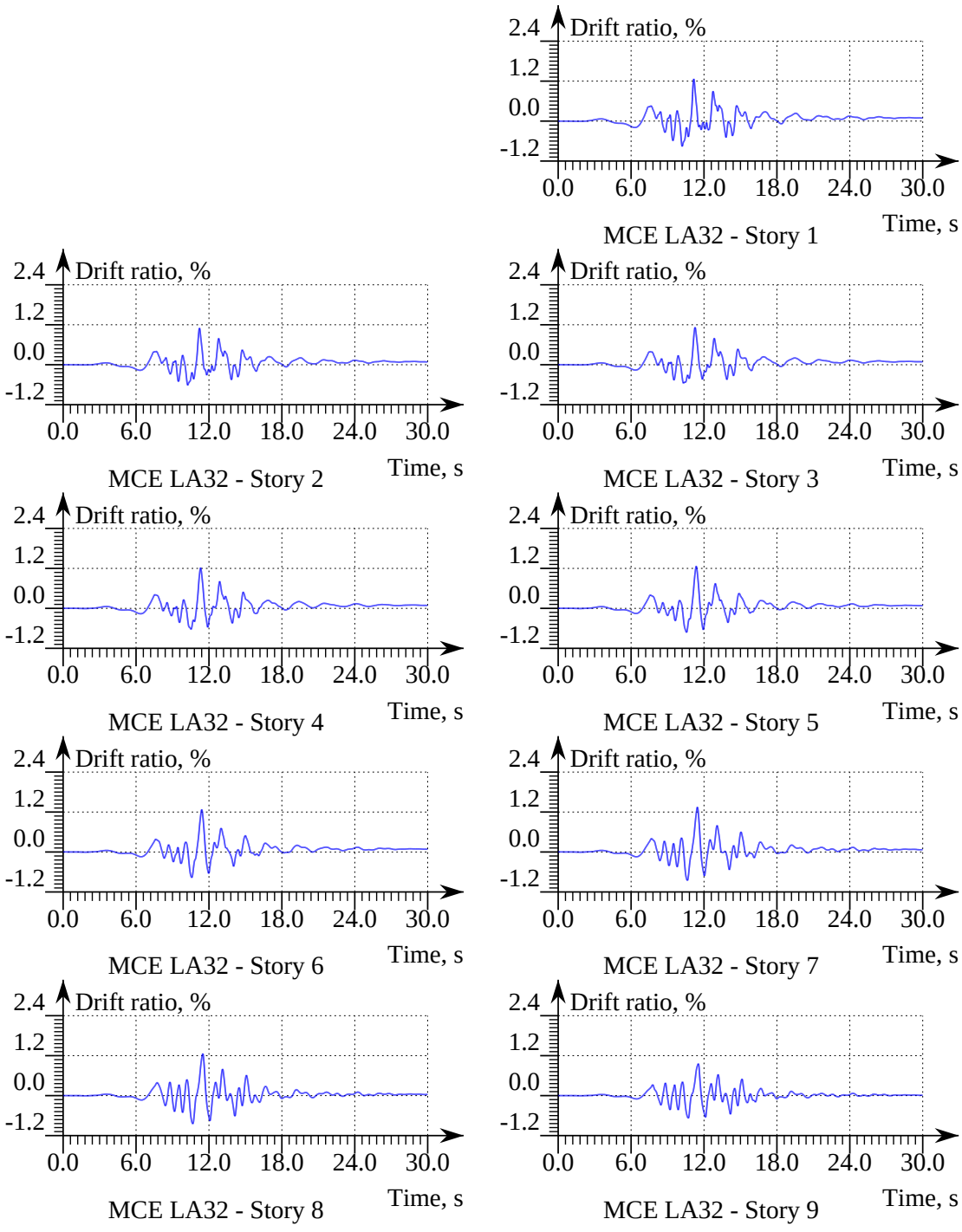

Figure A.12: Story Drift of the Benchmark Frame under MCE LA32.

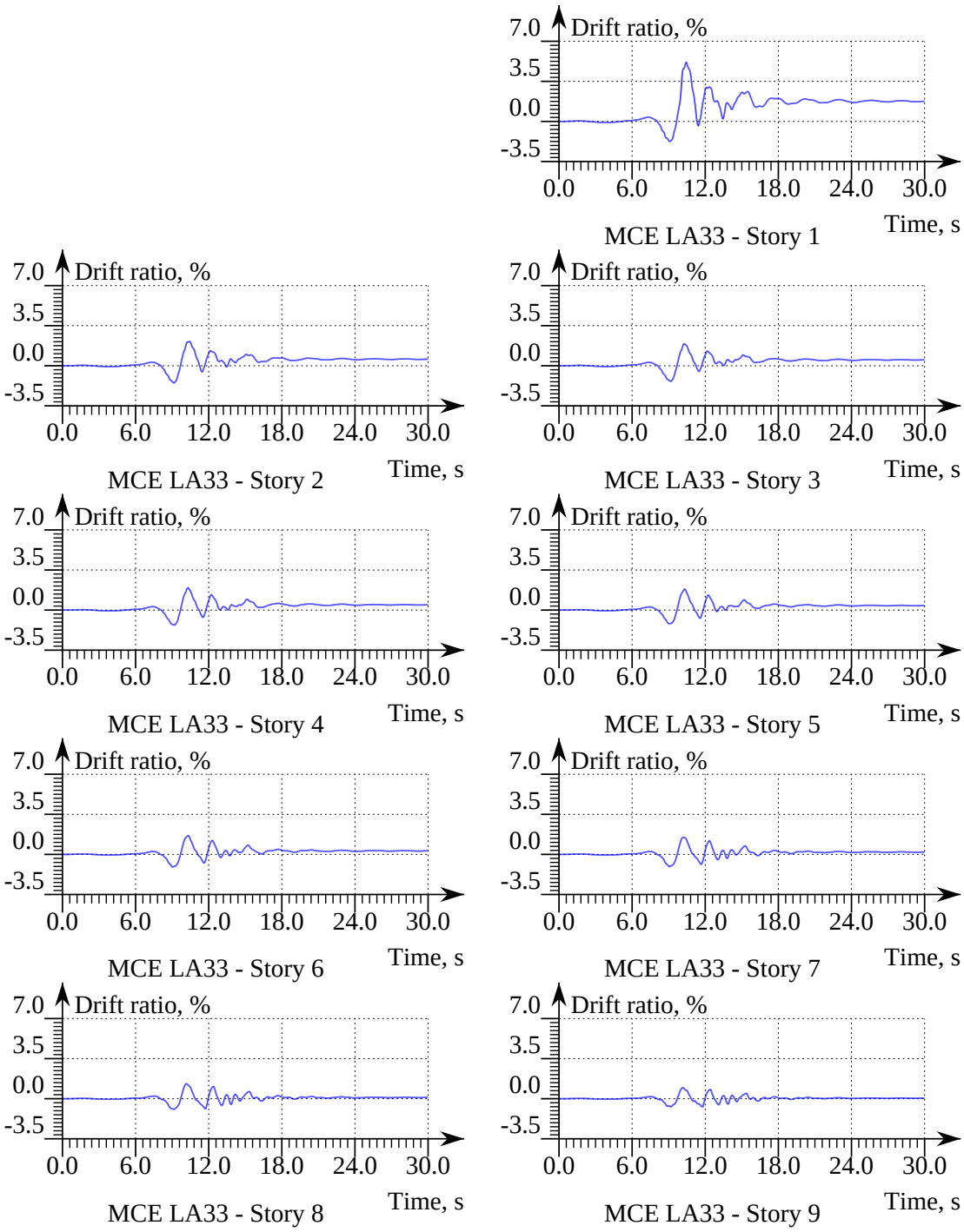

Figure A.13: Story Drift of the Benchmark Frame under MCE LA33.

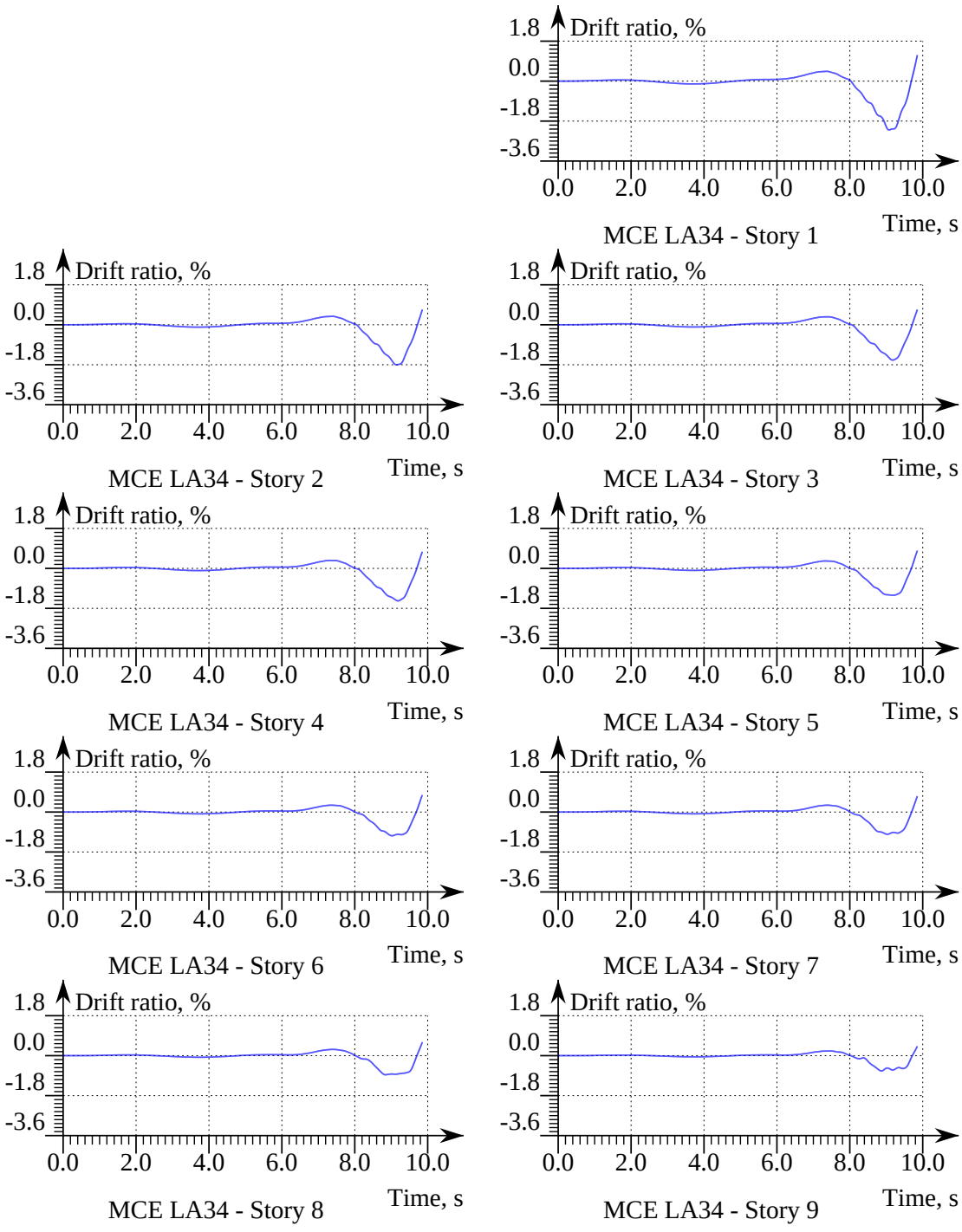

Figure A.14: Story Drift of the Benchmark Frame under MCE LA34.

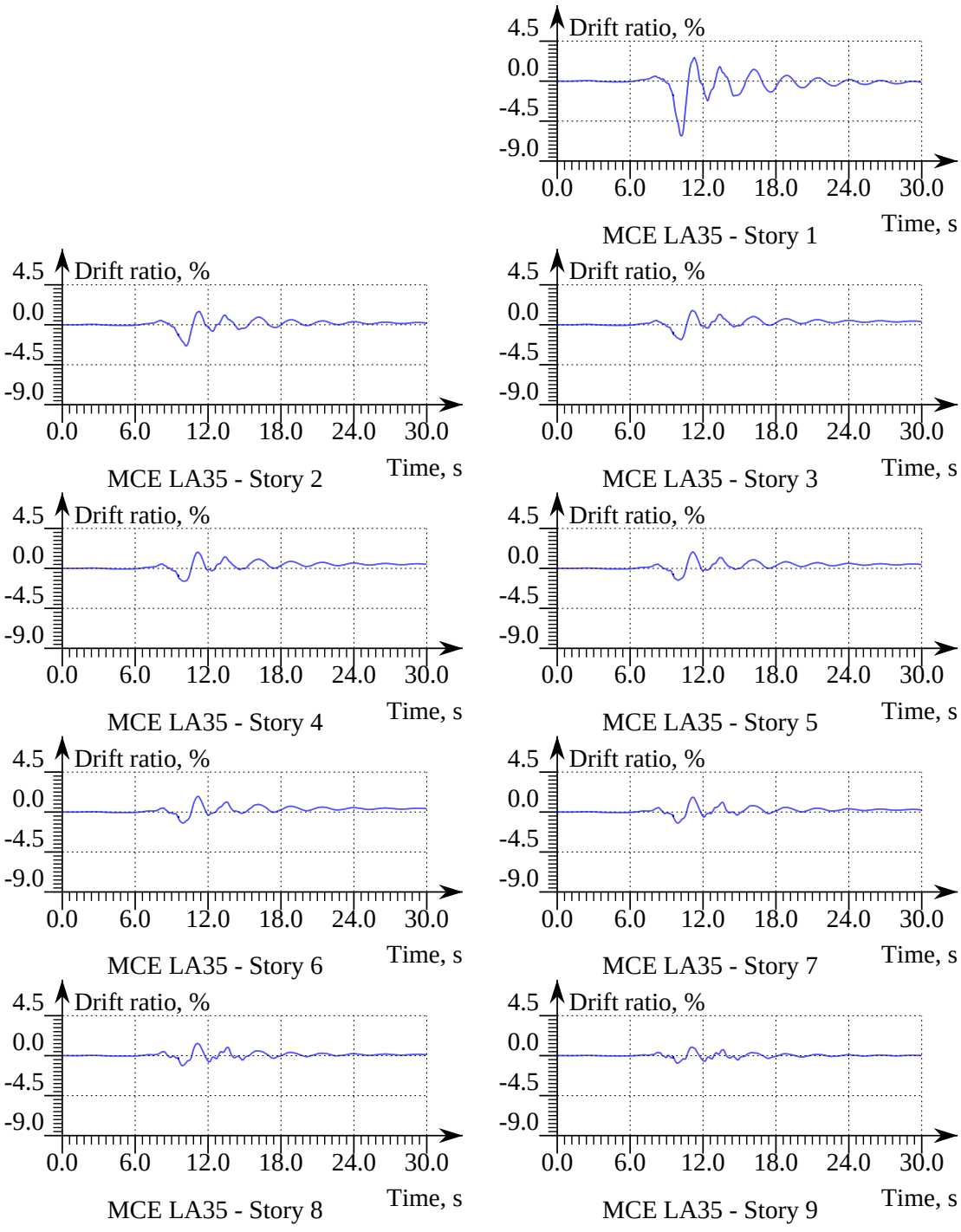

Figure A.15: Story Drift of the Benchmark Frame under MCE LA35.

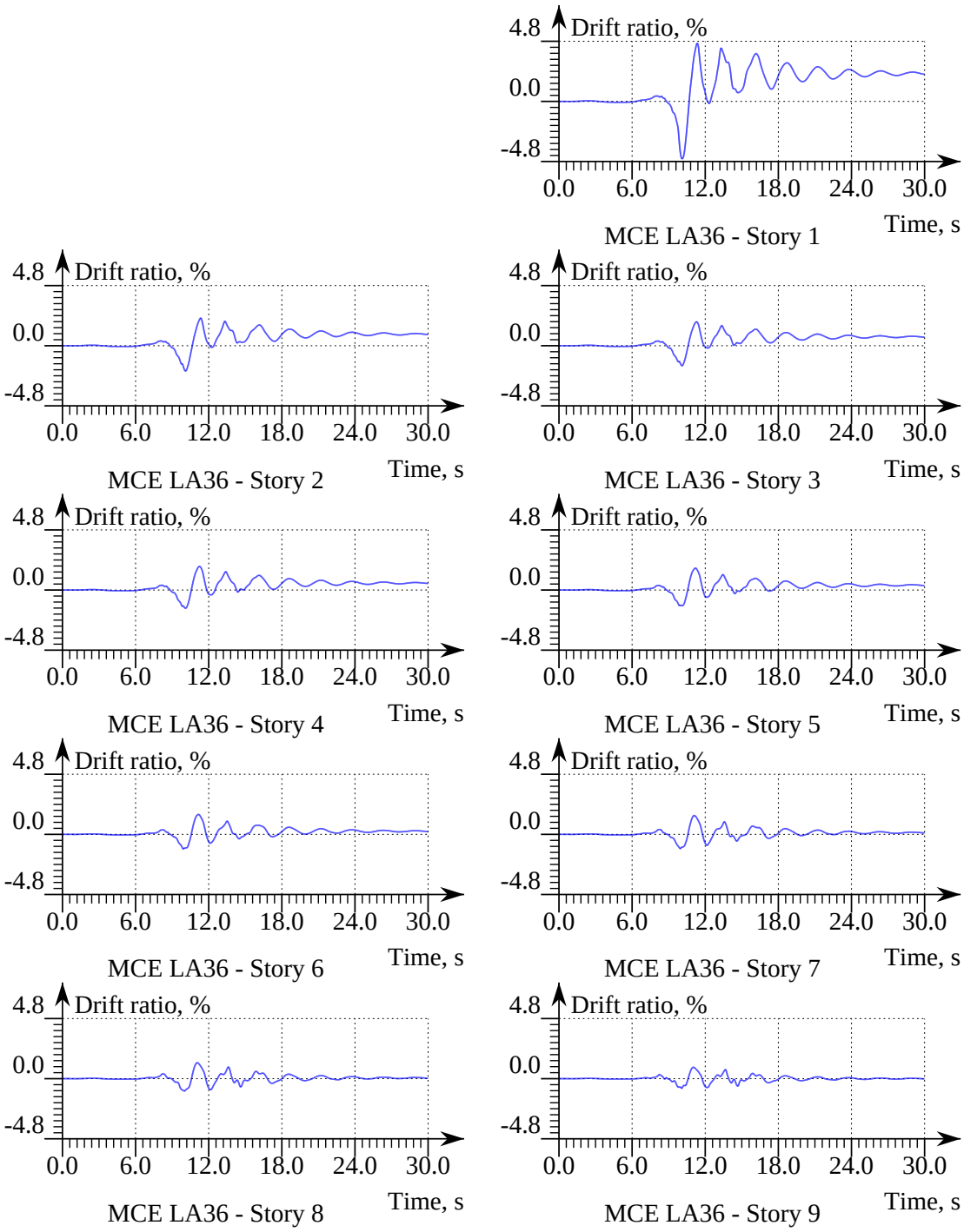

Figure A.16: Story Drift of the Benchmark Frame under MCE LA36.

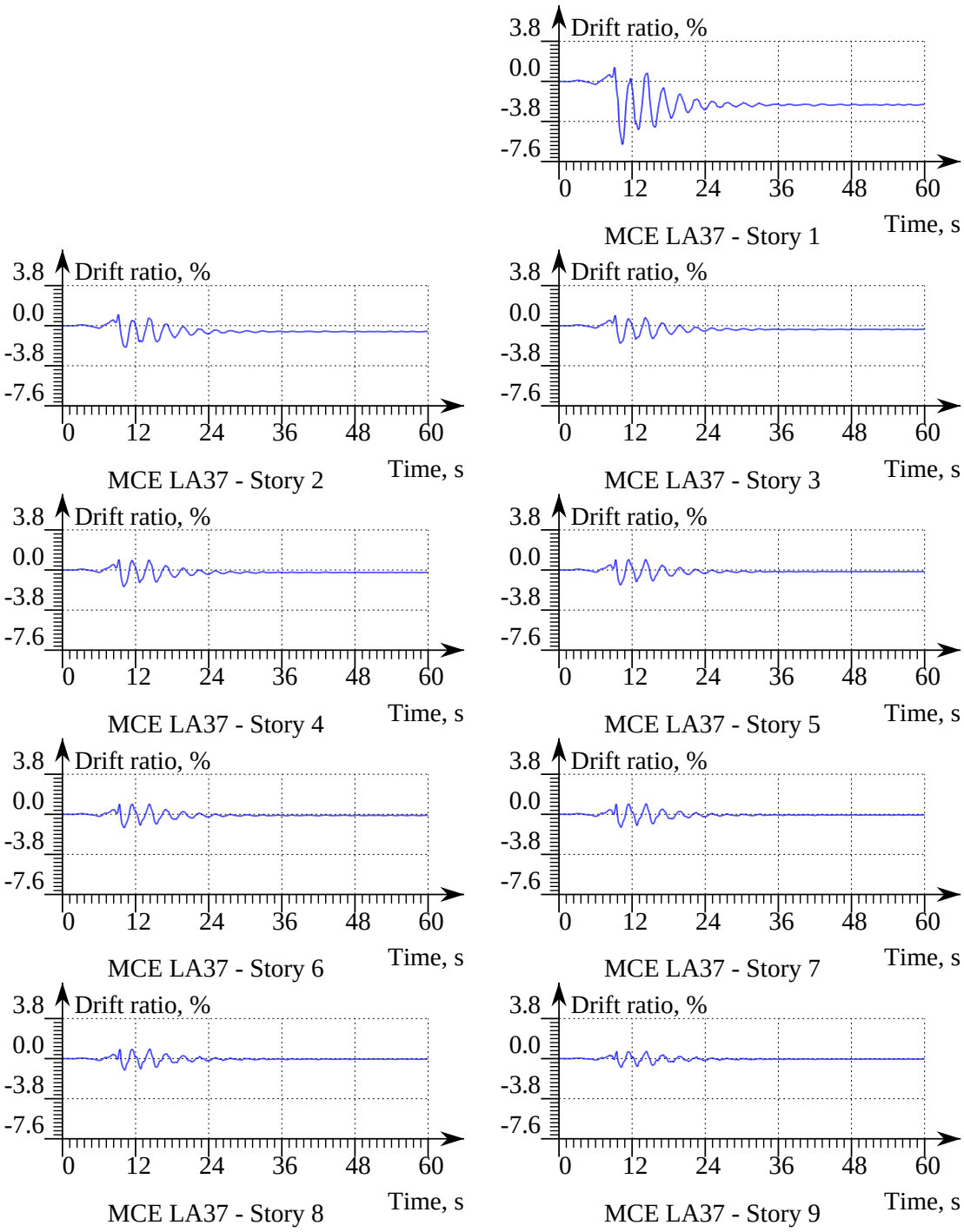

Figure A.17: Story Drift of the Benchmark Frame under MCE LA37.

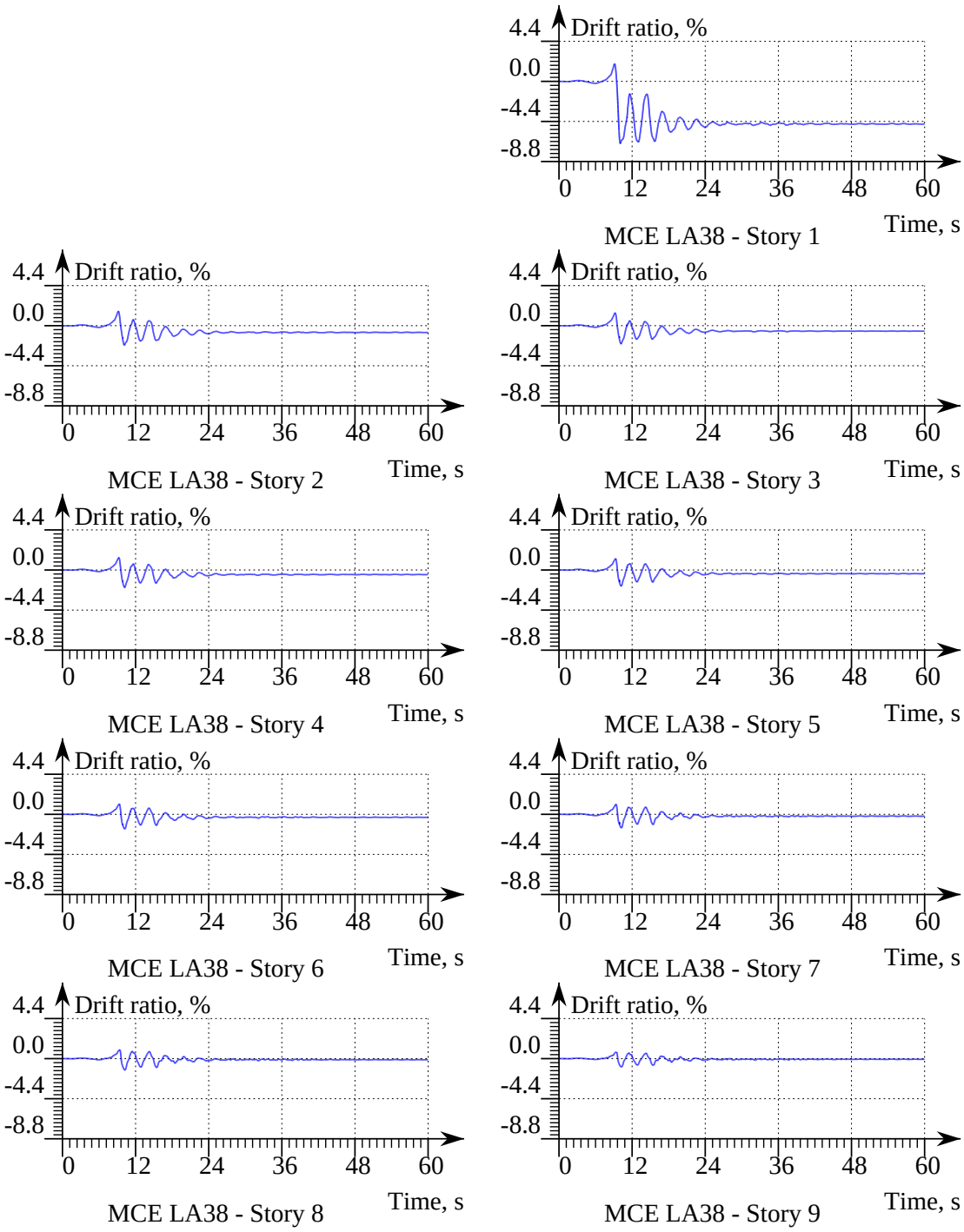

Figure A.18: Story Drift of the Benchmark Frame under MCE LA38.

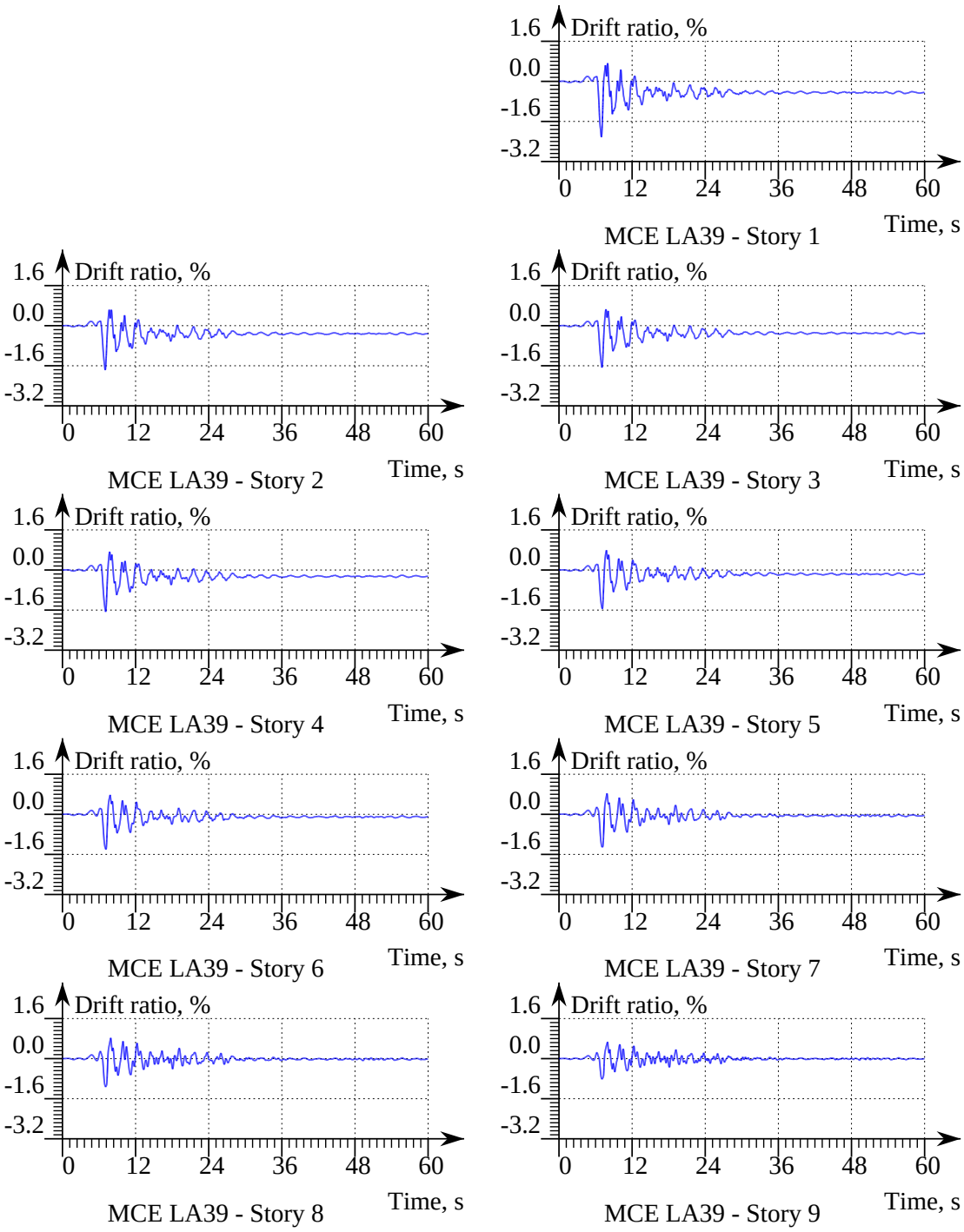

Figure A.19: Story Drift of the Benchmark Frame under MCE LA39.

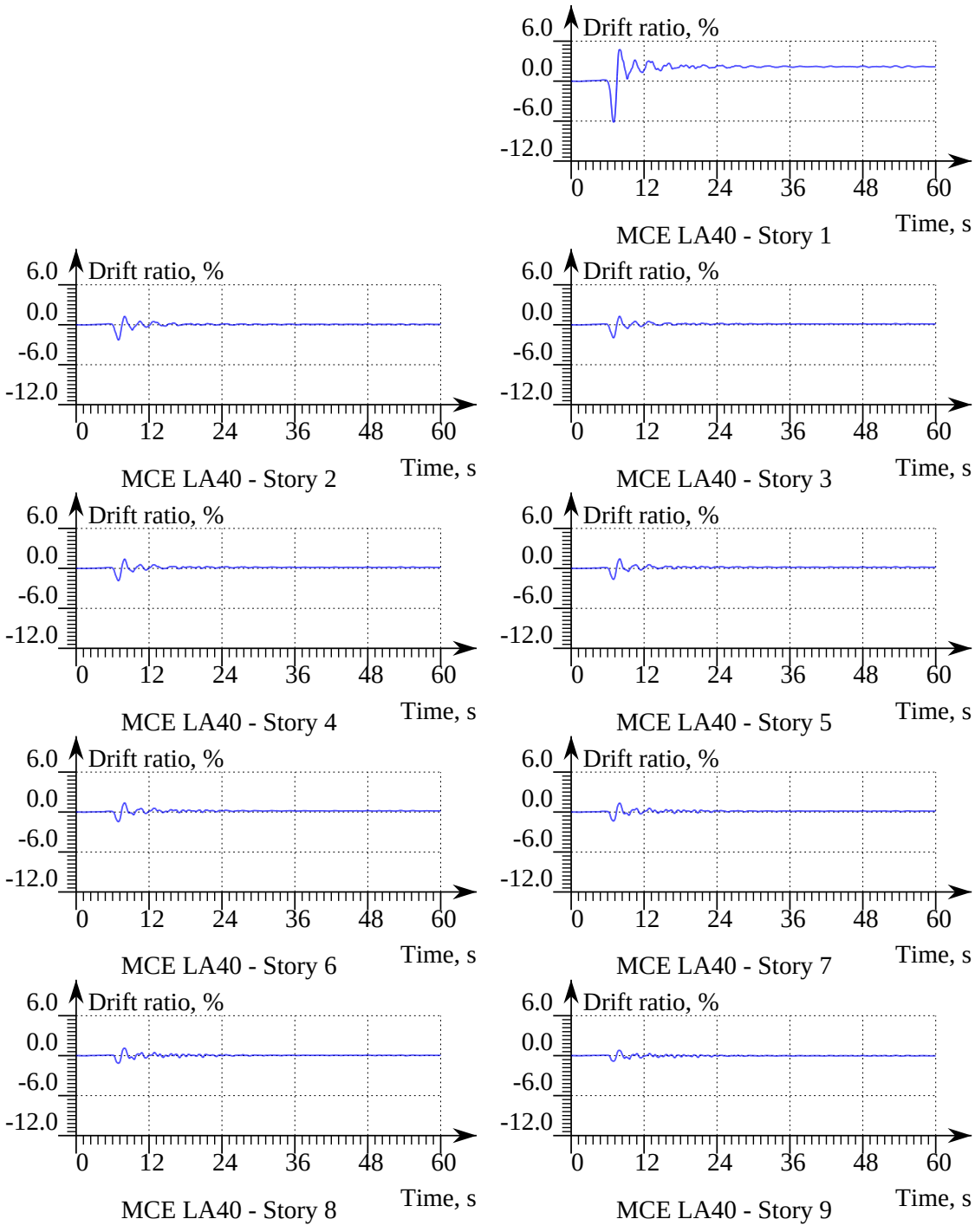

Figure A.20: Story Drift of the Benchmark Frame under MCE LA40.

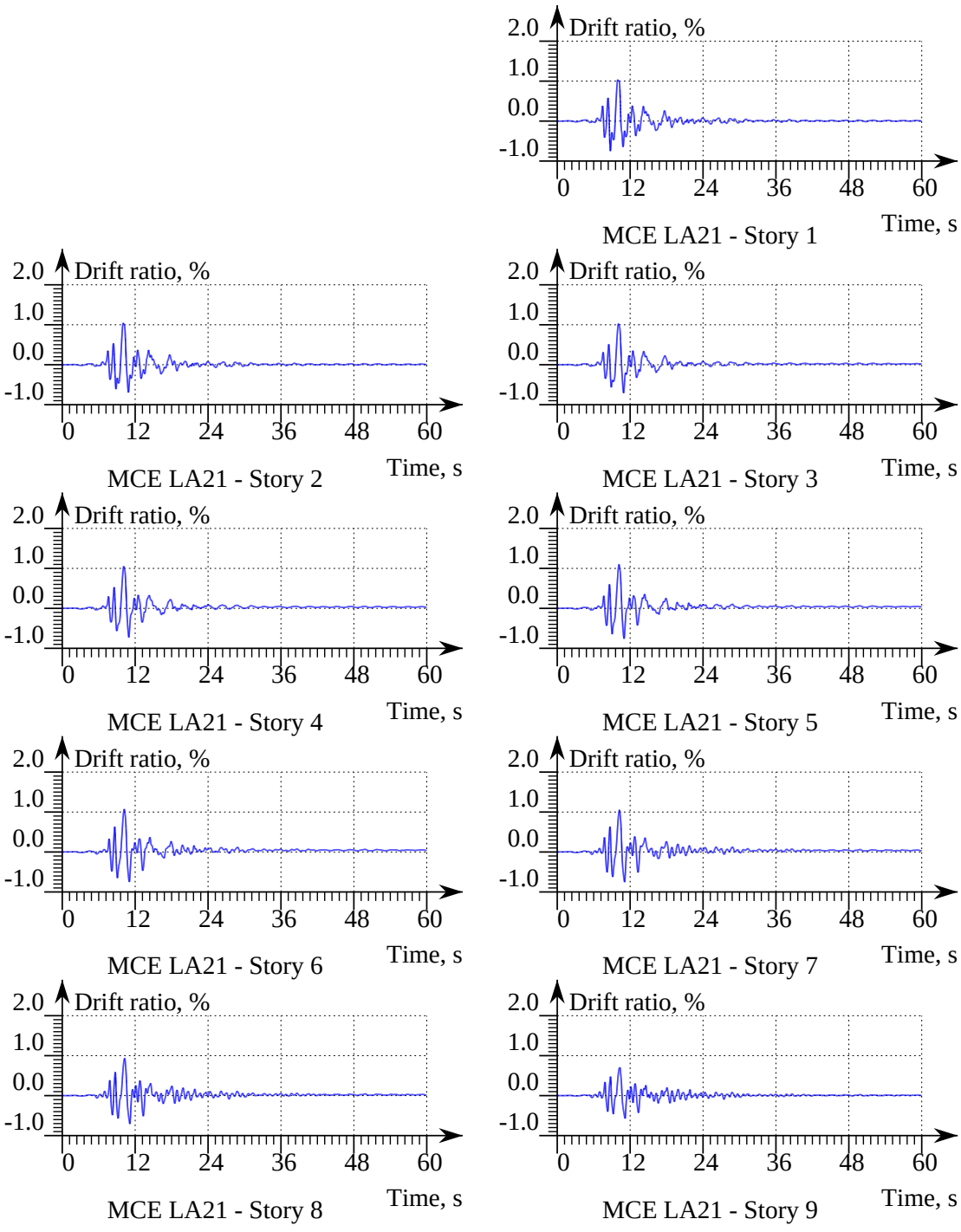

Figure A.21: Story Drift of the Optimal Frame under MCE LA21.

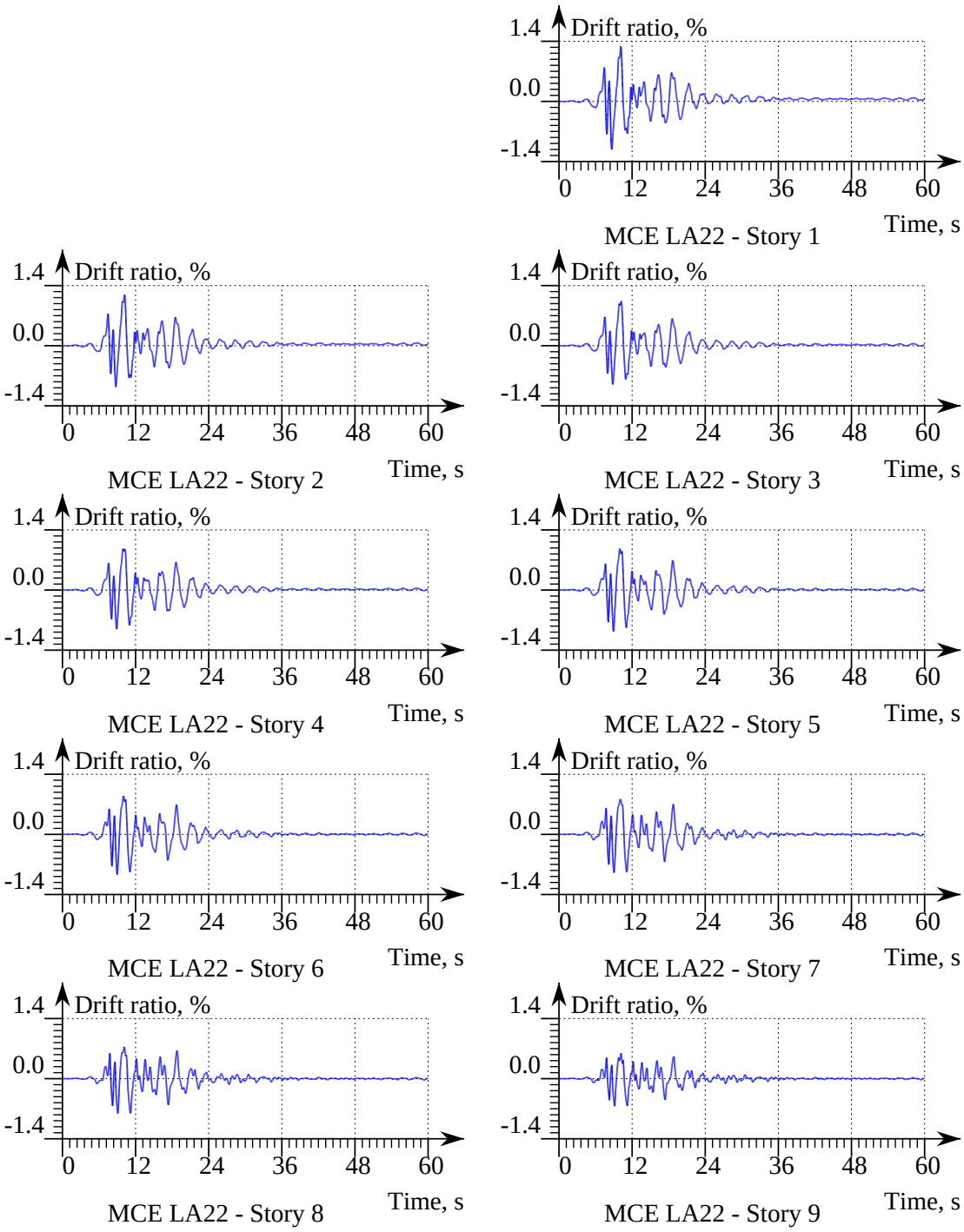

Figure A.22: Story Drift of the Optimal Frame under MCE LA22.

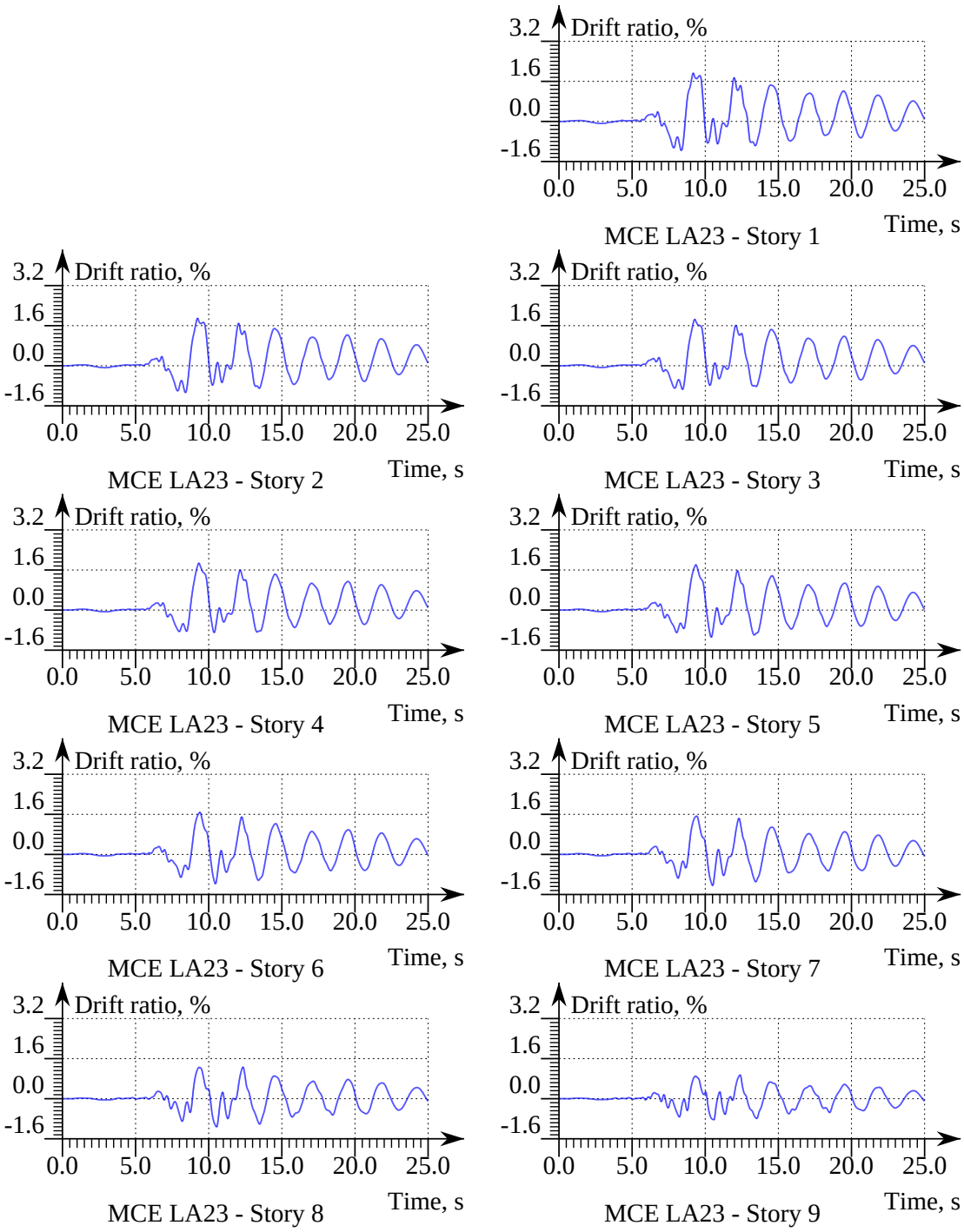

Figure A.23: Story Drift of the Optimal Frame under MCE LA23.

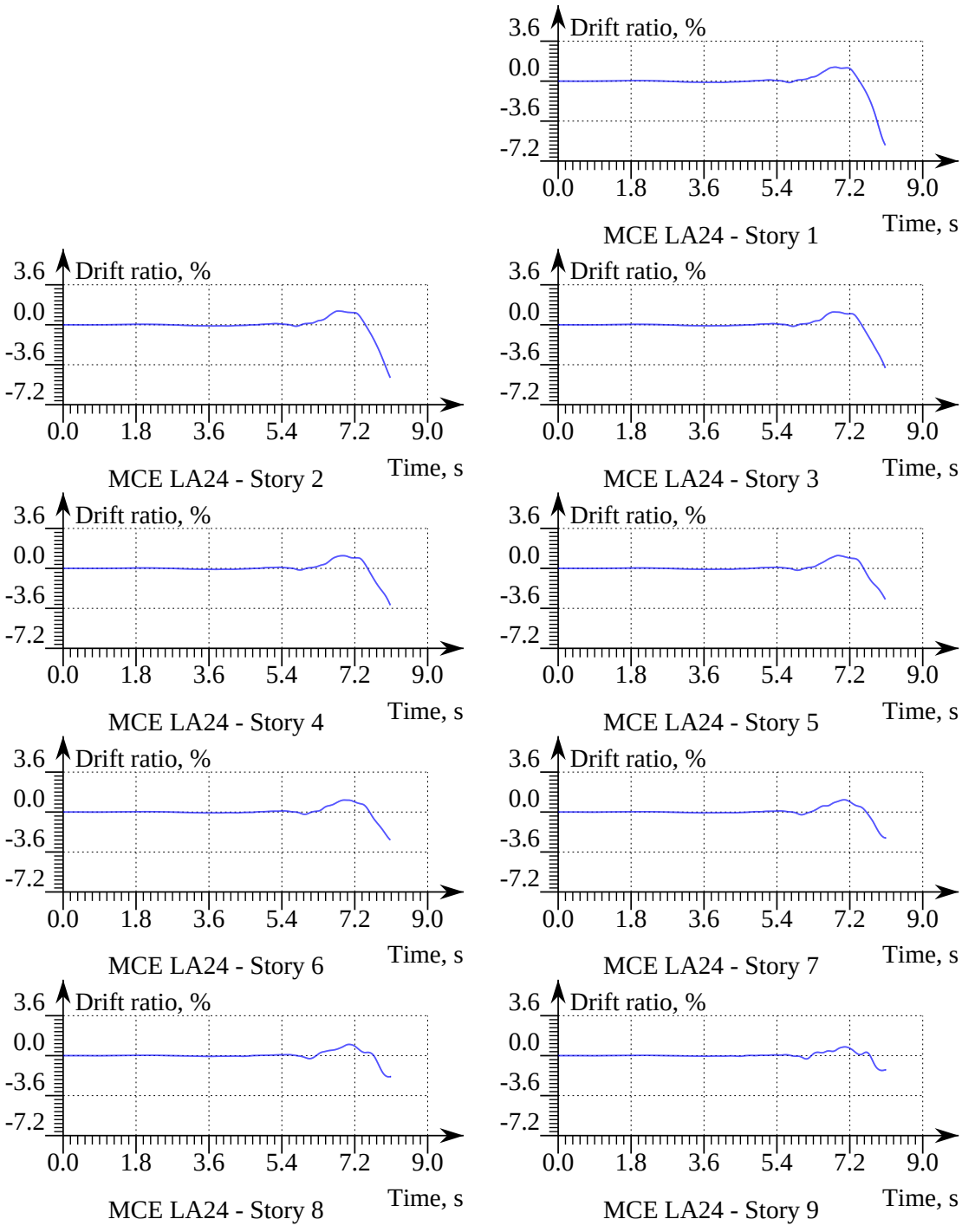

Figure A.24: Story Drift of the Optimal Frame under MCE LA24.

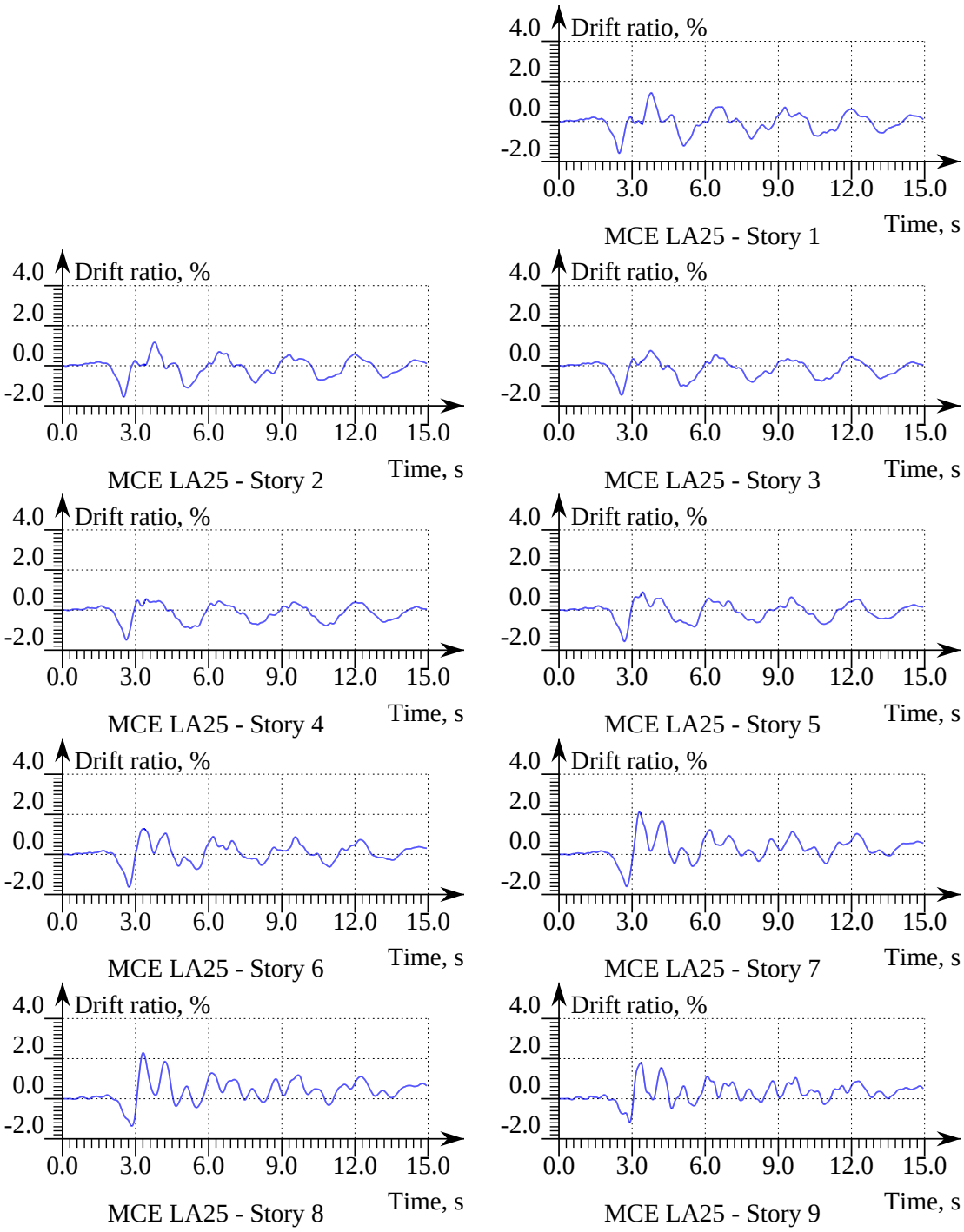

Figure A.25: Story Drift of the Optimal Frame under MCE LA25.

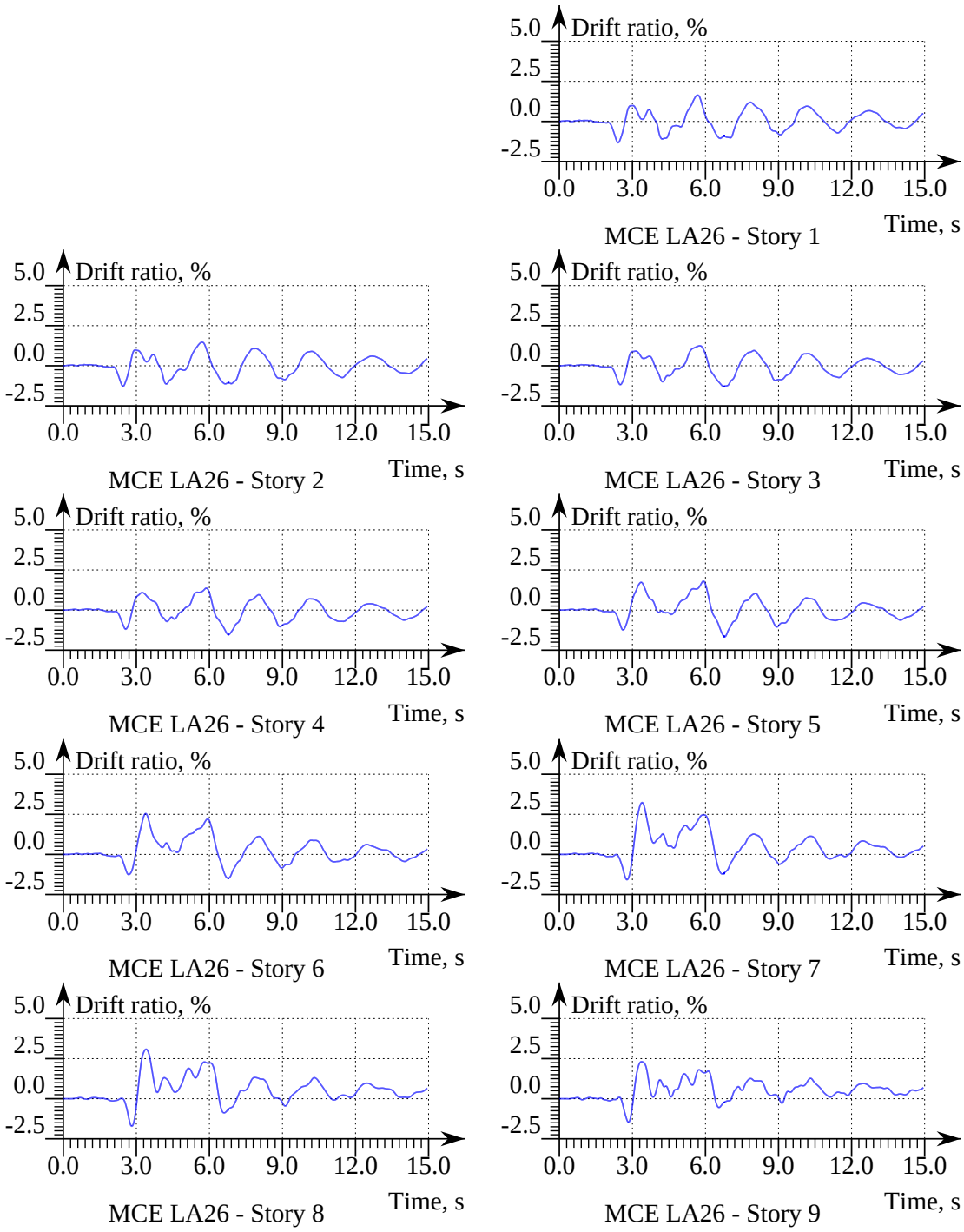

Figure A.26: Story Drift of the Optimal Frame under MCE LA26.

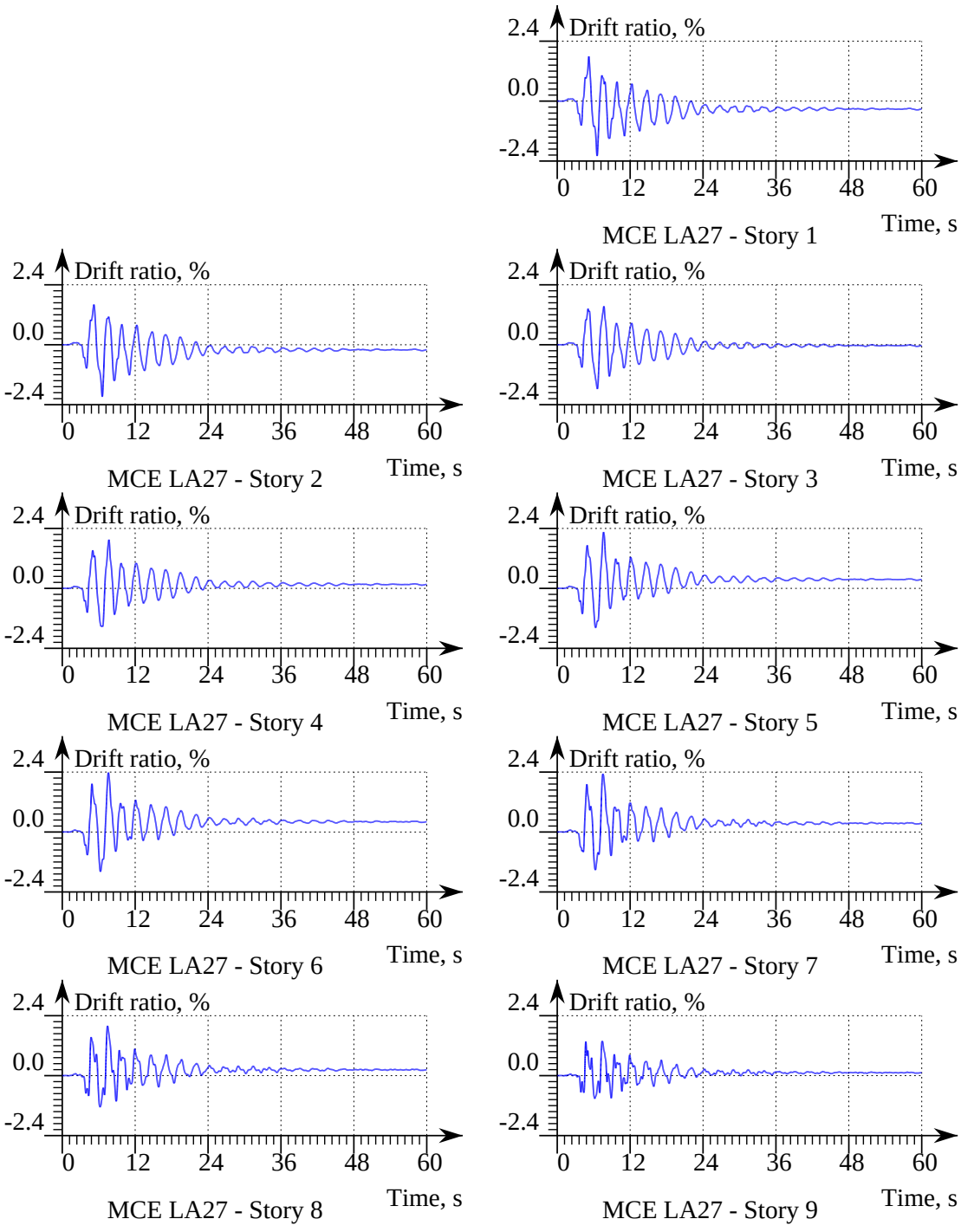

Figure A.27: Story Drift of the Optimal Frame under MCE LA27.

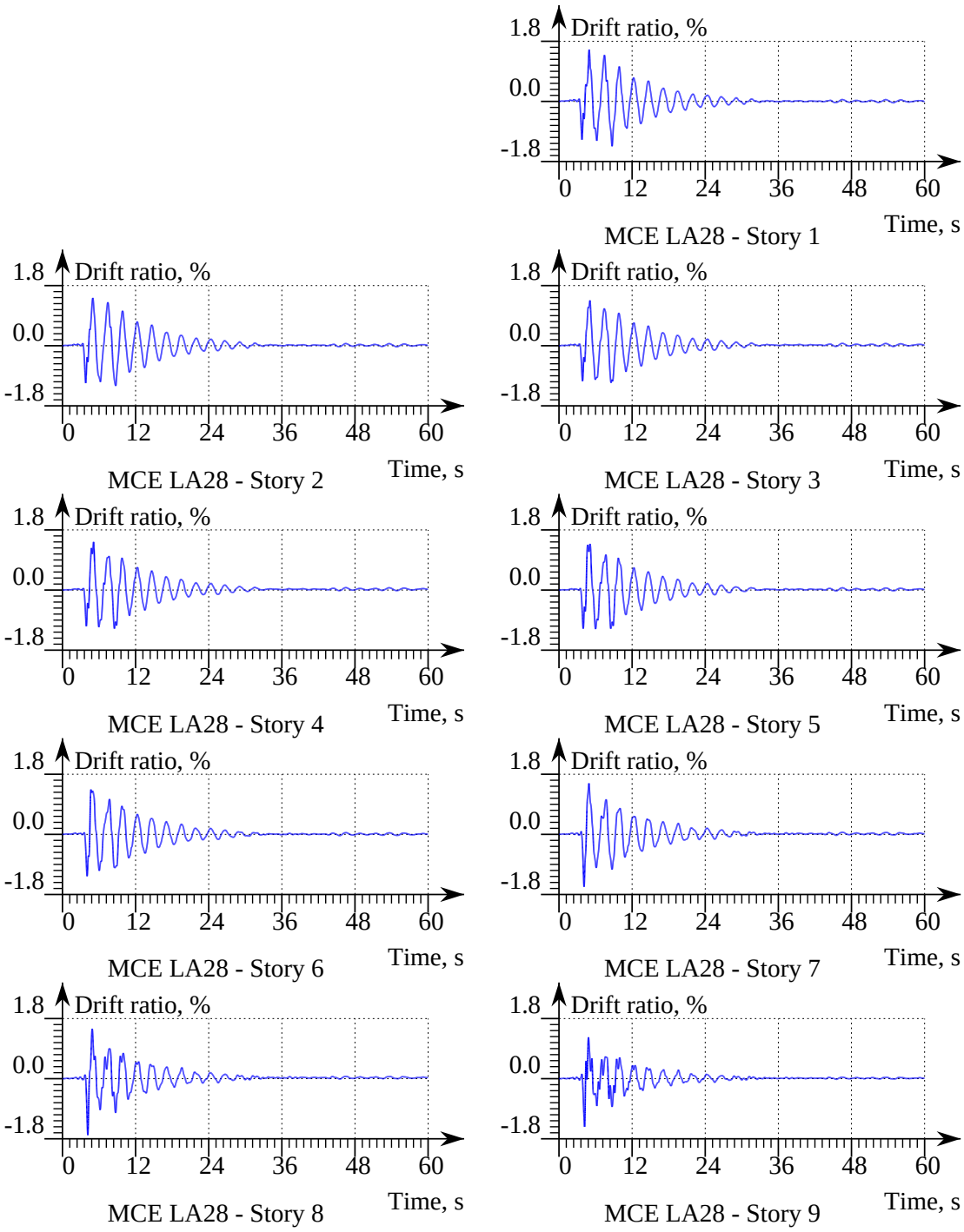

Figure A.28: Story Drift of the Optimal Frame under MCE LA28.

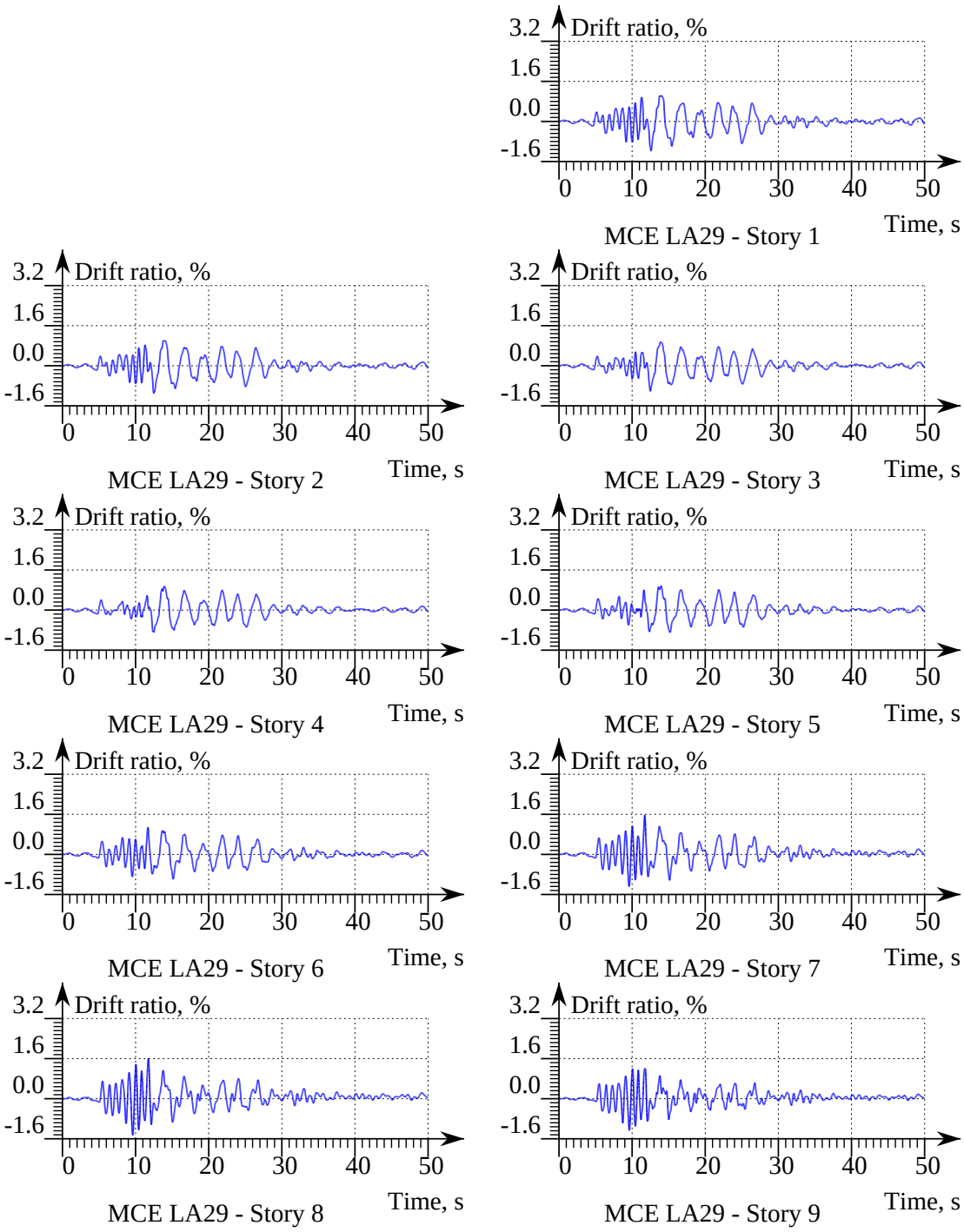

Figure A.29: Story Drift of the Optimal Frame under MCE LA29.

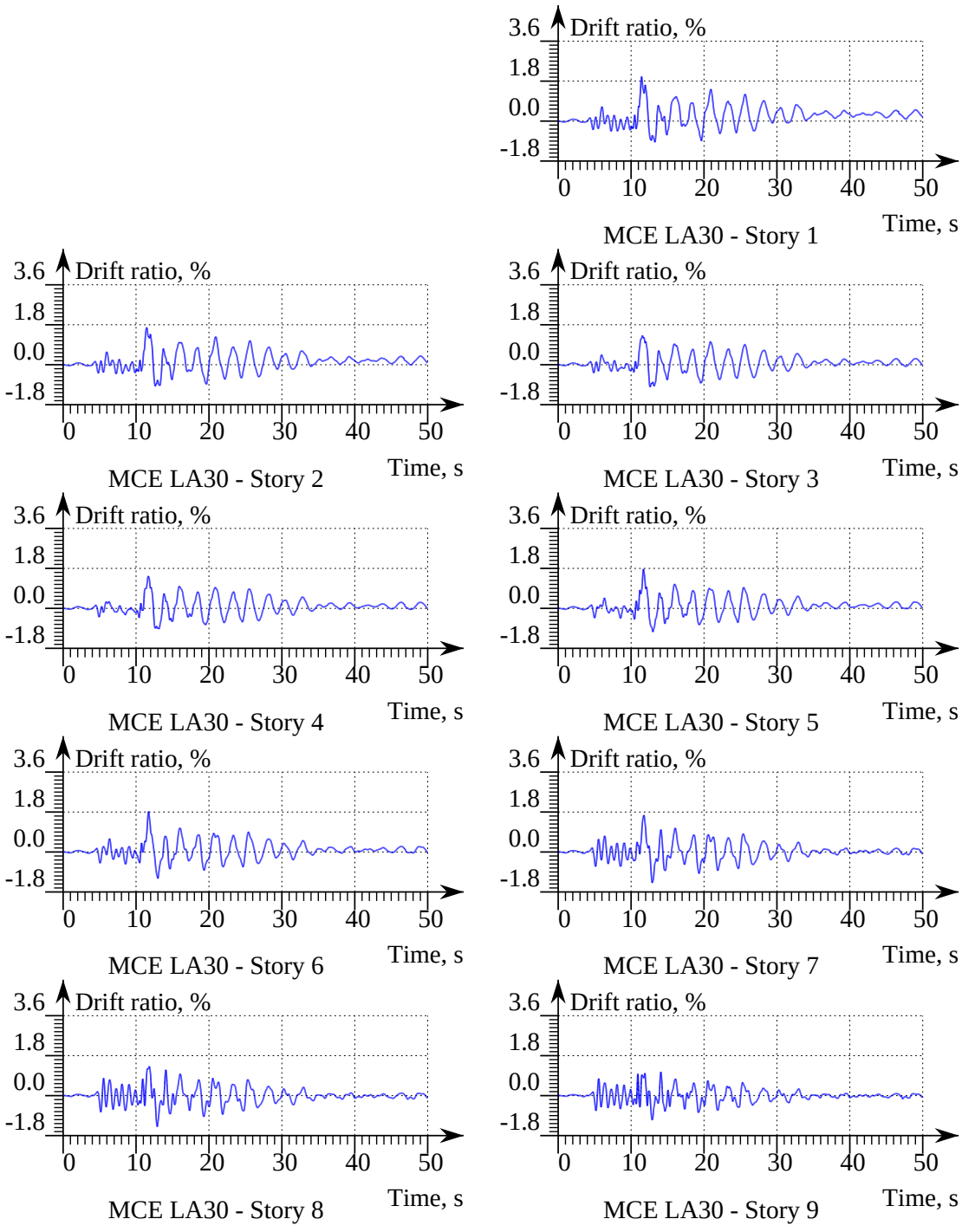

Figure A.30: Story Drift of the Optimal Frame under MCE LA30.

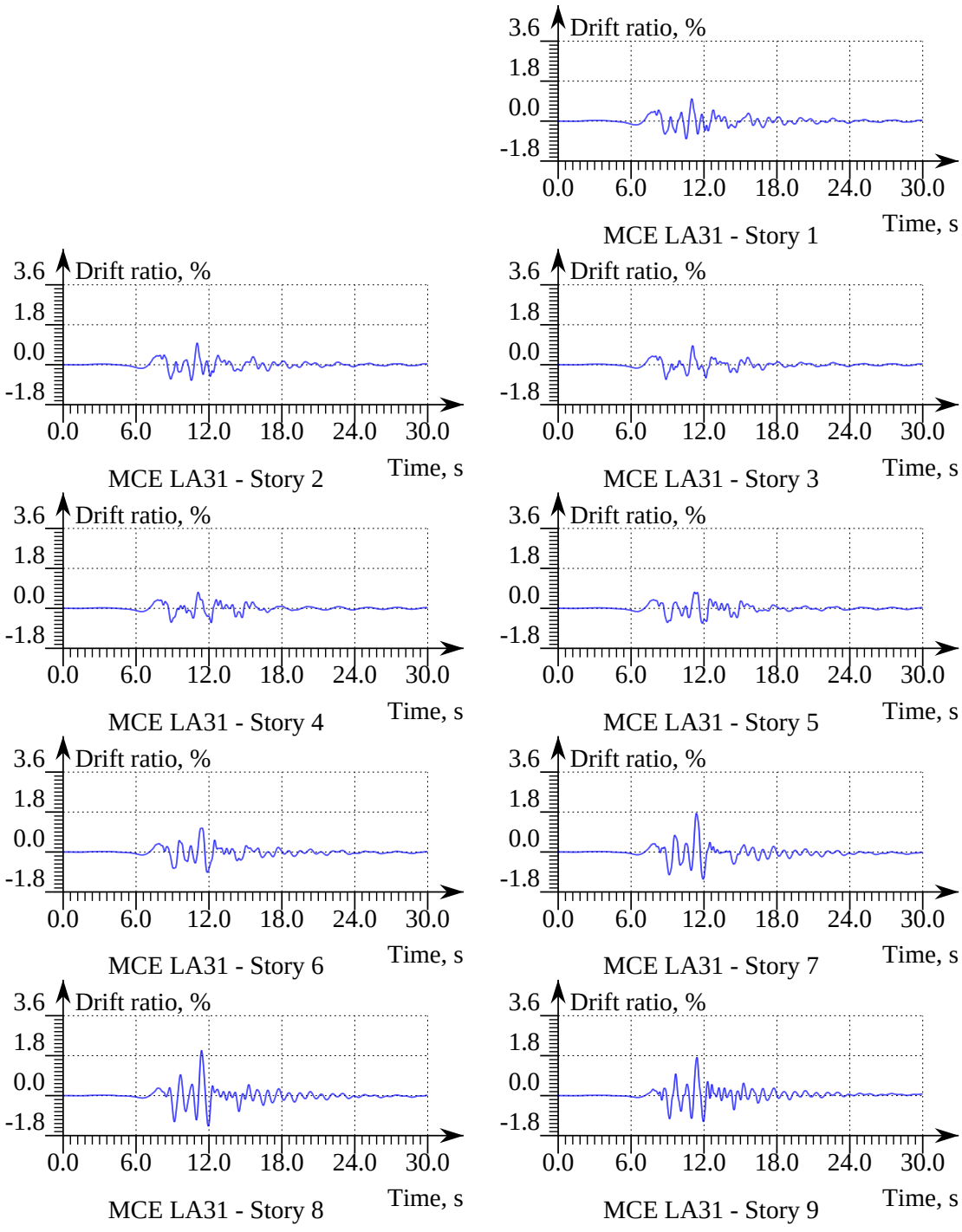

Figure A.31: Story Drift of the Optimal Frame under MCE LA31.

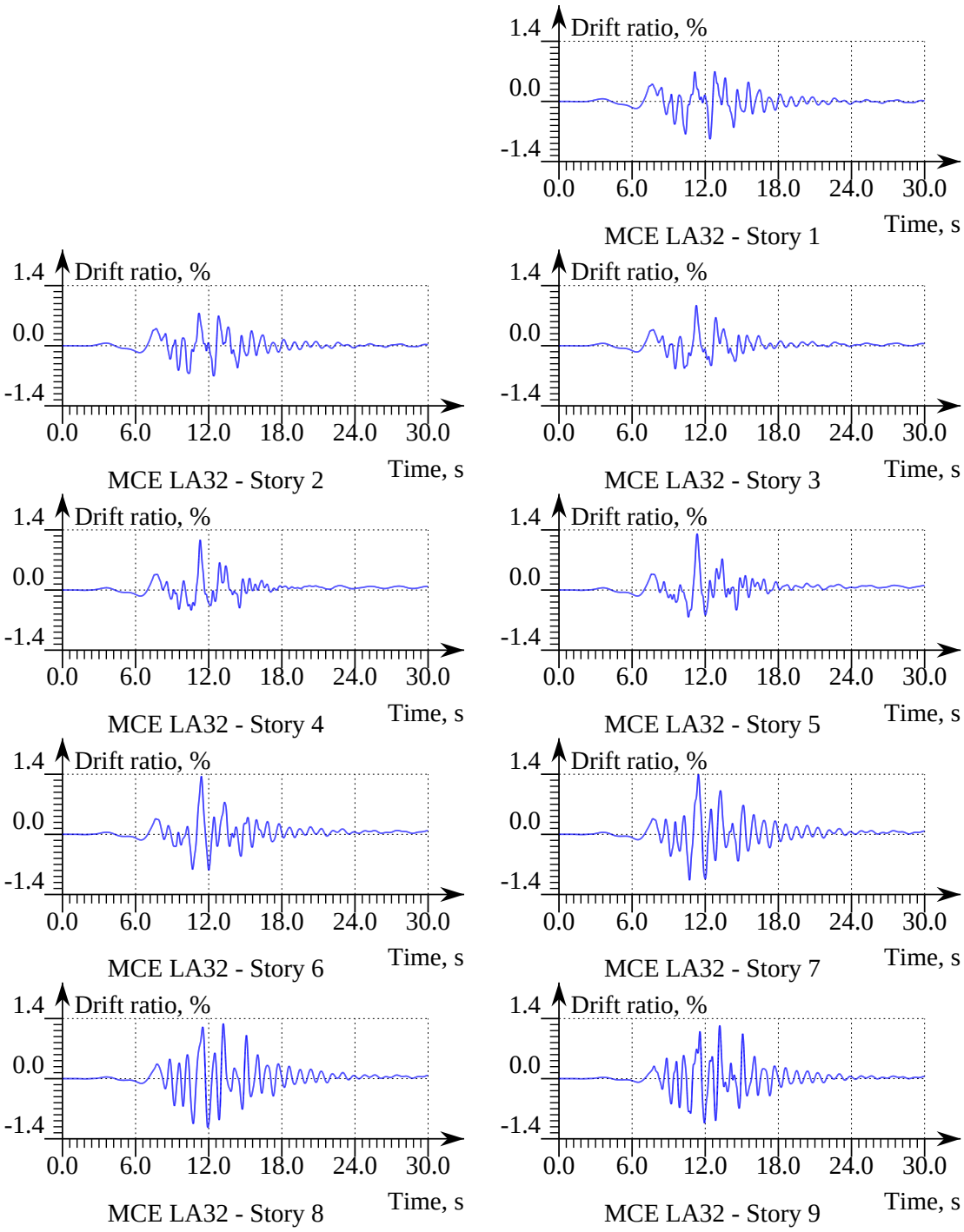

Figure A.32: Story Drift of the Optimal Frame under MCE LA32.

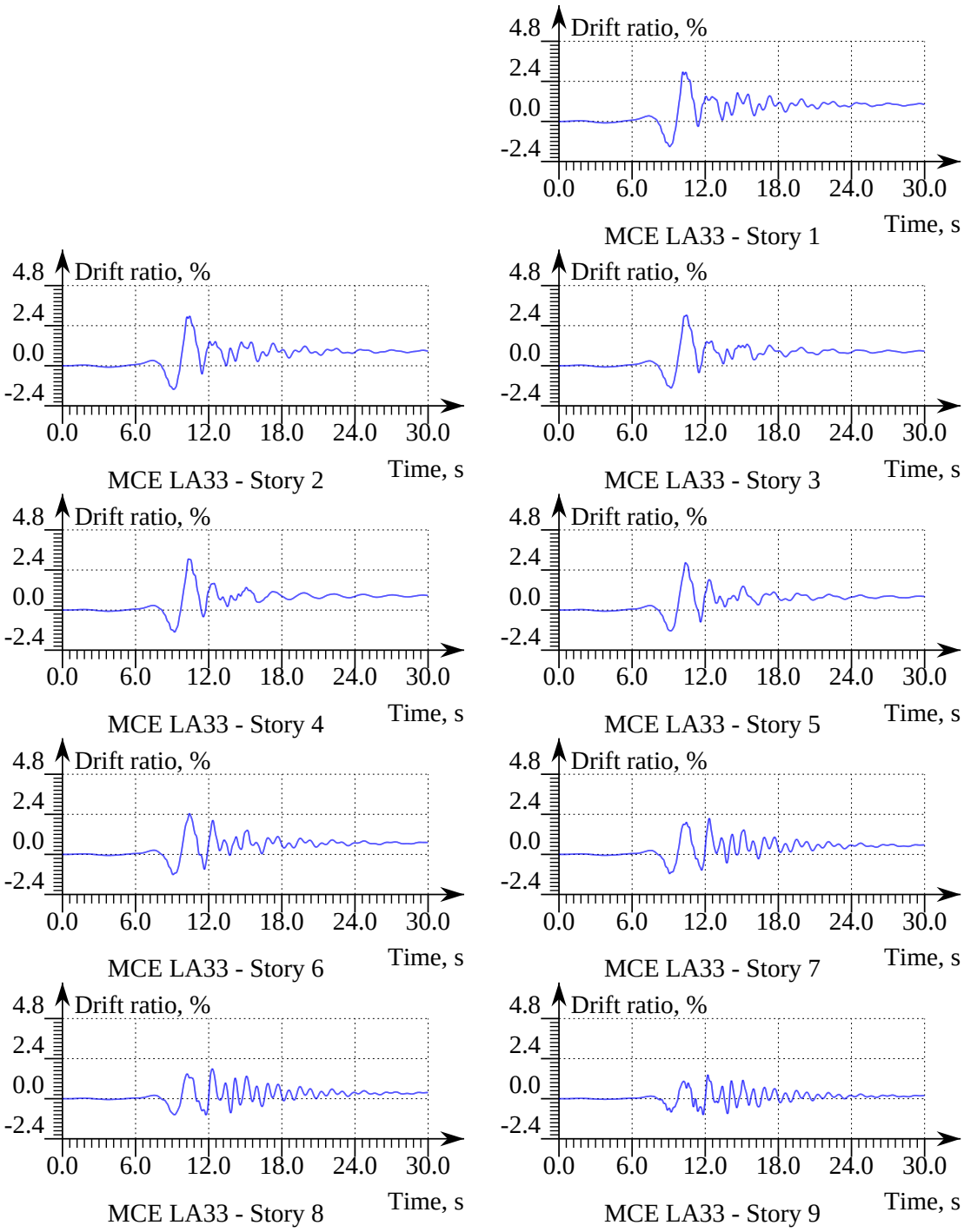

Figure A.33: Story Drift of the Optimal Frame under MCE LA33.

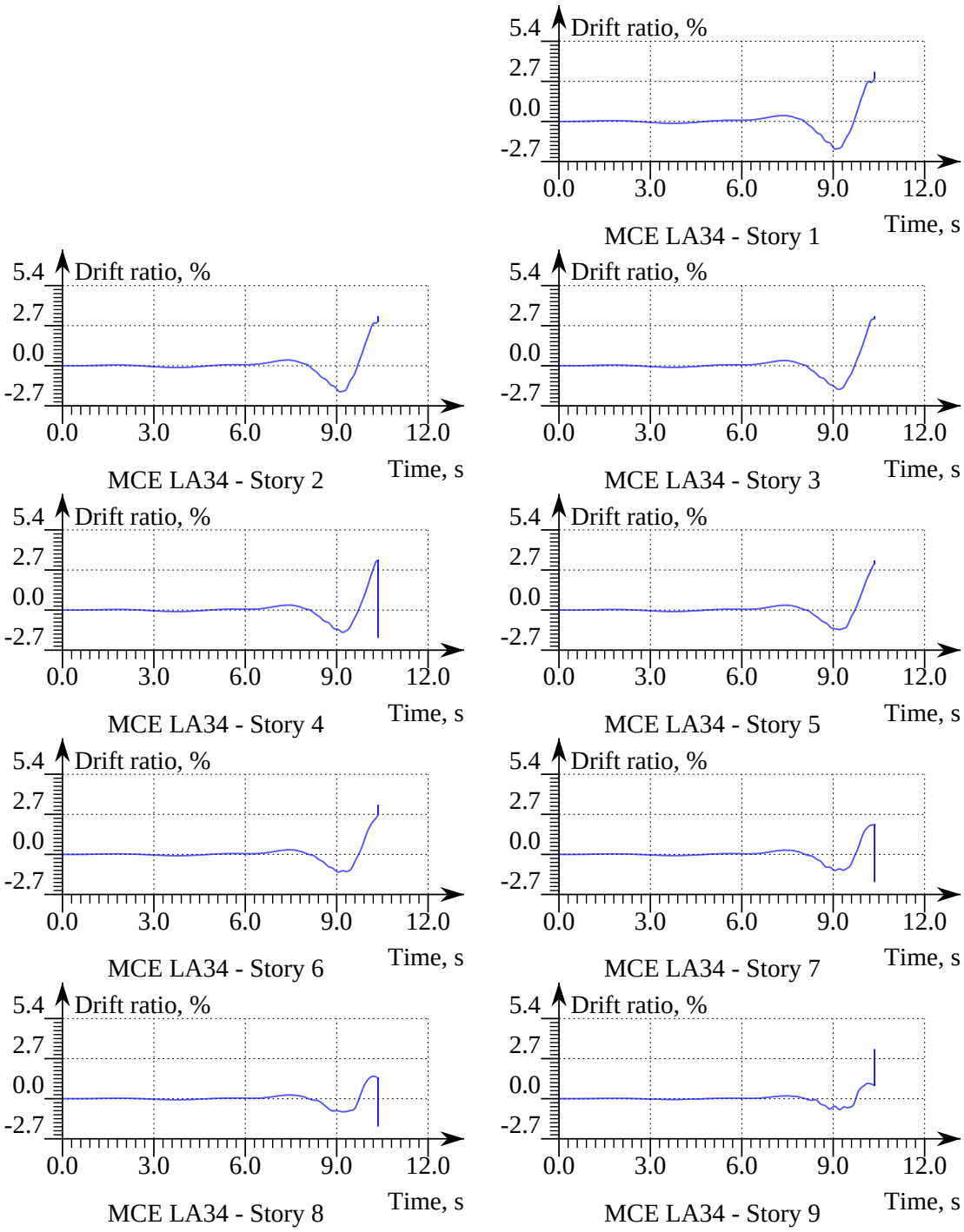

Figure A.34: Story Drift of the Optimal Frame under MCE LA34.

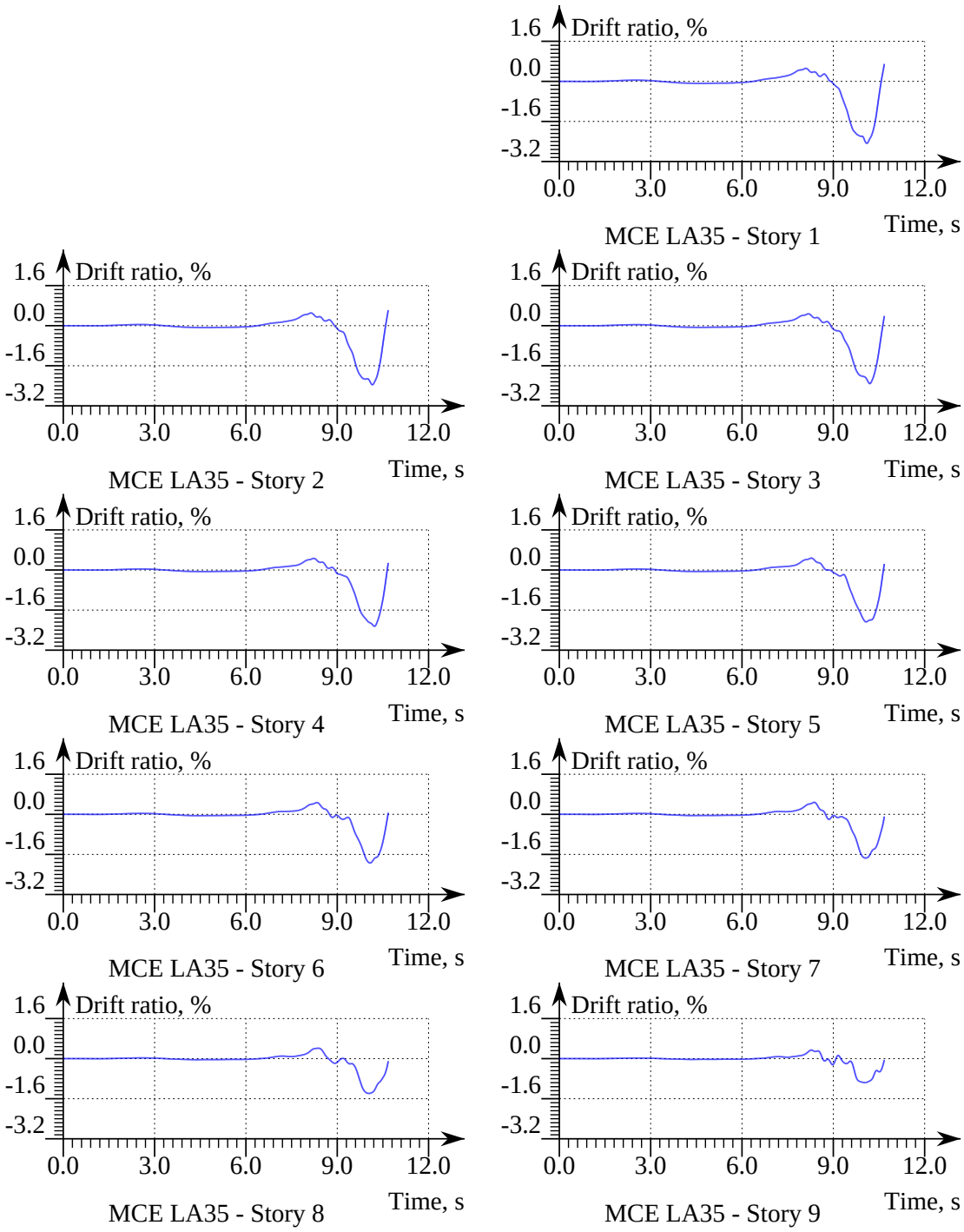

Figure A.35: Story Drift of the Optimal Frame under MCE LA35.

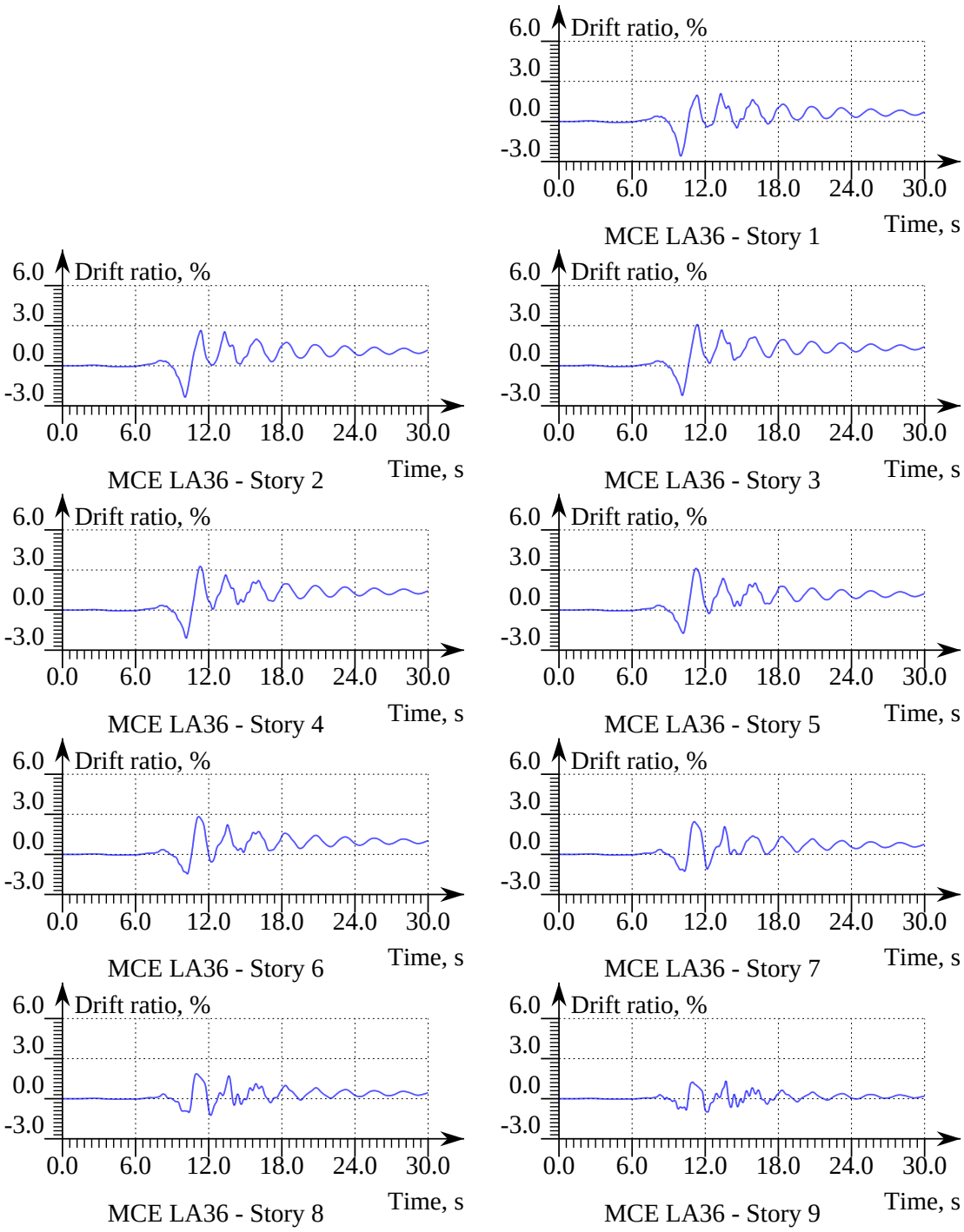

Figure A.36: Story Drift of the Optimal Frame under MCE LA36.

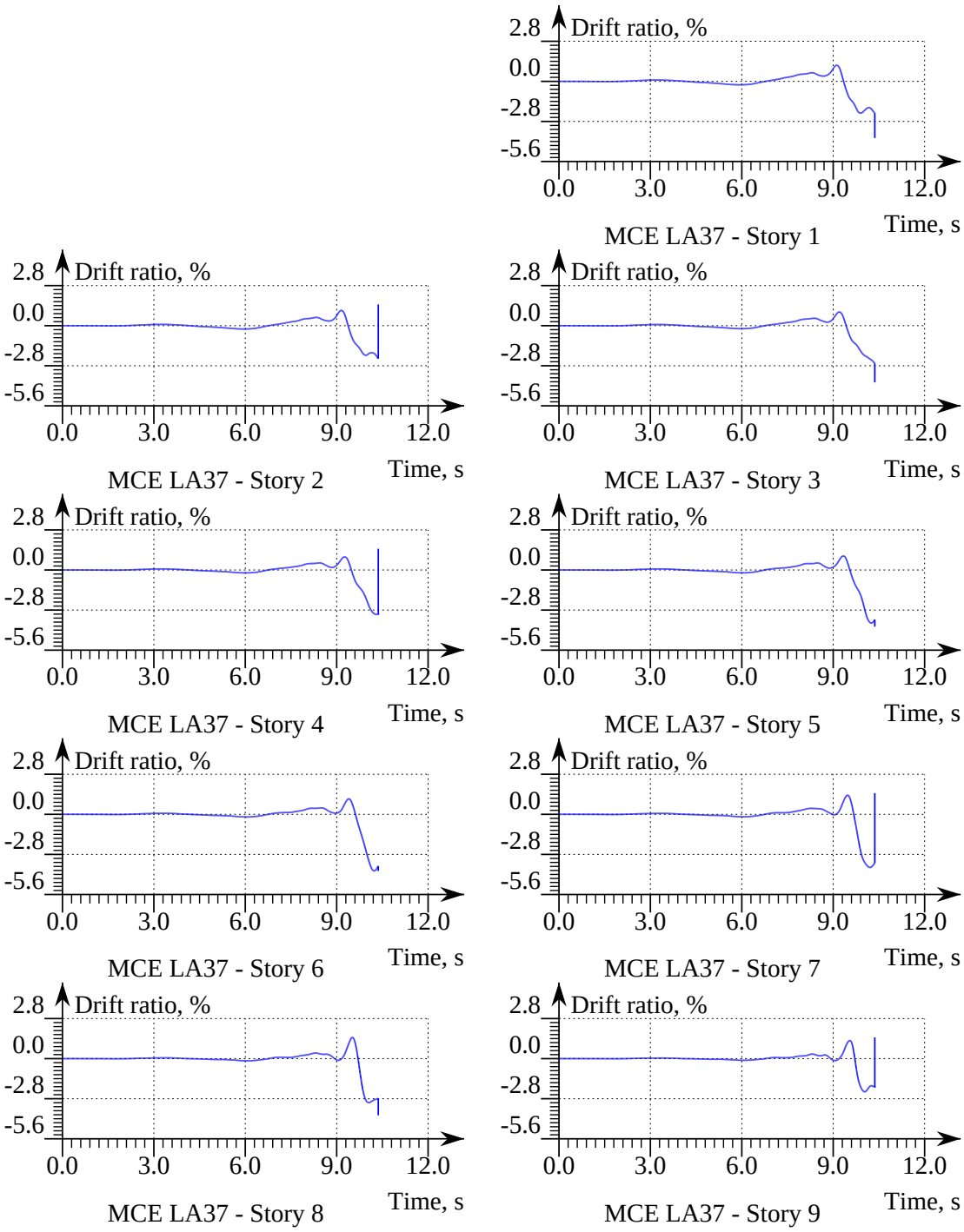

Figure A.37: Story Drift of the Optimal Frame under MCE LA37.

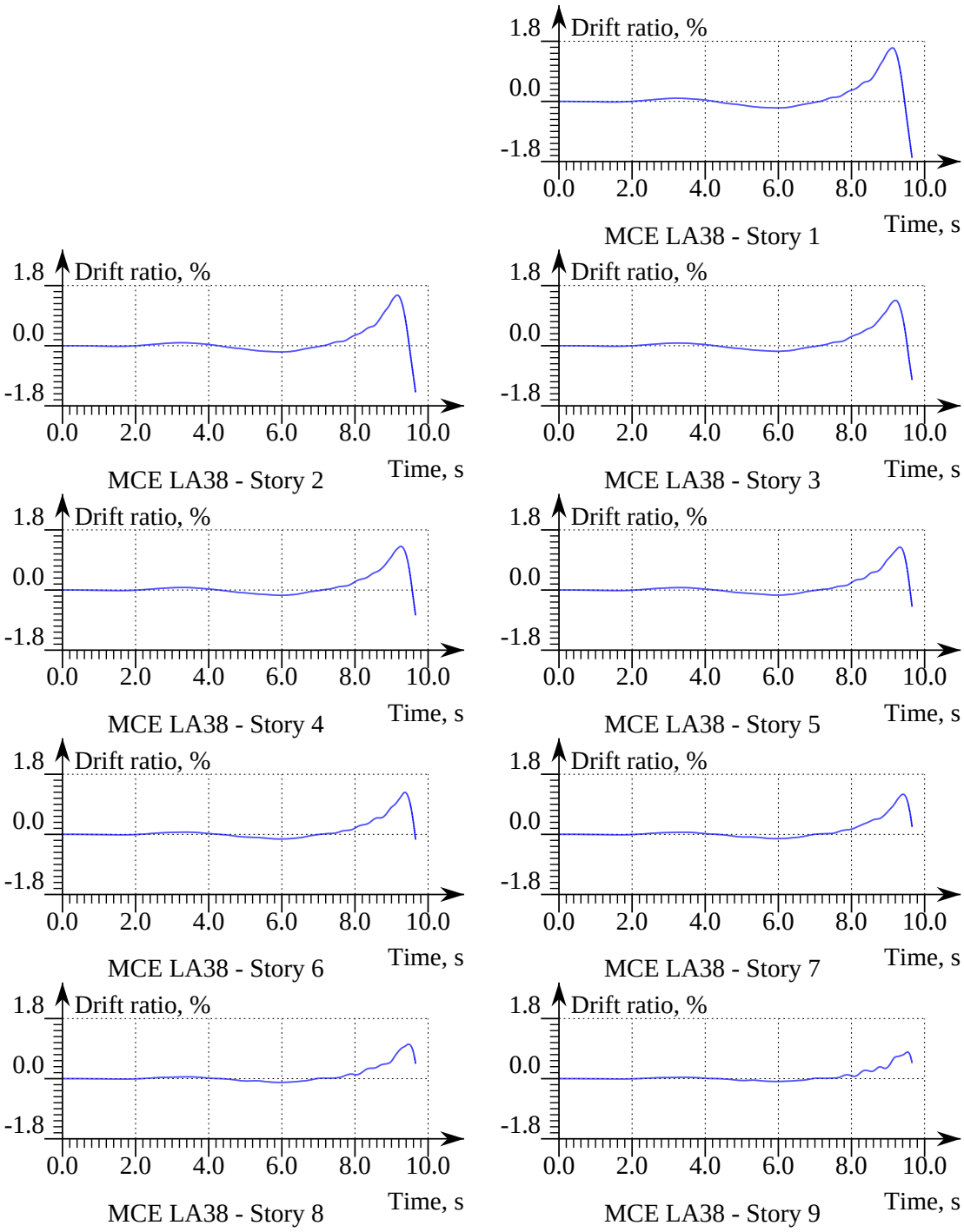

Figure A.38: Story Drift of the Optimal Frame under MCE LA38.

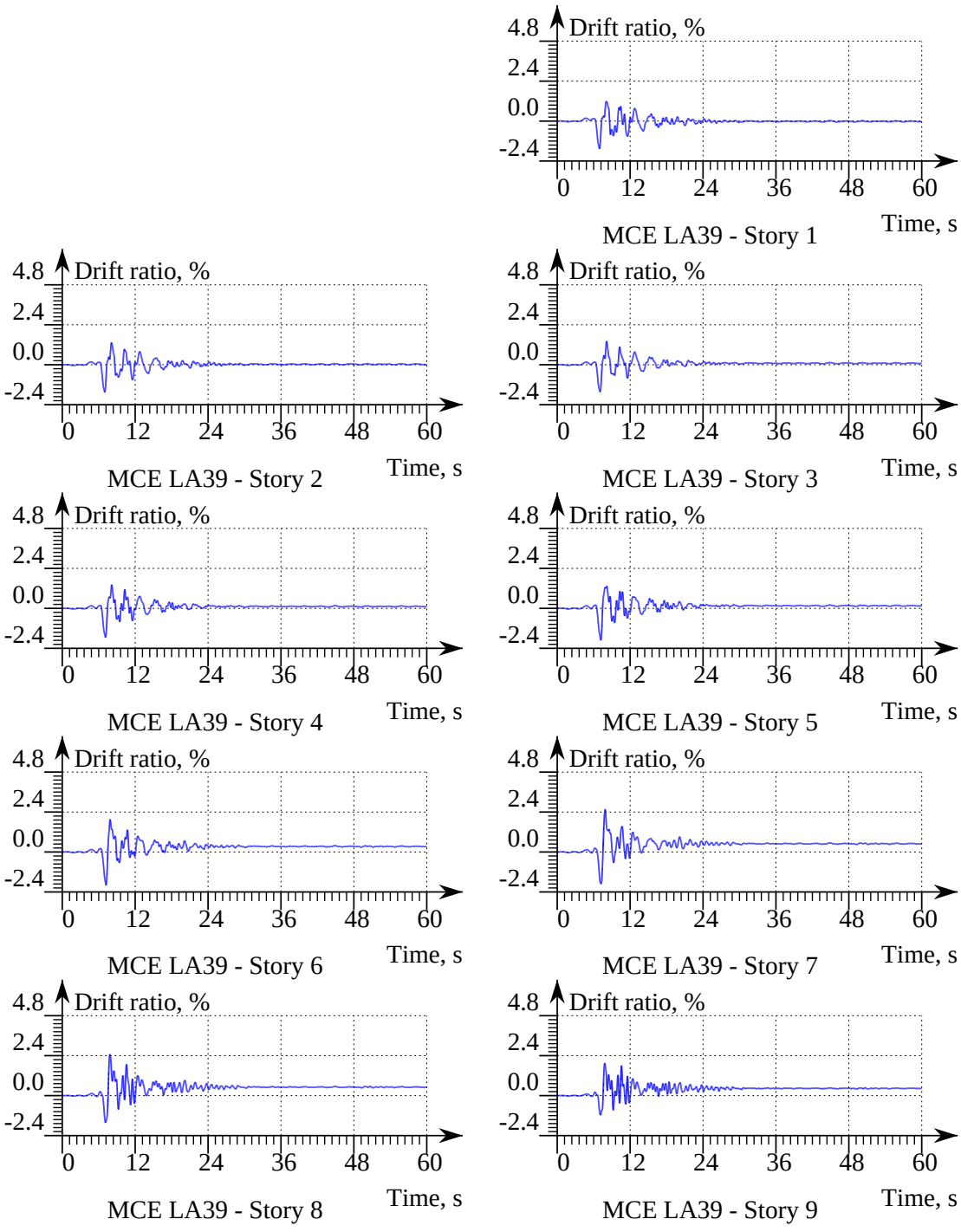

Figure A.39: Story Drift of the Optimal Frame under MCE LA39.

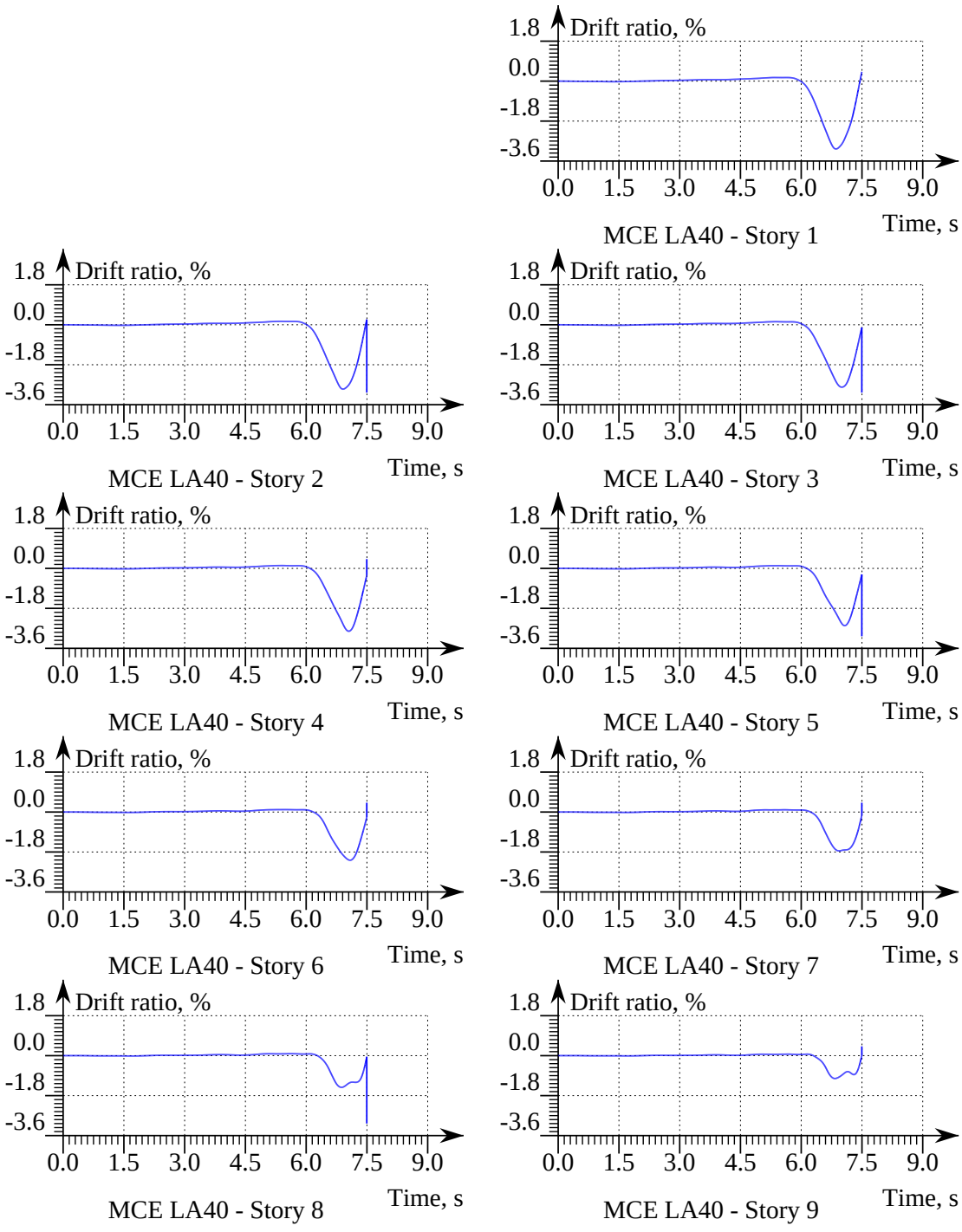

Figure A.40: Story Drift of the Optimal Frame under MCE LA40.

Table A.1: Summary of frame maximal story drifts–Scale = 1.0

Record	Benchmark frame			Optimized frame		
	Max drift, %	Story	FAIL/OK	Max drift, %	Story	FAIL/OK
MCE LA21	1.3	1	OK	1.1	5	OK
MCE LA22	1.3	1	OK	1.3	1	OK
MCE LA23	2.4	1	OK	1.9	1	OK
MCE LA24	22.0	1	FAIL	5.8	1	FAIL
MCE LA25	2.0	1	OK	2.3	8	OK
MCE LA26	1.9	4	OK	3.2	7	OK
MCE LA27	2.1	1	OK	2.4	6	OK
MCE LA28	1.4	1	OK	1.7	8	OK
MCE LA29	1.2	1	OK	1.6	8	OK
MCE LA30	1.8	1	OK	2.0	1	OK
MCE LA31	1.1	7	OK	2.0	8	OK
MCE LA32	1.3	7	OK	1.4	7	OK
MCE LA33	5.2	1	FAIL	3.1	4	OK
MCE LA34	2.2	1	OK	3.3	4	FAIL
MCE LA35	6.2	1	FAIL	2.5	1	FAIL
MCE LA36	4.6	1	FAIL	3.3	4	OK
MCE LA37	6.0	1	FAIL	4.0	6	FAIL
MCE LA38	6.8	1	FAIL	1.7	1	FAIL
MCE LA39	2.2	1	OK	2.6	7	OK
MCE LA40	6.2	1	FAIL	3.1	1	FAIL

Table A.2: Summary of frame maximal story drifts–Scale = 1.1

Record	Benchmark frame			Optimized frame		
	Max drift, %	Story	FAIL/OK	Max drift, %	Story	FAIL/OK
MCE LA21	3.1	8	OK	2.8	8	OK
MCE LA22	3.1	8	FAIL	3.0	8	FAIL
MCE LA23	2.3	1	FAIL	3.2	6	FAIL
MCE LA24	1.8	1	FAIL	11.7	1	FAIL
MCE LA25	2.8	8	OK	2.5	8	OK
MCE LA26	3.8	7	OK	3.5	7	OK
MCE LA27	2.9	7	OK	2.5	6	OK
MCE LA28	2.0	8	OK	1.8	8	OK
MCE LA29	2.0	8	FAIL	1.7	8	OK
MCE LA30	2.4	1	OK	2.3	1	OK
MCE LA31	2.6	8	OK	2.2	8	OK
MCE LA32	1.8	8	OK	1.6	7	OK
MCE LA33	3.6	1	FAIL	3.3	4	OK
MCE LA34	2.0	1	FAIL	3.6	4	OK
MCE LA35	3.5	1	FAIL	3.0	1	FAIL
MCE LA36	3.9	1	FAIL	3.1	1	FAIL
MCE LA37	2.0	1	FAIL	2.0	1	FAIL
MCE LA38	2.0	1	FAIL	5.4	5	FAIL
MCE LA39	2.9	8	OK	2.7	7	OK
MCE LA40	4.8	1	FAIL	3.6	1	FAIL

Table A.3: Summary of frame maximal story drifts–Scale = 1.2

Record	Benchmark frame			Optimized frame		
	Max drift, %	Story	FAIL/OK	Max drift, %	Story	FAIL/OK
MCE LA21	1.6	1	OK	1.3	5	OK
MCE LA22	3.4	1	FAIL	1.4	1	OK
MCE LA23	3.1	1	OK	2.4	1	OK
MCE LA24	29.5	1	FAIL	21.9	1	FAIL
MCE LA25	2.4	1	FAIL	2.0	1	OK
MCE LA26	2.1	4	OK	1.8	5	OK
MCE LA27	3.4	1	FAIL	2.3	1	OK
MCE LA28	2.2	1	FAIL	1.4	1	OK
MCE LA29	1.4	1	OK	1.1	1	OK
MCE LA30	4.3	1	FAIL	1.8	1	OK
MCE LA31	1.2	7	OK	1.0	7	OK
MCE LA32	1.9	7	FAIL	1.3	7	OK
MCE LA33	2.4	1	FAIL	4.8	1	FAIL
MCE LA34	2.2	1	FAIL	4.8	1	FAIL
MCE LA35	1.6	1	FAIL	4.5	1	FAIL
MCE LA36	2.4	1	FAIL	3.5	1	OK
MCE LA37	1.8	8	FAIL	5.9	1	FAIL
MCE LA38	2.7	1	FAIL	9.0	1	FAIL
MCE LA39	3.0	8	OK	2.2	1	OK
MCE LA40	1.7	1	FAIL	6.2	1	FAIL

Table A.4: Summary of frame maximal story drifts–Scale = 1.4

Record	Benchmark frame			Optimized frame		
	Max drift, %	Story	FAIL/OK	Max drift, %	Story	FAIL/OK
MCE LA21	1.9	8	FAIL	3.0	8	OK
MCE LA22	3.6	8	FAIL	3.2	8	FAIL
MCE LA23	2.0	1	FAIL	3.8	6	FAIL
MCE LA24	2.9	1	FAIL	10.4	1	FAIL
MCE LA25	3.1	1	OK	2.7	8	OK
MCE LA26	4.1	7	OK	3.9	7	OK
MCE LA27	2.8	7	FAIL	2.7	7	OK
MCE LA28	2.2	7	OK	2.1	8	OK
MCE LA29	2.3	7	FAIL	2.0	8	FAIL
MCE LA30	1.3	8	FAIL	2.5	1	FAIL
MCE LA31	2.9	8	OK	2.5	8	OK
MCE LA32	2.1	7	OK	2.0	7	OK
MCE LA33	2.5	1	FAIL	2.5	1	FAIL
MCE LA34	4.4	1	FAIL	3.4	1	FAIL
MCE LA35	1.9	1	FAIL	3.9	1	FAIL
MCE LA36	5.9	1	FAIL	4.6	1	FAIL
MCE LA37	4.8	1	FAIL	2.7	1	FAIL
MCE LA38	3.6	1	FAIL	2.4	1	FAIL
MCE LA39	1.3	1	FAIL	2.9	8	OK
MCE LA40	1.7	1	FAIL	2.8	1	FAIL

Table A.5: Summary of frame maximal story drifts–Scale = 1.5

Record	Benchmark frame			Optimized frame		
	Max drift, %	Story	FAIL/OK	Max drift, %	Story	FAIL/OK
MCE LA21	2.1	8	FAIL	1.8	7	FAIL
MCE LA22	3.7	8	FAIL	3.7	8	OK
MCE LA23	2.3	1	FAIL	2.1	1	FAIL
MCE LA24	2.8	1	FAIL	2.6	1	OK
MCE LA25	3.4	1	OK	2.8	8	OK
MCE LA26	2.7	1	FAIL	4.1	7	OK
MCE LA27	2.9	7	FAIL	2.8	7	OK
MCE LA28	1.3	1	FAIL	2.2	7	OK
MCE LA29	2.4	7	FAIL	2.2	8	OK
MCE LA30	2.2	1	FAIL	2.6	1	FAIL
MCE LA31	2.9	8	OK	2.6	8	OK
MCE LA32	2.2	7	OK	2.2	7	OK
MCE LA33	1.8	1	FAIL	2.9	1	FAIL
MCE LA34	1.8	1	FAIL	3.9	1	OK
MCE LA35	6.1	1	FAIL	1.8	1	FAIL
MCE LA36	6.7	1	FAIL	5.2	1	FAIL
MCE LA37	1.6	1	FAIL	2.3	1	FAIL
MCE LA38	2.2	1	FAIL	2.0	1	FAIL
MCE LA39	3.9	1	OK	3.1	5	OK
MCE LA40	1.7	1	FAIL	6.0	1	FAIL

Table A.6: Summary of frame maximal story drifts–Scale = 1.7

Record	Benchmark frame			Optimized frame		
	Max drift, %	Story	FAIL/OK	Max drift, %	Story	FAIL/OK
MCE LA21	2.9	8	FAIL	1.9	8	FAIL
MCE LA22	3.8	8	FAIL	3.6	8	FAIL
MCE LA23	2.6	1	FAIL	2.2	1	FAIL
MCE LA24	3.5	1	FAIL	2.9	1	FAIL
MCE LA25	4.1	1	OK	3.1	1	OK
MCE LA26	3.3	1	FAIL	1.8	1	FAIL
MCE LA27	2.2	1	FAIL	2.9	7	FAIL
MCE LA28	2.2	1	FAIL	2.4	7	OK
MCE LA29	2.5	7	OK	2.4	8	FAIL
MCE LA30	1.6	9	FAIL	3.3	1	FAIL
MCE LA31	2.9	8	OK	2.7	8	OK
MCE LA32	2.4	7	OK	2.5	7	OK
MCE LA33	1.8	1	FAIL	3.7	1	FAIL
MCE LA34	1.9	1	FAIL	4.9	1	FAIL
MCE LA35	7.6	1	FAIL	6.0	1	FAIL
MCE LA36	1.9	1	FAIL	6.4	1	FAIL
MCE LA37	1.5	1	FAIL	1.8	1	FAIL
MCE LA38	5.3	1	FAIL	3.9	1	FAIL
MCE LA39	1.6	1	FAIL	3.5	1	OK
MCE LA40	1.3	1	FAIL	1.9	1	FAIL

Table A.7: Summary of frame maximal story drifts–Scale = 2.0

Record	Benchmark frame			Optimized frame		
	Max drift, %	Story	FAIL/OK	Max drift, %	Story	FAIL/OK
MCE LA21	3.0	8	OK	3.0	8	OK
MCE LA22	4.0	8	FAIL	3.9	8	FAIL
MCE LA23	3.1	1	FAIL	2.5	1	FAIL
MCE LA24	1.4	1	FAIL	4.1	1	FAIL
MCE LA25	5.1	1	FAIL	3.9	1	FAIL
MCE LA26	4.1	1	FAIL	1.7	1	FAIL
MCE LA27	1.5	1	FAIL	2.3	1	FAIL
MCE LA28	1.5	1	FAIL	2.6	7	OK
MCE LA29	2.7	8	FAIL	2.6	8	FAIL
MCE LA30	1.9	9	FAIL	2.0	9	FAIL
MCE LA31	2.8	8	OK	2.6	8	OK
MCE LA32	2.7	7	OK	2.8	7	OK
MCE LA33	2.0	1	FAIL	1.8	1	FAIL
MCE LA34	2.3	1	FAIL	1.9	1	FAIL
MCE LA35	9.8	1	FAIL	2.1	1	FAIL
MCE LA36	2.2	1	FAIL	2.0	1	FAIL
MCE LA37	1.6	1	FAIL	1.5	1	OK
MCE LA38	7.3	1	OK	5.4	1	FAIL
MCE LA39	1.5	1	FAIL	4.6	1	FAIL
MCE LA40	1.8	1	FAIL	3.1	1	FAIL

Table A.8: Summary of frame maximal story drifts–Scale = 2.5

Record	Benchmark frame			Optimized frame		
	Max drift, %	Story	FAIL/OK	Max drift, %	Story	FAIL/OK
MCE LA21	3.4	8	FAIL	3.7	1	FAIL
MCE LA22	1.7	1	FAIL	6.0	1	FAIL
MCE LA23	4.2	1	FAIL	8.5	1	FAIL
MCE LA24	2.8	1	FAIL	9.1	1	FAIL
MCE LA25	7.9	1	OK	9.6	1	FAIL
MCE LA26	2.7	1	FAIL	1.6	1	OK
MCE LA27	1.6	1	FAIL	6.8	1	FAIL
MCE LA28	1.5	1	FAIL	4.7	1	FAIL
MCE LA29	2.8	8	FAIL	2.7	1	OK
MCE LA30	2.3	8	FAIL	13.2	1	FAIL
MCE LA31	2.9	8	FAIL	2.7	1	FAIL
MCE LA32	2.7	1	FAIL	2.9	1	FAIL
MCE LA33	10.2	1	FAIL	7.5	1	FAIL
MCE LA34	1.7	1	FAIL	10.0	1	OK
MCE LA35	3.8	1	FAIL	24.8	1	FAIL
MCE LA36	1.3	1	FAIL	15.6	1	FAIL
MCE LA37	6.1	1	FAIL	25.7	1	FAIL
MCE LA38	2.2	1	FAIL	11.2	1	FAIL
MCE LA39	1.5	1	FAIL	11.1	1	FAIL
MCE LA40	1.5	1	FAIL	22.1	1	FAIL